Construction and commissioning of a hadronic test-beam calorimeter to validate the particle-flow concept at the ILC

Dissertation
zur Erlangung des Doktorgrades
des Departments Physik
der Universität Hamburg

vorgelegt von
Marius Groll
aus Hamburg

Hamburg
Mai 2007

Abstract

This thesis discusses research and development studies performed for a hadronic calorimeter concept for the International Linear Collider (ILC). The requirements for a detector for the ILC are defined by the particle-flow concept in which the overall detector performance for jet reconstruction is optimised by reconstructing each particle individually. The calorimeter system has to have unprecedented granularity to fulfil the task of shower separation. The validation of the shower models used to simulate the detector performance is mandatory for the design and optimisation of the ILC detector. The construction and operation of a highly granular test-beam system will serve as a tool for this validation. This motivates the urgent need of research and development on calorimeter prototypes. One possible realisation of the hadronic calorimeter is based on a sampling structure of steel and plastic scintillator with analogue readout, where the sensitive scintillator layers are divided into tiles. A newly developed silicon based photo-detector (SiPM) offers the possibilities to design such a system. The SiPM is a multi-pixel avalanche photo-diode operated in Geiger mode. Due to its small dimensions it is possible to convert the light produced in the calorimeter to an electronic signal already inside the calorimeter volume. The basic developments on scintillator, tile and photo-detector studies provide the basis for prototype construction.

The main part of this thesis will discuss the construction and first commissioning of an analogue hadronic calorimeter prototype consisting of $\sim$8000 channels read out with SiPMs. The smallest calorimeter unit is the tile system including the SiPM. The production and characterisation chain of this unit is an essential step in the construction of a large scale prototype. These basic units are arranged on readout layers, which are already a multi-channel system of $\sim$200 channels. In addition, the new photo-detector requires dedicated readout electronics, which has to be suitable for the SiPM signal. Understanding the characteristics of the electronic chain and its interplay with the SiPM has been a central part of the commissioning effort.

First working experience with complete readout layers have been gained at DESY. The calibration procedure of the system has been studied by using well understood electromagnetic shower processes. Afterwards, the readout layers in combination with the steel absorber structure has been exposed to a hadronic test beam at the CERN facility. The fine segmentation of this calorimeter prototype gives for the first time the possibility to access intrinsic properties of hadronic showers. These properties can be used later to compare and validate various existing hadronic shower simulations to achieve a better understanding of the underlying processes of hadronic interactions in matter.

Zusammenfassung

Diese Arbeit beschreibt die Forschung und Entwicklung für ein hadronisches Kalorimeterkonzept für den International Linear Collider (ILC). Die Anforderungen an einen Detektor für den ILC sind bestimmt vom Particle-Flow Konzept. Particle-Flow versucht die Jet-Energieauflösung, durch die Rekonstruktion aller beteiligten Teilchen zu optimieren. Die Hauptanforderung an das Kalorimetersystem besteht in einer hohen Fähigkeit der Schauertrennung, welche durch eine beispiellose Granularität erreicht werden kann. Die Bestätigung der bekannten Simulationsmodelle, die zur Detektoroptimierung verwendet werden, ist wichtig, um den ILC Detektor zu optimieren. Der Bau und Betrieb eines Kalorimetersystems mit extrem hoher Granularität kann helfen, um diese Bestätigung zu erreichen. Dieser Zusammenhang motiviert die dringende Notwendigkeit von Forschung und Entwicklung an Kalorimeterprototypen, um ein solches System zu realisieren. Eine mögliche Realisierung eines solchen Systems beinhaltet als hadronisches Kalorimeter ein Samplingkalorimeter aus Stahlabsorber und Plastikszintillator mit analoger elektronischer Auslese. Die sensitiven Szintillatorlagen sind wiederum in einzelne Ziegel unterteilt, um die nötige laterale Granularität zu erreichen. Ein neu entwickelter Photodetektor, basierend auf einer Siliziumstruktur (SiPM), bietet die Möglichkeit, das produzierte Szintillationslicht bereits an der Szintillatorlage auszulesen und in ein elektronisches Signal zu konvertieren. Die grundlegende Entwicklung des Szintillator und Ziegelsystems, sowie Studien mit Photodetektoren legen die Basis zum Bau eines Vielkanal-Prototypens.

Das Hauptaugenmerk der vorliegenden Arbeit liegt auf der Konstruktion und Inbetriebnahme eines hadronischen Kalorimeterprototypens bestehend aus ∼8000 Kanälen mit SiPM-Auslese. Die kleinste Kalorimetereinheit besteht aus dem Szintillatorziegel, bereits verbunden mit dem SiPM. Die Produktion und Charakterisierung dieses Systems hat zentrale Bedeutung bei der Konstruktion des gesamten Prototypen. Die einzelnen Ziegeln werden in den Ausleselagen angeordnet und jede Lage bildet bereits ein Vielkanalsystem von ungefähr 200 Auslesekanälen. Eine zusätzliche Anforderung besteht in der Entwicklung von geeigneter und an das SiPM Signal angepasste Ausleseelektronik. Die Charakterisierung der Auslesekette und das Zusammenspiel mit dem SiPM bildet einen zentralen Anteil bei der Inbetriebnahme des Prototypens. Erste Betriebserfahrungen mit diesem System wurden an der DESY Teststrahleinrichtung gewonnen. Die Kalibrationsprozedur wurde untersucht und an Daten von elektromagnetischen Schauern angewendet. Danach wurden die Ausleselagen in Kombination mit der Stahlabsorberstruktur an einem Hadronteststrahl am CERN getestet. Die hohe Granularität des Kalorimeterprototypens ermöglicht erstmals überhaupt die innere Struktur von hadronischen Schauern aufzulösen. Dies eröffnet für die Zukunft die Möglichkeit des Vergleichs dieser Eigenschaften mit den existierenden Simulationsprogrammen für hadronische Schauer, um ein besseres Verständnis der grundlegenden Prozesse von hadronischer Wechselwirkung mit Materie zu erreichen.

Contents

Chapter 1

Introduction

There is the worldwide consensus that the next particle physics project after the proton-proton collider LHC, is to be the International Linear Collider (ILC) for electrons and positrons able to deliver energies at the interaction point ranging from 91 to about 1000 GeV, and capable of providing high luminosity above 10^{34} cm^{-2}s^{-1}. The ILC will extend the discoveries made at the LHC and provide a wealth of measurements that are essential for giving deeper understanding of these discoveries, and pointing the way to further evolution of particle physics in the future.

The high precision needed for the physics addressed at the ILC imposes stringent requirements on the detector. A typical ILC event will feature a multi-jet final state topology. Many physic channels have to be reconstructed with unconstrained kinematics, for instance WW scattering processes. In this case extremely high resolution of the calorimetric system is required to disentangle the two concurring processes of $WW\nu\nu$ and $ZZ\nu\nu$ from their di-jet final states [1, 2, 3]. Another example is the determination of the Higgs self coupling which requires the separation of an extremely small signal (0.2 fb, at 500 GeV) from a large multi-jet background. To achieve high energy resolution in the reconstruction of multi-jet final states, it is necessary to obtain the complete topology of each event. This requires a new approach, which exploits the synergy of hardware and software developments to the level of individual particle reconstruction. The particle-flow approach [4] has been identified as a possible solution for this problem.

This revolutionary approach relies on a detector with high efficiency and reliability (stability against unexpected background), maximum hermeticity, and on a highly-segmented calorimeter to allow shower separation. This last point stresses the need of high granularity in transverse and longitudinal directions for both electromagnetic (ECAL) and hadronic (HCAL) calorimeters, which is the main focus of this thesis. The design of a detector for the ILC has to keep these very stringent requirements in mind. Though various designs are emerging from the already advanced R&D studies carried out over the past years, it is widely accepted that the granularity of ECAL and HCAL has to be pushed to the limit; for both analogue and digital approaches are considered. The ECAL granularity has to be in comparison to the HCAL even higher due to the very high density of electromagnetic showers. The HCAL digital approach needs sensitive pads of sizes as small as 1×1 cm^2. In the more conservative analogue approach extracting the energy deposited on small scintillating tiles, the granularity would decrease to tile sizes of almost ten times as large as in the digital case. This still very fine segmentation can only be realised with new photo-detection methods. The detector presented in this thesis is based on a readout system with newly developed silicon-based photo-detectors (SiPM). These photo-detectors are at the basis of the construction, operation, calibration and test of the hadronic calorimeter prototype developed

for the ILC detector.

During the last three years the SiPM has been established as an excellent photo-detector for recording green light from a wavelength shifting fibre used to collect the light produced by individual scintillating tiles. Tests have proved the possibility of operating such a photo-detector in high magnetic fields [5], such as those foreseen for the ILC detector.

As an important step towards mass production, a technical prototype calorimeter equipped with 100 SiPM, has been successfully designed, constructed and operated in the e^+/e^- test beam at DESY [1] ([6, 7]).

Significant for the detector optimisation for the ILC physics reach is the proof of principle of the particle-flow approach. This topic will be addressed with the test of a prototype larger than the technical one, meant for physics studies of hadronic showers. In parallel to the hardware activities required to build and operate such a prototype, a deeper understanding of hadronic shower simulation is needed, together with the development of novel software tools for topological shower reconstruction and separation.

The operation of the technical prototype has provided valuable experience for the design, construction and operation of a 1 m^3 physics prototype with ∼8000 readout channels.

During the years '05-'06 the large prototype has been build and tested both at DESY and at the CERN [2] hadron test facility (SPS [3]), both as a stand alone detector and in combination with a prototype of the Si-W ECAL and steel scintillator tailcatcher. This large prototype will help to establish the technology and especially the new photo-detector SiPM for ILC applications and to perform particle-flow related studies. This includes the opportunity to study large scale application of SiPM; to develop calibration and monitoring procedures with a large prototype; and to develop analysis tools for shower reconstruction and separation. These data will allow for the first time to compare Monte Carlo simulations of hadronic showers with data of sufficiently high granularity to discriminate among the various existing models.

In this thesis the development from the first multi-channel device with SiPMs to the large hadronic prototype with its test-beam effort will be discussed. In order to set a theoretical ground the physics of calorimetry and of electromagnetic and hadronic showers are introduced in chapter 2. The requirements imposed on the calorimeter system by the physics of the ILC are exposed in chapter 3, together with a more generic description of the ILC detector. Chapter 4 presents preliminary R&D work required to establish the technology proposed. Chapter 5 outlines the design of the hadronic calorimeter prototype proposed for the ILC and deals with the commissioning of the physics prototype, in particular of the readout electronics including the data acquisition system for the combined test with the electromagnetic calorimeter.

In chapter 6 the calibration procedure for one calorimeter layer is discussed from studies at the DESY test beam. Finally, in chapter 7 results of the tests with the assembled prototype at the CERN test beam are shown. The physics of hadronic showers is investigated with unprecedented granularity data, and the results are compared to theoretical expectations. Furthermore, a preliminary study on the hadronic shower composition is performed applying an clustering algorithm capable of separating electromagnetic and hadronic shower components. Conclusions on the detector commissioning and performance are given in chapter 8.

---

[1]Deutsches Elektronen-Synchrotron.

[2]European centre of high energy physics in Geneva. The abbreviation stands for Conseil Européen pour Recherche Nucléare.

[3]Super Proton Synchrotron.

Chapter 2

Shower physics and calorimetry

This chapter deals with the complicated matter of electromagnetic and hadronic interaction, shower development in matter and their detection by calorimeters. A high energetic particle interacting with matter looses its energy. The initial energy E of the primary particle is converted into a cascade of particles, known as particle shower. In these iterative interactions with matter the primary energy is shared over more particles until their energy is too low to generate additional ones. After passing this limit the particles are slowed down by elastic interactions until they are stopped and the shower extinguishes.

Showers can be classified into two main types: electromagnetic and hadronic showers. Leptons do not undergo strong interactions, therefore, they can only contribute to electromagnetic showers. Hadrons having mass heavier in comparison to electrons and positrons are not initiating radiation processes, though characterising the second type of shower.

Since the calorimeter prototypes, which will be presented in this thesis, were tested with electromagnetic showers and, due to the fact that hadronic showers have also an electromagnetic sub-shower component, the physics and the detection of electromagnetic showers are introduced in section 2.2.

Afterwards, the properties of hadronic showers and their detection are discussed in section 2.3. A hadronic shower consists, in comparison to an electromagnetic one, of an even larger variety of processes. The exact contribution of each of them remains an open issue. The hadronic calorimeter prototype, discussed in this thesis, was built to measure the absolute contributions of varies processes to hadronic showers. The concept of sampling calorimeters is presented in section 2.4. Then the idea of identifying clusters inside the shower and assign them to one contribution is introduced in section 2.5.

2.1 Introduction

Calorimetry for high energy physics is using shower cascades to measure the initial energy of particles. Although the name calorimetry refers to temperature measurements the energies we are trying to measure generate in matter only temperature changes in the order of 10^{-8} K. Therefore, calorimeters exploit other processes to measure the energy of a particle, like light generation or ionisation effects of these particles. Calorimeters are instrumented blocks of matter in which the particle to be measured interacts and deposits all its energy in the form of a cascade of particles whose energy decreases progressively down to the threshold of ionisation and excitations that are detectable by the readout media. The deposited energy is detectable in the form of a signal which is roughly proportional to the incoming energy. This proportionality is the base of calorimetric measurements.

Since the tasks of calorimeters are manifold, several devices exist. Electromagnetic calorimeters are used to measure the energy deposited by electromagnetically interacting particles (electrons, positrons, photons) while the hadron (i.e. pion, kaon, proton) energy measurement is mainly performed by hadron calorimeters. Furthermore, calorimeters are classified into two types: homogeneous calorimeters, in which the incoming particle energy is measured in a homogeneous block of sensitive absorbing material; and sampling calorimeters, in which the incoming particle energy is measured in a number of sensitive layers interspersed with the layers of absorbing material, the later enabling a fast cascade process. Different materials can be used for both calorimeter types. Homogeneous calorimeters exist consisting of lead-glass, sodium iodide (NaI) crystal, etc. Typical materials for the absorber in sampling calorimeters are iron (Fe), copper (Cu), lead (Pb) or uranium (U) and for the active layers scintillator, silicon, liquid argon, gas etc. Since the prototypes discussed in this thesis are sampling calorimeter, the focus will be on this kind of calorimeters.

The total depth of the calorimeter must be large enough to allow a longitudinal containment of the shower in order to completely absorb the incoming energy. The necessary longitudinal depth of a calorimeter varies with the incoming energy, E, as $\ln(E)$ and therefore the calorimeter can remain a compact construction even at the high energies. The incoming energy being distributed among a large number of secondary particles, can be deposited at large angles with respect to the longitudinal axis of the initial particle trajectory. The result is that the transverse containment of the shower imposes a minimal radial extension of the calorimeter which has to reach at least several times the average radius of a shower. Therefore, the calorimeter dimensions must be large enough to avoid longitudinal and lateral leakage of showers. The granularity is another important requirement for a calorimeter and characterises the spatial separation between readout cells. The granularity is imposed by physics and is fixed in practise by the minimum angle between particles to be detected. In order to separate adjacent showers in a dense jet environment care should be taken in the choice of the transverse calorimeter cell size. In addition, the detailed measurement of the shower position during its development in the calorimeter volume also demands the best possible longitudinal granularity and, therefore, requires a longitudinal segmentation of the calorimeter readout.

Calorimeters must have an energy resolution compatible with the experimental goals. In the case of hadron calorimeters, this possibility is mostly dictated by their relative response to the electromagnetic (e) and hadronic (π) shower, measured by the e/π signal ratio. The equalisation between the electromagnetic and hadronic signals ($e/\pi = 1$, i.e. the compensation condition) is the condition for obtaining the linearity of the energy response of the calorimeter to incoming hadronic showers, and to achieve an energy resolution that improves as the incident energy increases.

The physics conditions met in the experimental zone by a test calorimeter differ from those encountered in an operating beam collision experiment. For instance, the energy resolution of a test calorimeter is assessed from the measurement, in its volume, of the energy deposition from particles of well known dedicated beams, while a calorimeter operating in a physics experiment will face particles produced in collisions. The energy of these particles will cover a large range and many will be produced with relatively low energy, leading to a degradation of the calorimeter energy resolution. The calorimeter performance is also affected by the amount of material in front and by beam conditions, such as the momentum spread of the beam and its degradation due to detectors in front of the calorimeter; and by the precision of beam counters.

In the next section the electromagnetic shower and its underlying processes will be discussed. These processes are responsible for the energy loss of particles and therefore for the

creation of the measurable signal.

2.2 Electromagnetic shower

Electromagnetic calorimeters are built to measure the energy deposited in their volume by processes induced by incident electrons, positrons and photons. This interaction of the incident particle results in a multiplicative process, whose combination of internal processes is dependent on the particle energy. High-energy electrons lose most of their energy by radiation via Bremsstrahlung effect and therefore produce high-energy photons. These high-energy photons undergo materialisation via pair production process (dominant beyond 100 MeV) mainly in the Coulomb field of the nucleus or produce Compton electrons. These alternating processes are going on until the energy becomes too small and the shower stops. In such a particle cascade, initiated by an electron or a photon, the generated particles are electrons, positrons and photons and the cascade is called electromagnetic shower. Low energetic photons mainly interact via the photoelectric process, while low energetic electrons dissipate their energy through collisions. In the showering process, the multiplication process is almost stopped when the electron energy finally reaches the critical energy ϵ_c. The critical energy is the energy at which an electron looses as much energy in collisions as in radiation. The critical energy can be approximately given by

$$\epsilon_c \approx \frac{550}{Z}[MeV], \tag{2.1}$$

with $\frac{\Delta\epsilon_c}{\epsilon_c} \leq 10\%$ for Z $\geq$ 13. For lead the critical energy is around 7 MeV and for steel 24 MeV.

In the following the mentioned processes inside of a electromagnetic shower are discussed, first, the energy loss of charged particles, then the photon interactions with matter.

2.2.1 Energy loss due to ionisation and excitation of atoms

The differential energy loss $-dE$ on a path dx for heavy, charged particles is given by the Bethe-Bloch-Formula [8]:

$$\left\langle \frac{dE}{dx} \right\rangle = \frac{4\pi Q^2 e^2 nZ}{m\beta^2 c^2}\left[ln\left(\frac{2m\beta^2 c^2}{\bar{I}} \cdot \gamma^2\right) - \beta^2 \right], \tag{2.2}$$

where m is the rest mass of an electron, $\beta = v/c$ is the particle velocity relative to the speed of light in vacuum, γ is the particle Lorentz factor $(1 - \beta^2)^{-1/2}$, $Q = ze$ is the particle charge, Z is the atomic number of the medium, $\bar{I}$ denotes the average energy needed to ionise an atom in the medium, and n is the number of atoms per unit volume. The units of dE/dx are usually described in terms of MeV· cm^2/g, which is obtained by dividing equation 2.2 by the density of the traversed material, to obtain a material-independent measure of the energy loss. The value of $\left\langle \frac{dE}{dx} \right\rangle$ for relativistic muons initially falls with increasing energy, and reaches a minimum of $1-2$ MeV/g·cm^2 near $\beta = 0.96$, depending on the transversed material. Particles with energies near this minimum are called minimum ionising particle (mip) [1]. At higher energies, $\left\langle \frac{dE}{dx} \right\rangle$ undergoes a relativistic rise, and levels off at about $2-3$ MeV/g·cm^2 in most materials [9]. Muons with momentum in the GeV/c range have a comparable energy loss

---

[1]A mip is an imaginary particle that loses energy only by ionisation and whose energy loss per unit length is equal to the minimum value for the material concerned.

to mips. Due to the low rate of energy loss, the depth of material needed to contain muons is therefore very large. Thus, calorimeters are not designed for this purpose.

2.2.2   Energy loss of charged particles due to Bremsstrahlung

The energy loss process of electrons and positrons responsible for the development of the electromagnetic cascade is Bremsstrahlung. In general, high energetic charged particles interact with the Coulomb field of atomic nuclei or their orbital electrons and loose energy by radiating photons. The cross-section of the Bremsstrahlung process depends on the mass as $1/m$. Therefore, for particles heavier than electrons it becomes relevant only at energies above 100 GeV or even in the TeV range. The amount of photons N_γ which are radiated in an energy range dE_γ is following the Born approximation and is proportional to Z^2/E_γ. Therefore, Bremsstrahlung is more significant in materials with a high atomic number Z and the radiated photons have most of the time small energies.

The differential energy loss $-dE$ introduced by Bremsstrahlung on a path dx for electrons with energy E is given by:

$$-\frac{dE}{dx}\bigg|_{Brems} = \frac{E}{X_0}. \tag{2.3}$$

The unit radiation length X_0 is defined as the mean distance in a material (A,Z) after which an electron has lost $1/e$ of its initial energy. The radiation length is parameterised by [10]:

$$X_0 \sim 716.4 \frac{1}{\rho} \cdot \frac{A}{Z(Z+1)ln(287/\sqrt{Z})} [g/cm^2]. \tag{2.4}$$

This approximation is better than 2.5 % for all elements except helium (He). The integral of equation 2.3 shows that the energy of a high energetic particle drops after one radiation length to $1/e$ of its initial energy, where e is the Euler number.

In figure 2.1 (a) is shown that the energy loss due to radiation or Bremsstrahlung becomes dominant for energies higher than the critical energy ϵ_c. If the electrons or positrons have energies below ϵ_c the production of photons via Bremsstrahlung stops.

In addition to the discussed interactions ionisation, excitation of atoms and Bremsstrahlung, electrons and positrons are interacting with matter via Møller and Bhabba scattering, annihilation to γ's and multiple scattering on nuclei.

The electromagnetic shower needs on one hand the creation of photons by electron/positrons and on the other hand the creation of charged particles by photon interactions, which are discussed in the following.

2.2.3   Interaction of photons with matter

The main interactions of photons with matter are described by the following processes: photoeffect, Compton scattering, Rayleigh scattering and pair production. The energy dependence of the cross-sections is shown for iron in figure 2.1 (b). For low energetic photons the photoeffect is the dominant process. High energetic photons instead are mostly annihilated due to electron-positron pair production. High energetic means that their energy has to be above the $2m_e c^2$ threshold. The mean free path length λ_{pair} for the pair production is given as [11]:

$$\lambda_{pair} = 9/7 X_0. \tag{2.5}$$

(a)   (b)
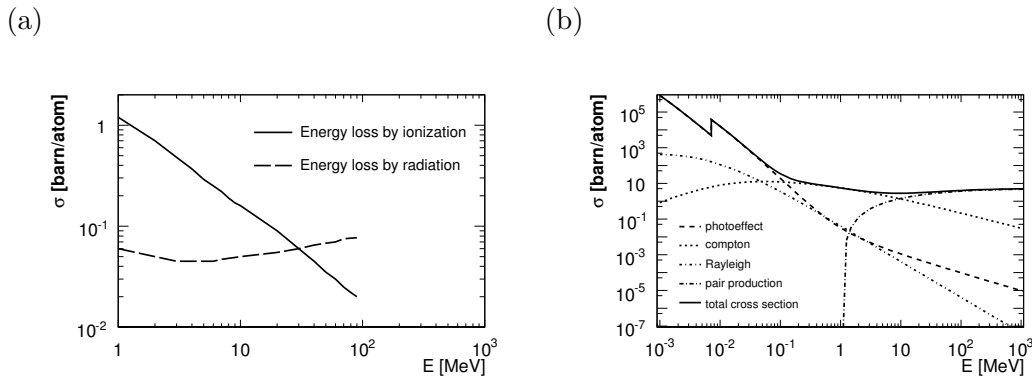
Figure 2.1: *Energy loss mechanisms for electromagnetic processes as a function of particle energy. In (a) the electron processes and in (b) the photon processes in ^{26}Fe are shown. Pair production process becomes dominant from 10 MeV upwards, and energy loss by radiation in the electron case becomes dominant above the critical energy of 28 MeV [12].*

2.2.4 Electromagnetic shower properties

Bremsstrahlung and pair production are the dominant interaction processes for high-energy electrons and photons, respectively. Their cross-sections become almost energy-independent and therefore X_0 has the unit of length. Several radiation lengths have been calculated and tabulated [13, 14] in table 2.1.

material	Z	A	ρ	dE/dx	λ_0	X_0	R_M	ϵ
			[g/cm^3]	[MeV/cm]	[cm]	[cm]	[cm]	[MeV]
Al	13	27.0	2.70	4.37	37.2	8.9	4.68	39.3
Liq. Ar	18	40.0	1.40	2.11	80.9	14.0		29.8
Fe	26	55.9	7.87	11.6	17.1	1.76	1.77	20.5
Cu	29	63.5	8.96	12.9	14.8	1.43	1.60	18.7
W	74	183.9	19.3	22.6	10.3	0.35	0.92	7.9
Pb	82	207.2	11.35	12.8	18.5	0.56	1.60	7.2
U	92	238.0	18.95	20.7	12.0	0.32	1.00	6.6
NaI			3.67	4.84	41.3	2.59		12.4
Plastic scintillator			1.032	2.03	68.5	42.9		87.1

Table 2.1: *Values of atomic number (Z), atomic weight (A), density (ρ), interaction length (λ), radiation length (X_0), Molière radius (R_M) and critical energy (ϵ_c) for several materials commonly used in calorimeters.*

The radiation length can be expressed as X_0 in cm or as X_{g0} in in g/cm^2 by multiplying X_0 with the density ρ. When the absorber is a composition of more than one material, the overall radiation length can be expressed as

$$\frac{1}{X_{g0}} = \sum_i \frac{f_i}{X_{g0i}}, \tag{2.6}$$

where f_i and X_{g0} are the fraction by weight and the radiation length of the absorber i in

g/cm^2, respectively. The corresponding density can be calculated from

$$\frac{1}{\rho} = \sum_i \frac{f_i}{\rho_i},$$
(2.7)

where ρ_i is the density of the absorber i. When calculating the combined radiation length of a sampling structure made of separated materials and not of a composition, equation 2.6 can be used by replacing X_{g0} by X_0 and using f_i as the fraction of length.

One important quantity is the total track length T, which is the summed length of all individual tracks of charged particles showering and dissipating their energy in the calorimeter medium. It is given by

$$T = \frac{E}{\epsilon_c}[X_0].$$
(2.8)

This relation is valid because the energy absorption in matter proceeds mainly via collision losses at the constant rate, per unit of length, of $\approx \frac{\epsilon_c}{X_0}$. Therefore, the total path of cascade charged particles in the absorber will be $\approx E/(\frac{\epsilon_c}{X_0})$.

Simulation codes have been written which reproduce the behaviour of electromagnetic showers in various media with good accuracy. These codes consist of the convolution of all the possible interactions tuned with experimentally achieved parameterisations [13]. To derive some phenomenological quantities we concentrate on the following approximation to describe electromagnetic particle cascades.

Electron and positron multiplication occurs for energy larger than ϵ_c. For energies smaller than ϵ_c collision losses become dominant. The number of charged particles and photons increases rapidly with depth until the maximum of the shower, located at the depth t_{max}, is reached. An incoming photon of energy E, after a depth of ≈ 1 X_0, generates a e^+e^- pair, each carrying $E/2$. After an additional distance of ≈ 1 X_0 both the electron and positron will emit a Bremsstrahlung photon. By continuing the process and assuming equal energy sharing among the generated particles, particles will double every radiation length. The number of particles at the depth t is $N(t) \approx 2^t$, while their energy is $E_p(t) \approx \frac{E}{N(t)} = E \cdot 2^{-t}$, where t is measured in units of X_0. When the particle energy is $E_p \approx \epsilon_c$, the multiplication stops. This occurs at the maximum depth t_{max}, for which $\epsilon_c \approx E \cdot 2^{-t_{max}}$. The maximum depth is given by [13]

$$t_{max} = \left[ln(\frac{E}{\epsilon_c}) + c\right][X_0],$$
(2.9)

where c = -0.5 or 0.5 for incident electrons or photons, respectively.

The probability of pair production and the energy loss due to Bremsstrahlung of electrons and positrons is scaling with the length a particle is traversing the material in units of X_0. Therefore, it is useful to quote distances in the direction of the primary particle x in multiples of X_0: $t = x/X_0$.

In addition it is possible to describe the complete longitudinal profile by

$$\frac{dE}{dt} = at^\omega \cdot e^{-bt},$$
(2.10)

where the first term describes the fast rise to the maximum and the second term describes the exponential decay with parameter b.

The shower maximum is reached after t_{max} radiation lengths from the beginning of the absorber. The slow exponential decay of the shower beyond the maximum is often expressed as e^{-t/λ_a}, where $\lambda_a = \frac{1}{b}$ is the longitudinal attenuation length. The attenuation length show

little dependence on the incoming particle energy due to the fact that at large depths the shower consists mainly of low-energy photons attenuated with rates corresponding to the value of λ_a.

The necessary depth to absorb 98% of the primary energy is given as [15]:

$$L_{0.98} = 3 \cdot (t_{max} + 1.5)[X_0]. \tag{2.11}$$

The lateral spread of the shower, i.e. its development along the direction orthogonal to that of the primary particle, is caused by several physical processes. The photoelectric and Compton scattering generate secondary electrons which are no longer aligned with the incoming photon direction and can even be emitted in the backward hemisphere. Furthermore, multiple Coulomb scatterings of those electrons that cannot radiate but have enough energy to travel away, lead to the spread of electron directions out of the axis defined by the primary particle direction.

The transverse depth unit of a shower is the Molière radius defined as

$$R_M = \left(\frac{E_M}{\epsilon_c}\right)X_0, \tag{2.12}$$

where $E_M = 21.2$ MeV. Values of R_M for various absorbers are listed in table 2.1. In a material made of several absorbers, when none of them is negligible in units of X_0, an estimate of the overall Molière radius can be obtained from the expression

$$\frac{1}{R_M} = \frac{1}{E_M} \sum_i \left(f_i \frac{\epsilon_{c,i}}{X_{0i}}\right), \tag{2.13}$$

where f_i, $\epsilon_{c,i}$ and X_{0i} are the length fraction, critical energy and radiation length of the absorber i, respectively. Energy is deposited beyond the cylindrical volume defined in units of the Molière radius. Outside 1 R_M $\approx$10% of the energy is deposited. The 95% radial containment (R_e) for electromagnetic particle cascades is given by

$$R_e(95\%) = 2R_M \tag{2.14}$$

and in three R_M 99% of the shower is contained.

The lateral distribution of the shower depends on the calorimeter depth at which it is measured. At least, a two component structure is needed to describe the transverse profile of the electromagnetic shower which displays a narrow central and a broad peripheral part. The central part scales as R_M, and is mainly due to multiple scattering effects produced by the fast electrons responsible for the deposition of most of the incident energy. The peripheral part is mainly due to the propagation of photons. The spatial distribution of this latter component is determined by the minimum value of an attenuation coefficient which depends strongly on the absorber medium. The contribution of pair production and Bremsstrahlung to the transversal shower profile are negligible, because their opening angles are small. One possible function to describe the transversal shape is given by

$$f(z) = A_1 exp\left(-\frac{|z - z_0|}{b_1}\right) + A_2 exp\left(-\frac{|z - z_0|}{b_2}\right), \tag{2.15}$$

where z is the transverse coordinate (in cm), z_0 is the impact point of the shower and b_1 and b_2 are the two lateral attenuation, representing the central and peripheral shower components, respectively, with their contribution A_1 and A_2.

2.3   Hadronic shower

In this section hadronic showers are discussed. First, the particle cascade mechanism with the underlying processes are explained, before some phenomenological quantities are derived.

The absorption in matter of hadronic particles, which undergo strong interactions, develops as a cascade process called hadronic shower. The nuclear interactions and the subsequently strongly interacting particles govern this development. In each interaction of the cascade in the calorimeter volume a wide spectrum of secondary particles are produced which have again a variety of subsequent interactions with the nuclei of the absorber. Within the sequence, photons from π^0 decay are produced, which initiate localised electromagnetic showers within the hadronic cascade. During the shower development, the charged particles lose energy through ionisation. In addition to the multiplication of particles that results from the strong interactions, nuclear binding energy losses play a role. This effect is constituted on the resulting energy loss from de-excitation of involved nuclei, which releases a host of low energy nucleons. Thus, part of the incoming energy will not be deposited and therefore not be detectable by collision losses and become *invisible energy*.

The understanding of the calorimeter response to hadronic showers requires insight in the processes occurring in all stages of the shower development. In the case of hadronic showers, the wide variety of processes that may occur at all stages of the shower development makes their description and the calculation of the resulting calorimeter response rather more complicated than in the purely electromagnetic case. A complete theory does not exist, because there is no proven description of nuclear matter. Therefore, simulation of showers must rely on models based on phenomenological understanding or parameterisations of data. These models have to take into account the physical processes during the intra-nuclear cascading and the various many-body final states interactions.

2.3.1   Hadronic shower processes

As long as the hadron is not interacting inelastically with a nucleus of the absorber material it is only loosing energy by ionising and exciting atoms of the absorber material. The probability of an inelastic hadron-nucleus interaction P_I after a distance x is given by

$$P_I = 1 - e^{-x/\lambda_0}, \tag{2.16}$$

where λ_0 is the *nuclear interaction length* which can be approximated for a material with mass number A and density ρ [15] as

$$\lambda_0 \sim \frac{35 A^{1/3}}{\rho} [g/cm^2]. \tag{2.17}$$

As in the case of X_0 also λ_0 is independent of the type and energy of the hadron.

In figure 2.2 a sketch of a hadronic cascade is shown. The path before the incoming particle interacts is statistically given by the nuclear interaction length. In general the cascade can be divided in three parts: the hadronic component, which includes produced mesons, nuclear fragments and nucleons (p,n), the electromagnetic component, which is initiated by the π^0 decay, and the neutron component. In the following the possible strong interactions are discussed in detail.
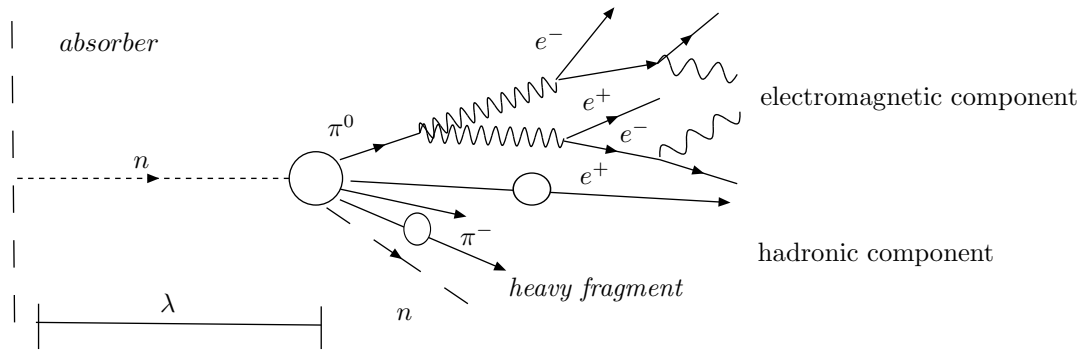
Figure 2.2: *A schematic of the hadronic shower development and its sub-processes.*

Intra-nuclear and inter-nuclear cascade

After entering a nucleus a hadron can collide with a nucleon. In this case a intra-nuclear cascade is created which is spatially localised in the nucleus. A result of this intra-nuclear cascade is the spallation or break-up of the nucleus, which means that new particles are produced in this process. These kind of reactions are manifold. A detailed description and the measured cross-sections can be found in [16]. The secondary particles which are leaving after the spallation the nucleus are high energetic charged and uncharged pions, protons, neutrons and any hadrons (e.g. λ, Σ, Ω).

The produced high energetic secondary particles are also interacting inelastically with other nuclei after a certain distance. This development can be called inter-nuclear cascade. In between two hadron-nucleon interactions charged hadrons continue to lose energy due to ionisation and excitation of atoms in the absorber.

Evaporation and nuclear fission

A nucleus in an excited state tends to lose the additional energy by reducing its mass number A. For light nuclei, the dominant de-excitation process is evaporation, which means that some nucleons or small nuclear fragments like deuteron, tritium (^{3}H$^+$), ^{3}He nucleus and α particles are leaving the nucleus, until the excitation energy is less than the binding energy of one nucleon. The remaining energy, typically a few MeV, is released in the form of γ rays [17]. For heavy nuclei, nuclear fission is another possibility for de-excitation of the nucleus. The ratio between nuclear fission and the evaporation probability for lead is 0.05 whereas for uranium it is 0.8 [18]. After the nuclear fission the produced fragments are de-excited by evaporation.

The time scale in which spallation processes take place are in the order of 10^{-22} s. This is much different in comparison to the time scale of nuclear de-excitation, which is between 10^{-18} s and 10^{-13} s. This difference enables us to regard both processes separately.

2.3.2 Hadronic shower composition

The hadronic shower is propagated through a succession of various inelastic interactions leading to particle production characterised by a multiplicity increasing logarithmically with the available energy. In a hadron interaction, about half of the incoming energy is carried away by leading particles and the remaining part is absorbed in the production of secondaries. The average neutral pion fraction is a third of all produced pions. The nuclear processes involved

in the generation of the hadron cascade produce relativistic hadrons, mainly pions, nucleons from spallation and from evaporation, break-up and recoiling nuclear fragments. An important fraction of the secondaries produced in the process consist of particles, mainly π^0 (η) mesons, which decay via electromagnetic interaction and generate an electromagnetic cascade and are the reason why every hadronic cascade has an electromagnetic shower component. The uncharged pions decay into two gammas in 98.8% and into an electron-positron pair plus an additional gamma in 1.2% of the cases. The number of π^0 and their energy fluctuates from event to event. The average fraction, f_{em}, of incoming hadron energy deposited by electromagnetic cascades of secondary particles as a function of the incoming hadron energy E is [19, 20]

$$f_{em} \simeq f_{\pi^0} \approx (0.11 - 0.12) \cdot ln(E/GeV). \tag{2.18}$$

The size of this electromagnetic component is largely determined by the production of π^0 (and η) in the first interaction and therefore fluctuates heavily from event to event. The average fraction converted into electromagnetic cascade increases with energy. Equation 2.18 gives unreasonable values for low and very high energies. For low energies smaller than 1 GeV the logarithmic part becomes negative and for energies higher than 22 TeV f_{em} becomes bigger than 1.
The π^0 induced electromagnetic showers are the major contribution to f_{em}. A small contribution to f_{em} is provided by gamma radiation of excited nucleus. This contribution belongs to f_{em} because the energy of the produced gammas is deposited in electromagnetic processes and is smaller than two percent.

In principle all the energy which is not deposited by electrons, positrons or gammas contribute to the hadronic component of the hadronic shower. The hadronic component, f_{had}, of the hadron shower deposits its energy in the calorimeter via several mechanisms:

- Ionisation and excitation by the primary particle before the first inelastic interaction.

- Ionisation and excitation by the secondary particles like protons and charged pions.

- Ionisation by heavy nuclear fragments.

- Nuclear binding energy losses by nuclear break-up and recoil of nuclear fragments (spallation, evaporation and fission).

All ionisation processes are responsible for 40-60 % of the complete energy deposition, decreasing with increasing A of the absorber material. The binding energy losses explains between 30 and 45 % [21], decreasing with decreasing A. In addition a neutron component exists due to generated low energetic neutrons with energies too low to produce π^0. The neutron component is between 10 and 15 %, decreasing with decreasing A. An additional small contribution about one percent to the total hadronic shower energy is carried by neutrinos which are produced from secondary charged pions over the decay chain $\pi \rightarrow \mu \rightarrow e$. [13]

As long as binding energy losses are neglected the following equation is valid [22],

$$f_{had} \simeq (1 - f_{\pi^0})^{N_G}, \tag{2.19}$$

where N_G is the number of generations of intra-nuclear cascades inside of the internuclear cascade. Since N_G increases with increasing primary particle energy, f_{had} decreases with increasing primary particle energy.

2.3.3 Spatial development of hadronic shower

After the short overview of physics processes involved in a hadronic shower, the following section will deal with some general properties of hadronic shower like its spatial distribution. In [13] a summary of experimental earned knowledge of properties of the spatial distribution of hadronic shower is given.

Longitudinal shower shape

The longitudinal development of a hadronic shower along the direction of motion of the incoming particle is described in units of nuclear interaction length, λ_0, which is given by

$$\lambda_0 = \frac{A}{N\rho\sigma_{nA(inelastic)}}, \tag{2.20}$$

where $\sigma_{nA(inelastic)}$ is the inelastic cross-section (in cm^{-2}) on the nucleus of atomic weight A and A, N, ρ are the atomic weight, the Avogadro number and the density of the material (g cm^{-3}). Values for λ_0 for some absorber materials are listed in table 2.1. The nuclear interaction length in g cm^{-2}, is defined in equation 2.17. In case of a composition of different materials the combined nuclear interaction length can be calculated by the following formula

$$\frac{1}{\lambda_g 0} = \sum_i \frac{f_i}{\lambda_{g0,i}}, \tag{2.21}$$

where f_i is the fraction of weight and $\lambda_{g0,i}$ the nuclear interaction length of the used materials in g cm^{-2}. When calculating the combined nuclear interaction length of a structure of separated materials and not of a composition, equation 2.21 can be used by replacing λ_{g0} by λ_0 and using f_i as the fraction of the total structure depth.

The position of the shower maximum scales with the nuclear interaction length λ_0. It is reached after the length $t_{max} \cdot \lambda_0$ after the primary hadron has entered the absorber material. Several parameterisations exist, which give different results. For illustration two parameterisations of experimental data are shown in figure 2.3. The following equation is presented in reference [13]:

$$t_{max} \simeq 0.2\ln(E/GeV) + 0.7. \tag{2.22}$$

A different parametrisation for iron is given in [14] and predicts a different shower shape:

$$t_{max} \simeq 0.58\ln(E/GeV) - 0.23. \tag{2.23}$$

Both equation determine t_{max} in units of λ_0. For illustration the two described parameterisations are shown in figure 2.3 (a).

The hadron shower, similarly to the electromagnetic shower, develops in average along the incoming particle direction, as long as the produced secondaries have enough energy to continue the multiplication process. The 95% longitudinal containment of hadronic shower cascades, $L_{95\%}$ is given to a first approximation by [13]

$$L_{95\%} \approx t_{max} + 2.5\lambda_a, \tag{2.24}$$

where λ_a describes the exponential decay of the shower beyond t_{max} and varies with the energy as $\lambda_a[cm] = (E[GeV])^{0.13}$ and is referred to as *attenuation length*. This approximation is valid for the energy range of a few GeV to a few hundred GeV within $\approx 10\%$ and is shown in figure 2.3 (b) from 6 to 20 GeV. The complete longitudinal shower profile can be parametrized with the same function as for electromagnetic showers but has much higher fluctuations along
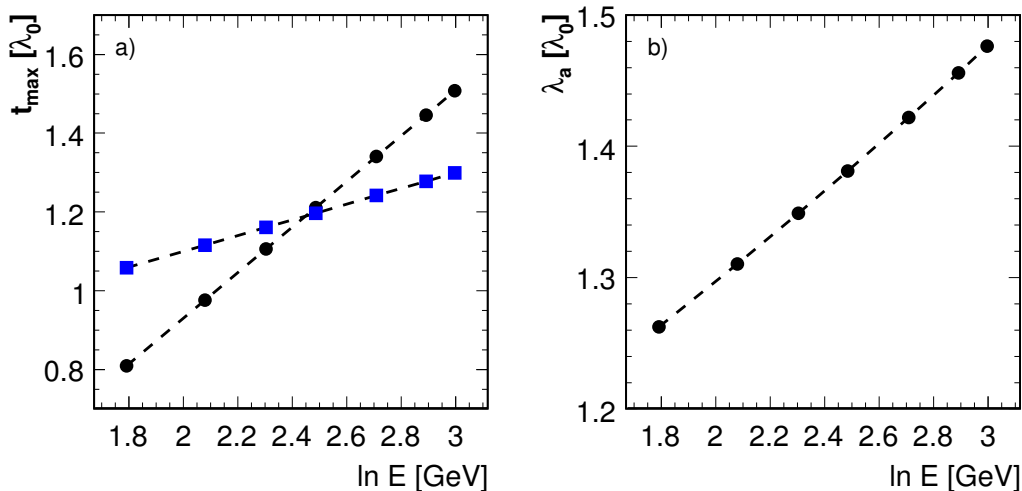
Figure 2.3: *(a) Parameterisations of the depth of the shower maximum dependence on energy according to reference [14](full points) for iron and to reference [13](full squares). (b) Parameterisation of the attenuation length λ_a dependence on energy according to reference [13]. The shown energy range is from 6 to 20 GeV.*

this shape. Figure 2.4 (a) demonstrates the good agreement between various hadronic shower measurements and the parameterisation of equation 2.10.

To have a longitudinal containment of about 95% between 4.5 and 5.5 λ are needed for hadron energies between 10 and 50 GeV. For lead absorber it would mean to have a total absorber thickness of 77 cm. The large absorber depth needed is a main reason why homogeneous calorimeters can hardly be used in hadronic calorimeters at high energies. Therefore, hadronic calorimeters are usually sampling devices.

Lateral shower shape

The hadronic shower has a lateral spread due to the production of secondaries at large angles. The shape and width of the lateral shower profile are dependent on the depth of the shower. The width of the shower core in the longitudinal middle of the shower is approximately 0.1 up to 0.5 nuclear interaction length. Its overall transverse dependence can be approximately described by two components: a main component along the shower axis which decays fast, and a large and long peripheral component composed mostly of low-energy particles (including neutrons), which carries a relevant fraction of energy away from the shower axis. A possible description of the transverse profile is given by the sum of two exponential terms which represents the central core of the shower and its halo like in the electromagnetic case shown in equation 2.15. These two components are visible in figure 2.4 (b) below and above $\approx$6 cm. The 95 % radial containment ($R_{95\%}$) for hadronic showers is

$$R_{95\%} \approx 1\lambda_0. \tag{2.25}$$

(a)

(b)
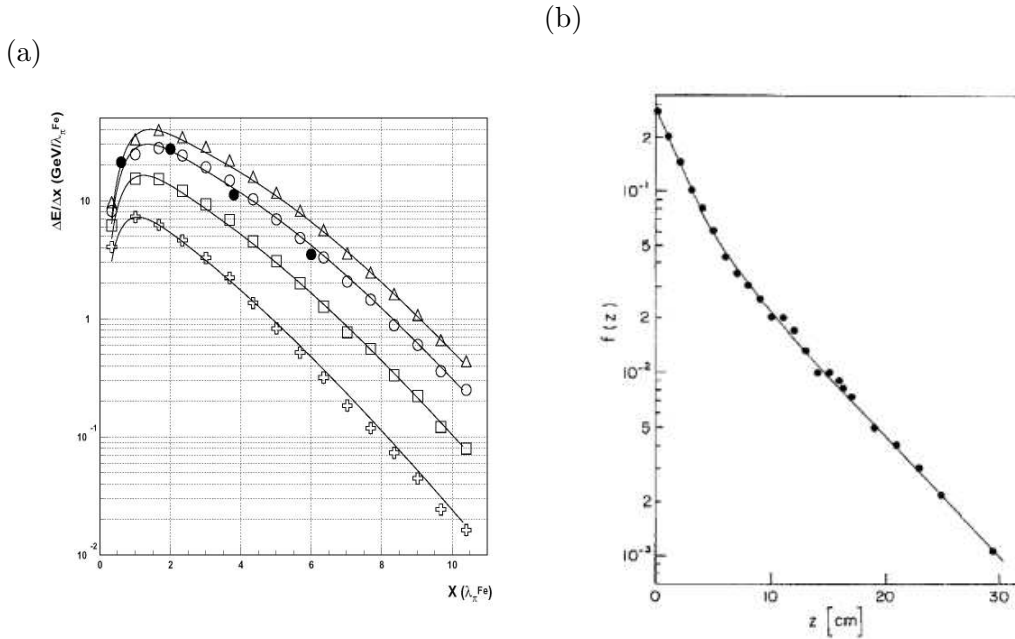
Figure 2.4: *(a) Longitudinal profiles of hadron showers of 20 GeV (crosses), 50 GeV (squares), 100 GeV (open circles) and 140 GeV (triangles) energies as a function of the longitudinal co-ordinate x in units of λ_0 for conventional iron-scintillator calorimeter and of 100 GeV (black circles) for the ATLAS tile iron-scintillator calorimeter. The solid lines are parameterisa-tions [23]. (b) Mean differential lateral profile, $f(z)$ as a function of the lateral distance z in cm for incoming anti-protons of 25 GeV [24].*

2.4 Sampling Calorimeter

After the discussion of electromagnetic and hadronic shower physics and properties, the focus in this section will be on how to measure these properties with sampling calorimeters. This thesis will describe the results obtained from two sampling calorimeter prototypes. Since the properties of electromagnetic and hadronic sampling calorimeters are for a large fraction the same, both types will be discussed together.

The energy measurement with a sampling calorimeter is based on the shower development characteristics. The shower profile is sampled by a combination of absorber and sensitive read-out media. A special and often used kind of sampling calorimeter is the sandwich calorimeter. In this case the absorber and the readout materials are built in an alternating layer structure. The absorber material usually has a high atomic number and it is mainly responsible for the shower development. The readout material usually has lower density and a low atomic number. The energy of incoming particles is measured in active layers, usually with a thickness in units of radiation length much smaller than the thickness of the corresponding passive samplers, while the cascade process is generated in the passive layers. Some components of the shower produce in the readout material a measurable signal. This signal is statistically proportional to the energy deposited by the shower and defines the calorimeter response. These kind of measurable signals are for example light produced in a scintillator or the produced charge in an ionisation chamber. This detected energy is called visible energy ϵ_{vis} and is usually a tiny fraction of the incoming particle energy and corresponds to the measurement of a fraction of

the total track length (see equation 2.8) and is therefore

$$\epsilon_{vis} \propto E. \tag{2.26}$$

Equation 2.26 is the basic principle of sampling calorimeter and has the consequence that the calorimeter response is expected to have a linear dependence on the incident particle energy. This equation holds for electromagnetic showers in which almost all the incoming particle energy is finally dissipated by processes of atomic ionisation and excitation.

2.4.1   Calorimeter response

In general, the calorimeter responds differently depending on the incident particle. To compare the signals of different particles in the calorimeter it is mandatory to compare their sampling fraction. The sampling fraction is defined as the ratio of the detected ionisation energy to the total ionisation energy deposited in the whole calorimeter, i.e. active and passive layers. In principle, the sampling fraction is only defined for charged particles, since they are the only ones that lose energy by ionisation. However, this concept is extended also to neutral particles, which interact elastically or inelastically with nuclei or protons, generating charged products.
As a scale for the calorimeter signal the sampling fraction for a mip is used. The energy deposited by a mip depends mainly on the thickness of the traversed material and only weakly on the material itself. The sampling fraction of a mip is commonly used to define the sampling fraction of a calorimeter. Typical sampling fractions for sampling calorimeters with plastic scintillator readout amount to about 2-10 %, $\approx$1 % for silicon readout and $\approx$10^{-4} for gaseous detectors.
In the following these response differences are discussed in detail for different particles.

The e/mip ratio

In a sampling calorimeter, the visible energy is the result of collision losses in the active readout layers. Therefore, the calorimeter response to minimum-ionising and non-showering particles (mip) can be used as a scale or as a measurement unit of response to electromagnetic (e) and hadronic showers (h). Since the fictitious mip-particle cannot be used in practise to calibrate an existing calorimeter, one uses muons for calibration and derives from the measured muon signal the signal for a mip. Only at low energies (several hundred MeV) does the muon have the energy loss of a mip. At higher muon energies the relativistic rise, Bremsstrahlung, pair production and nuclear interactions become important.

A e/mip ratio equal to 1 means that the average signal for a muon that traverses a volume and loses, for example, 500 MeV in that process is equal to the average signal generated by a 500 MeV electron or photon that is absorbed by shower development in the same volume. The ratio between total and visible energy is referred to as the *sampling factor*

$$SF = \frac{E_{tot}}{\epsilon_{vis}}. \tag{2.27}$$

In practise this ratio is the inverse of the sampling fraction value. The e/mip ratio is given then by

$$\frac{e}{mip} = \frac{a(e)}{a(mip)}, \tag{2.28}$$

and should be in case of a steel-scintillator sampling calorimeter around 0.9. This ratio is energy independent. The e/mip ratio is a fundamental characteristic of the structure of sampling calorimeters, essentially related to the difference between the readout and absorber Z values of the materials. The e/mip ratios are smaller than 1 for $Z_{absorber} > Z_{readout}$, approximately 1 for $Z_{absorber} = Z_{readout}$, and bigger than 1 for $Z_{absorber} < Z_{readout}$. This is due to soft photons which are generated, and in low Z materials locally absorbed. In high Z materials soft photons can travel longer distances [13].

The e/h, e/π, h/mip and π/mip ratios

The considerations made in this section so far are valid for both electromagnetic and hadronic calorimeters. However, the larger amount of processes involved in hadronic showers has implications on the performance of hadronic calorimeters, which are discussed in the next section.

While the energy deposited in active layers, ϵ_{vis}, comes mainly from processes of energy loss by collisions of charged particles produced during the multiplication process, the interactions leading to the generation of charged secondary particles in electromagnetic and hadronic cascades are different. In hadronic showers there is a large A-dependent fraction of the incoming hadron energy spent in releasing nucleons and nucleon aggregates (like α-particles), that are bound in atomic nuclei. This process has no equivalent in electromagnetic cascades and largely contributes to the invisible hadronic energy, also referred to as binding energy. Therefore, at the same incoming energy, the signal for electrons (or photons), e, differs from the signal for ideal hadrons, h. These ideal hadrons are hadrons not accompanied by electromagnetic cascading processes ($f_{em} = 0$). The e/h ratio is given by

$$e/h \equiv \frac{\epsilon_{vis}(e)}{\epsilon_{vis}(h)}, \tag{2.29}$$

where $\epsilon_{vis}(e)$ and $\epsilon_{vis}(h)$ are the visible energies, at the same incoming particle energy. The e/h ratio is usually larger then 1. As in the case of electromagnetic showers for which $\epsilon_{vis}(e)$ is proportional to the incoming particle energy, also $\epsilon_{vis}(h)$ is proportional to the incoming ideal hadron energy. Therefore, the e/h ratio is an intrinsic energy independent property of the calorimeter.

The shower of a real hadron is made of a pure electromagnetic component and a pure hadronic component. The respective fractions of the total incoming energy are f_{em} and $(1-f_{em})$. Where the binding energy is artificially associated to the hadronic component. The term f_{em} has an approximate logarithmic energy dependence. The visible energy, $\epsilon_{vis}(\pi)$, corresponding to a real pion signal can be written as

$$\epsilon_{vis}(\pi) = f_{em}\epsilon_{vis}(e) + (1 - f_{em})\epsilon_{vis}(h). \tag{2.30}$$

Therefore, the e/π ratio is

$$e/\pi \equiv \frac{\epsilon_{vis}(e)}{\epsilon_{vis}(\pi)} = \frac{\epsilon_{vis}(e)}{f_{em}\epsilon_{vis}(e) + (1 - f_{em})\epsilon_{vis}(h)} = \frac{e/h}{1 - f_{em}(1 - e/h)}. \tag{2.31}$$

The e/π ratio contains the energy dependent term f_{em} and, therefore, depends on the energy of the incoming particle hadron, on the atomic weight of the absorber, and on the Z-values of the passive samplers and active layers. Using equation 2.31 the e/h ratio can be written

$$e/h = \frac{(e/\pi)(1 - f_{em})}{1 - f_{em}(e/\pi)}. \tag{2.32}$$

The e/h ratio of a calorimeter can be evaluated experimentally by measuring the e/π ratio at the same incoming energy of electrons and pions.

As in the case of electromagnetic calorimeters, the hadronic calorimeter response to mips or to muons, can be used as a scale of measurement of the response to hadronic showers. The h/mip and π/mip ratios, for ideal and real hadrons, are defined by

$$h/mip \equiv \frac{\epsilon_{vis}(h)}{\epsilon_{vis}(mip)}, \qquad \pi/mip \equiv \frac{\epsilon_{vis}(\pi)}{\epsilon_{vis}(mip)}. \qquad (2.33)$$

The h/mip ratio is an intrinsic energy-independent property of the calorimeter like the e/h ratio. The π/mip ratio instead depends on the hadron incoming energy, due to the energy-dependent term f_{em}.

In calorimeters, where neutrons contribute in a minimal way to the overall visible energy and the active media have a linear response to the energy deposited by collisions, the h/mip ratio is expected to be slightly larger than ≈ 0.4 (≈ 0.6) for high-A (low-A) nuclei. The corresponding values of e/mip ratios are about 0.50-0.65 and 0.70-0.85, respectively.

Both e/h and h/mip ratios are energy-independent intrinsic properties of a sampling calorimeter. In case of e/h=1, also e/π = 1 and vice versa and therefore the ratio e/π becomes energy-independent. The condition e/h=e/π=1 is called the *compensating condition*. In this case also h/mip = π/mip = e/mip is valid. In equation 2.30 is shown that the response to pions depends on the energy-dependent quantity f_{em}. Only in case of compensation e/h = 1 the energy-dependence of f_{em} cancels that of $(1 - f_{em})$. This can be seen from equation 2.30, which becomes $\epsilon_{vis}(\pi) = \epsilon_{vis}(h)$. Otherwise, due to the energy dependence of f_{em} the response is non-linear.

However, compensation does not remove possible energy dependencies introduced by the binding energy in the term $(1 - f_{em})$. In the case of hadron calorimeters, an energy-dependent fraction of the incoming energy goes in breaking up of nuclei, in low-energy neutrons and in undetectable neutrinos, thus preventing a linear calorimeter response to the incoming hadron energy. The goal of compensation is the restoration of equation 2.26, this may not be possible if in a given calorimeter the fraction of invisible energy depends on the incoming energy.

Most of the calorimeters actually in use are non-compensating. Missing compensation does not lead only to different signals from electromagnetic and hadronic showers, but it also degrades the energy resolution for hadrons. This effect comes from the large event to event fluctuation of f_{em} in hadronic showers. In general, the average ratio between signals from electromagnetic and hadronic particles of the same incident energy is calorimeter- and energy-dependent, and for non-compensating calorimeters there is a higher response for electromagnetic particles, typically $e/h \simeq 1.1 - 1.35$.

Various approaches to the realisation of the compensation condition exist. In principle two different possibilities have to be considered: hardware-compensation and software-compensation. The hardware approach tries to enhance the hadron signal or to attenuate the electron signal magnitude. The software approach tries to identify the electromagnetic sub-shower contribution in the hadron shower and to use weighting techniques.

The increase of the hadronic signal can be obtained by detecting part of the energy carried by neutrons, which are generated in the cascade process. For example in hydrogen-rich materials like plastic scintillators neutron-proton scattering processes generate fast recoiling and ionising protons in the active material. Another possibility is to use U^{238} as absorber, because due to its fission capability slow neutrons contribute to the visible energy. Another approach is to tune the ratio by an appropriate choice of both passive and active media. Instead of increasing the hadron signal it is also possible to decrease the electromagnetic response by shielding the active layers by thin sheets of low-Z material to suppress contributions from soft photons in

electromagnetic showers [9].

If high resolution is not required during readout, e.g. for triggering, corrections corresponding to compensation can be applied by an a posteriori algorithm ("off-line"), when the shower profile (mostly the longitudinal distribution) is known [25, 26]. Just how much can be recovered by calibrations of this type, is strongly detector-dependent. In [27] the authors explored the possibilities for a specific non-compensating sampling calorimeter, using individual weights for sampling layers.

2.4.2   Energy resolution of sampling calorimeter

The detection of particle showers in calorimeters is based on statistical processes. This is valid for electromagnetic and hadronic calorimeters. In sampling devices the visible energy is proportional to the number of secondary ionising particles N_P. The statistical energy sampling fluctuations on N_P affects the visible energy resolution proportional to $\sqrt{N_P}$. Therefore, the energy resolution of a sampling calorimeter is

$$\frac{\sigma(E)}{E} \propto \frac{\sigma(\epsilon_{vis})}{\epsilon_{vis}} \propto \frac{1}{\sqrt{E}}, \tag{2.34}$$

for a sampling calorimeter with constant sampling fraction, where $\sigma(\epsilon_{vis})$ is the standard deviation of the visible energy ϵ_{vis}. In the case of different sampling fractions it is needed to scale the ϵ_{vis} to the total energy as described in section 2.4.1.

Ideally, the calorimeter must be of sufficient thickness to allow the particle to deposit all its energy inside the detector volume in the subsequent cascade of increasingly lower energy particles. The total depth of the calorimeter must be large enough to allow a longitudinal containment of the shower in order to completely absorb the incoming energy. The necessary longitudinal depth of a calorimeter varies with the incoming energy as $ln(E)$. The energy resolution is expected to improve, so that $\frac{\sigma(E)}{E}$ decreases with increasing energy. When particles generate fully contained showers, the resulting visible energy distribution is almost Gaussian with a peak located at the position of the mean visible energy. The width of the distribution defines the energy resolution and is related to the sampling fluctuations.

In addition two effects can worsen the energy resolution of a sampling calorimeter: path length fluctuations and Landau fluctuations. These effects explain the degradation of the energy resolution because of different path of large-angle particles (path length fluctuations) through the readout material and of large energy transfers in the ionisation process (Landau fluctuations). The latter fluctuations add a minor contribution to the deterioration of the calorimeter energy resolution.

In hadronic showers, the visible energy $\epsilon_{vis}(\pi)$ is usually not proportional to the incoming hadron energy since there is always an electromagnetic component, whose fraction varies with the energy. This fraction, f_{em}, undergoes fluctuations on the event-by-event basis. As the e/π ratio becomes different from 1 (non-compensation), the contribution of fluctuations (which are of a non-Gaussian nature) in f_{em} is more and more important and affects the $\frac{1}{\sqrt{E}}$ behaviour of the energy resolution. Likewise, fluctuations in the invisible energy contribute.

These intrinsic limitation in hadronic shower due to the fluctuations in the manifold production processes are much larger than for electromagnetic processes and are the major ingredient of the final performance of a hadron calorimeter. Intrinsic shower fluctuations are between $\frac{0.20}{\sqrt{E}[GeV]}$ to $\frac{0.45}{\sqrt{E}[GeV]}$ depending on the capability to compensate for nuclear effects and on the sensitivity of the readout material to neutrons [13]. As a consequence, compensating calorimeters with hydrogenous readout are expected to minimise the contribution from the

intrinsic resolution. These numbers refer to single hadronic particles. The $\sigma(E)/E$ for jets is typically higher by a factor 1.3 or more, because a jet consists of several particles like π and electrons, which is another source for fluctuations. Since well-optimised electromagnetic calorimeters can reach energy resolutions of $\approx \frac{0.10}{\sqrt{E[GeV]}}$ or better, hadronic calorimeters have a worse energy resolution. For example a energy resolutions of $\frac{0.43}{\sqrt{E[GeV]}}$ has been achieved for a compensating lead calorimeter [21].

The total energy resolution for the detection of hadronic showers can be described by the following expression:

$$\frac{\sigma(E)}{E} = \frac{a_{samp} \oplus a_{intr} \oplus a_{pe}}{\sqrt{E}} \oplus b \oplus \frac{c}{E}, \tag{2.35}$$

where a_{samp}, a_{intr} and a_{pe} correspond to the sampling, intrinsic shower and photo-statistics fluctuations. The term b contains the contribution from non-compensation, calibration errors, non-uniformities and non-linearities in photo-detectors and ADCs. This component is called constant term and limits the calorimeter performance at very high energies. In case of longitudinal and lateral leakage the constant term would increases. The term $\frac{c}{E}$ corresponds to noise fluctuations introduced by instrumental effects. The instrumental noise and detection statistics affect the overall energy resolution and particularly limit the detector performance at low energies.

2.4.3   Position measurement

The impact point of the primary particle on a calorimeter can be measured by exploiting the longitudinal segmentation and transversal granularity, which define the cell size. If the granularity is chosen to be equal or smaller than the Molière radius, the lateral spread of the electromagnetic shower over several cells allows the reconstruction of the impact point. The position is usually measured by using the centre of gravity of the energies, E_i, deposited in the cells:

$$\bar{x} = \frac{\sum_i x_i E_i}{\sum_i E_i}, \tag{2.36}$$

where x_i are the coordinates of each cell hit with respect to the central one, and E_i is the energy deposited in the cell i. The precision of this measurement increases with the number of calorimeter cells hit by the cascade particles and decreases with the cell size. If in electromagnetic showers the incoming energy increases the number of cascade particles increases as well but the lateral size remains almost unchanged, because the production angle of Bremsstrahlung and multiple scattering decreases. Therefore, the precision improves with energy.

2.4.4   Electron-hadron separation

The separation between electrons, photons and hadrons is achieved in sampling calorimeters by installing an electromagnetic calorimeter in front of a hadron calorimeter. This takes advantage of the difference in the lateral and longitudinal shower profile of hadrons and electrons. This is accomplished by dividing the sampling calorimeter into an electromagnetic section several radiation lengths deep and a hadronic section with a depth of several nuclear interaction lengths. This system provides already a 99% pion/electron separation. If the ECAL consists of an absorber material with very different radiation and nuclear interaction lengths and is around one nuclear interaction length deep, it serves also as a discriminator between electrons

and hadrons by itself. In case of tungsten the ratio between interaction length and radiation length is around 30. This reduces the probability for hadronic interaction in an ECAL of about 1 λ_0 length, still ensuring high electromagnetic containment.

2.4.5 Detection of neutron energy

In hadronic showers, neutrons are produced either by spallation or, mostly, are evaporated from highly excited nuclear fragments. The energy spectrum has a peak around 2 MeV and is finished at 20 MeV (Watt spectrum [28]). For fissionable nuclei (U^{238}), a large amount of fast neutrons are generated owing to subsequent fission processes. Those neutrons with energies larger than about 1 MeV dissipate their energy through inelastic (n,γ) reactions on heavy nuclei. At lower energies (below 100 keV), neutrons are captured by nuclei. In spallation neutrons with energies above 10 MeV can be produced. Some of the high energetic neutrons can travel some distance inside the calorimeter before interacting mainly elastically. As already mentioned plastic scintillator can detect neutrons by neutron-hydrogen collisions. In this elastic scattering process half of the neutron energy can be transferred to the recoil proton, which leads to an increase of the hadronic signal.
The increase of the hadronic signal is limited by the saturation of the scintillator response, which occurs in the presence of dense ionisation losses. This phenomenon has been studied and is described by the Birk's law [29].
However, a organic scintillator calorimeter should be able to measure the additional energy deposited by neutrons and therefore suffer less from the neutron fluctuations.

2.5 Clustering of hadronic showers

Event reconstruction using *particle-flow algorithms (PFA)* requires the knowledge of the detailed structure of electromagnetic and hadronic showers. Current simulation models are affected by large uncertainties associated with the hadronic shower development. The calorimeter design has a strong impact on the overall ILC detector architecture and cost but the optimisation of such a detector cannot be done reliably with such uncertainties. More information about hadronic shower can be obtained exploiting the very high granularity of new calorimeter prototypes capable to track single particles in the shower. This approach needs a novel way to identify and cluster sub-shower components. Each cluster type can then be studied independently, and its properties compared separately to the different Monte-Carlo models.
In the following section a short overview about the status of hadronic shower simulation is given. Afterwards one example of a three-dimensional clustering algorithm is introduced, the *deep analysis*.

2.5.1 Shower simulation

Several simulation codes for hadronic showers are available. In high-energy physics the Geant simulation package is normally used to simulate electromagnetic and hadronic showers. Geant gives the possibility to implement a detector geometry by describing different volumes and materials. In this simulation the primary particle and all generated particles are tracked until their energy drops below a certain energy cut. All the discussed interaction processes and their cross-section dependence on the particle energy are implemented in Geant. For each possible process a random generator creates a free path length at which the process would

take place. The process with the shortest path length takes place after the particle has travelled the extracted path length.

This random number procedure is not applicable for the more complex hadronic shower simulation. In this case different approaches have to be chosen. Some of them are following parameterisations of measured cross-sections whereas others are using theoretical calculations. There exist a large variety of physics models to describe hadronic showers in the Geant simulation package [30]. The most common packages are GHEISHA [31], FLUKA [32, 33] and CALOR [34, 35]. They show significant differences in important shower parameters like lateral and longitudinal distributions.

A comparative study of 12 models implemented in Geant [36] was performed. A 10 GeV pion shower has been simulated in a detector similiar to the hadronic calorimeter prototype discussed in this thesis. Four models implemented in Geant3 and eight models in Geant4 are compared. Among them the GHEISHA phenomenological models are presented as G3-GHEISHA, G4-LHEP-GN, G4-QGSP-GN. Where LHEP is based on parameterisations of existing data and QGSP is based on theoretical calculations. The models including Bertini intra-nuclear cascade are G3-FLUKA, G4-LHEP-BE, G4-QGSP-BE. The models G3-FLUKA+M(icap), G4-LHEP-HP, G4-QGSP-HP have in addition nuclear transport models switched on. G3-CALOR is a special low-energy neutron code implemented in Geant3. The two physics lists G4-FLC and G4-FLC-50 are specially tuned by the author. Figure 2.5 shows the comparison between the models of the μ/π ratio (a) and the energy resolution (b). Variations up to 80 % are observed between the models. The correlation between reconstructed energy and total number of hits in a 10 GeV pion shower is shown in figure 2.6. Significant differences in the correlation shapes are observed between the models. Figure 2.7 illustrates the results from an independent study [37] on the shower radius prediction for a 10 GeV pion shower. Also for this quantity a variation of 60 % is observed.
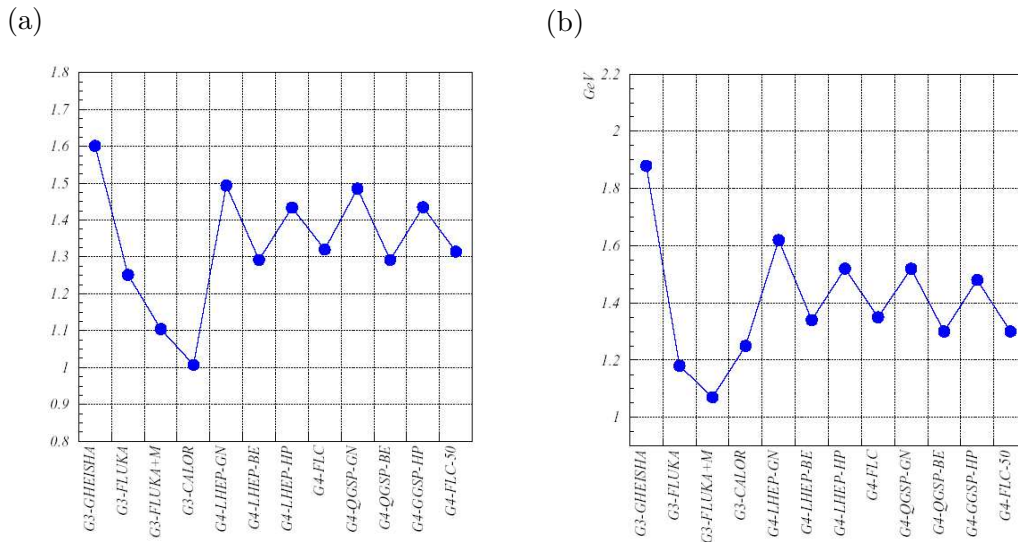
Figure 2.5: *Comparison of MC predictions for (a) μ/π ratio, and (b) the energy resolution of a 10 GeV pion shower [36].*
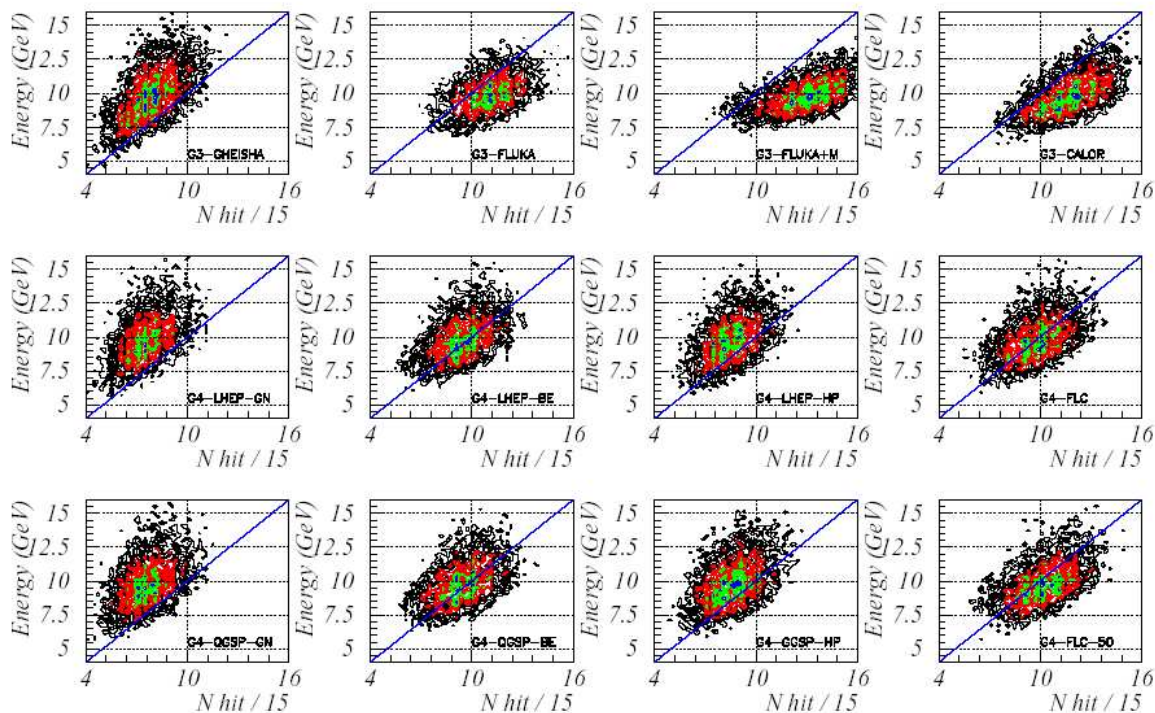
Figure 2.6: *Correlation between total energy and number of hits/15 for 10 GeV pion as predicted by various MC models [36].*
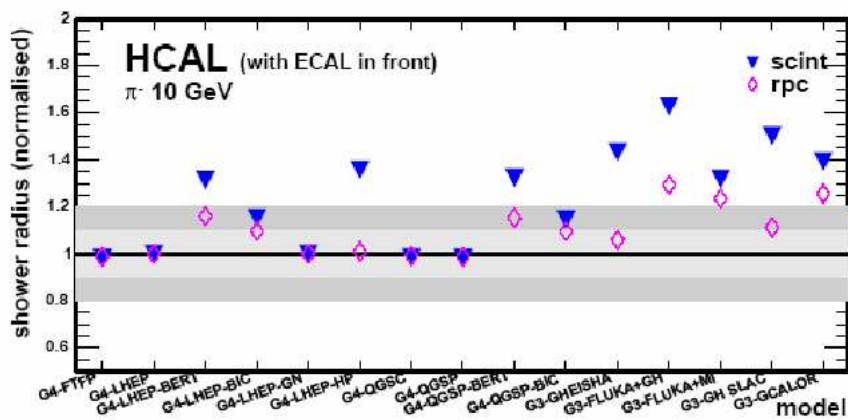
Figure 2.7: *Comparisons of shower radius prediction in different hadronic models for 10 GeV π^-. The results are normalised to the prediction of the LHEP model in Geant4. The shaded bands denote 10% and 20% differences. Two readout options are compared, scintillator tiles and resistive plate chambers (rpc) with digital pads [37].*

2.5.2 Deep analysis

In the previous sub-section it has been shown that the various Monte-Carlo models give significantly different response for hadronic shower quantities. A new approach to improve the knowledge of hadronic showers is necessary, which makes use of the very high granularity calorimeter information to track single particles in a hadronic cascade. For this purpose a three-dimensional clustering algorithm has been developed.

The deep analysis algorithm for hadron shower decomposition proceeds sequentially through the three basic steps: hit classification, hit clustering and joining of clusters. The hits are classified according to their energy into three types: *track-like*, *hadron-like* and *electromagnetic-like*. Figure 2.8 (a) shows the energy spectrum of single hits and an example of energy cuts to identify the types. These energy boundaries are parameters of the algorithm, normally set to 0.5-1.7 mips (track-like), 1.7-3.5 mips (hadron-like) and larger than 3.5 mips (electromagnetic-like). An additional hit class is introduced for *neutron-like* hits, which is not based on energy information and it will be discussed after clustering. After hit classification a two-dimensional clustering is performed in each calorimeter layer. Subsequently, clusters in consecutive layers are joined in a three-dimensional procedure using their topological properties. The track-like clusters are classified as having large eccentricity and low hit density. The hadron-like clusters have relatively small eccentricity and low hit density. The electromagnetic-like clusters have high hit density and large eccentricity. The electromagnetic-like and the hadron-like clusters have to be connected by track-like clusters. The remaining isolated hits not assigned during this procedure are regarded as neutron-like hits. These hits are by definition disconnected from the shower tree but they get assigned to the shower if their distance from the shower axis is less than a defined parameter. Three examples of the manifold event spectrum in hadronic shower are shown in figure 2.8 (b)-(d). The deep analysis disentangles between these different contributions, which occur together in a hadronic shower. A hadron-like event is shown in (b) where the blue track indicates a hadron created in the first nuclear interaction travelling through the calorimeter before undergoing a nuclear interaction. A neutron-like event is shown in (c) where instead of the creation of a charged hadron in the first nuclear interaction a neutron has been created, which travels through the calorimeter before undergoing a nuclear interaction. The last example in (d) shows an electromagnetic-like event in which an electromagnetic shower with high energetic hits (red) is initiated by a gamma entering the calorimeter.

The deep analysis clustering procedure results in a separation of the total energy into different components. This information can be used to weight each component differently since each of them has a different response in the calorimeter. This weighting leads to an improved energy resolution as shown in [38]. The deep analysis algorithm can be used not only to improve energy resolution of single showers but most importantly to separate adjacent showers in the calorimeter. The shower separation efficiency has a major impact on the performance of particle-flow algorithms.
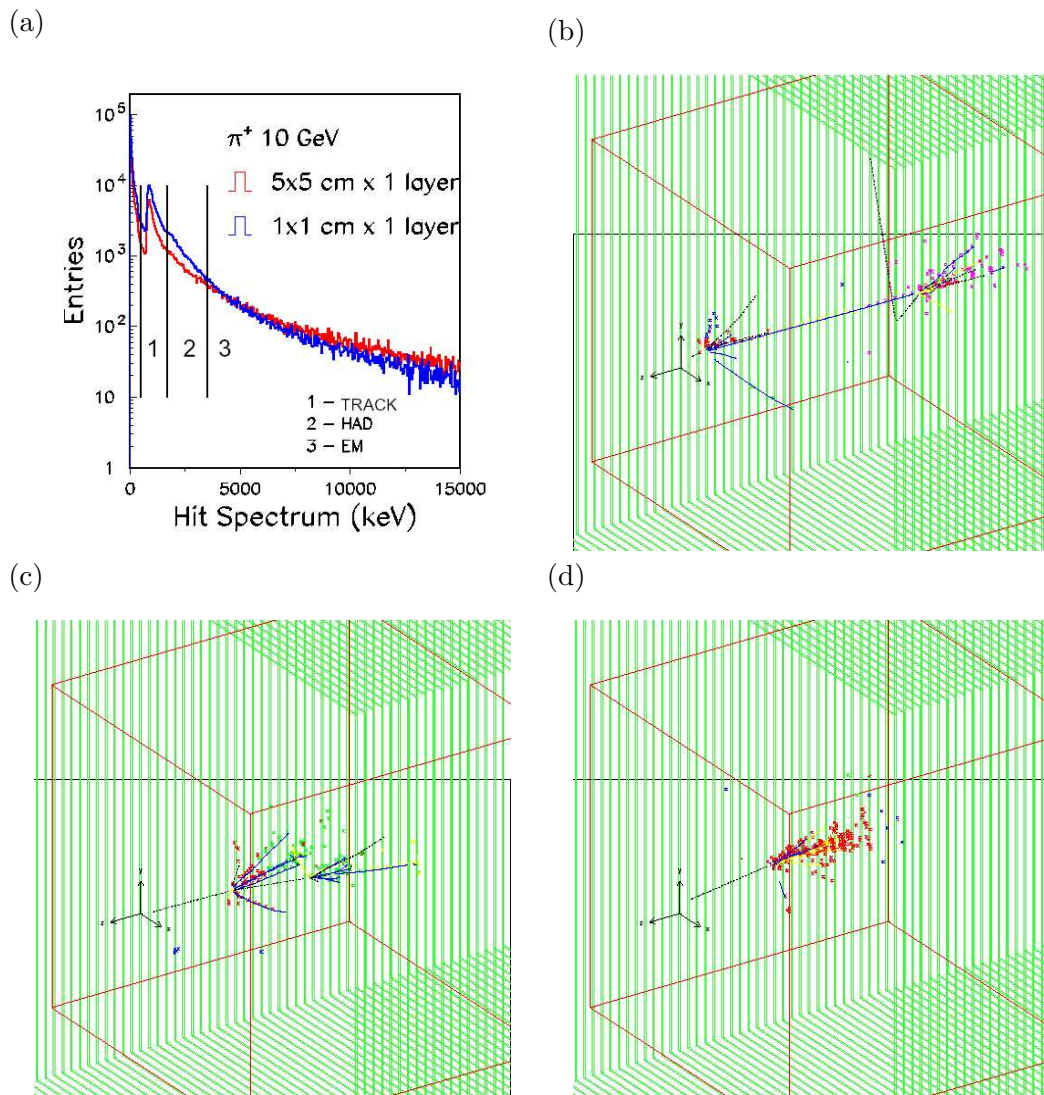
Figure 2.8: *(a) Hit class classification by hit energy. (b) hadron-like event: the blue track indicates a hadron created in the first nuclear interaction travelling through the calorimeter before initiating a nuclear interaction by itself. (c) neutron-like event: instead of the creation of a charged hadron in the first nuclear interaction a neutron or gamma has been created, which travels through the calorimeter before initiating a nuclear interaction by itself. (d) electromagnetic-like event: an electromagnetic shower with high energetic hits (red) is initiated by a gamma entering the calorimeter.*

Chapter 3

Calorimetry at the International Linear Collider

The International Linear Collider (ILC) is an e^+e^- collider of the next generation. This machine and its experiments will operate at the forefront of science and provide novel and deep insight into the most fundamental aspects of nature, complementing and extending the capabilities of the LHC (the hadron-hadron collider under construction at CERN).

It is planned that the machine will be initially operated at centre of mass energies ranging from $\sqrt{s} = 91$ to 500 GeV, and up to 1 TeV in the second stage. This energy range combined with the clean initial state condition gives the possibility of a deeper investigation of the Standard Model (SM) as well as its possible extensions like Supersymmetry (SUSY) or extra dimensions. This physics program is complementary to the LHC one, which should see its first data in the end of this year [39]. The LHC, due to its high centre of mass energy of 14 TeV, will be a powerful discovery machine to reveal the new physics which is expected on the TeV scale. The ILC will be better adapted to perform high precision tests like the determination of the Higgs properties.

In August 2004 an International Technology Recommendation Panel advised to use superconducting acceleration technology for the ILC. Since then efforts around the world were directed toward producing a design report for the accelerator including cost estimate, which has been presented in February 2007 [40].

In figure 3.1 a sketch of the current ILC design is shown. Two 12 km long linacs, one for electrons and one for positrons, will accelerate the particle bunches towards the collision point. Each linac consists of $\approx$8000 superconducting niobium cavities inside of modules, which cool down the cavities to $-271°$ C. Electromagnetic waves with a radio-frequency of 1.3 GHz inside the cavities will accelerate the particles up to 500 GeV with a gradient of 31.5 MV/m. This superconducting technology has been successfully developed at the TESLA Test Facility (TTF) in an international collaboration at DESY and will be employed in the European X-Ray Laser Project XFEL [41]. Before accelerating electrons and positrons they have to be produced. High-intensity, two nanosecond short laser pulses focused on a target knock out billions of electrons. Electric and magnetic fields will create bunches of particles, which will be boosted to 5 GeV in a 250 m long linear accelerator. To produce the not naturally existing antimatter partner of the electron, the electron beam is steered through a undulator, which forces the electrons to radiate photons. Afterwards the electrons return in the main accelerator, while the created photon will hit a target and produce electron-positron pairs. The positrons will be collected and launched into their own 250 m long 5 GeV accelerator. When created, neither the electron nor the positron bunches are compact enough to yield the high density needed to

produce collisions at the interaction point. Two seven-kilometre-circumference damping rings
have to compress the electron and positron bunches by forcing them to emit photons in so
called wiggler magnets. Afterwards the bunches will be a few millimetres long and only half
a micrometre thin. The high density of particles in each bunch leads to energy loss in the
interaction region by means of the Beamstrahlung effect. Beamstrahlung describes the effect
that particles emit synchrotron radiation in the strong electromagnetic space-charge field of
the opposing bunch. The consequences are a reduction and spread of the collision energy as
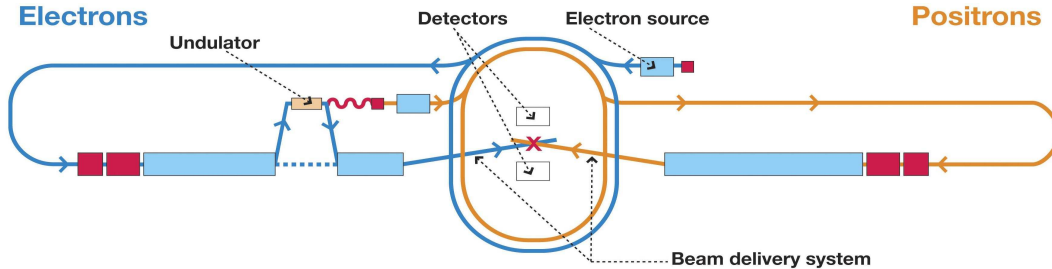well as background contamination in the detector [42].

Figure 3.1: *Sketch of the ILC. Two 12 km long linacs, one for electrons and one for positrons,
will accelerate the particle bunches towards the collision point. Electromagnetic waves inside
the cavities will accelerate the particles up to 500 GeV.*

Among the main physics interest to be addressed by the ILC will be precise measurements
of Higgs boson properties, accurate investigation of the SUSY spectrum, probing strong elec-
troweak symmetry breaking, and precision top quark physics [43]. A common requirement
for most of these physics studies is a good measurement of hadronic jet energies. One way
to achieve the required jet energy precision is to use particle flow. Particle flow is the logical
advancement of an earlier approach already introduced at some LEP experiments known as
energy-flow, which attempted to use the information of all detector components to improve
the jet energy resolution and not the calorimetric system alone. One limitation to this ap-
proach at the LEP experiments was the too coarse spatial segmentation of the calorimeter,
which made it impossible to track single particles inside a jet after they have left the tracking
system. Particle flow tries to identify and measure every single particle in a jet. This requires
separation of each particle and its deposited energy, which obvious stress on high granularity
and spatial resolution more than on single-particle energy resolution. The high granular de-
tectors proposed to fulfil this task are often referred to as tracking calorimeters. In addition,
particle flow sets requirements for the complete detector design, because it is based on the
interplay between the different detector components.

3.1   A detector for the ILC

At the ILC, given the precise knowledge of the initial state, the Standard Model Higgs can
be measured as the recoil mass of processes like $e^+e^- \rightarrow ZH$ (see figure 3.2 (a)) where the
Z-boson decays leptonically into l^+l^-. The resolution of this measurement is limited by the
intrinsic width of the Z, if the resolution of the transverse momentum of charged particles in
the trackers is $\delta p_t/p_t^2 \leq 5 \times 10^{-5} (GeV/c)^{-1}$ [44].
If the Higgs is found, the determination of its branching ratios and couplings will allow to
distinguish between different underlying physics models, i.e. SM or MSSM. For this an excel-
lent capability of flavor tag is required, which imposes limits for the charged-particle impact

parameter resolution to be better than 3 μm at high momentum and better than 10 μm at p=1 GeV/c.

If the Higgs mechanism is not the method chosen by Nature to obtain electroweak symmetry breaking, a precise measurement of the WW scattering (see figure 3.2 (c)) will become essential for the understanding of new physics. In order to disentangle the two concurring processes of $WW\nu\nu$ and $ZZ\nu\nu$ from their di-jet final states, a jet energy resolution of 30 %/$\sqrt{E(GeV)}$ is necessary. This can be achieved by combining the potentials of the particle-flow approach with high granularity in transverse and longitudinal directions for both electromagnetic (ECAL) and hadronic (HCAL) calorimeters. The needed multi-jet reconstruction stresses the calorimeter jet separation capability. A large amount of the benchmark physics processes include multi-jet final states from W and Z bosons decays. Precise top quark mass M_t measurements require even the reconstruction of 4- and 6-jet events coming from $e^+e^- \rightarrow t\bar{t}$ events. For final states including neutrinos the initial beam energy constraint will be not available. For final states consisting of four or more jets the beam energy degradation due to Beamstrahlung losses before the interactions affects the reconstruction. This degradation is in the order of 2 % [42]. Interesting physics processes reachable with the ILC are characterised by small cross-sections like $e^+e^- \rightarrow ZHH$ (see figure 3.2 (b)), which has only a cross-section of 0.2 fb. Good jet separation capability will reduce the need of statistics to access these channels.

The energy range relevant in hadronic final state processes at the ILC is considerably lower than average jet energies at the LHC on which the current simulation validation is ongoing. Minimum energy threshold for LHC events is around 20 GeV while the average ILC particle energy will be 5 to 10 GeV [44]. This is the energy for which the ILC calorimeter system has to be optimised and for which simulation validation is most strongly required.
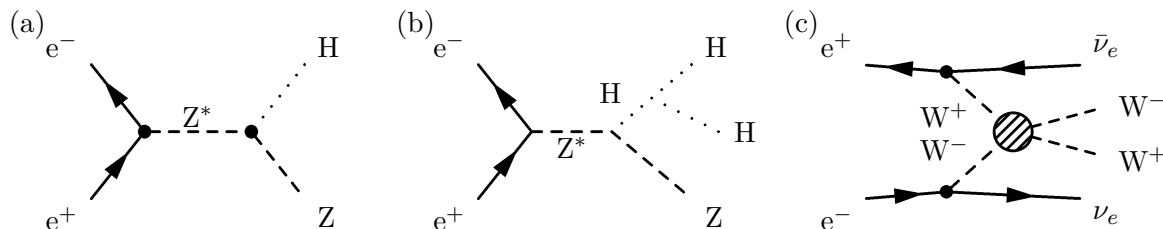
Figure 3.2: *Feynman diagrams of some interesting processes at the ILC: (a) Higgsstrahlung, (b) Higgs self coupling and (c) WW scattering.*

Before further discussing detector design and optimisation for the ILC it is necessary to understand in detail what particle flow is and what are the requirements that this method imposes on the detector.

3.1.1 The concept of particle flow

The LEP experiments introduced the energy-flow technique in 1994-1995. With the simplest event reconstruction, consisting in the simple sum of the raw energy found in all calorimeter cells without performing any particle identification, the ALEPH experiment achieved an energy resolution of $\sigma(E)/E = 1.2/\sqrt{E(GeV)}$ for hadronic decays of the Z-boson. In order to improve this resolution, an energy-flow reconstruction algorithm was developed, which make use of the measured track momenta, and of the photon, electron and muon identification capability of the detector. The basic idea is that only the neutral hadrons are exclusively measured by the hadronic calorimeter, which has from all sub-detectors the worst

resolution. To improve on jet energy resolution the momentum of all charged particles should be measured from the tracking system, which (up to about 100 GeV) delivers a much more precise information than the energy measured in the calorimeter. The superior resolution of trackers compared to that of calorimeters is illustrated in figure 3.3 (a) from a simulation study performed for the ILC detector optimisation [45].

The energy flow approach, explained in detail in [46], starts with an extrapolation of the charged particle tracks to the calorimeters. In addition, calorimeter objects are defined by grouping topologically connected tracks and clusters. For all the calorimeter objects that can be assigned to a track, and are therefore belonging to charged particles like charged pions, electrons and muons, the total energy is replaced by the momentum sum as obtained from the tracking system. A dedicated reconstruction identifies photons and π^0 clusters, assigns them as neutral electromagnetic energy and removes them from the list of calorimeter objects. At this stage, the remaining calorimeter objects should belong to neutral hadron showers. Only for these objects the energy resolution of the hadronic calorimeter plays a role.

This method is hardware limited in LEP-type detectors by the coarse calorimeter segmentation, by the missing or small magnetic field to better separate adjacent tracks, and by the presence of additional dead material in front of the calorimeter which degrades the track association to calorimeter objects. Figure 3.3 (b) summarises all these problems encountered in the application of energy-flow on the ALEPH detector. The separated tracks in the tracker leave not obviously separable entries in the calorimeter system.

To exploit the full power of the energy flow method the next generation of HEP detectors has to be built such to enable the reconstruction of the four-vector of all charged and neutral particles in an event. This method which requires the synergy of the detector and of the reconstruction software to achieve single particle separation and reconstruction is referred to as particle flow.

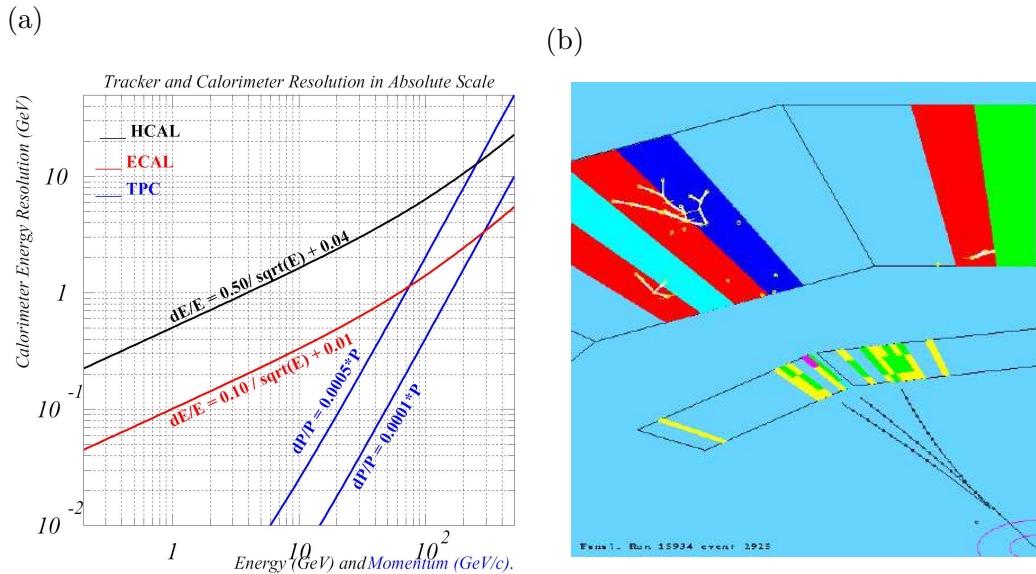Figure 3.3: *(a) Tracker and calorimeter resolution in energy. The tracker momentum resolution is much better than the calorimeter energy resolution in the wide energy range [45]. (b) Event display from the ALEPH experiment. The worse longitudinal segmentation, missing lateral granularity and the gap between the calorimeters due to the magnet coil, limits the possibility to match tracks and clusters in the calorimeter.*

Applying the particle-flow method the energy resolution for a single jet, or a jet with no shower overlap to neighbouring ones, is calculated as the sum in quadrature of the resolutions for the various particle types contributing to the jet, as

$$\sigma_{jet}^2 = \sigma_{h^\pm,l^\pm}^2 + \sigma_\gamma^2 + \sigma_{h^0}^2, \tag{3.1}$$

with $\sigma_{h^\pm,l^\pm}^2$ the energy resolution for all charged particles (hadrons and leptons), σ_γ^2 that for photons, and $\sigma_{h^0}^2$ the energy resolution for neutral hadrons. Assuming the design momentum resolution from the tracking system the charge component of a jet (approximately 60 %) can be recontructed with $\delta p_t/p_t^2 < 5 \times 10^{-5}(GeV/c)^{-1}$. The photons which account for about 30 % of the total jet energy are reconstructed with an electromagnetic calorimeter resolution of $0.11/\sqrt{E_\gamma(GeV)}$. This leaves the residual neutral hadron energy to be measured directly in the hadronic calorimeter. The combined jet energy resolution weighted by the fractional content in a jet can be as good as $\frac{\sigma_{jet}}{E_{jet}} \approx 0.14/\sqrt{E_{jet}(GeV)}$ if one does not take into account real detector limitations [47]. It should be noted, however, that there will be classes of events having jets with lower charged components and a potentially much higher neutral hadron component. Such events may will show a degraded jet energy resolution, depending on the efficiency achieved by the particle-flow algorithm.

For a real collider detector, there is also the contribution coming from the mixing of the deposited energy between neutral and debris of the charged hadrons interaction in the calorimeter ($\sigma_{confusion}$), the losses of particles due to imperfect reconstruction and geometric inefficiencies (σ_{losses}) and the threshold of energy for each species which integrate the fluctuation at low energy of the jet fragmentation ($\sigma_{threshold}$). Equation 3.1 should be rewritten to include all these contributes

$$\sigma_{jet}^2 = \sigma_{h^\pm,l^\pm}^2 + \sigma_\gamma^2 + \sigma_{h^0}^2 + \sigma_{confusion}^2 + \sigma_{losses}^2 + \sigma_{threshold}^2. \tag{3.2}$$

Accounting for these additional terms preliminary simulations studies have shown that it is possible to aim for a jet energy resolution of 30 %$/\sqrt{E(GeV)}$ [45]. The main problem in the reconstruction is the determination of the number of particles which have contributed to the signal in a calorimeter region, known as the confusion problem. That leads to the shower overlapping in the same calorimeter region. The major tool in the reconstruction of the information provided by the calorimeter is clustering. Clustering routines merge individual hits in the calorimeters to defined groups of hits (see section 2.5.2). Different approaches of clustering are under development. The differences consist in the kind of information used to perform the hit merging. Most of the algorithms are based on topological approaches neglecting the cell amplitude measurement, which would be available for an analogue hadronic calorimeter. This is one example of the complexity and difficulties of the detector performance comparison, because especially in a particle-flow approach the interplay in the reconstruction between hardware and software is immense. A well performing cluster algorithm for a digital calorimeter with small cell size but without analogue information will not give the best possible performance running on data obtained with an analogue hadronic calorimeter and vice versa. However, independently on the final calorimeter readout realisation equation 3.2 and table 3.1 show that the single particle resolution is not the dominating contribution to the jet energy resolution but the confusion term. Therefore the conclusion for an optimised calorimeter system for particle-flow application is that granularity is more important than single particle energy resolution.

component	detector	frac. of jet energy	particle resolution	jet energy resolution
charged particles $X^{\pm}$	tracker	0.6	$5{\cdot}10^{-4}\,E_X$	neg.
photons γ	ECAL	0.3	$0.11/\sqrt{E_\gamma}$	$0.06\sqrt{E_{jet}}$
neutral hadrons h^0	HCAL	0.1	$0.4/\sqrt{E_h}$	$0.13\sqrt{E_{jet}}$

Table 3.1: *Jet energy resolution contribution from the sub-detector systems [47].*
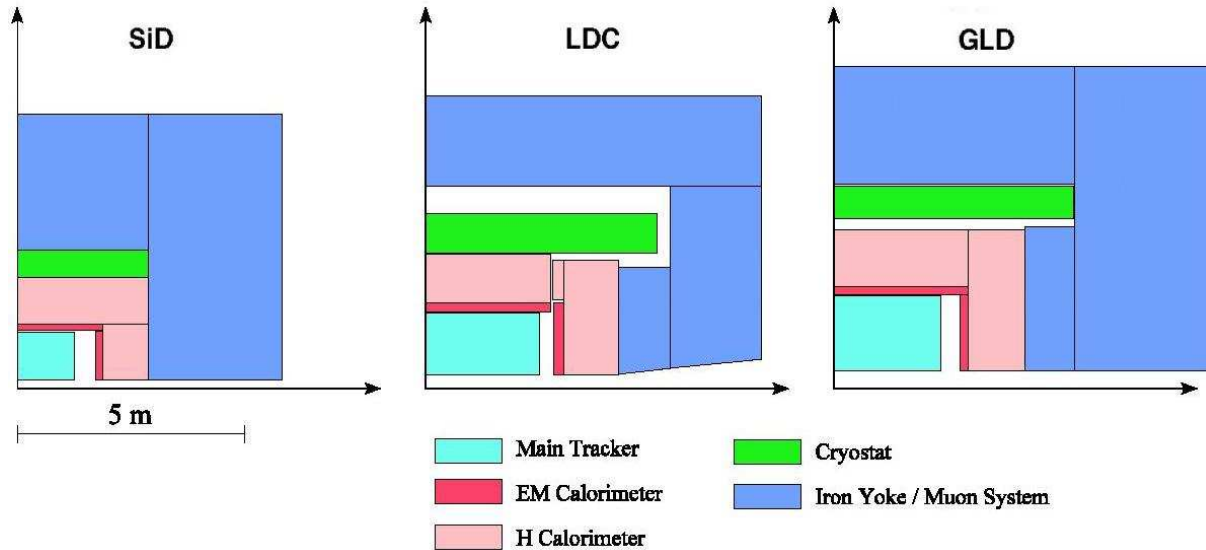

Figure 3.4: *Three detector concepts for the international linear collider ILC: SiD, LDC and GLD.*

3.1.2 ILC detector concepts

With the very stringent requirements in mind as imposed by particle flow, four world-wide concepts for an ILC detector are emerging. Three detector concepts assume particle flow as the conceptual model for event reconstruction. The fourth concept takes an alternative approach to jet reconstruction, based on hardware-compensating calorimetry. When applying the particle-flow algorithm photons are measured by the electromagnetic calorimeter, electrons/positrons and charged hadrons by the tracker, and neutral long-living hadrons by the hadronic calorimeter, which also serves as a muon tagger. In addition, lepton identifications down to low momenta is important in order to separate purely hadronic jets from jets containing leptonic decays. The three detector designs differ mainly in the choice of the technology for the tracking chamber, a five layer solid-state tracker and a large-volume Time Projection Chamber (TPC) are proposed. The other main difference is the detector size, which has a direct influence on the required magnetic field of the solenoid (between 3 to 5 T from the largest to the most compact design).

The Silicon Detector Design (SiD) [48] has the smallest size (see figure 3.4) but therefore the highest magnetic field of 5 T. The Large Detector Concept (LDC) [49] uses a TPC as tracker and a magnetic field of 4 T, whereas the Global Large Detector (GLD) [50] needs only 3 T but therefore a bigger radius for the central gaseous tracker. In figure 3.4 one quadrant of each of the three concepts is shown. Despite of the different sizes the general design is the

same. A main tracker is surrounded by an electromagnetic and hadronic calorimeter which are both inside the magnet coil. This system is surrounded by an instrumented return yoke to tag muons leaving the detector. The fourth concept which is not based on particle flow will not be discussed in the following.

The design of the detector is dictated by the complexity of the events resulting from the high energy and luminosity. The requirements for the detector can be summarised in four points: vertexing, track momentum resolution, hermeticity and particle flow.

Vertexing

The main task of the vertexing is to provide tagging information about b and c jets. The baseline vertex detector concept consists of 5 layers of 22×22 μm^2 CCD pixels, with a space point resolution of 5 μm, and with an overall material budget of 0.12 % X_0 per layer, the inner one being at 1.2 cm from the beam trajectory. The main issue for vertex detectors at the ILC is to maintain the occupancy below 0.1 % during the foreseen $\sim$3000 bunch crossings (of 300 ns intervals) per train. Given the proposed pixel size and the bunch structure fixed by the chosen cold RF-cavity technology in the ILC machine, the occupancy during a bunch train would be approximately 20 times the required one. Solutions have being investigated and prototypes have already shown very encouraging results. One approach to keep the occupancy below 1 % is to readout the pixels 20 times during a bunch train. Examples of this technology are the Charge-Coupled Devices (CCD) [51] with column parallel readout, the Monolithic Active Pixel Sensors [1] (MAPS), the DEpleted P-channel Field Effect Transistor (DEPFET) [52], and the Silicon on Insulator (SoI). MAPS and DEPFET are both examples of monolithic approach in which part of the readout circuitry is implemented directly onto the pixel sensor.

A different approach is offered by the possibility to store charge in situ during the bunch train and subsequently read out the storage cells in between bunches. This technology is represented by the Imagine Sensor with In-situ Storage (ISIS) and the Hybrid Pixel Sensors (HAPS). The charge collected during fixed time periods is shifted through subsequent n-channel storage wells on the pixel surface, where it remains stored till the next clock cycle. An elegant alternative to the complication of multiple readout during a bunch train is to reduce the pixel area by about a factor of 20. A matrix of Fine Pixel CCD (FPCCD) has been industrially produced with pixel size of 5×5 μm^2 and is under study.

Track momentum resolution

The track momentum resolution has to be excellent to determine recoil mass against the $Z \rightarrow l^+ l^-$ system in $e^+ e^- \rightarrow HZ$ events with high precision. The three detector designs differ mainly in the choice of the technology for the tracking chamber, a five layer solid-state tracker and a large-volume Time Projection Chamber (TPC) are proposed.

The main advantages of a large-volume TPC over a Si-tracker are the fully three-dimensional track information and the large number of space points, which make the track reconstruction straight-forward. Also, the minimum material budget in the barrel detector makes it possible to extend tracking to large radii. The large magnetic field of $\sim$4 T, in which the ILC detector has to be operated to reduce $e^+ e^-$ background, will also reduce the transverse diffusion in the TPC improving the momentum resolution. Various TPC prototypes have been tested in magnetic fields up to 5.3 T to verify the improvement in space point-resolution.

---

[1]One example being the sequence of MIMOSA chips produced by LEPSI electronics and IRES (Strasburg).

To achieve best point-resolution new gas amplification techniques as Gas Electron Multipliers [53] (GEM) and Micromegas [54] are being optimised. The very compact and localised electron avalanche produced in the micro holes of the gas amplifiers are sensed by conducting pads with a typical pitch of 1-3 mm [2]. The possible problem of overlap of events from several bunch crossings due to the slow drift time ($\sim$100 μsec) can be overcome by associating tracks in the TPC with time correlated track segments in the vertex detector, recovering in this way the single bunch-crossing information.

An alternative to gaseous detectors is a central tracker composed of five or more layers of silicon strips detectors. The key issue in this design is to minimise the material budget of sensors plus electronics, mechanical support, power and data traces, and cooling lines to below 1.5 % of a radiation length per layer. Various proposals exist in this direction. Power cycling during the 200 ms gap between bunch trains reduces the power dissipation eliminating the need for active cooling, and avoiding the associated cooling system material. Studies are also ongoing to produce single silicon ladder of half the total detector length (up to 170 cm). In this way the readout electronics could be placed outside the barrel reducing the material in the tracking volume. Such long sensors with low noise are a serious challenge for the silicon technology and have not been produced before.

In addition for the comparison of the two technologies it should be added that pattern recognition for non-pointing tracks is easier in TPC (important for particle flow) but, on the other hand, the large amount of material in front of ECAL end-cap needed for the TPC end-plate is a point in favour of Si-trackers.

Hermeticity

Missing energy is the signature of several processes of interest, therefore hermeticity and particle detection capability at small angles is required. Especially the equipment of the forward region plays an essential role and is a special challenge due to the high radiation near the beam-line. The forward region will be equipped with a set of calorimeters to minimise the losses to the beam-line. A detailed description about this detector region can be found in [44] and in the detector proposals [48, 49, 50].

Particle flow and the calorimeter system

Particle flow requires an efficient association of the particles in the tracker to those in the calorimeters. This association becomes more effective if the material between the tracker and the calorimeter system is minimised as much as possible. Therefore the calorimeter should be also contained inside the magnet. A high magnetic field strongly bends particle trajectories which hardly never travel perpendicular to the detector layers. This maximises the amount of material seen by the particles, and at the same time the particle separability. The design of the calorimeter in a particle flow driven design is almost completely independent of the detector concept. In view of the demanding requirements of the particle-flow approach both ECAL and HCAL need to have unprecedented longitudinal segmentation and transverse granularity.

The particle-flow concept requires a new approach to optimise the calorimeter system. Quantities like compensation behaviour play a minor role in comparison to shower separation capabilities, because the importance of hadronic energy resolution is reduced. However, high

---

[2]An independent approach to the electronic readout of micro-pattern gas detectors is a 55×55 μm^2 CMOS pixel sensor, Medipix2, proposed by NIKHEF, Saclay and Bonn.

granularity provides possibilities for software compensation. Due to the particle-flow requirements the calorimeter system should have two separated parts: ECAL and HCAL. These two detectors are expected to have different absorbers and sampling structures to achieve the best possible longitudinal segmentation at a reasonable cost. Such a calorimeter system is therefore non-compensating by definition. The traditional way to optimise calorimeter systems is to achieve the compensation condition (see section 2.4.1) to gain a homogeneous response for different particle types and to optimise the energy resolution for single particles in the hadronic calorimeter. In the particle-flow method this aspect has to step back to allow the optimisation for the best shower separation possible. From equation 3.2 and table 3.1 becomes clear that the confusion term, which is dependent on the shower separability of the calorimeter system dominates. This has of course implications for the calorimeter design, e.g. the choice of the absorber material. The atomic number of the absorber material iron (Fe) in the hadronic calorimeter has a small neutron yield for the hadronic cascade, which leads to a smaller amount of overlapping showers. This, on the other hand, does not help to achieve compensation, where the neutron response should be enriched. A sandwich structure alternating high-Z absorber material to active layers is proposed for both calorimeters. One of the important decisions for each calorimeter is the choice of the absorber material. Each material has different characteristics in term of radiation length X_0 and nuclear absorption length λ_0, which implies that different amounts of material are needed to contain the same particle shower. For particle flow to work, the HCAL must have imaging capabilities like the ECAL. Tungsten as absorber would be probably the best choice for both. While for the ECAL this choice is mandatory, for the HCAL steel is generally chosen for costs reasons.

To exploit the small Molière radius of tungsten, a very compact readout structure is required with a very high segmentation. Active layers with 1×1 cm^2 readout cells are proposed. This can be achieved with silicon pads according to the broadly accepted Si-W design; or eventually with small scintillating tiles or strips; or with a hybrid structure alternating silicon and scintillator layers.

In the HCAL the minimum required segmentation is of the order of 3×3 cm^2 to match the Molière radius of steel. Two possible designs are being pursued: a steel-scintillator structure with analogue readout of 3×3 cm^2 tiles; and a steel-radiator structure with gaseous signal amplification and digital readout of 1×1 cm^2 pixels.

A calorimeter system optimised for particle-flow applications should first have very well shower separation capabilities to reduce the influence of the confusion term to the overall jet energy resolution and should be in second order optimised for the best single particle response and energy resolution by fulfilling the compensation condition. The major R&D activities on calorimetry are pioneered by the CALICE collaboration. In the following section the calorimeter concepts developed by CALICE are discussed in more details.

3.2 The CALICE Calorimeter

CALICE [3] is an international collaboration of 39 institutes from 12 countries, whose main objective is the development of the next generation of calorimeters for future HEP detectors, based on innovative technologies to allow unprecedented granularity and segmentation of all detector components [1]. The R&D activities of CALICE are driven by the aim of a detector exploiting the particle-flow approach. This makes it especially important to develop the entire calorimetric system as a whole and not only optimise the performance of each component

---

[3]Calorimeter for a Linear Collider Experiment.

separately. Within CALICE prototypes of electromagnetic and hadronic calorimeters, as well as of a tailcatcher and muon tracker, are being pursued. The combined performance of these prototypes will be tested in electron and hadron test beams.

3.2.1   The electromagnetic calorimeter (ECAL)

The electromagnetic calorimeter has a sandwich structure of tungsten absorber and silicon readout. The silicon wafer diodes have a pad size of $1{\times}1$ cm^2 to match the Molière radius of tungsten. The prototype consists of 30 layers grouped into three stacks with different thicknesses of absorber. This choice ensures a good resolution at low energy, due to the thin tungsten (0.4 X_0 per layer) in the first stack, and a good containment of electromagnetic showers, due to tungsten thicknesses two and three times larger in the second and third stacks, respectively. The overall thickness is about 20 cm or 24 X_0. The tungsten layers are wrapped in a carbon fibre structure for stability reasons [55].
The 500 μm thick silicon wafers are cut to a size of $62{\times}62$ mm^2 which contains an array of 6×6 pads, with a space reserved for one unique guard ring per wafer. The operational bias voltage to reach overdepleated mode is around 250 V. The $\approx$10000 silicon wafer diodes are independently read by an ASIC chip developed by the LAL-Orsay group member of CALICE [56]. It consists of a preamplifier with two gains, a shaper and a multiplexer. This chip handles 18 channels and has low noise and a large dynamic range.

3.2.2   The analogue hadron calorimeter (AHCAL)

A first hadronic calorimeter option tested by CALICE is a steel scintillator sandwich calorimeter. Longitudinally the calorimeter consists of 38 active layers separated by 2 cm of steel. Each active scintillator layer is divided into 216 tiles. The highly granular core of 30×30 cm^2 is covered by a matrix of 100 3×3 cm^2 tiles; for cost reasons, this core is surrounded by three rows of 6×6 cm^2 tiles; the outer most part of the active layer is divided in 12×12 cm^2 tiles. The scintillation light produced in the tile is collected via a wavelength shifter fibre and coupled to a newly developed silicon-based photo-detector (SiPM). The prototype will consist of $\sim$8000 scintillator tiles with analogue readout performed via SiPM directly mounted on each tile. A dedicated ASIC chip has been developed (also by the LAL-Orsay group) to match the requirements of large dynamic range, low noise, high precision and large number of readout channels needed [57]. The very front-end (VFE) electronics to steer the chip settings and readout has been designed at DESY and it is matched to the VME based data acquisition developed by the British group members of CALICE.
The analogue hadronic calorimeter prototype is the main topic of this thesis and is discussed in much more details in chapter 5.

3.2.3   The digital hadron calorimeter (DHCAL)

An alternative to the scintillator tile readout for a hadronic calorimeter is a digital approach also investigated within the CALICE collaboration. To maintain the linear relation between number of hits and energy in a hadronic shower the segmentation of the readout has to be kept below $1{\times}1$ cm^2. For each readout cell or pad the information of a hit above a fixed threshold is recorded with no additional amplitude information. To reach this fine granularity ionisation gas chambers are used with fine copper pad readout. Different amplification technologies are under study for this prototype: resistive plate chambers (RPCs) or thin

chambers with gas electron multiplier (GEM) foils. Several groups have optimised RPC operation parameters and have chosen the safer avalanche mode of operation [58]. For both RPC and GEM options one still needs to develop large area detectors and demonstrate their long-term reliability. However, given the huge number of about 40 million channels, the biggest challenge is to develop concepts for low cost electronics.

3.2.4 Digital versus analogue readout for the hadronic calorimeter

Simulation studies of energy resolution of hadronic showers show that with a pad size of about 1 cm^2 in the digital approach the resolution is expected to be better than in the analogue case at low energies, due to the suppression of Landau fluctuations in the deposited energy. The degradation of the resolution at higher energies is due to an increasing probability of multiple hits per cell in dense showers. It can be overcome by reducing the cell size further, or by adding minimum amplitude information in the form of thresholds. Scintillator as active medium allows to balance between granularity and dynamic range. A semi-digital option can be considered, which consists of a moderate choice of granularity combined with a 2 bit readout.

The hit distribution (ignoring any amplitude information) seen in a gaseous calorimeter appears more compact than in a scintillator, due to a different response to low momentum neutrons and electrons, and thus seems to favour gas detectors for their imaging performance. However, it could be shown that by adding amplitude or even only local hit density information, the effect can be compensated.

It was proven in simulation studies [38] that with $3 \times 3 \text{ cm}^2$ tiles with analogue readout, it is possible to reconstruct the internal structure of hadron showers and to separate neighbouring particles even in the case of partial overlap of the hadronic cascade.

Though, in theory both approaches can be used for hadronic calorimeter, the choice between analogue and digital readout will only be possible after accurate comparison of prototype detectors under the same experimental conditions. This comparative test is planed by the CALICE collaboration to happen at the FermiLab test facility in the years 2007-2008.

3.2.5 The tailcatcher and muon tracker (TCMT)

The calorimeter system is completed by a muon tracker with calorimetric capabilities. In the final detector it can be used as a tailcatcher after the magnet. For the combined test of the prototype system it serves as an extension of the hadronic calorimeter. It is built as steel-scintillator sandwich like the AHCAL but with different scintillator geometry. One meter long and five centimetre wide strips with a central wavelength shifting fibre are used to collect the ionisation light. As photo-detector the same type as used by the AHCAL has been chosen, and therefore, the same VFE readout electronics is used as well. The TCMT has two different absorber structures. The first eight layers have a fine longitudinal segmentation of 2 cm steel and 0.5 mm scintillator and is therefore comparable to the fine AHCAL structure. The other eight layers have a coarse longitudinal segmentation of 10 cm thick steel. In total the TCMT has more than $5 \lambda_0$. The scintillator strip layers are alternating between horizontal and vertical orientation and give therefore the opportunity to reconstruct the hit position.

3.2.6   The test-beam data acquisition system

For the test-beam efforts a common data acquisition system is developed based on the VME [4] standard. A readout card hosting trigger logic, analogue to digital conversion and steering of front-end settings is developed, the so called CALICE Readout Card (CRC) (see [59]). The DAQ is capable of reading the almost 20000 channels of the combined CALICE prototypes with a rate of about 100 Hz. More details on the logic and structure of the DAQ are to be found in chapter 5.

---

[4]Versa Module Europa is a standardised bus system for experimental electronics.

Chapter 4

The analogue hadronic calorimeter technology

The last two chapters have motivated the need of a new concept for a hadronic calorimeter. The requirements imposed from the particle-flow concept lead to a combined calorimeter system with no dead material between calorimeters and no gap between the calorimeter system and the central tracker. This configuration is needed to match tracks identified in the tracker to clusters in the calorimeters. Both calorimeters must be located inside of the magnetic coil. Therefore, the detection devices should be independent of the applied magnetic field. Several proposals exist to realise such detectors, this thesis focuses on the technological choice for an analogue hadronic calorimeter (AHCAL), which uses scintillator as sensitive readout material. The technology proposed to realise a high granular hadronic calorimeter based on scintillator tiles is discussed in section 4.1. The selection of an appropriate photodetector for the readout of single tiles, insensitive to magnetic field, leads to the novel Silicon Photomultiplier (SiPM) described in section 4.2. The validation of a multi-channel system operated with SiPMs is presented in section 4.3. This step is necessary to establish the technology on which the AHCAL is based before the construction of a larger prototype to study the physics of hadronic showers.

4.1 The scintillator and wavelength shifter fibre

The basic detector unit for a highly granular analogue calorimeter is a scintillator tile of 0.5 cm thickness. An example of a 6×6 cm^2 tile is shown in figure 4.1 (a). A green wavelength shifter (WLS) fibre is inserted into a circular groove on the tile. The combination of scintillator and WLS fibre will be referred to as tile-fibre system. One side of the WLS fibre is coupled to a photodetector (a SiPM in figure 4.1 (a)). The other end is covered with a mirror obtained by 3M reflector foil to increase the light collection efficiency. The two faces of a tile are covered with 3M super reflector foil, while the four sides are chemically treated (matted) providing a diffuse reflector.

Particles are crossing the scintillator tiles and deposit energy producing ultraviolet (UV) light photons as described in figure 4.1 (b). The number of scintillation photons is proportional to the absorbed energy. The signal of a mip is the smallest physical signal that has to be detected with this kind of system. A mip produces ∼5000 scintillation photons. These photons have to be absorbed by the WLS fibre and transported to a photodetector. The WLS fibre absorbs the UV light and transforms it to the green wavelength, because the considered photodetectors have better efficiency in this wavelength range. At this point the energy absorbed in the

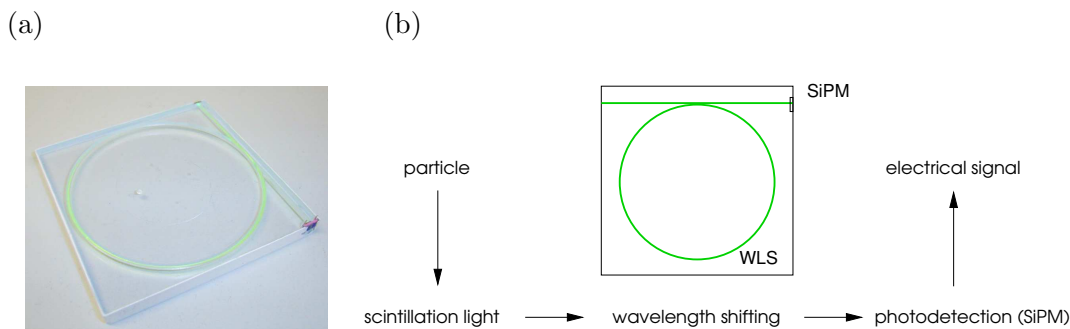scintillator has been converted into an electrical signal.

(a)   (b)

Figure 4.1: *(a) A scintillator tile with inserted WLS fibre and attached SiPM in the lower right corner. (b) Particle detection with scintillation detectors. Schematics of the order of the occurring processes in a single tile [60].*

In the following the individual components of the system are introduced: the scintillator, the WLS fibre and the SiPM.

Several kinds of scintillators exit, which can be sorted as inorganic or organic. The used scintillator in the following discussed system is an organic one and therefore no further information about inorganic scintillators is given. A detailed overview about different scintillator can be found in [61]. A plastic scintillator consists of a solid solution of organic scintillating molecules in a polymerised solvent. Several kind of plastic scintillators are available and often used for radiation measurement systems. Plastic scintillators are easy to shape and fabricate and are often the only practical choice if very large volume solid scintillators are required. In principle, scintillators emit photons when they have been excited by a charged particle. Photon production in organic scintillator is a molecular process in which the energy deposited by a charged particle or photon results in an excited state in which the excess energy is carried away as an emitted photon. This fluorescent emission produces approximately 1 photon with ultra-violet (UV) wavelength per every 100 eV of deposited energy. Because the energy required to produce an excited state exceeds that carried away by photons, the probability for re-absorption of the emitted photon is small; i.e. the scintillator is transparent to the light that it generates. The scintillation spectrum characterises the spectral distribution of emitted light wavelengths and has to be matched to the spectral sensitivity range of the photodetector or has to be transformed to another wavelength range by wavelength-shifter fibre. The spectrum is characterised by two parameters: the wavelength corresponding to the maximum of the light emission, and the full width at half maximum (FWHM) of the emission band. The scintillation emission of a typical plastic scintillator has a maximum around 400 nm, and a FWHM of about 50 nm.
The response time of a scintillator is generally larger than the time needed to detect an ionising particle in the scintillator. The scintillation pulse initially increases in a finite time and then decreases for most of the scintillators exponentially with a decay time which defines the rapidity of the scintillator. The light yield of organic scintillators is smaller than for inorganic ones but the response is faster (several ns instead of several 100 ns).
An important property of scintillators is the scintillation efficiency defined as the ratio of the average number of emitted photons to the incident radiation energy absorbed. It determines the efficiency and resolution of the scintillator. In general, the efficiency decreases for heavier particles like protons [62]. The light output is different for different types of particles at the

same energy [63]. The mechanism by which the radiation interacts with the molecules of the scintillator material depends on the particle type and therefore also the probability of inter-actions occurring in the scintillator volume. As soon as no direct ionisation takes place this quantity is given by the mean free path of photons in the scintillator material, which is in plas-tic scintillator ∼40 cm. Therefore, the detection of neutral particles need quite large sensitive detector volumes. The efficiency of most scintillators for electrons is quite high, whereas for gammas and neutrons the efficiency depends on the dominant process to transfer their energy to a charged particle capable of ionising and exciting the scintillator material. For gammas the three basic interactions: photoelectric effect, Compton scattering and pair production (see section 2.2.3) play a role and for neutrons the detection relies mainly on detecting the recoil proton in scattering processes. As already mentioned in section 2.4.5 plastic and other organic scintillators are convenient in this respect, since they contain large amount of hydrogenous material. However, gamma radiation deposits energy in the detector through electrons while neutrons deposit energy through protons. For a given energy, the stopping power of a proton is greater than that of an electron. Because of this difference, protons deposit energy more densely than electrons, which can lead to saturation effects as discussed in section 2.4.5 (Birk's law [29]).
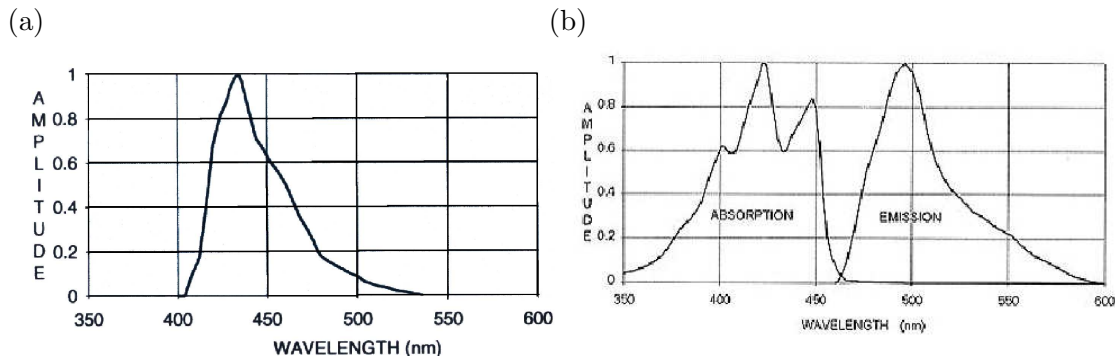
(a)   (b)

Figure 4.2: *(a) The emission spectrum of an example scintillator. (b) The absorption and emission spectrum of the used WLS-fibre.*

The tile-fibre system design shown in figure 4.1 (a) consists of the main scintillator tile and the WLS fibre, made of two different scintillator materials (polystyrene and polyfluor). This secondary scintillator is used to shift the emitted light to longer wavelengths, near the maximum of the photodetector spectral-response curve. For the used green wavelength shifter fibres, the absorbing spectrum has a mean of $\lambda = 420$ nm and the emitting spectrum of $\lambda = 500$ nm (see figure 4.2). The absorption and emission spectra for several WLS can be found in [64]. The green light is emitted inside the fibre and has a small probability (typically 2-6 %) to be collected inside the fibre and led to the photodetector [65]. The collection efficiency depends on the geometric integration of the fibre into the scintillator tiles. More contact area means higher probability of light collection into the WLS. On the other hand attenuation becomes an issue for longer WLS fibres and bending leads to light losses as well [65]. To keep the emitted light inside the fibre, the fibre is cladded with a material with larger refraction index than the surrounding scintillator. This configuration leads to total reflexion for photons hitting the clad with an angle larger than $sin\ \alpha = \frac{n_0}{n_1}$. More than one cladding with decreasing refraction indices around the core of the fibre can increase the collection efficiency or lower the losses caused by bending [65]. The second reason to use the WLS fibre is to achieve a uniform light collection over the tile.

Several different scintillators have been studied [66, 67]. In [65] several results of the optimisation of the tile-fibre system are explained in detail. The final choice is Vladimir BASF-143 which is based on polystyrene and fulfils the light yield and cost criteria. As a WLS fibre Kuraray Y11(300 ppm) is used.

4.2   Silicon Photomultiplier

During the last ten years a new type of silicon-based photodetector was developed which is at the basis of the R&D project discussed in this thesis. The device commonly known as *Silicon Photomultiplier (SiPM)* consists of a series of avalanche photo-diodes operated in Geiger mode. Each diode is in itself the equivalent of a $p-n$-junction, sketched in figure 4.3 (a), to which an external reverse bias voltage (U_{bias}) is applied.
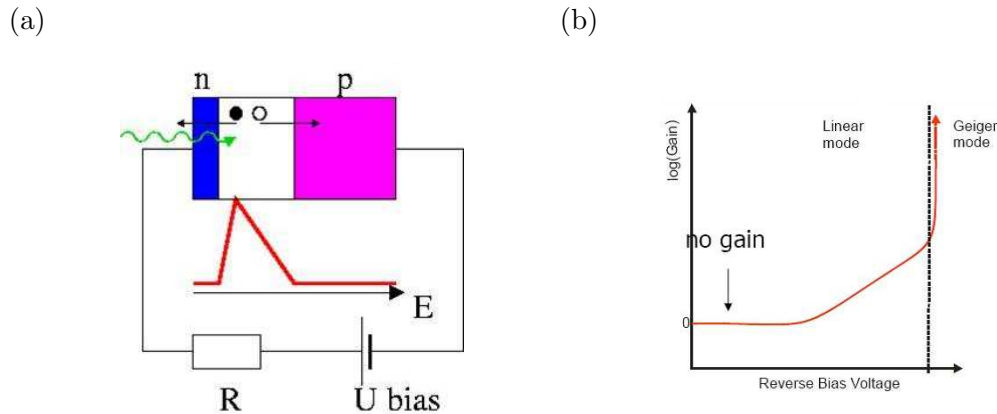
(a)   (b)

Figure 4.3:   *(a) SiPM diode scheme: $p-n$-junction. (b) Gain dependence on bias voltage.*

The depletion region necessary for a photon in the visible range (350-700 nm) to be absorbed and create an electron-hole pair (> 1.1 eV required in Silicon) is of the order of $2-3$ microns of depth. This number is quite small if compared to the $100-300$ μm thickness of typical semiconductors devices used to detect charged particles. Figure 4.4 (a) sketches the process of photon absorption and electron-hole pair creation in a reversely-biased $p-n$-junction. Electron and hole are pulled apart by the electric field present in the depletion region. The electric field nearby the junction in the depletion region can be of the order of 10^5 V/cm. In such a field the free carriers are drifting with a velocity of 10^7 cm/s toward the electrodes. Due to the fast drift electrons can gain enough energy to collide with the crystal lattice and generate another electron-hole pair, losing some of its kinetic energy. This process is known as impact ionisation. This process can repeat itself endlessly, hence the term *avalanche*.

If the magnitude of U_{bias} exceeds a value commonly known as *breakdown voltage* the growth in population of electron-hole pairs out-paces the collection rate at the electrodes, leading to exponential growth of current. Figure 4.4 (b) illustrates the Geiger avalanche resulting from this operation mode. In figure 4.3 (b) the gain, or avalanche multiplicity growth with voltage is sketched.

Photodetectors operated in Geiger mode achieve gains of 10^5-10^6 electrons for each photoelectron. This number is independent of the energy of the incoming photon and it can be compared with the much smaller gain of proportional avalanche photo-diodes (APD) which ranges between 10^2 and 10^4.
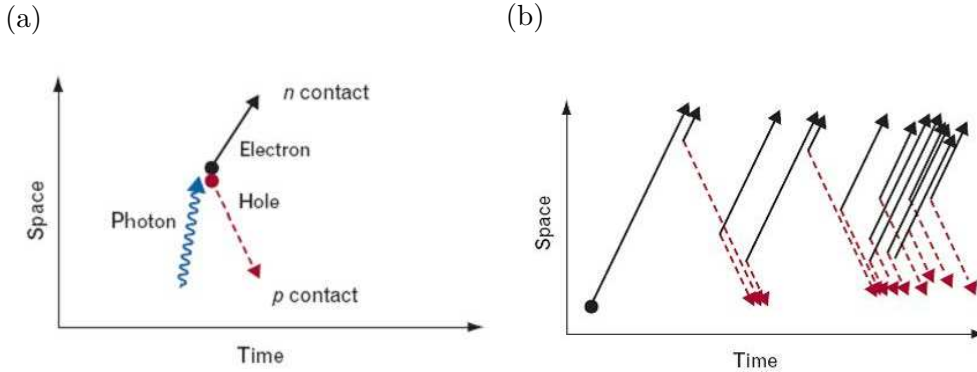
Figure 4.4: (a) Photon detection in a photo-diode represented in a space-time diagram. The absorption of the photon creates an electron-hole pair. The two oppositely charged particles drift in opposite directions under the influence of the electric field in the vicinity of the reversed-biased $p-n$-junction. (b) Concept of avalanche breakdown voltage. In Geiger mode the growth in population of electrons and holes due to impact ionisation out-paces the rate at which they can be extracted, leading to exponential growth of current.

The limited Geiger mode operation of the silicon photodetectors is well known for at least 30 years and is reviewed in [68, 69]. The Single Photon Avalanche Diode (SPAD) described in [68, 69] is just a single small ($20-200$ μm size) pixel, operating with bias voltage $10-15$ % higher than the breakdown voltage. Gains up to 10^9 have been reached with SAPD. However, this device is just a very small size single photon counter, a one bit binary device not capable of measureing light intensity. This limitation is overcome in the SiPM by joining together on common silicon substrate a large number of SAPD pixels, all working on common load (see figure 4.5 (a)). The typical size of each pixel is $20-30$ μm (with a capacitance $C_{pixel} \sim 50$ fF), the typical number of pixels per squared millimetre ranges between $0.5 \cdot 10^3$ and $5 \cdot 10^3$. The Geiger avalanche in each pixel is quenched passively by a polysilicon resistor, such that each pixel can be seen as a diode in series with a resistor. Typical values for the quenching resistor R_{pixel} are in the range of $0.5-20$ MΩ.

The SiPM can be viewed as the parallel sum of all diode-resistor components. The polysilicon resistor has as secondary function that of electrically decoupling each pixel from its neighbours to limit inter-pixel crosstalk. In addition, specially designed boundaries between pixels are added to the design in order to prevent the electrical coupling due to inter-pixel currents in silicon itself. Unfortunately, these boundaries cover some of the active area of the SiPM. The geometrical packing reduces the photo-detection efficiency of the device as it will be seen below.

4.2.1 Single pixel response

The very high gain of this device gives the possibility to observe the signal of a SiPM directly on an oscilloscope without additional amplification. The signal corresponding to a very low intensity of light on the SiPM surface is shown in figure 4.6 (a) as observed on the oscilloscope, and in figure 4.6 (b) as recorded by a QDC.

In both cases the typical single-pixel separation is clearly visible. From figure 4.6 (b) it can also be observed that the SiPM signal is very fast, with a rise time of < 1 ns (the horizontal scale of the picture is given with 2 ns / division and the vertical scale with 2 mV / division). The decay time of the signal is composed of two parts. A fast component arising from the
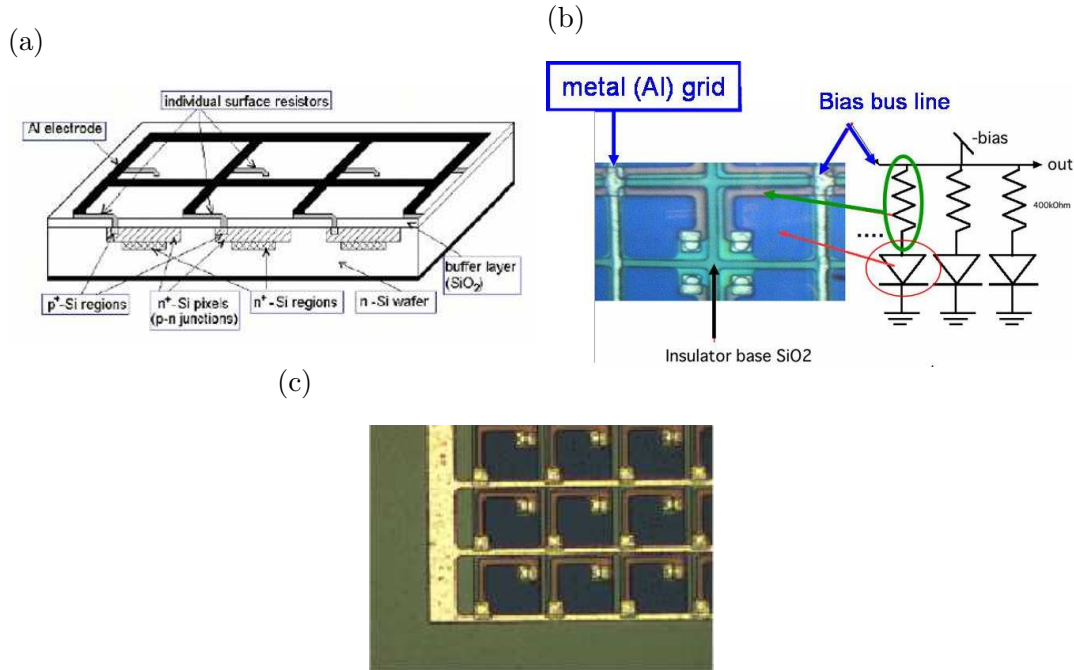
Figure 4.5: *(a) Schematic view of a multi-pixel Silicon Photomultiplier (SiPM). (b) Micro-scopic picture of a SiPM with schematics of the equivalent electronic circuit. (c) Photograph of an enlargement of the single pixel structure.*
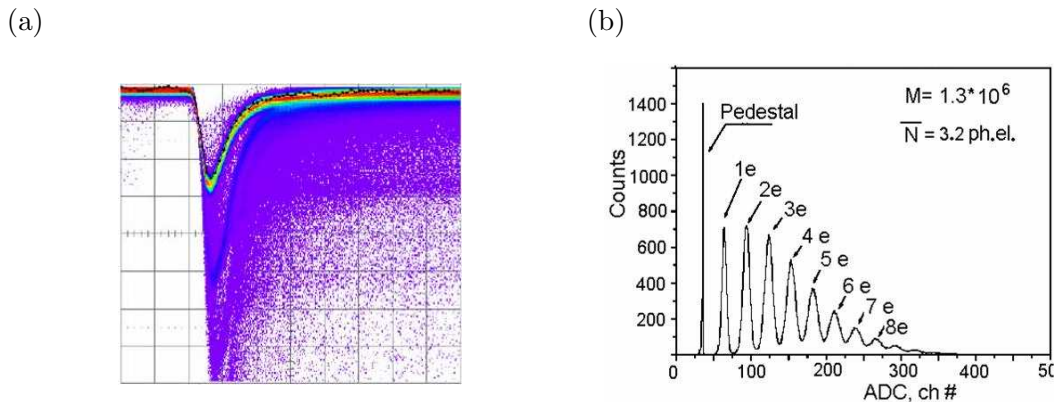

Figure 4.6: *(a) An oscilloscope picture of SiPM signal. The various bands are visible which correspond to single pixels fired. (b) The QDC spectrum of low light intensity recorded by a SiPM. The single pixels fired give rise to the various peaks in the spectrum.*

fast charge collection due to the high drift velocity, and a slower intrinsic component related to the pixel charge up time $\tau = R_{pixel} \cdot C_{pixel} \sim 20 - 500$ ns.
The SiPM gives a signal

$$A = N \cdot Q_{pix} \qquad N = 0, 1, ..., 1156, \tag{4.1}$$

which is N times the charge Q_{pix} of a single firing pixel. The gain of a SiPM $G = \frac{Q_{pix}}{e}$ is defined as the ratio between the charge released from one firing pixel and the electron charge e. The charge created in a pixel will vary from avalanche to avalanche due to fluctuations in the multiplication process and due to small differences between the pixels. The distance between the mean signal $\Delta_i = < A_{i+1} > - < A_i >$ for $i+1$ and i fired pixels is proportional to the charge of one pixel.
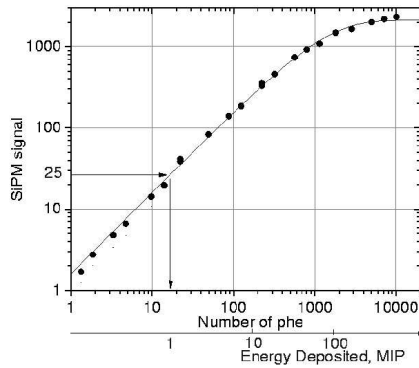
(a)   (b)

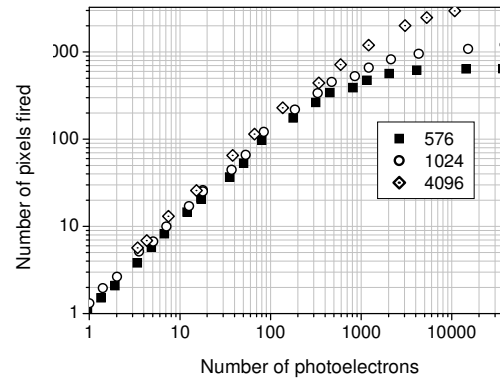

Figure 4.7: (a) SiPM (1056 pixels/mm^2) response curve dependence on the input signal in photo-electrons and in deposited energy in mips, assuming that 1 mip corresponds to 15 pixels. LED light is used as input [6]. (b) SiPM response curve for three devices with increasing number of pixels per square millimetre from 576 to 4096. On a double logarithmic scale the response is non-linear over almost the entire range. The light signal is produced by a fast laser (40 ps) [6].

As already mentioned the SiPM signal is the sum of all pixel fired at the time of the measurement. Due to the limited number of pixels and the finite recovery time this leads to a non-linear response curve for numbers of impinging photons comparable to the number of pixels. This behaviour is illustrated in figure 4.7 (a) where the SiPM response is plot versus the true light intensity in photo-electrons and mips. Three measured curves are given in figure 4.7 (b) which represent the SiPM output in terms of number of pixels fired as a function of the calculated number of photo-electrons seen by the device. The three curves are for SiPMs with different number of pixels / mm^2. The smaller the number of pixels the earlier the inset of saturation occurs on the device.
As a very simple approximation the saturation of SiPM can be described by the expression

$$N_{pixels} = N_{tot} \cdot \left[1 - exp\left(\frac{N_{pe}}{N_{tot}} \right) \right], \tag{4.2}$$

where N_{tot} is the total number of pixels of a given SiPM and N_{pe} the number of photo-electrons. According to this expression if 50% of the pixels are fired the SiPM response deviates from linearity of about 20%. Some more complex correction functions are discussed in chapter 6.

4.2.2   Photo-detection efficiency

The most important parameter characterising a photodetector is its photo-detection efficiency (PDE). Figure 4.8 (a) offers a comparison of photon-detection efficiencies for vacuum and silicon devices. For photomultiplier tubes (PMT), avalanche photo-diodes (APD) and hybrid photo-diodes (HPD) the PDE is actually a quantum efficiency QE, whereas for SiPM (Pulsar) it is less than that mainly due to geometrical packing factor (ϵ_{geom}= sensitive area/total area). The geometrical efficiency decreases with increasing number of pixels/mm^2 as demonstrated by the Hamamatsu measurements reported in figure 4.8 (b). To the reduced SiPM PDE contributes also the Geiger efficiency, which is the probability that the primary electron-hole pair originates a Geiger discharge. The value of the Geiger efficiency is normally very high around 99 % when SiPMs are operated above breakdown voltage, but can vary significantly with bias voltage variations.
The shapes of PDE curves for SiPM and APD (or other silicon photodetectors) are rather similar. The SiPM PDE is at present comparable to PMT QE for blue-green light and larger for yellow-red light.

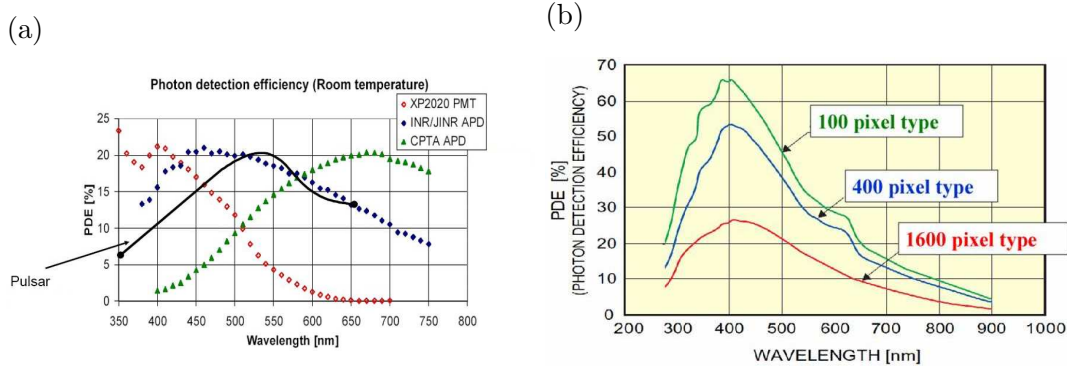(a)   (b)

Figure 4.8:   (a) Comparison of photon-detection efficiency for PMT [70], APD [44] and SiPM [71]. (b) Comparison of photo-detection efficiency for three types Multi Pixel Proportional Counters (MPPC) from Hamamatsu [72]. This new version of SiPM has also a sensitive area of 1 mm^2 with different number of pixels and it has a higher sensitivity in the blue wavelength range.

4.2.3   Dark-rate

There are mainly two mechanisms responsible for the random generation of an electron-hole pair in the depleted region of a silicon device: thermal excitation and tunnelling, illustrated in figure 4.9 (a) and (b) respectively. The thermal contribution decreases very rapidly with temperature and its effect can be cured with cooling. The electric field assisted (or tunnelling) component [73] contributes significantly because of the high electric field of $\sim 3 \cdot 10^5$V/cm.
Due to the Geiger operation these electron-hole pairs generated as *dark* events can initiate an avalanche, leading to an electric pulse, indistinguishable from that of photo-detection. In the usage of SiPM for photon counting to measure intensity these events inflate the count. The average error can be measured and subtracted, but its statistical variance contributes as a noise source.
    The number of dark-current-induced events per second is the *dark count rate*. This rate can be minimised reducing the temperature of operation of the detector, or by improving the quality of the material (Si) and the fabrication techniques to reduce the number of impurities
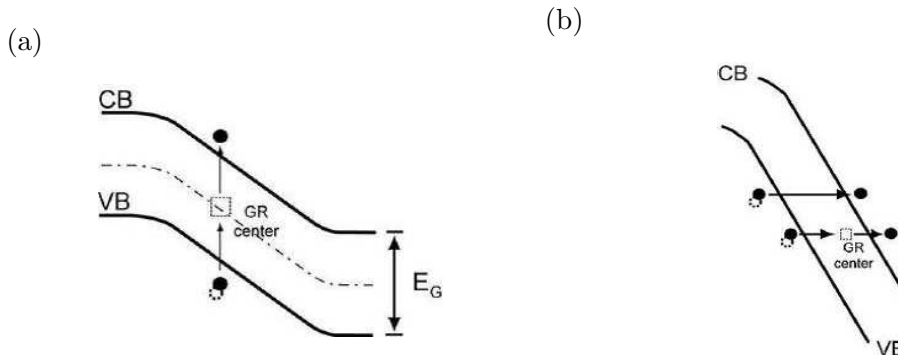
Figure 4.9: *The two main mechanisms responsible for the generation of an electron-hole pair in the depleted region of a silicon device: thermal excitation (a) and tunnelling (b).*

and defects that contribute to the dark current.

Typical values of dark-rate above a threshold of half of a pixel are around $1 - 3$ MHz at room temperature for a ~ 1000 pixel/mm^2 device operated at a gain of 10^6. This value rapidly decreases at higher thresholds, such that for signals above $3 - 4$ pixels amplitude the dark-rate can be below 1 kHz.

4.2.4   Optical crosstalk

The effect of inter-pixel crosstalk caused by photons traversing the electromagnetic boundary between two pixels and their initiation of a second discharge is commonly referred to as optical crosstalk. Measurements of radiation from Si devices indicate that about $3 \cdot 10^{-5}$ photons are emitted with energies greater than the band-gap ($E_{gap} = 1.14$ eV) for every carrier that crosses the junction [74]. In the emission spectrum of SiPM pixels in figure 4.10 (a) the effect of optical crosstalk is clearly visible as a second pixel fired to the right of the pixel in Geiger avalanche.
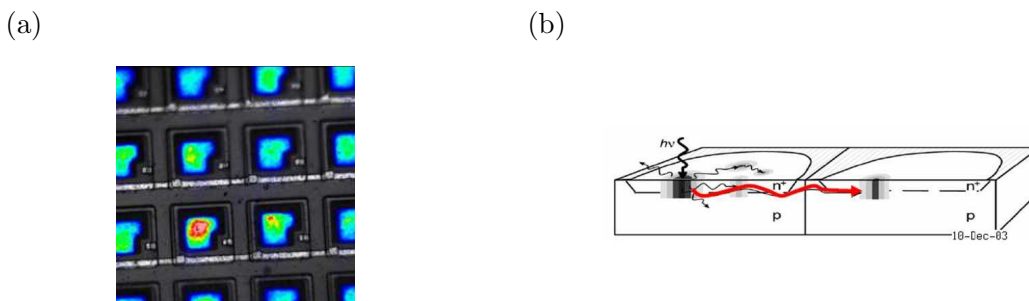
Figure 4.10:   *(a) Emission spectrum of SiPM pixels. Visible is one pixel fired by dark-rate and its neighbour fired by optical crosstalk. (b) Sketch of the optical crosstalk effect.*

Figure 4.10 (b) illustrates the process of photon propagation between neighbouring pixels. Optical crosstalk in SiPM can be reduced by decrease of operation voltage, though decreasing the PDE and therefore the SiPM performance. Better solutions are technological improvements, either by inter-pixel trenches or by minimisation of the parasitic capacitance of each pixel. Typical values of optical crosstalk on present SiPM devices are between 10 and 25 % and depend strongly on the operation voltage.

4.2.5 Voltage dependence of SiPM parameters

The bias voltage of operation of a SiPM determines the depth of its depletion region and therefore the value of all its characteristics. Figure 4.11 (a) and (c) show linear voltage dependence for optical crosstalk and dark-rate. The dark-rate above 0.5 mip, in figure 4.11 (b), is dependent on a threshold which by itself strongly varies with voltage. At low voltage the mip efficiency drops and the threshold cuts harder into the noise tail. For voltages 1.5 V above the nominal setting the noise increases exponentially. Thus, this quantity is most relevant for practical application of SiPM to calorimetry.

(a)   b)   (c)
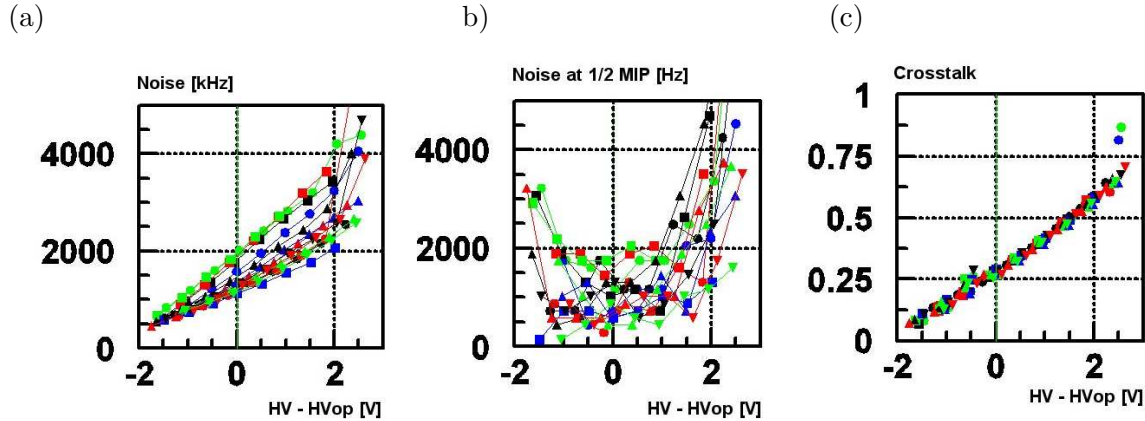
Figure 4.11: *Voltage dependence of SiPM parameters in the range ± 2 V from the optimal operation voltage. (a) Dark-rate above 0.5 pixel threshold. (b) Dark-rate above 0.5 mip threshold. (c) Inter-pixel crosstalk.*

(a)   (b)

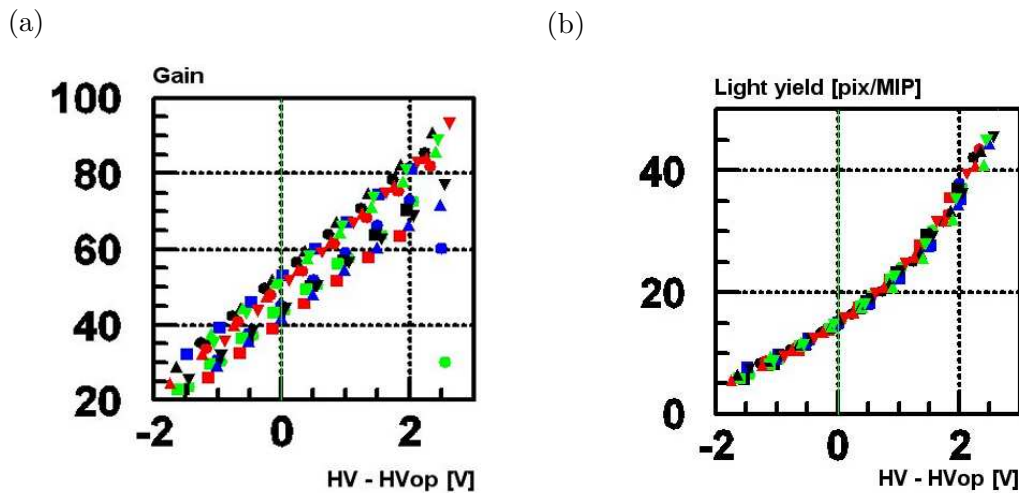Figure 4.12: *Voltage dependence of SiPM parameters in the range ± 2 V from the optimal operation voltage. (a) SiPM gain. (b) SiPM light yield.*

Figure 4.12 (a)-(b) display the voltage dependence of SiPM gain and light yield respectively, where SiPM light yield is sensitive to both gain and PDE voltage dependencies. The values for the voltage dependencies of the various parameters at standard operating condition of ∼3 V

above breakdown voltage:

$$\begin{aligned}
dG/dV &\approx 2.5\%/0.1V, \\
dG/dT &\approx -1.7\%/K, \\
dQ/dV &\approx 7\%/0.1V, \\
dQ/dT &\approx -4.5\%/K.
\end{aligned}$$

(4.3)

4.2.6 Magnetic field test

The hadronic calorimeter in a ILC detector will be operated in a 3-5 T magnetic field. The operation of SiPMs has been tested at DESY in a magnetic field up to 4 T for two orientations of the field: parallel and perpendicular to the SiPM detector surface. The light amplitude of a LED signal has been recorded as a function of the magnetic field in comparison to zero-field measurement. As shown in figure 4.13 the SiPM signal is constant within a 1 % measurement accuracy. Furthermore, the dark current, noise frequency, gain and inter-pixel crosstalk of a SiPM have been measured at 4 T and found to be magnetic field independent. The detailed measurement and result description can be found in [5].
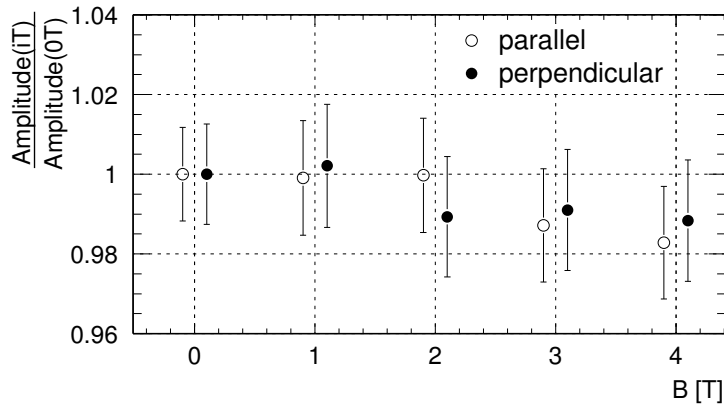
Figure 4.13: *SiPM signal amplitude dependence on magnetic field for two orientations of the field perpendicular and parallel to the photodetector surface.*

4.2.7 SiPM coupling to tile-fibre system

The SiPM offers due to its small dimensions the possibility to mount it directly on tile. The in the following used SiPM is the MEPHI [1] type, which is a product of the Russian PULSAR enterprise and MEPHI supported by DESY. The most recent status about this photodetector and its application can be found in [75]. The SiPM has to be placed and positioned at one edge of the tile, where the WLS fibre ends. In addition, it needs a two pin connection to provide supply voltage and readout. The SiPM and the two connection pins are glued on a ceramic plate and connected over two boundings (see figure 4.14). The position has to be adjusted such that the WLS fibre with its 1 mm diameter is shining to the middle of the sensitive area of the SiPM and the gap in between should be below 100 μm.

---

[1]Moscow Engineering Physics Institute.

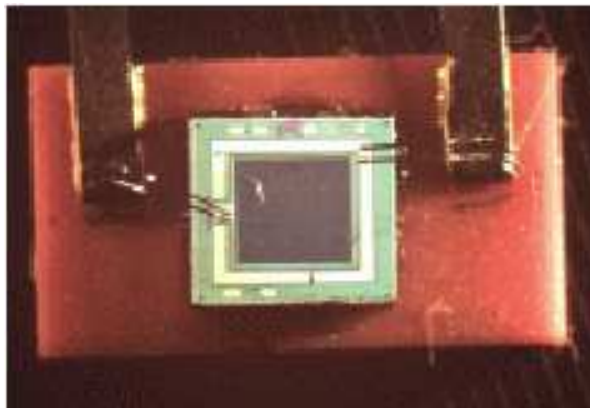Figure 4.14:   *Picture of a SiPM glued on a ceramic support plane and connected to readout pins.*

The tiles are produced by injection moulding. The tiles have been equipped with WLS fibre and SiPMs at ITEP. The groove is machined with a computer controlled milling device which can produce also the fitting for the SiPM with sufficient mechanical accuracy.

4.3   Technical prototype: MiniCal

The MiniCal is a flexible calorimeter technical prototype to be operated with cosmic rays and in the DESY electron/positron test beam at energies from 1 to 6 GeV. It consists of a multi-channel system of tiles as described in 4.1. The goal of this prototype has been to acquire operational experience with a system with 100 readout channels, and to use well understood electromagnetic showers for a detailed detector understanding. This program is considered as an important step on the way to a large hadronic test beam prototype.

The MiniCal is built as a 11 layers sandwich structure with 2 cm steel absorber plates and 1 cm gaps to accommodate the active detector modules. These modules are aluminium cassettes equipped with 3×3 scintillator tile arrays. This structure provides 96 % containment of a 6 GeV electromagnetic shower. The scintillator tile size is $5 \times 5 \times 0.5$ cm^3. The readout layers can be easily exchanged to compare different readout technologies. Three versions of active layers have been tested in which the readout proceeds either via 108 directly coupled SiPMs, or via longer WLS fibres routed to 36 APDs or 3 16-channel multi-anode photomultipliers (MAPM). The material in the MiniCal at normal incidence amounts to 1.15 radiation lengths (X_0) and to 0.12 interaction length per layer. More details about the MiniCal design, construction and quality control can be found in [76].

The following focuses on the SiPM readout option. Details about the analysis of the other two readout options can be found in [6] and [77].

4.3.1   Experimental setup at the DESY test beam

The data have been collected at the beam-line T21, which is one of the three test beam-lines providing electrons and positrons at DESY. The momentum of the electrons reaching the experimental area can be selected between 1 and 6 GeV/c. The beam energy spread from the smallest collimator slit ranges from 6 % at 1 GeV to 2 % at $3 - 6$ GeV. A schematic layout
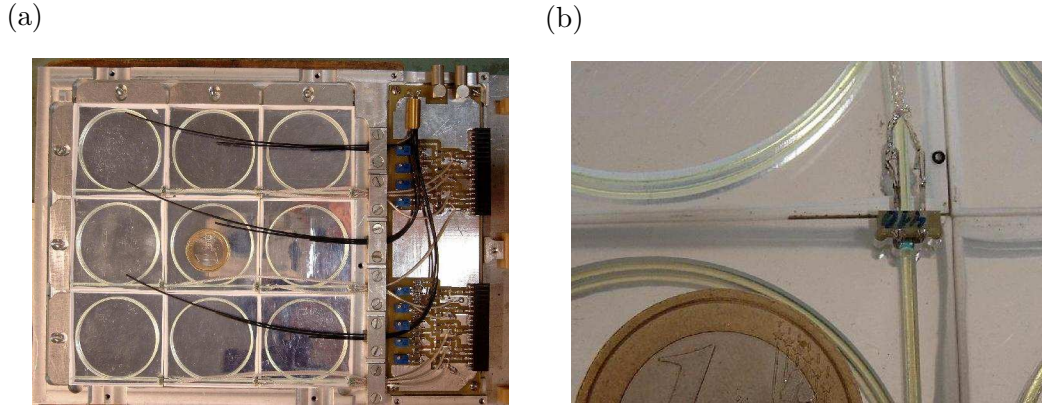
(a) (b)

Figure 4.15: *(a) An open cassette housing 9 tiles with a WLS fibre placed in a circular groove read out by a SiPM. (b) Zoom on the SiPM connection on tile. The SiPM mounted on a ceramic support is inserted in the tile in front of the open end of a WLS fibre. The signal is read out from the two rear pins via a coaxial cable.*

and description of the test-beam line can be found in [78].

A beam trigger is obtained by requiring coincident hits from two perpendicular scintillator counters with a cross-section of 2×2 mm^2 and a veto signal from a hole counter. In addition, a pedestal and an LED trigger are installed. The MiniCal has no electronics close to the detector. The analogue signal from the SiPMs is directly sent to a LeCroy 2249A 10-bit charge sensitive ADC via 25 m long 50 Ω cables. The typical mip pulse size is 2.5 pC in 20 ns, with a fall time of $\sim$60 ns. For gain calibration, the signal is amplified by a factor of 20. A trigger gate of 100 ns is used for the ADC. The ADCs are read out via CAMAC [2] with a speed of about 700 events/s.

4.3.2 Calibration procedure

For calibration, the spectrum generated by the passage of the beam through the cassettes outside of the steel absorber structure is used. The observed signal corresponds to the deposited energy by a mip and the distribution follows in principle a Landau distribution. The most probable value defines the mip and constitutes the common energy scale for data and simulation. This value is affected by different light yields in the tile and by different photodetector gains. A typical pulse height distribution for a mip signal from SiPM is shown in figure 4.16. To determine the mip value a Gaussian function is used to describe the pedestal contribution and a linear combination of a Gaussian function and a Landau function to describe the energy distribution deposited by the mip. The resulting fit is shown by the solid line, while the dashed lines show the separate contribution of the Gaussian and Landau functions to the fit. The mip amplitude for each tile is defined to be the difference between the most probable value of the signal and the mean value of the pedestal. The average signal-to-noise ratio for the mip signal is $\sim$30.

Calibration and stability checks are described in [6]. Beam position scans over the tiles have been performed and give a systematic uncertainty of 2 %. A LED system monitored by photodiodes (PIN) allows to measure response changes due to temperature differences and to apply corrections. To determine SiPM non-linearity corrections, LED runs were taken to measure the number of fired pixels corresponding to the mip signals. By amplifying the SiPM signal

---

[2]Computer Automated Measurement And Control is a standard bus for data acquisition.

by a factor 20, it is possible to observe the single photo-electron spectrum from low intensity LED light. The distances between the observed peaks can be used to determine the gain as described in section 4.2.1. The ratio of mip signal to gain determines the light yield. The average light yield obtained for all 99 channels is 25 ± 4 pixels/mip.
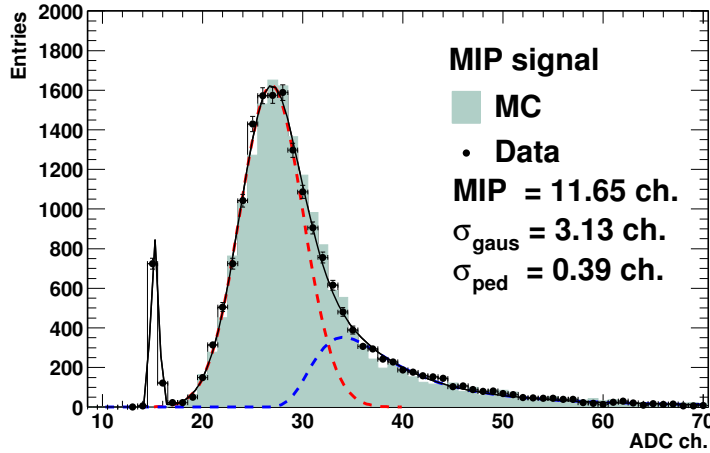

Figure 4.16:   *Mip spectrum from SiPM fitted with the function described in section 4.3.2 (solid line). The dashed lines show the contribution of the Gaussian and Landau functions to the fit. The MC prediction (full histogram) is discussed in section 4.3.3.*

4.3.3   Simulation of detector effects

The MiniCal structure has been implemented in a Geant4 simulation. The simulation (MC) of the idealised detector response is completed by a step which models the signal formation and accounts for the finite photo-electron statistics and for the non-linear SiPM response. The agreement of data to MC of mean values is not affected by this implementation but it is needed to achieve agreement in single channel distributions like for the mip distribution in figure 4.16, longitudinal and lateral shower profiles (see [6]) and in the energy resolution, shown in figure 4.18. The signal chain has been included in a digitisation step to include photon detection chain until the photodetector response and readout electronics influence as proposed in [79]. For all channels the ADC spectrum of a mip was reproduced in simulation by using the measured light yield and noise values. In addition, the non-linear SiPM response has been implemented to perform the same correction as in the data. In figure 4.16 the pulse height spectrum in ADC channels are shown and compared to the MC prediction after digitisation step. The mip spectrum is well reproduced by the simulation.

For an ideal detector response an energy resolution of $18.5 \%/\sqrt{E[GeV]} \oplus 2$ %, following equation 2.35, is expected from the energy deposition in 11 layers. The constant term of 2 % is mainly due to shower leakage. Up to 4 % of the total energy for a 6 GeV beam escapes the detector. Lateral leakage is negligible. A major effect to achieve agreement in the energy resolution was to integrate the real beam energy spread discussed in section 4.3.1 into the Geant simulation.

4.3.4 Linearity and energy resolution

Figure 7.19 shows the energy deposition summed over all tiles of the 11 layers of the MiniCal obtained with SiPM (circles) and compared to the results obtained from MAPM (squares) readout for beam energies from 1 GeV to 6 GeV.
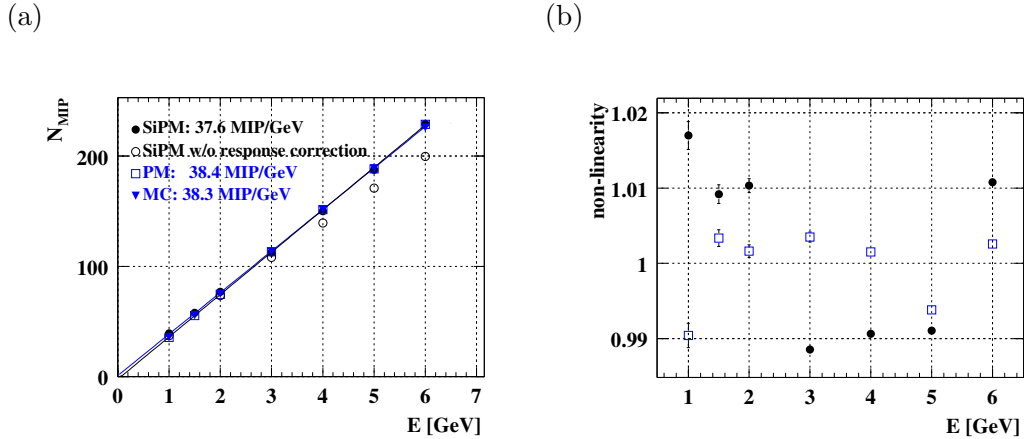
(a)   (b)

Figure 4.17: *(a) Total signal normalised to number of mips versus beam energy, where solid points (open circles) show SiPM data with (without) response function correction, squares MAPM data and triangles MC prediction respectively. (b) Deviation of the measurements from a linear fit.*

A linear fit is performed to the data to extract the slope parameter in units of mip/GeV. The slopes for the two photodetectors agree at the 2% level. By constraining the fit to the zero point the slope changes by 2% with respect to the unconstrained fit. The linear behavior of the SiPM result (better than 2%, as seen in figure 7.19 (b)) demonstrates that the applied saturation correction is reliable. The magnitude of such a correction can be as large as 15% at 6 GeV as the uncorrected data (open circles) indicate. The MC prediction for the total number of mips including detector response and beam energy spread is also in good agreement with the data as shown in figure 7.19 (a) (triangles).

The energy resolution for the two data sets is plot in figure 4.18. The stochastic terms of the energy resolution for both SiPM data and MAPM data are in very good agreement. In both cases, a value of the order of 21% is obtained, also well reproduced by the MC simulation. The constant term is about 2 % as expected from the MC simulation. The very good agreement between SiPM and MAPM results shown in figure 4.18 implies that the non-linearity of SiPM does not affect the energy resolution in the range probed by these studies.
The error includes both statistic and systematic uncertainties added in quadrature. The statistical error is typically of the order of 1.6-1.8 %. The main source of the systematic uncertainties is electronic noise, which contributes more significantly at low energies than at high energies (spanning from 5 to 2 % for SiPM and from 8.4 to 3.3 % for MAPM). The uncertainty due to photodetector non-linearity is 1.5 % for SiPM and less than 1 % for MAPM.

4.4 Conclusion

In this chapter the technology chosen for the construction of a large-scale high-granular hadronic calorimeter prototype has been presented. The basic unit of the calorimeter is intro-
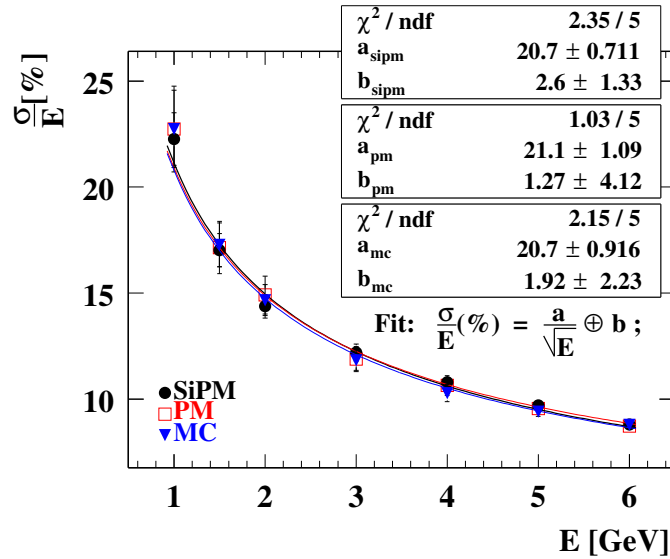
Figure 4.18: *Measured energy resolution for SiPM with (solid points), MAPM (squares) and MC prediction (triangles).*

duced, the tile-fibre system. A novel silicon-based photodetector has been described, which fulfils the requirements for a ILC detector. This detector is insensitive to magnetic field and can be employed for direct readout of the tile-fibre system.

The results of the operation of a 100-channels technical prototype built with this technology are encouraging. A calorimeter with SiPM readout has been compared to the more conservative readout option via photomultiplier tubes, and to simulation on the basis of well understood electromagnetic shower reconstruction. This results prove that the correction of the non-linear response of the SiPM is under control and does not deteriorate the energy resolution with respect to a linear detector. The good agreement between technologies and the good understanding provided by the simulation comparison reinforce the decision to build a large prototype to study hadronic shower reconstruction with this technology.

Chapter 5

The analogue hadronic calorimeter prototype

After the excellent experience with the SiPM in the MiniCal, it was decided to build with the same technology a test-beam calorimeter with 7608 channels fully equipped with SiPMs. This second prototype is a 1 m^3 in volume divided in 38 sampling layers covering a total thickness of 4.6 interaction lengths. The entire structure will be placed on a movable stage providing flexibility to select specific positions on the front face of the calorimeter and angles with respect to the incident beam. The analogue hadronic calorimeter prototype (AHCAL) is meant to be tested in combination with a highly granular electromagnetic silicon-tungsten calorimeter (ECAL) and with a tail catcher and muon tracker (TCMT), both introduced in chapter 3 and built by the CALICE collaboration.

This chapter focuses on the description of the AHCAL, its readout electronics and data acquisition system (DAQ). The phases of construction, assembly of components and commissioning are described. The steps of mass production and quality control of SiPMs and readout chip are discussed. The first results of the commissioning of the readout electronics are presented.

5.1   The analogue hadronic calorimeter

The analogue hadron calorimeter (AHCAL) test-beam prototype is a 38-layer sampling calorimeter made of scintillator-steel sandwich structure with a lateral dimension of about 1×1 m^2. Each layer consists of 2 cm thick steel absorber plates and a plane of 0.5 cm thick plastic scintillator tiles housed in a steel cassette. With respect to the MiniCal prototype it has been established by simulation studies [38] that the lateral granularity required for optimum shower separation is 3×3 cm^2. It was therefore decided to equip at least the core of the prototype with such a high granularity of tiles. For the first 30 layers, the tile sizes vary from 3×3 cm^2 for a matrix of 10×10 tiles in the centre of the module, to 6×6 cm^2 in the intermediate region (4×24 tiles) and 12×12 cm^2 (4×5 tiles) in the outer ring (see figure 5.1). In the last eight layers, the granularity is decreased to 6×6 cm^2 in the central region to reduce the costs. This configuration leads to a total amount of channels of 7608 which is summarised in table 5.1.

Each tile has, as in the MiniCal case, a wavelength-shifting (WLS) fibre inserted in a groove and coupled to a SiPM via an air gap on one end. In the 3×3 cm^2 tiles the grooves are quarter-circle shaped and in all other tiles they have a full-circle shape. A total of 216 tiles per layer are positioned and enclosed in a metal cassette with the following composition:
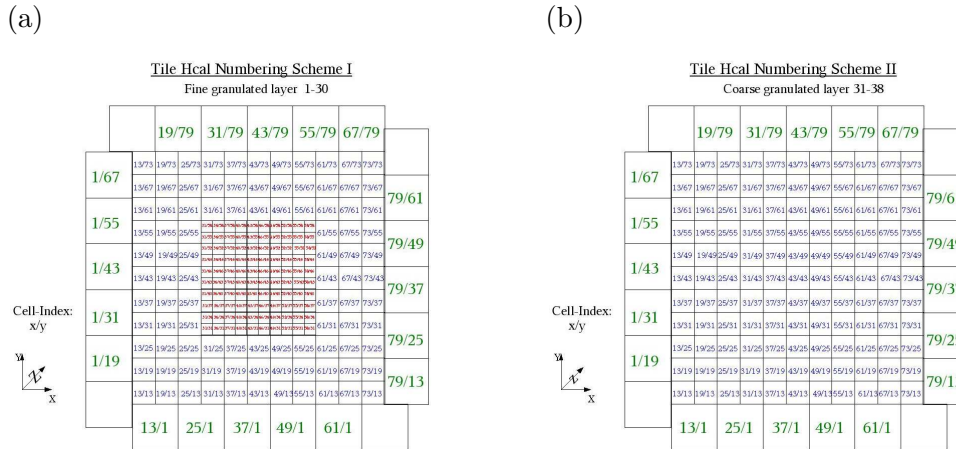
(a)　　　　　　　　　　　　　　　　　　　　　　　(b)

Figure 5.1: *(a) AHCAL module fine granularity for the first 30 layers. (b) AHCAL module coarse granularity for the last 8 layers.*

- 2 mm steel housing - rear plate,

- 115 μm 3M reflector foil,

- 5 mm scintillator tile,

- 115 μm 3M reflector foil,

- 1 mm FR4 plastic board,

- 1 mm cable fibre air mixture (PVC, fibre),

- 2 mm steel housing - front plate.

To this structure 16 mm of steel S235 is added to complete a sampling layer. About 1 mm of air gap is left between the steel cassette and the main absorber on both sides. Since the cassette housing has a total thickness of 4 mm, the total absorber thickness per layer adds up to 2 cm of steel. S235 is a standard steel product and is a composition of iron, nickel, chrome, carbon, manganese, phosphor and sulphur. The FR4 plastic board and the 3M reflector foil glued on it have for every tile two drilled holes. One hole is needed to solder the SiPM contact pins to the cable which provides the voltage and the readout line. The other hole is needed to inject UV-light distributed by clear fibres from a LED. The SiPM pins are soldered to copper strips on a specially designed printed circuit. The other end of the flexible strips are connected via coaxial cables to the very front-end base boards, also referred to as *HCAL Base Boards (HBAB)*[1]. Two base boards are needed to read out all 216 tiles of a module. Each base board houses six *HCAL Analog Boards (HAB)*, which hosts each one ILC-SiPM chip. The ILC-SiPM chip has been produced by the LAL [2] Orsay group [80] and is described in detail in section 5.3.4. It houses 18 individual channels, each containing a variable-gain charge-sensitive amplifier, a variable shaper, track and hold stage and a multiplexing unit. In addition it has an 8-bit DAC, which gives the possibility to perform single channel voltage adjustment in the range between 0 and 5 V. On the other edge of the cassette a *calibration and monitoring board (CMB)* is mounted, which holds and flashes the LED and is described shortly in section 5.3.1.

---

[1]in the following addressed as base board

[2]Laboratoire de l'Accélérateur Linéare

granularity	# modules	channels/ module	total # channels
fine	30	216	6480
coarse	8	141	1128
	38	/	7608

Table 5.1: *AHCAL total amount of readout channels.*

AHCAL layer quantities and properties

The nuclear interaction length λ_0 (equation 2.21), the radiation length X_0 (equation 2.6) and the Molière radius R_M (equation 2.13) for a AHCAL layer has been calculated using the quoted equations introduced in chapter 2.

material	ρ	λ_0	λ_{0g}	X_0	X_{0g}	R_M
	g/cm^3	cm	g/cm^2	cm	g/cm^2	cm
Fe	7.87	16.8	131.9	1.76	13.85	1.77
Ni	8.9	15.28	136.0	1.42	12.64	1.44
Cr	7.19	18.17	130.6	2.26	16.25	1.98
steel	7.83	16.86	132.0	1.8	14.09	1.78
scint.	1.032	68.5	70.7	42.4	43.76	10.32
FR4	1.85	53.6	99.2	17.4	32.19	7.85
air	0.00129	66312	85.5	28516	36.79	8904
AHCAL layer	5.95	22.84	135.9	2.62	15.59	2.47

Table 5.2: *AHCAL material and structure composition.*

To calculate these properties for the AHCAL layer, first the values for the material composition for steel has to be calculated. The values for steel are close to iron. The density ρ for example has a value of 7.83 g/cm^3 for steel and 7.87 g/cm^3 for iron. Afterwards, the additional materials of the AHCAL layer structure are weighted by their fraction to the total depth to get λ_0, X_0 and R_M for the complete AHCAL structure. Although, the contributions of the additional material seem to be small it has an impact on the total thickness in terms of nuclear interaction length for the calorimeter. Summing only the steel layers the total absorber thickness is $38 \cdot 2$ cm + 1.6 cm [3] = 77.6 cm. The total thickness can be divided by the nuclear interaction length of steel 77.6 cm / 16.86 cm which gives 4.6 λ_0. This calculation neglects the additional material. Considering the complete structure we have a total thickness of $38 \cdot 2.973$ cm + 1.6 cm = 114.57 cm, which results to 5 λ_0 by dividing by the nuclear interaction length of 22.84 cm.

5.2 The Silicon Photomultiplier and tile mass production chain

The SiPM and tile-fibre mass production is divided in several steps. First, the produced SiPMs are characterised and their operation voltage (U_{bias}) is adjusted. Afterwards, the complete

---

[3]An additional steel plate in the back of the last AHCAL active layer.

SiPM and tile-fibre system is build and together characterised. After the production the tiles are transported from Moscow to the module production at DESY, where a quality check for detection of possible degradations is performed.

5.2.1 The SiPM production

The SiPM has been introduced in section 4.2. In comparison to the used SiPM in the MiniCal prototype the one chosen for the AHCAL prototype have more pixels, 1156 instead of 1024, to provide more dynamic range. One of the biggest challenges was to produce SiPMs in a large quantity with similar characteristics. To have a uniform calorimeter especially the photodetector in combination with the tile-fibre system has to have a similar response to the traversing particles. The quantities on which SiPMs are characterised and selected are the gain, the noise properties: dark rate and inter-pixel crosstalk, the total number of working pixels, the quenching resistor and pixel capacitance, which has a direct influence on the signal time characteristics. Moreover, the SiPM and tile-fibre system has to be characterised by the value of the light yield. An additional requirement has to be imposed on the SiPM operation voltage, which has to vary less than 5 V for samples of 108 SiPMs due to the fact that they are connected to one high voltage channel.
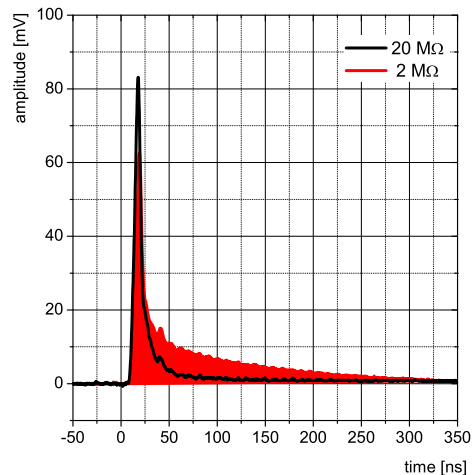
Figure 5.2: *SiPM signals with different quenching resistors observed on the oscilloscope. The red filled area is the signal obtained from a SiPM with a 2 MΩ resistivity and the black solid line from a 20 MΩ.*

In figure 5.2 two SiPM signals with different quenching resistors are shown as seen on the oscilloscope. The change in decay time of the signal due to change in resistivity ($\tau = RC$) is clearly visible. For the red curve corresponding to a low quenching resistor around 60 % of the signal is in the tail, where tail means signal after ≈20 ns from the signal maximum. In case of the black curve only 45 % of the signal is in the tail.

In the meantime, the whole sample of 7608 has been produced. The characterisation is

performed at ITEP Moscow [4] in an automatic setup, where 15 SiPMs are simultaneously illuminated with a calibrated UV LED light source. The U_{bias} working point is chosen as that yielding 15 pixels for a mip-like signal provided by the calibrated LED. During the first 48 hours, the SiPMs are operated at an increased reverse-bias voltage $\sim$2 V above the nominal operation voltage. Afterwards, the gain, noise and relative efficiency with respect to a reference photomultiplier tube are recorded as a function of the operation voltage U_{bias}.

At the working point several SiPM properties are measured. With low-intensity LED light, single-pixel spectra used for the gain calibration are recorded. A typical single-pixel spectrum is shown in figure 5.3 (a). From this measurement the SiPM gain can be calculated, which has to be above $4.3 \cdot 10^5$. The response function of 4000 individual SiPMs, depicting the number of fired pixels versus intrinsic LED light over the entire range from zero pixel to saturation is plot in figure 5.4 (b). The individual curves lie all within $\pm$15 %. The minimum required amount of active pixels is 900. Noise rate at half of a mip threshold, inter-pixel crosstalk and SiPM current are measured in addition. Figure 5.3 (b) shows the noise rate distribution. The arrow at 1.8 kHz shows the selection cutoff. This cutoff has been released to 3.0 kHz to enlarge the selected sample. In addition, the noise rate at zero-pixel level should be below 3.0 MHz. Figure 5.3 (c) illustrates the current distribution. The mean current value is around 0.5 μA and the cut value is 2 μA. An additional requirement on the current is its stability, which should be inside of 20 nA. Figure 5.4 (a) shows the cross-talk distribution for the produced SiPMs. The mean value for the cross-talk is $\sim$25 % and should not extend to values larger than 35 %.

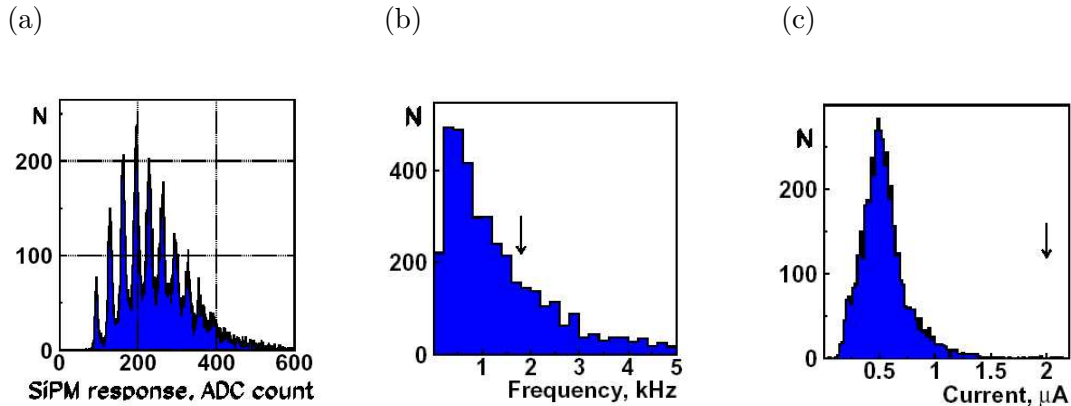(a)   (b)   (c)

Figure 5.3: *(a) SiPM spectrum for low-intensity light, the distance between the pixel peaks determines the gain. (b) The noise distribution of SiPMs at half of a mip threshold. (c) The current distribution of SiPMs [81].*

Such a high number of SiPMs has to be produced from more than one silicon wafer. The properties of a SiPM is partially defined by the properties and quality of this wafer. Therefore, the SiPMs used in the test-beam prototype have slightly different properties. The samples vary in their quenching resistor and therefore in the time characteristics of the signal (decay time), in the amount of dark-rate and inter-pixel crosstalk and in their operation voltage. The voltage range of the used SiPMs varies from 30 V up to 80 V. In addition the SiPM properties are temperature and voltage dependent. The two most important parameters which have to be monitored and corrected during operation are the gain and the overall light response, which is the product of the gain and the photon detection efficiency. Both quantities have

---

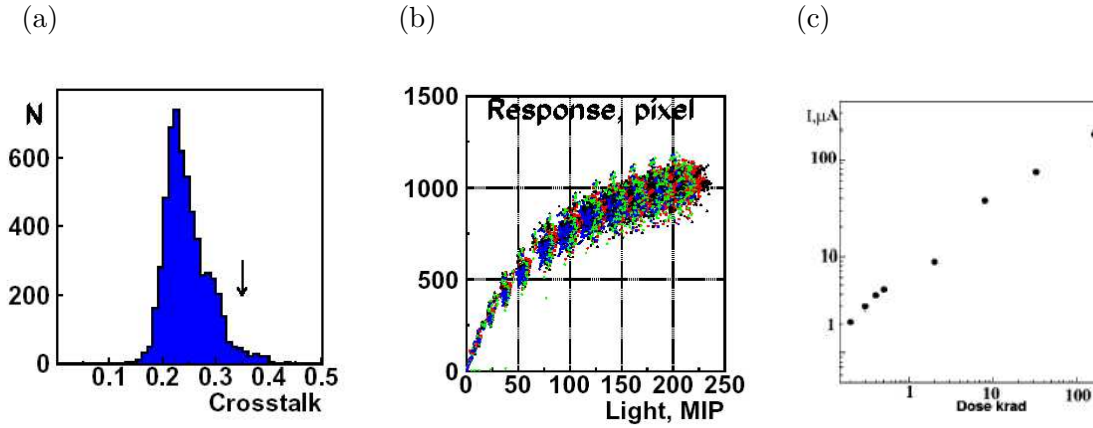[4]Institute for Theoretical and Experimental Physics.

Figure 5.4: *(a) Cross-talk distribution and (b) SiPM response function for 4000 SiPMs [81]. (c) SiPM current as a function of radiation dose for 200 MeV protons [82].*

been introduced in chapter 4. These dependencies have been measured and are summarised in equation 4.3. The light yield is the ratio of both quantities and therefore the light yield voltage and temperature dependencies are also the ratios of the single quantity dependencies. The light yield dependencies are summarised in equation 5.1,

$$
\begin{aligned}
dLY/dV &\approx 2.8\%/0.1V, \\
dLY/dT &\approx -2.7\%/K.
\end{aligned}
\tag{5.1}
$$

5.2.2   Tile production and tests

The important quality parameter in the tile production is the light yield for each calorimeter tile. In order to cover the full dynamic range but still be able to reveal a clear signal above noise, the mip signal from each tile should lie in the 10-20 pixel range. Before positioning the SiPM on tile, the SiPM bias voltage is adjusted to deliver around 15 pixels per mip for a standard tile. This value is a compromise between mip detection efficiency and dynamic range. In figure 5.5 it is shown that a mip signal with a light yield of 15 pixels is still quite narrow and depending on the threshold chosen can lead to a mip detection efficiency of 99 % (see figure 5.5 (b)). In ITEP the SiPMs are connected to the tiles and the working point is checked on the base of these measurements. For each tile, the mip response is measured using triggered electrons from a ^{90}Sr source. The most probable value of the mip response varies from tile to tile due to different light collection efficiency. This inefficiency has manifold reasons like differences in the scintillator quality, cracks in the WLS fibre and mechanical issues like too large air gap or displacement between the end of the WLS fibre and the SiPM.

The measured light yield at ITEP for the first 24 delivered modules is shown in figure 5.6 (a). A mean value of 15.8 pixels per mip with a spread of 2.6 pixels per mip, which corresponds to 15 % is achieved. In figure 5.6 (b)-(d) the light yield is plot for the three different tile sizes. The 12×12 tiles have a lower light yield than the two other types of tiles.

For a subsample of the SiPMs detailed studies have been performed to determine their behaviour and dependencies. The dependencies for the gain and the overall light response are following the expected relations shown in equations 4.3. The other measured dependencies are:
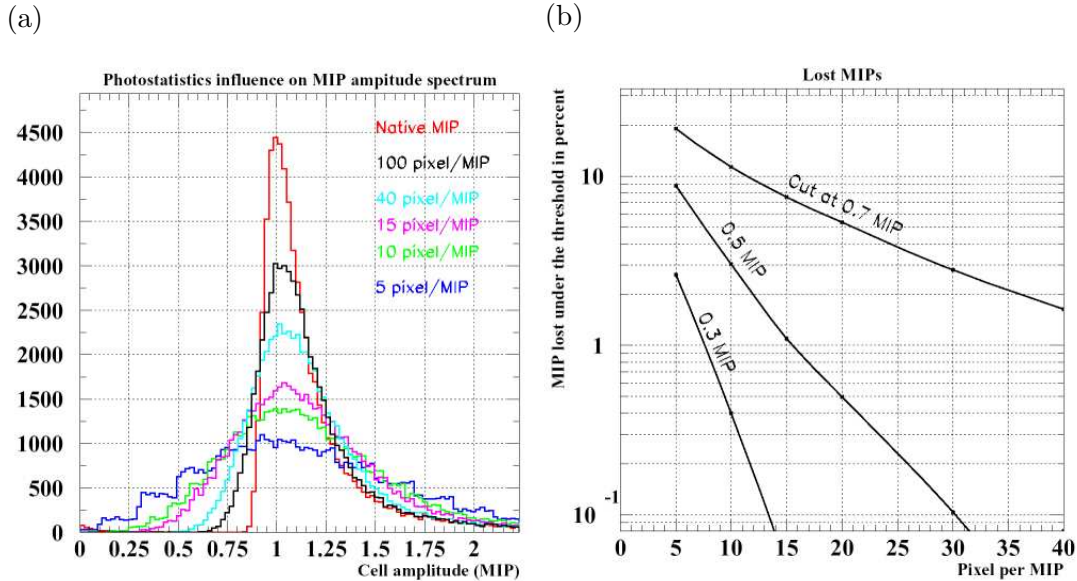
(a) (b)

Figure 5.5: *(a) A signal of a mip in AHCAL scintillator tile with different photo-statistic (light yield). (b) Tile efficiency as function of different light yields and noise cuts [83].*

$$
\begin{aligned}
\text{light yield:} \quad & dLY/dV & \approx 3.6\%/0.1V \\
\text{mip efficiency:} \quad & dEff/dV & \approx 2.2\%/0.1V \\
\text{dark-rate:} \quad & dDR/dV & \approx 3.5\%/0.1V \\
\text{inter-pixel crosstalk:} \quad & dXT/dV & \approx 4.7\%/0.1V
\end{aligned}
\tag{5.2}
$$

These variations have to be taken into account when compensating a light yield drop due to temperature increase. Although the light yield will increase by increasing the SiPM bias voltage, the SiPM noise, which consists of the dark-rate and inter-pixel crosstalk, will increase with approximately the same slope. These dependencies are valid for a range of -2 up to 2 V around the adjusted SiPM bias voltage. The spread of the distributions, which is in the order of ≈ 20 % to 40 %, shows the quite large non-uniformity of the tile-SiPM system.

5.2.3 Tile test at DESY

After production and testing of the tile-SiPM system at ITEP the tiles are sent module-wise to DESY. After this trip all tiles are tested in a dedicated setup to check their status. For the first two modules for each tile the mip response, the gain of the SiPM and therefore the light yield, as the ratio of both, has been measured. The SiPM dark current has been also measured. The light yield can be compared to the ITEP measurements. The setup of this test bench is shown in figure 5.7. A special box based on a PC housing has been built. The CD-Rom draw has been modified in this way that instead of CD-Roms tiles can be inserted. Due to flexible power and fibre connections for the LED light the tile exchange is a fast procedure. The box has the LED included to measure the single pixel spectrum. In addition, underneath the CD-Rom draw a small scintillator plate readout by a photomultiplier is placed, which gives the external trigger when collecting mip data from a source. The supply voltage distribution
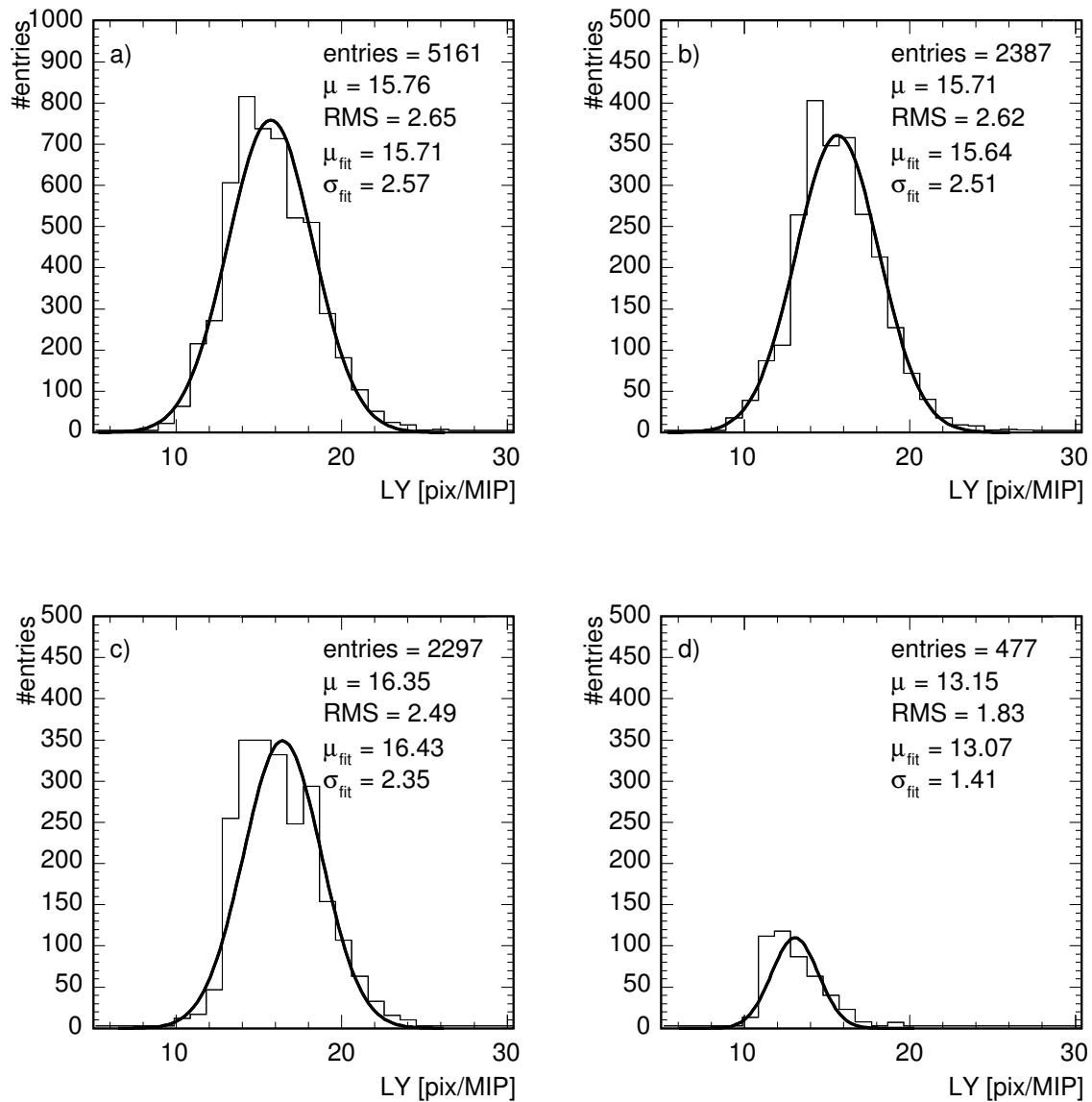
Figure 5.6: *(a) Light yield measured at ITEP for the first 24 modules. (b) Light yield measured at ITEP for different tile sizes (b) 3×3, (c) 6×6 and (d) 12×12.*

for the SiPM is connected to a interlock system which only enables the SiPM supply voltage in case the CD-Rom draw is closed and the source or a dummy probe is inserted. The trigger photomultiplier needs a supply voltage of 1.1 kV (provided by Heinzinger NCL3 3000-20ng). The SiPM bias voltage is in the range between 30 V up to 80 V (provided by Voltcraft PPS-12008). The SiPM power supply is also connected to a Picoamperemeter (Keithley 487) to measure the current of the SiPM. The trigger and the pulse for the LED flash is provided by an external pulser. The SiPM signal has to be amplified with an amplifier (Philips Scientific Fast Pulse Preamplifier Model 6954) with a gain of 100 before the signal is inverted, shifted and finally digitised in a CAMAC ADC (LeCroy 2249A). The inversion is necessary because the readout scheme inside the box is similar to the test-beam prototype connection scheme. The prototype readout electronics expect a positive signal but the CAMAC ADCs accept only negative signals. The additional shift using a FAN IN/OUT unit is necessary because the ADC has shown a non-linear range below $\approx$250 ADC channels. In addition to the signal chain a 140 ns long gate for the charge collection has to be generated and connected to the ADC.

For the measurement of the mip response a Ruthenium 106 source is used. Ruthenium has a half life of 1.02 years and decays over a beta-decay with a broad energy spectrum with a maximum energy of 3.51 MeV. For the gain measurement the pulser has to be set to provide the LED with a short pulse width. Therefore, the pulse should have a fast rise and fall time and the width should be set to $\approx$20 ns. The single photo-electron spectrum can be disturbed by low energetic particles from the source. To minimise the influence of this effect two different pulser frequencies are used. At the beginning of the data collection the mip events are collected and therefore the pulser is set to a low frequency, long periodic time of 100 ms. After collecting the necessary statistic of 10000 mip events the pulser periodic time is set to 100 μs and approximately 20000 low amplitude light events are collected fast. A typical measurement is presented in figure 5.8. The histogram in (a) shows the single pixel spectrum measured with low amplitude LED light and plot (b) shows the mip response. The pedestal entries in the mip response histogram are mainly caused by the noise of the photomultiplier trigger since no coincidence is used. The gain is extracted from the single pixel spectrum by fitting a multi-Gaussian to the single peaks. The average peak distance is taken as the gain in ADC channels. The most probable value of the mip response is determined by a simple Gaussian fit. The ratio of mip response and gain gives the light yield or in other words the mip amplitude in number of pixels. This quantity is compared in detail to the measurements in ITEP to quantify a possible tile quality degradation during the transportation.

The light yield comparison has been performed for the first two modules for each delivered tile. Afterwards, the mip response and gain measurements have been limited to 20 % of the delivered tiles. In figure 5.9 (a) the light yield comparison between ITEP and DESY is shown. The DESY values are corrected for temperature differences between the two measurements. For this a light yield dependency from equation 5.1 is assumed. The temperature for the DESY measurement was higher than in ITEP. The obtained mean light yield value without temperature correction is $\langle LY_{DESY} \rangle = 13.6$ pix/mip and with temperature correction $\langle LY_{DESY} \rangle = 15.3$ pix/mip both with a spread of $\sigma_{LY} = 2.5$ pix/mip. The light yield mean value obtained in ITEP is $\langle LY_{ITEP} \rangle = 15.7$ and therefore in average 0.4 pixel per mip higher than the DESY value (see figure 5.9 (b)). Although the mean value is after temperature correction equivalent, the spread in the light yield difference of 18 % gives a large uncertainty of this comparison.

In addition, some SiPM studies have been performed with the tile tester. In figure 5.10 (a) the SiPM gain dependence of the bias voltage is shown for nine tile-SiPM systems. In average the gain dependence is determined to (3.2 ± 0.4) %/0.1 V, which is higher than

(a)
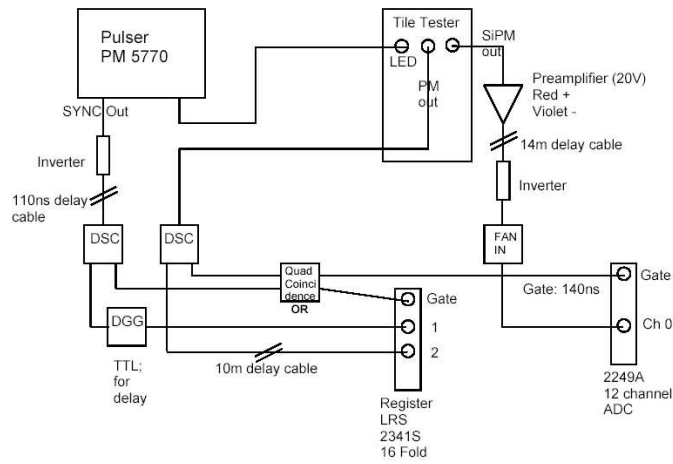
Figure 5.7:   *(a) Tile tester readout scheme. (b) Photograph of the tile tester setup.*
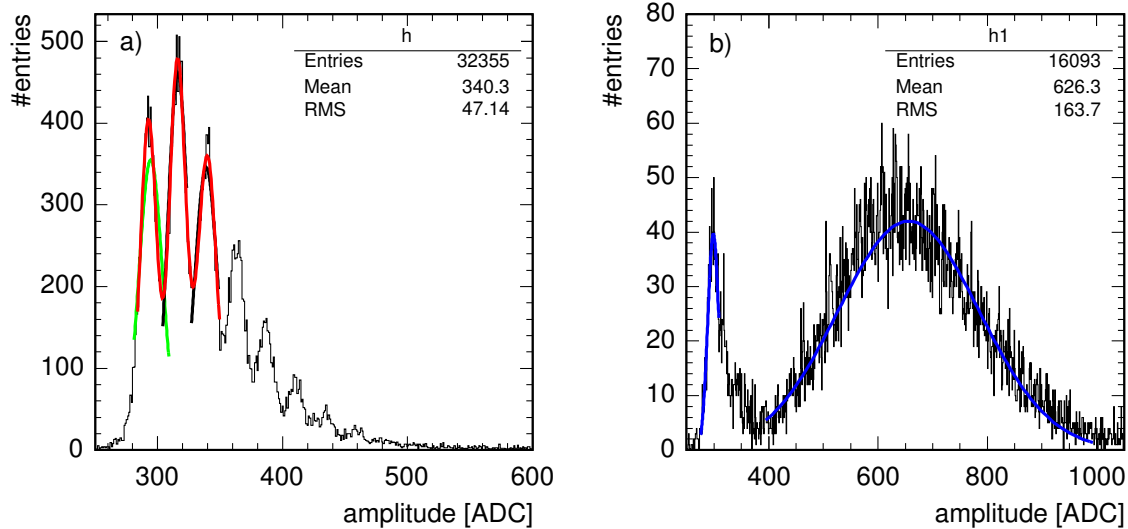
Figure 5.8:   *(a) Single pixel spectrum measured in the tile tester. (b) Mip response measured in the tile tester.*
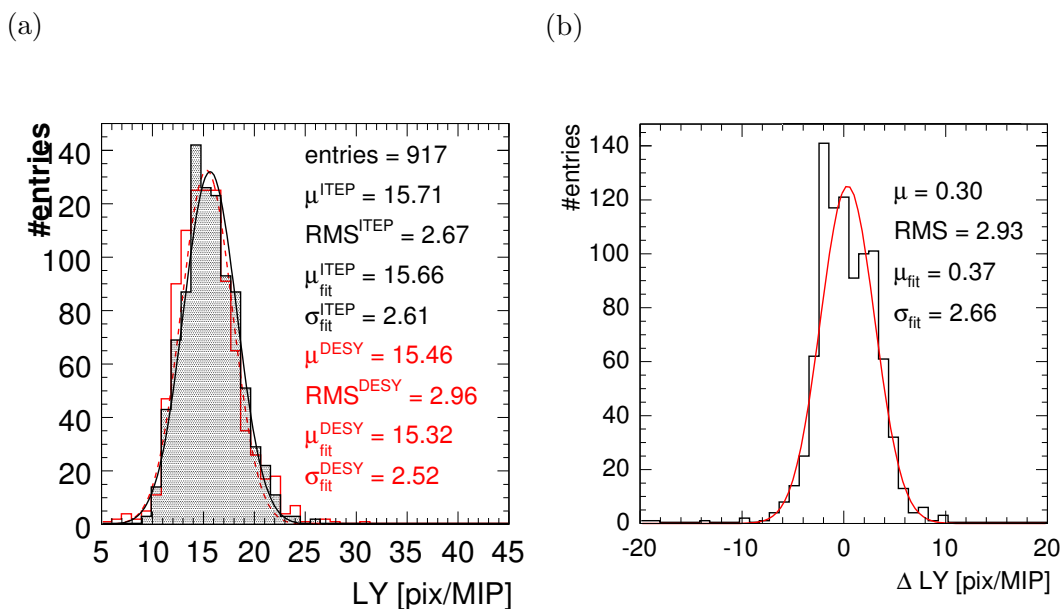
Figure 5.9: *(a) Light yield comparison between ITEP (solid black line) and DESY tile test (dotted red line) measurements in pixels per mip. (b) Light yield difference in pixels per mip.*
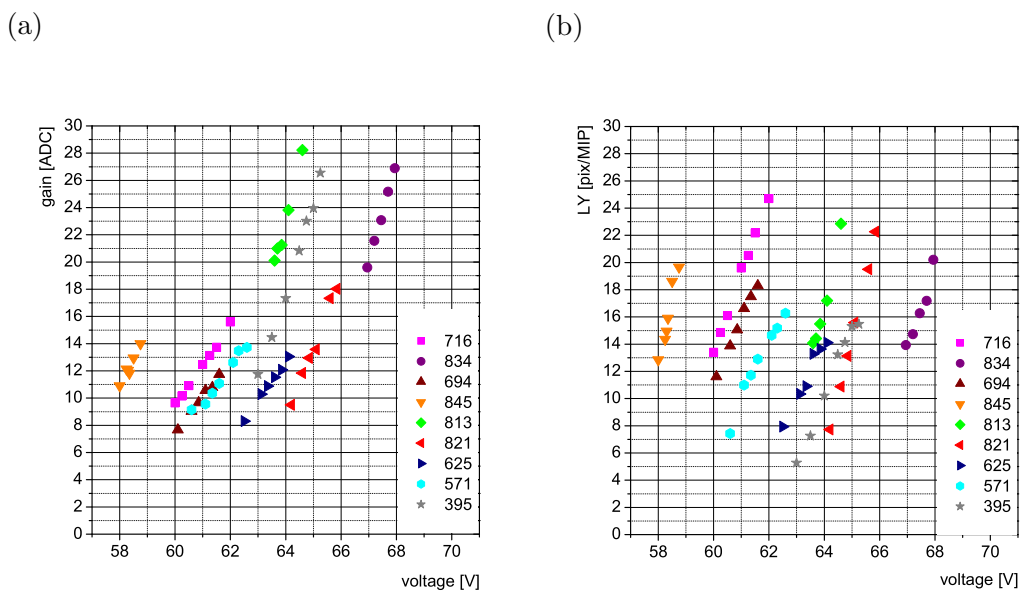

Figure 5.10: *(a) SiPM gain dependence on the bias voltage and (b) SiPM light yield dependence on the bias voltage both measured in the tile tester.*

the expected value $\approx$2.5 %/0.1 V. In figure 5.10 (b) the tile-SiPM light yield dependence of the bias voltage is shown for the same set of tile-SiPM systems. In average the light yield dependence is determined to (4.2 ± 0.5) %/0.1 V, which is also higher than the expectation of $\approx$3.6 %/0.1 V. However, the expected dependencies are the average of many SiPMs, where these measurements are only based on a sample of 9 SiPMs. This small statistics results also in the relatively large uncertainty on the measured mean values. The expected dependencies are still in the 2 σ range. The spread on these measurements is three-times the uncertainty on the mean value and shows the large difference in the SiPM property dependencies. This spread will affect any changes in the overall system due to temperature changes or voltage adjustments.
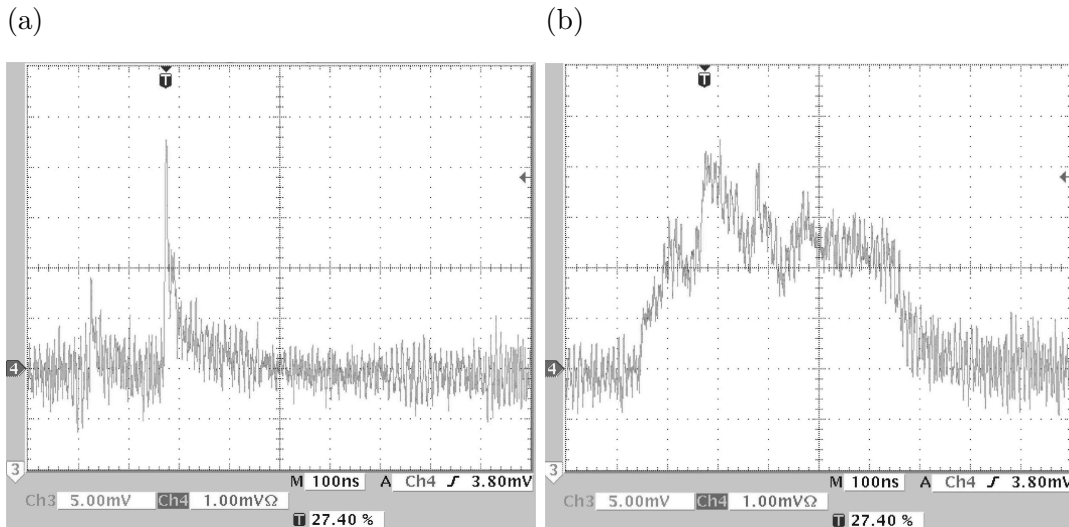
(a)   (b)

Figure 5.11:   (a) Normal SiPM noise signal on the oscilloscope.   (b) Long-discharge SiPM noise signal on the oscilloscope.

5.2.4   Long-discharge observation

During the start up of the module production a serious problem has been discovered. After gaining the first working experience with the new produced SiPMs some of them have shown high currents which have their origin in long signal pulses. These pulses are visible on the oscilloscope (see figure 5.11). The typical exponential decay, visible in 5.11 (a), due to the quenching of the charge avalanche is missing in figure 5.11 (b). The reason is mechanical damage to the surface of the SiPM pixel structure due to production failures. These damages lead to pixels with missing quenching resistors and therefore to long pulses and high currents. The frequency of these kind of events is dependent on the level of damage of the surface and the bias voltage since the damaged pixels have a higher probability to discharge accidentally. This is a serious problem for the production since these SiPMs have an additional source of noise over the half of a mip threshold. To identify long-discharge SiPMs the tile test has been modified to include the direct observation of every SiPM signal on the oscilloscope with up to 2 V higher voltage than the nominal one. In case of long-discharge signals these SiPM and tile systems are removed from module production.

5.2.5   SiPM radiation hardness and ageing studies

One important point in using SiPMs in a hadronic calorimeter is their radiation hardness and their change of properties with time. First dedicated radiation hardness tests of SiPMs have been performed with a 200 MeV proton beam at ITEP synchrotron in Moscow. Figure 5.4 (c) shows the SiPM current as a function of accumulated dose [82]. The current increase is compatible with that observed in other silicon detectors. However, SiPMs are more sensitive to radiation damage due to their high amplification of $\sim 10^6$ and a small noise signal amplitude. Both are only possible due to the isolated pixel structure and are mandatory for observing the single photo-electron spectrum. This self-calibrating property of the SiPM is lost for doses above 1 krad, since the individual pixel peaks are not resolved anymore due to damage to the pixel structure. Nevertheless, the SiPMs are still functioning even for radiation doses much higher than 1 krad, but their noise is increased. Assuming a standard mip signal at 15 pixels per mip this additional noise can lead to inefficiencies in case it rises above the half of a mip threshold cut. These studies are ongoing and can be also addressed by using the data collected with the test-beam prototype since it will be mainly used in hadron beams. The expected neutron flux in an ILC detector has been studied in [84] and seems to lead to acceptable radiation damage to the SiPM.

5.3   Electronic development and commissioning

The produced modules are equipped with two kinds of electronics. One side is responsible for the readout of the SiPMs and their connection to the supply voltages. This *very front-end (VFE)* electronics will be discussed in detail in the following. The other side of the module is equipped with electronics, which fulfils the purpose of calibration and monitoring. In the following a short overview of the calibration and monitoring electronic is given. Afterwards the readout signal chain is introduced and the central component of the VFE electronics is described and characterised: the ILC-SiPM ASIC. In addition, some basic electronic quantities are explained. The integration of the ASIC to the VFE electronics and the adaptation to the DAQ system is discussed.

5.3.1   The calibration and monitoring system and the slow control system

For the test-beam operation it is important to monitor during data taking the stability of the entire readout system. This includes the complete signal chain starting from the scintillator, WLS fibre, SiPM going to the electronic components like amplifier and readout electronics. In particular the SiPM gain and SiPM response has to be monitored since both are temperature and voltage dependent. The SiPM gain can be monitored by its response to low-intensity light. The SiPM response monitoring needs a higher amplitude of around a few mips. This settings also allows to make an inter-calibration between different used electronic readout modes. This task is achieved with an LED-fibre system that distributes UV light from a LED via clear fibres to each tile. A total of 19 fibres are coupled to one LED, of which 18 fibres distribute light to 18 tiles and one fibre is readout by a PIN photo-diode to monitor the LED light output. Each AHCAL plane is therefore equipped with 12 LEDs and 12 PIN photo-diodes to monitor all 216 tiles. The crucial parameter of this system is the light intensity spread between different fibres. The light output of all fibres in one AHCAL module has been measured. For fixed LED intensity the light intensity seen by the tile lies within a factor of 2 between maximum and minimum intensities. This is sufficient for all needed calibration and monitoring tasks,

because it gives the possibility to observe the single photo-electron structure for one or two LED amplitude settings and the maximum light in each channel should be sufficient to measure the upper part of the SiPM response function as well.

These LEDs are mounted on a CMB which is controlled by a slow-control system (SC) [85]. This system allows to enable or disable single LEDs and to change the amplitude of light. In addition it records the temperature of five sensors inside each module, plus four sensors on each base board and two sensors on each CMB. Furthermore, all high voltage settings for each channel and their currents are measured and stored. A detailed description of the complete system can be found in [86].

5.3.2 The very front-end electronics

The first part of the digitisation of the SiPM signals are done in the VFE electronics. This part of the electronics is directly mounted at each module and therefore the longest cable length between the SiPM signal creation and the first signal handling is maximum 1 m. The design of the VFE electronics has to fulfil several requirements. The electrical signal from the SiPM, which is a short current pulse, has to be decoupled, amplified and multiplexed before the signal is transported over a ~5 m long cable to the ADC for digitisation. The operation of a large number of SiPMs with different bias voltages has to be possible and requires individual channel voltage adjustment. The calorimeter prototype has to work in a test-beam environment, which means that the signal has to be delayed until the trigger decision has been taken ($\approx$150 ns). The electronic should be able to exploit the SiPM gain calibration, which requires to minimise the amplifier noise and a short signal shaping time in order to prevent noise pile-up. The expected physics signal needs a large dynamic range from 0.5 mip up to 100 mip. Finally the electronics should use multiplexing to achieve the needed concentration of channels. In addition to these primary properties of the electronic readout system, other considerations can be equally or even more important, e.g. radiation hardness, low power consumption, robustness and of course cost. The discussed VFE electronic is meant to be used for a dedicated test-beam experiment and has not been optimised in the sense of scalability for the final linear collider detector. Therefore, these issues have played a minor role, but they are very important for the next generation of prototypes.

The task of observing the single photo-electron structure has opposite requirements to the electronics than the collection of physics signal in a test-beam environment. Therefore, the implementation of two different readout modes is needed. This means in particular the possibility to change the readout modes between a short-shaping time which has been optimised to resolve the single photo-electron structure, and a long-shaping time in which it is possible to read out events triggered by an external source.

5.3.3 Signal chain

The purpose of signal processing is to improve the signal-to-noise ratio. The minimum detectable signal and the precision of the amplitude measurement are limited by fluctuations. Particles are crossing the scintillator tiles and deposit energy, which produce ultraviolet light photons (see figure 5.12). The number of scintillation photons is proportional to the absorbed energy. The signal of a mip is the smallest physical signal one wants to detect. A mip produces ~5000 scintillation photons in 0.5 cm scintillator plastic. These produced photons have to be absorbed by the wavelength shifter fibre and transported to the sensitive surface of the SiPM, which consists of a multi-pixel structure. At this stage approximately 200 photons

remain due to collection and transport efficiency (4 %) as discussed in section 4.1. Each pixel can absorb photons which produce an electron-hole pair. The produced electron is amplified in a Geiger discharge. Since the photo-detection efficiency of the SiPM is around 10%, ∼20 pixels are firing. At this point energy absorbed in the scintillator has been converted into an electrical signal. An important role has the SiPM which amplifies this signal by a factor of 10^6. The signal at the SiPM output is a current pulse $i_S(t)$. It has a very fast rise time below one nanosecond, followed by an exponential decay of up to several hundred nanoseconds (see section 5.2). Integrated over time this pulse gives a charge, which is proportional to the absorbed energy [5].

$$E \propto Q_S = \int i_S(t)dt. \tag{5.3}$$

In the next step the signal passes through the ILC-SiPM ASIC, which is an integrated circuit containing an amplifier and a shaping stage. The signal treatment inside the ASIC is illustrated in figure 5.13 taken from [60]. The magnitude of the sensor signal (5.13 (a)) is subject to statistical fluctuations and electronic noise smears the signal in addition. This noise alters both the amplitude and shape of the signal. Both kind of effects give fluctuations to the measured peak amplitude, since one changes the pulse height and the other the time of the peak [87]. The noise level determines the minimum signal whose presence can be discerned. In an optimised system, the time scale of the fluctuations is comparable to that of the signal, so the peak amplitude fluctuates randomly above and below the average value.

If the pulse shape does not change with signal charge, the peak amplitude or the pulse height is a measure of the signal charge. This method is called pulse height analysis. The primary function of a pulse shaper is to improve the signal-to-noise ratio. The signal pulses, which are fed into the amplifier have of course not only a time-varying distribution but are also distributed in the frequency space. The frequency spectrum of the signal and the noise differ, therefore, it is possible to improve the signal-to-noise ratio by applying a filter that tailors the frequency response to favour the signal while attenuating the noise. By changing the frequency response also the time response is changed, which is the pulse shape and therefore this function is called pulse shaping. In general, improving the signal-to-noise ratio commonly implies reducing the bandwidth, which increases the duration of the pulse. The amplified and shaped signal is shown in 5.13 (b).

The pulse shaper can serve multiple functions in addition. One is to tailor the pulse shape to the ADC. Since the ADC requires a finite time to acquire the signal, the input pulse may not be too short and it should have a gradually rounded peak. Another function is to delay the pulse height in relation to the trigger response. This functionality is needed in multiplexing signal and hold systems, in which more than one signal peak has to be stored before going to the multiplexer stage which delivers then to the ADC a series of peak amplitudes.

The pulse shape length has to be in agreement with the signal rate assumed in the detector. Too large pulse width will lead to pile-up of successive pulses. The measurement of the peak amplitude of the second pulse will give an erroneous result.

After shaping the signal is held at its maximum amplitude with a track and hold method (5.13 (c)) and multiplexed by an 18-channel multiplexer to provide a single analog output to the ADC (5.13 (d)), which converts the analog signal into a bit-pattern suitable for subsequent digital storage and processing.

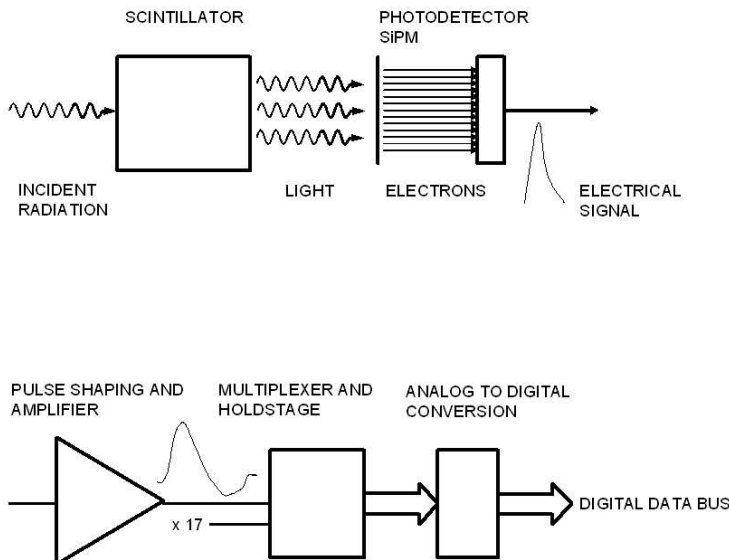[5]after SiPM non-linearity correction.

Figure 5.12:   *The signal chain starting from the scintillator light to the electronic digitisation.*

5.3.4   The ILC-SiPM ASIC chip

This 18-channel ASIC chip dedicated to SiPM readout has been developed starting from the design, in AMS 0.8 μm CMOS technology, already in use for the Si-W ECAL prototype readout. Figure 5.14 shows a schematic view of this ILC-SIPM ASIC chip. The integrated components allow the choice between 16 selectable amplification gain factors from 1 to 100 mV/pC, and between 16 $CR(RC)^2$ shapers with shaping times from 40 to 180 ns. The shaping times are expressed for a voltage step input function.

The ILC-SiPM ASIC chip has been developed at LAL in Orsay. The ASIC is divided in total in four stages. Three are responsible for the processing of the signal and one for the SiPM high voltage adjustment (DAC). The first stage in the signal processing chain is a variable gain charge amplifier, followed by a variable pulse shaper $(CR(RC)^2)$ stage and finally leads to a hold stage. The hold stage consists of a switched capacitor array consisting of five feedback capacitor units and an analogue memory to store the measured charge amplitudes. Each of these stages is independently designed to use it easily in a different circuit and to simplify the error recovery.

In order to describe the properties and key parameters of the ASIC chip it is necessary to enter in more details in the mathematical treatment of charge amplification and pulse shaping. In the next sections the individual ASIC stages are shortly discussed and relevant equations to quantify the behaviour and performance of the chip are introduced.

SiPM supply voltage adjustment

The SiPM operation voltage may vary from device to device. Therefore, the electronics has to be able to individually tune the bias voltage for each channel. The ASIC chip has for each input channel an integrated 8 bit digital to analog converter (DAC) with a range from 0 - 5 V, giving a step resolution of $\sim$0.02 V. The connecting scheme in figure 5.15 shows how this voltage is used to reduce a common positive bias voltage. Without this feature each channel would need its own high voltage power supply, resulting in very high costs and for sure fragile cabling. On the other hand, this method's accuracy depends on the quality of the DAC and
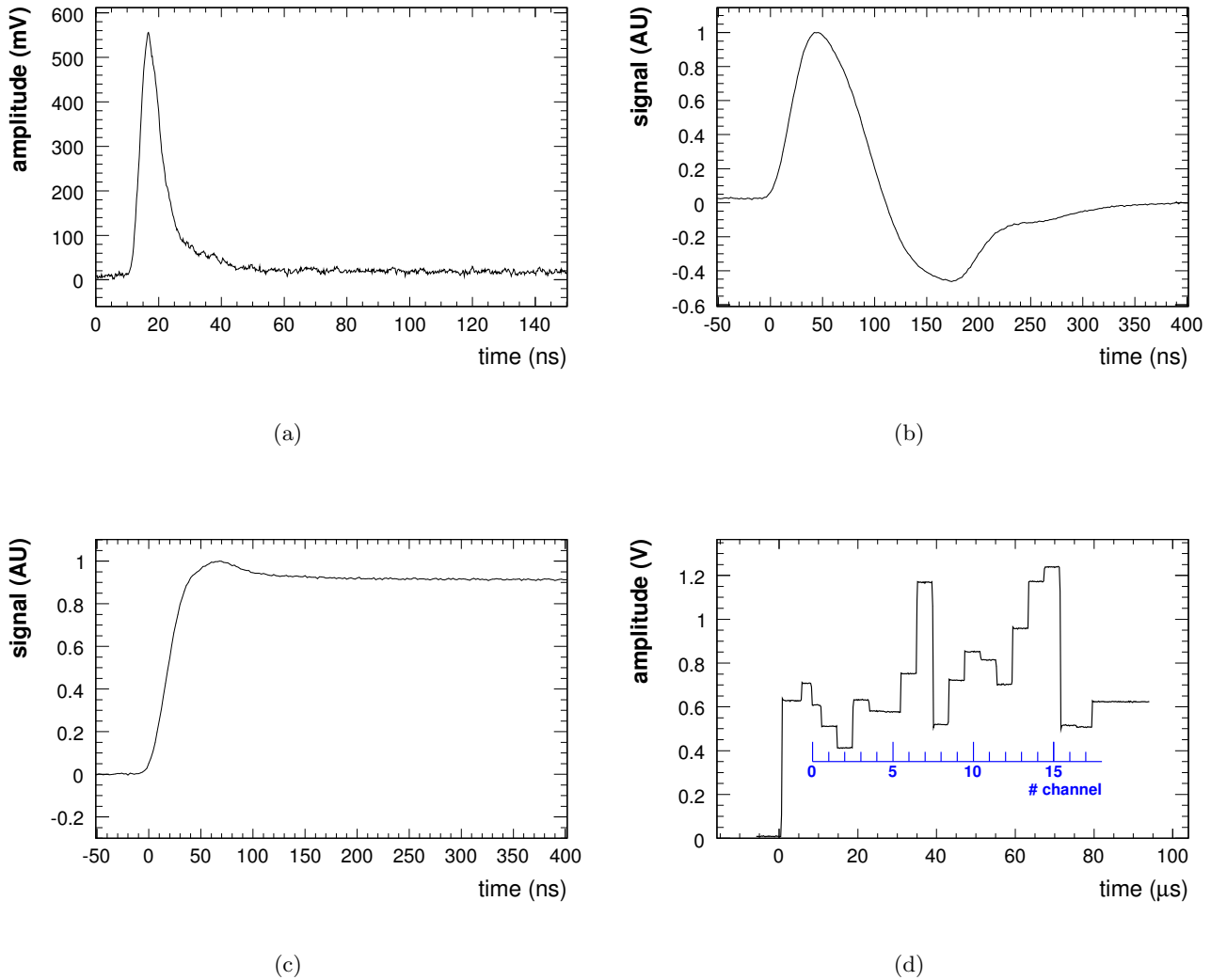
(a)

(b)

(c)

(d)

Figure 5.13: *Electrical signal processing in the ASIC. (a) Input (x18), (b) amplified and shaped (x18), (c) held (x18), (d) multiplexed (x1) signal [60].*

no monitoring of current or voltage for single channels is available [60].

Variable gain charge amplifier stage

The integration of the SiPM current according to equation 5.3 can be performed in different ways. An ideal amplifier delivers a voltage proportional to the incoming charge. The discussed ASIC uses an integrating or charge-sensitive amplifier. One important feature of this circuit is the possibility to switch between different gain settings. This multi-gain capability is achieved by implementing four different capacitors, which can be activated by switches. The capacitor values are 0.1 pF, 0.2 pF, 0.4 pF and 0.8 pF. Therefore, the feedback capacitor C_f, which defines the gain, can vary from 0.1 pF up to 1.5 pF.

Figure 5.16 shows the principle of a feedback amplifier that performs integration. The feedback capacitor C_f determines the factor for charge to voltage conversion. The basic
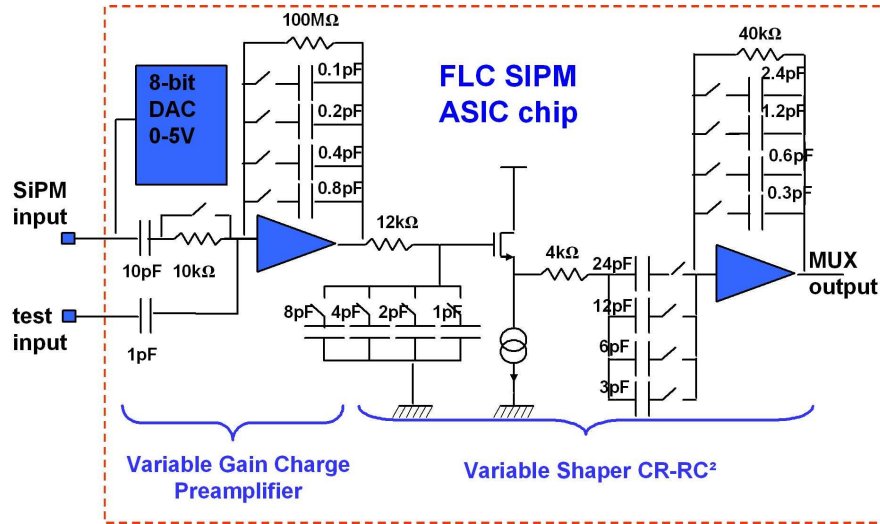
Figure 5.14: *Schematic view of the ILC-SiPM ASIC components.*
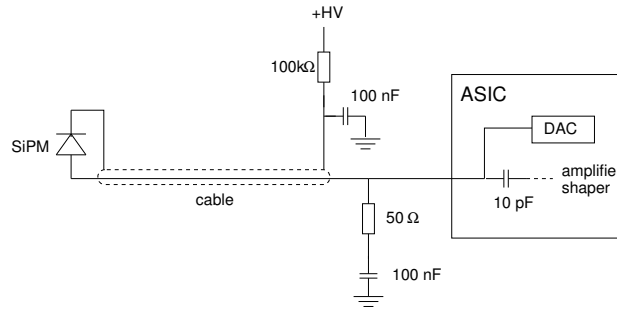
Figure 5.15: *SiPM connection scheme [60].*
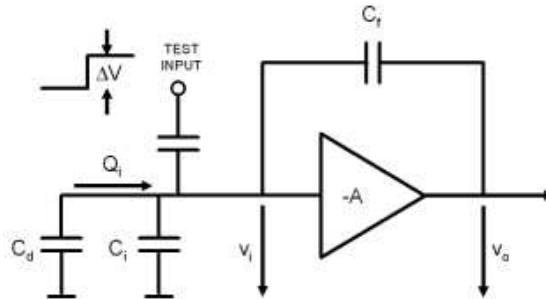
Figure 5.16: *Scheme of a charge-sensitive amplifier with charge calibration option.*

idea is to integrate the charge carried by the incoming pulse Q_i on the capacitor C_f. From figure 5.16 it can be seen that the following relation is valid

$$V_o - V_i = -\frac{Q_i}{C_f}. \tag{5.4}$$

The output voltage is always proportional to the ratio of the amount of the incoming charge and the size of the feedback capacitor, so that the dependence on the detector capacitance has been removed. The collected charge on C_f has to be removed by a discharge

through a resistor, usually placed in parallel with C_f.

A useful feature of an integrating amplifier is the ease of charge calibration. By adding a test capacitor as shown in figure 5.16 and also in the ASIC schematics 5.14, a voltage step injects a well-defined charge $C_T \Delta V$ into the input node. This signal is used to test the readout electronics and to perform stability checks independently of the detector.

Electronic noise

The noise performance of the amplification stage is very important for the overall detector. Many noise sources contribute to the total noise at the amplifier. For details see [87]. Besides of external noise sources, which can be minimised by shielding and correct grounding, intrinsic or internal noise sources exist as well. Intrinsic noise is present in almost all electronic components.

The discrete nature of the electrons as charge carriers gives rise to a permanent fluctuation of currents in electrical circuits. Assuming a current flow of n electrons moving with velocity v between two electrodes, the induced current depends on the spacing l between the electrodes

$$i = \frac{nev}{l}. \tag{5.5}$$

The fluctuation of this current is given by the total differential

$$< di >^2 = \left(\frac{ne}{l} < dv > \right)^2 + \left(\frac{ev}{l} < dn > \right)^2, \tag{5.6}$$

where the two terms add in quadrature, as they are statistically uncorrelated. From this equation it is visible that two mechanisms contribute to the total noise, fluctuations in velocity and in number of charge carriers.

Thermal noise is present in all elements containing resistance. It describes velocity fluctuations originating from thermal motion and is caused by random thermally excited vibrations of charge carriers in a conductor. Normal temperature variations have a small effect on the value of thermal noise [88]. The thermal noise is proportional to the square root of the bandwidth and the square of the resistance. It would, therefore, be advantageous to minimise the resistance and bandwidth of the system to reduce the thermal noise. Thermal noise is a random signal and has therefore a normal distribution of amplitude with time and frequency (white noise). *Shot* noise is associated with current flow across a potential barrier. It is due to the fluctuation of current around an average value resulting from the random emission of electrons (or holes). This noise occurs in vacuum tubes and semiconductors. In semiconductors, shot noise is due to random diffusion of carriers through the base of a transistor and the random generation and recombination of hole electron pairs. Shot noise is also white noise and has the same characteristic as thermal noise. *Contact* or *flicker* noise is caused by fluctuating conductivity due to imperfect contact between two materials. It occurs when two conductors are joined together, such as in switches, relays and transistors. Due to its frequency characteristic is often called *1/f noise*.
These kind of noise occur in the amplifier and in the detector, the SiPM, as well. Also the components needed for the connection between SiPM and amplifier add noise. All noise contributions can be expressed as a voltage fluctuation or a current fluctuation, depending on the load impedance. Therefore, the complete noise at the input of the electronics can be modelled by two noise sources. One is introducing a serial voltage e_n and the other one is a parallel current noise source i_n. The sources expressed by series voltage sources are thermal noise in

the input channel of the amplifier, contact noise, noise from series resistors on the detector or from resistors between detector and amplifier. Noise sources described by the current contribution are noise due to the detector dark current, noise due to the feedback resistor, and noise due to the bias resistor of the detector. Noise voltages, or currents, produced independently with no relation between each other are uncorrelated. The noise contributions can be added in quadrature. The total noise is obtained by integrating over the relevant range of the system, the bandwidth. The total noise increases with bandwidth. Since small bandwidth corresponds to large rise-times, increasing the speed of a pulse measurement system will increase the noise at constant gain. The amplitude distribution of the noise is Gaussian, so noise fluctuations superimposed on the signal also yield to a Gaussian distribution. Thus, by measuring the width of the amplitude spectrum of a well-defined signal, one can determine the noise. Noise measurements are usually performed at the output of a circuit or amplifier. If a value of equivalent input noise is required, the output noise is measured and divided by the circuit gain to obtain the equivalent input noise. The ultimate effect of noise depends not only on the noise voltage/current but also on the amplification factors and pulse shaping. Therefore the noise can be expressed in terms of *Equivalent Noise Charge (ENC)*. The ENC describes the noise pulse in terms of the charge pulse at the detector needed to create the same output. To minimise the total contribution at the output of an amplifier system additional stages have to be used. One very often used possibility is to reduce the accepted bandwidth of the system so that the complete signal will pass the circuitry but not the complete noise contribution.

Coherent noise

In a multi-channel system like an ASIC some components are shared between the different readout channels, e.g. the supply voltages. Therefore, the noise of one single channel consists besides of an incoherent also of a coherent noise contribution. Coherent noise contributions result in a common fluctuation of all channels in one electronic component, whereas incoherent noise contributions are independent from channel to channel. To quantify the two contributions the following formula apply,

$$
\begin{aligned}
RMS_{incoherent} &\equiv RMS_{alt.sum}/\sqrt{n_{channels}}, \\
RMS_{coherent} &\equiv \sqrt{RMS_{dir.sum}^2 - RMS_{alt.sum}^2}/\sqrt{n_{channels}}.
\end{aligned}
\tag{5.7}
$$

The direct sum $RMS_{dir.sum}$ describes the sum of amplitudes of all 18 channels of 1 ASIC. The alternating sum $RMS_{alt.sum}$ describes the amplitudes of even channels minus the sum of amplitudes of odd channels. The idea is that the coherent contributions are cancelled in the alternating sum.

Variable pulse shaper

The output signal shape is determined by the input signal shape (characteristic of detector) and the filter (amplifier-shaper) characteristic. Pulse shaping has always two conflicting objectives. The first is to restrict the bandwidth to match the measurement time. A large accepted bandwidth will increase the noise without increasing the signal. Typically, the pulse shaper transforms a narrow sensor pulse into a broader pulse with gradually rounded maximum at the peaking time. The signal amplitude is measured at the peaking time T_p. The second objective is to constrain the pulse width so that successive signal pulses can be measured without overlap (pile-up). Reducing the pulse duration increases the allowed signal rate, at the expense of electronic noise. Due to these conflicting goals every shaper is a
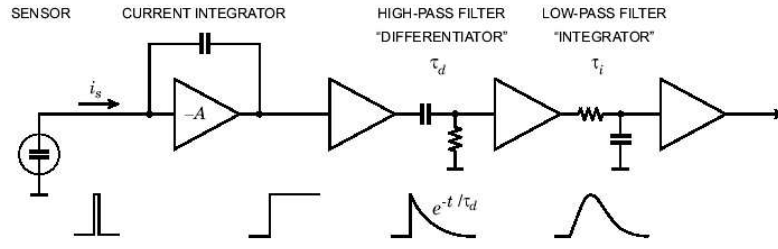
Figure 5.17: *A simple pulse shaper using a CR differentiator as a high-pass and an RC integrator as a low-pass filter. The illustrated signal shapes are valid for a δ-function like input pulse.*

compromise between them and is therefore highly dependent on its application.

A simple shaper is shown in figure 5.17. After the amplifier a high-pass filter sets the duration of the pulse by introducing a decay time constant τ_d. Afterwards, a low-pass filter increases the rise time to limit the noise bandwidth. The high-pass is often referred to as a *differentiator*, since for short pulses it forms the derivative. Correspondingly, the low-pass is called *integrator*. Since the high-pass filter is implemented with a CR section and the low-pass with an RC, this shaper is referred to as a CR-RC shaper. Although pulse shapers are often more sophisticated and complicated, the CR-RC shaper contains the essential feature of all pulse shapers, a lower frequency bound and an upper frequency bound.

The ILC-SiPM ASIC contains a CR-RC^2 shaper or filter, which is behind the amplifier stage. The transfer function of such a system in the frequency domain is

$$H(\omega) = \frac{i\omega\tau}{(1 + i\omega\tau)^3}. \tag{5.8}$$

To get the output after the shaper stage this function has to be multiplied with the input to the shaper stage, which is the output of the amplifier stage $V_a(\omega)$:

$$V_{filter}(\omega) = \frac{i\omega\tau V_a(\omega)}{(1 + i\omega\tau)^3}. \tag{5.9}$$

$V_a(t)$ is ideally a voltage step with

$$V_a(t \leq 0) = 0 \vee V_a(t > 0) = \frac{Q_{in}}{C_f}. \tag{5.10}$$

Therefore the derivative is

$$\frac{dV_a(t)}{dt} = \frac{Q_{in}}{C_f}\delta(t), \tag{5.11}$$

and in the frequency domain

$$i\omega V_a(\omega) = \frac{Q_{in}}{C_f}. \tag{5.12}$$

Substituting equation 5.12 into 5.9 one gets:

$$V_{filter}(\omega) = \frac{Q_{in}\tau}{C_f(1 + i\omega\tau)^3}. \tag{5.13}$$

The Fourier transformation of $\frac{\tau}{(1+i\omega\tau)^3}$ gives $\frac{1}{2}\left(\frac{t}{\tau}\right)^2 e^{-t/\tau}$ for $t > 0$. Applying the Fourier transformation to equation 5.13 one obtains

$$V_{filter}(t > 0) = \frac{Q_{in}}{2C}\left(\frac{t}{\tau}\right)^2 e^{-t/\tau}. \tag{5.14}$$

The maximum of the shaped output is therefore at $t = 2\tau$ with an amplitude of $V_{max} = \frac{2e^{-2}Q_{in}}{C_f}$.

As mentioned in the beginning this set of relations is valid for a step-like input function to the shaper. This is only the case if the amplifier input signal is a δ-function like pulse, as schematised in figure 5.17. The rise time of the SiPM signal is very short but in addition it has also a relatively long decay time of $\tau_{SiPM} = R \cdot C = 50$ fF $\cdot 20$ M$\Omega = 100$ ns. Therefore, it cannot be approximated with a δ-function like pulse. This leads to a non-step like function at the amplifier output. To get the response of this kind of input signal the equation for the step function 5.14 has to be derived.

$$V_{filter} = \frac{Q_{in}}{2C}\left(\frac{2t}{\tau} - \left(\frac{t}{\tau}\right)^2\right)e^{-t/\tau} \tag{5.15}$$

To get the maximum of this function the derivative of equation 5.15 is calculated:

$$\frac{dV_{filter}}{d(t/\tau)} = \frac{Q_{in}}{2C_f}\left(\left(\frac{t}{\tau}\right)^2 - 4\frac{t}{\tau} + 2\right)e^{-t/\tau}. \tag{5.16}$$

The root of this function is $t/\tau = 2 \pm \sqrt{2}$ and therefore $0.6 \cdot \tau$ and $3.4 \cdot \tau$, which shows the bipolar behaviour. In case of the step input function the root is 0 and 2τ and therefore the output signal has a unipolar shape.
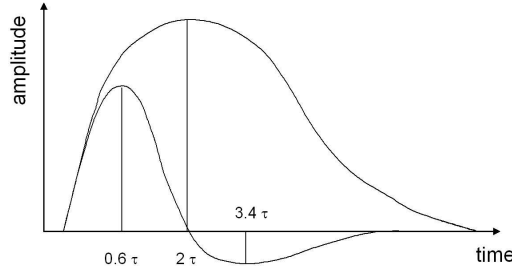
Figure 5.18: *Different response of a CR-RC^2 shaper for a step and pulse input function.*

The signal amplitude is also affected by the relation of the shaping time to the detector signal duration. If the peaking time of the pulse shaper is shorter than the collection time of the input detector signal, some of the signal is lost. This effect is called *ballistic deficit*.

5.4 Characterisation of ILC-SiPM properties

Before accepting the ASIC design and ordering around 1000 ASIC chips a prototype chip has been checked on a dedicated test setup. After receiving the production a subsample of ≈ 10 ASIC chips have been studied as well. In the following the measurements and results of these tests will be discussed.

The properties of the ASIC chip relevant to the operation in conjunction with the SiPM have been tested using the single channel test setup sketched in figure 5.19. These properties are the *amplification gain*, *linearity*, *channel to channel crosstalk* and *noise*, which can be divided in the noise introduced by the signal processing stages and by the DAC.

5.4.1 Gain and Linearity

The gain of an amplifier is not the same for different types of input signals. This is the result of a limited shaper bandwidth or of saturation effects for large signals. The linearity of the ASIC gain with increasing signal amplitude is especially important when using a already non-linear input signal from the SiPM. A setup based on CAMAC readout was built to measure the linearity of the ASIC gain and is shown in figure 5.19. The gain is defined as the output voltage divided by the input charge.

$$G = \frac{V_{out}}{Q_{in}} \qquad \left[\frac{\text{mV}}{\text{pC}}\right]. \qquad (5.17)$$

The study of the linearity range of the ASIC chip for various combinations of gain and shaping time has been performed injecting a charge from an external capacitor (C1) to the ASIC chip input. By varying the value of the capacitor C1 it is possible to change the duration of the injected charge to mimic the real shape of a SiPM signal.
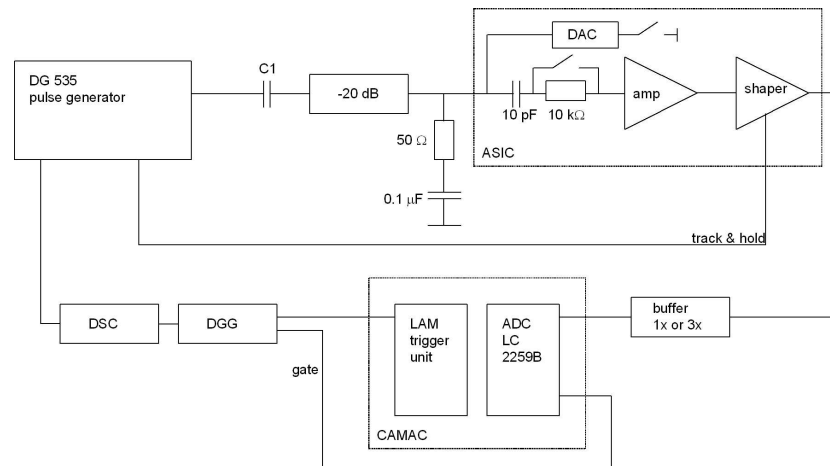

Figure 5.19: *Electronic setup for ASIC chip studies with external charge injection.*

Figure 5.20 demonstrates how the shape of the input signal is adjusted choosing a 68 pF capacitor to get a short pulse of known charge. The charge is $Q_{in} = C \cdot V_{in}$. Each input channel of the ASIC chip is grounded via a 50 Ω resistor and a 0.1 μF capacitor. For the measurement of the ASIC mode with the highest gain an attenuator of -20 dB was used to decrease the signal by one tenth. The low gain physics mode was measured without this attenuator. The output signal of the ASIC is measured with a peak-sensing LeCroy 2259B 11bit ADC ranging from 0 to 2 V. The linearity of this device was checked with a voltage source controlled by a KEITHLEY 2001 multimeter. The accuracy of this device is 1 μV. The relation between input voltage V_{in} and ADC channels is $A = (0.9944 \pm 0.0001) \frac{\text{chan}}{\text{mV}} \cdot V_{in} - (107.2 \pm 0.1)$ chan. The gain of 1 is in agreement with the specification of the producer. The lower range (< 250 ADC channels) have not been used for the measurements since it has shown a large non-linearity. The maximum error due to non-linearity of the ADC is one

channel in the range of the measurement. For each point the mean was measured with a statistic of at least 10000 entries. The width σ_{gauss} of the resulting Gaussian was equal or smaller than 3.0 channels. This defines the error of a measured point as $\approx$1 ADC channel. For high output amplitudes an oscilloscope was used to measure, as the ASIC output voltage exceeded the input voltage of the ADC.

The output signal of each amplifier and shaper stage is held at its maximum value by an external track & hold signal timed with the generator. The duration of the hold time is determined by the width of the hold signal, generally about 2-5 μs. A signal amplitude drop of 1 mV per 500 ns independent on the signal amplitude is observed. During this time the signal is measured with a gate of 400 ns, which is also created from the generator. The linearity range of the ASIC chip operated with longest shaping time ($\sim$180 ns) is presented in figure 5.21 (a). The saturation of the input charge is visible which depends on the shape of the injected signal (or the value of the input capacitor C1). In the lower plot of figure 5.21 (a) the gain factors for the various choices of capacitors are shown, which are calculated from a fit to the linear ($\pm$ 3 %) part of the curves in figure 5.21 (a). The same values are evaluated from figure 5.21 (b) for the shortest shaping time ($\sim$40 ns). If the input is not saturated, the ASIC chip output saturates between 1.7 and 1.9 V depending on the gain. While the slopes of the curves in figure 5.21, as well as the absolute gain values reported, are strongly changing depending on the value of the input capacitor C1, the output saturation level stays quite constant. The ASIC chip can be used for SiPM-like signal readout in a linear range up to 1.3 V for all combinations of gains and shaping times.

After scanning the possible parameter space two settings have been chosen to be further investigated. One mode, referred to as *calibration mode*, should be used to collect the SiPM
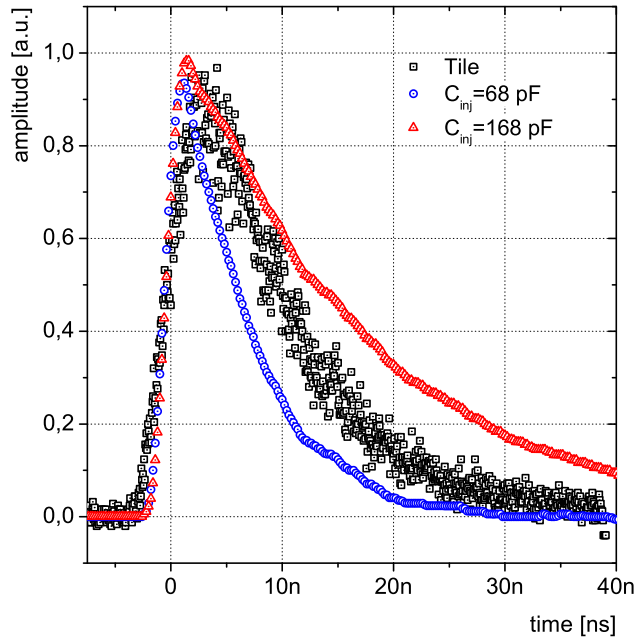

Figure 5.20: *Comparison of charge injected signal to real SiPM signal obtained with light from a tile (squares).*
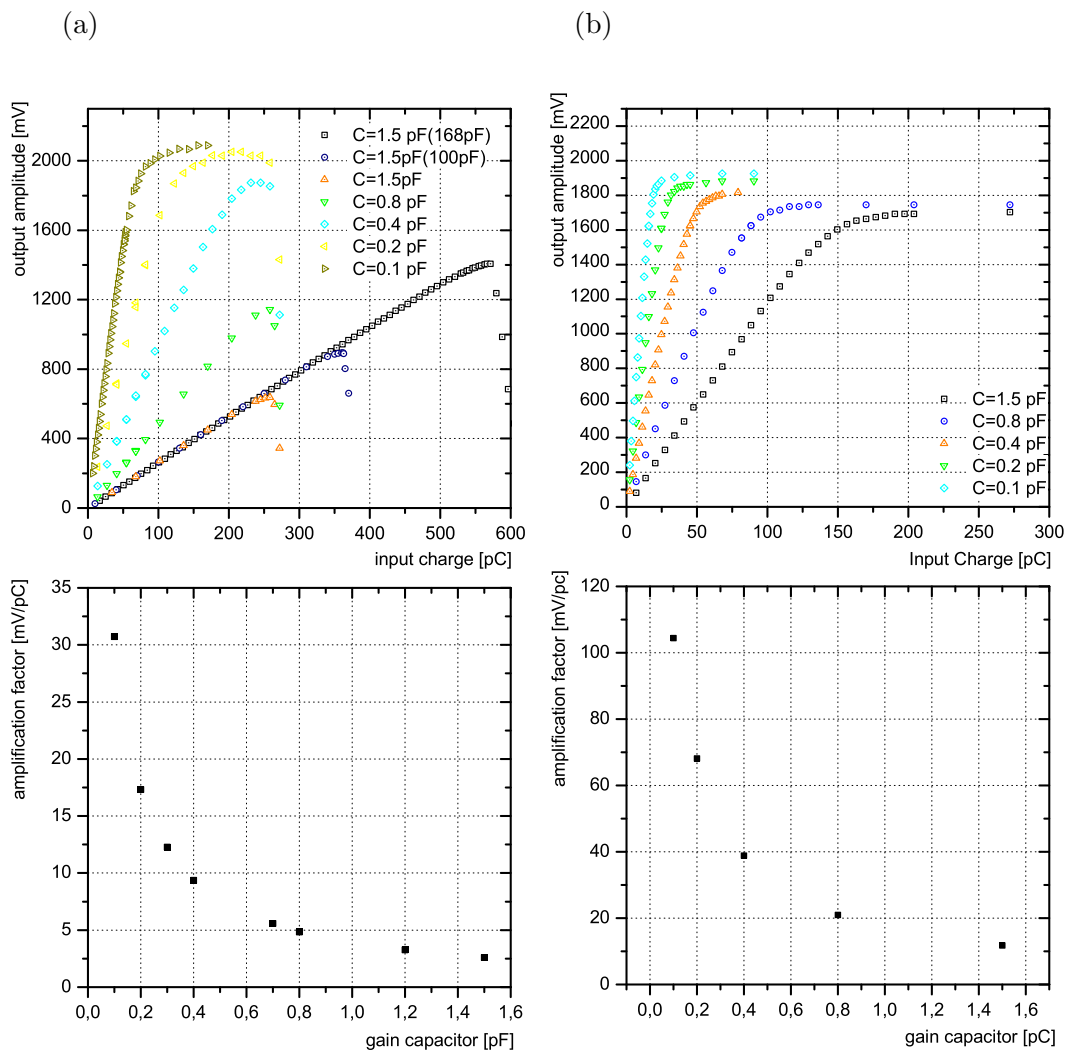
Figure 5.21: *Linearity of ASIC chip output signal for the longest (a) and shortest (b) shaping time and various gains. The lower plots show the relative gain factors as a function of the chosen capacitor.*

single photo-electron spectrum. It has the highest gain and the shortest shaping time to have the best signal-to-noise ratio. The second mode, *physics mode*, is used to collect physics data in test-beam or cosmic setups. It needs the longest shaping time to delay the amplitude maximum after the trigger decision, which is creating the hold signal, and a medium gain to fit into the ADC range. A 10 kΩ resistor (Ri) can be added at the input of the amplifier to further delay the signal peaking time, which increases the noise by 40-50 %, but is needed to obtain a sufficient delay in comparison to the generated trigger signal. The charge coming from one SiPM pixel can be determined by $G_{SiPM} \cdot q_e = 10^6 \cdot 1.6 10^{-19} = 0.16$ pC. Assuming an ASIC gain of 100 mV/pC the ASIC output would be: 100 mV/pC $\cdot$0.16 pC = 16 mV for one pixel. The measurements described above have shown that the linear range of the ASIC in the high gain mode is limited to 1300 mV. This leads to a dynamic range of 1300 mV/16 mV = 80 pixels which is around 5 mips. This gives enough dynamic range in the calibration mode. In the physics mode the maximum charge is $Q_{max} = G_{SiPM} \cdot N_{pixel} \cdot q_e = 10^6 \cdot 1156 \cdot 1.6 10^{-19} = 190$ pC. This corresponds to a output voltage of $U = 190$ pC $\cdot$8 mV/pC = 1500 mV. Therefore, also the physics mode has been chosen to fulfil the observed requirements since the expected maximum output voltage is contained in the ADC range. In addition, the charge coming from the SiPM seems to be below the charge input limit of the ASIC as well.

The following measurements are investigating these two modes in detail with the described ASIC subsample after production delivery.

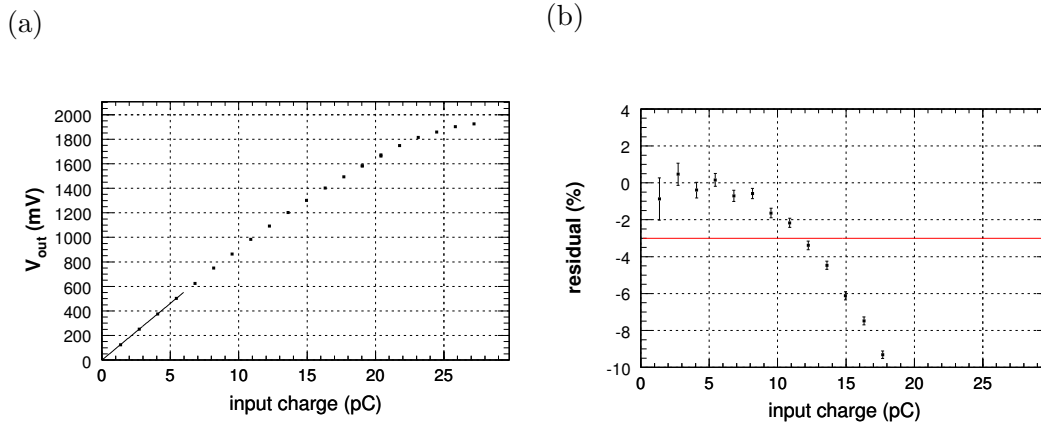(a)   (b)

Figure 5.22:   *Calibration mode linearity [60]. In (a) ASIC response function and in (b) the residual of the response function to a linear fit.*

Figure 5.22 (a) shows the response function of the ASIC in the calibration mode. The measured values are pedestal subtracted, $y = A_i - A_0$ and $\delta_y = \sqrt{2} \cdot \delta_A$. The statistical error on the x-axis is given by the precision of the pulse generator $\delta_{V_{in}} \approx 0.009$ mV

$$\delta_x = x \cdot \frac{\delta_{V_{in}}}{V_{in}}. \tag{5.18}$$

The accuracy of the capacitor adds a 10 % systematical error on the x-axis. For the linear range and the gain this uncertainty is applied in the same way. In the results only the statistical error is displayed.

The gain of the amplifier is measured for low amplitudes by a linear fit to the first part of the curve. The chosen range should allow a fit, which is independent on the non-linearity at higher values. The fit is constrained to the origin. The gain determined in this way is: $G = (92.3 \pm 0.2) \frac{mV}{pC}$. The deviation $y_{res} = \left(\frac{y}{G \cdot x} - 1\right) \cdot 100\%$ of the measured points to the fit of

the first 4 points is plotted in figure 5.22 (b). Here the limited range of constant amplification can be seen easily. If a maximum deviation of 3% is accepted the range reaches up to 11.5 pC in this mode. The error for the y-axis determined by all three input quantity errors.

Figures 5.23 (a) and 5.23 (b) show the same measurement for the physics mode. The gain found is $(8.178 \pm 0.007) \frac{mV}{pC}$.

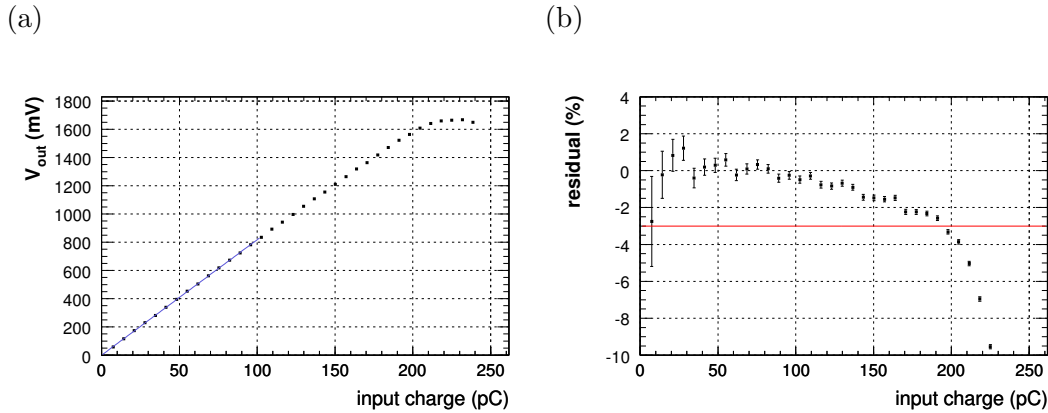(a)   (b)

Figure 5.23: *Physics mode linearity [60]. In (a) ASIC response function and in (b) the residual of the response function to a linear fit.*

The gains for both modes have been found to be in agreement between the prototype and the mass production [89].

5.4.2   Temperature dependence of the ASIC

The SiPM response is dependent on temperature and bias voltage variations, in particular the temperature variation of the SiPM gain at room temperature is measured to be 4.5%/°K.
The temperature dependence of the ASIC chip has also been investigated to ensure its minor contribution to the system. For this purpose one ASIC chip with its driving board have been placed into a thermal box where the temperature was varied between 10 and 70°C.
The temperature dependence of the ASIC chip signal has been measured for calibration and physics mode and for both the signal and the test input channels of the ASIC chip.
In all cases it is found that the time peak position and the signal noise do not depend on temperature. The temperature dependency of the gain is summarised in table 5.3 for all investigated combinations.

ASIC chip input	signal	test input
$\Delta G/\Delta T$ (calibration mode)	-0.27%/°K	-0.12%/°K
$\Delta G/\Delta T$ (physics mode)	-0.11%/°K	-0.021%/°K

Table 5.3: *Temperature dependence of ASIC chip gain [80].*

5.4.3   Single ASIC channel noise

The noise is defined here as the standard deviation (σ) of the Gaussian fit to the noise spectrum of the ASIC chip for various combinations of gains and shaping times. In order to measure the noise contribution of the ASIC chip amplifier the input line was grounded only via a 50 Ω

resistor using the setup shown in figure 5.19, removing the 0.1 μF capacitor. In this way, the noise of the DAC component is neglected. To increase the resolution the buffer gain was increased to a factor three. The noise of the setup alone was measured by replacing the ASIC with a 1.2 V battery and it results in $\sigma_{setup} = (1.64 \pm 0.01)$ channels. Under the assumption that the signal distributions of the ASIC and the setup are Gaussian and uncorrelated, the total noise σ_{tot} is given by

$$\sigma_{tot} = \sqrt{\sigma_{ASIC}^2 + \sigma_{setup}^2} \quad \Rightarrow \sigma_{ASIC} = \sqrt{\sigma_{tot}^2 - \sigma_{setup}^2} \tag{5.19}$$

from which the ASIC noise σ_{ASIC} can be derived.

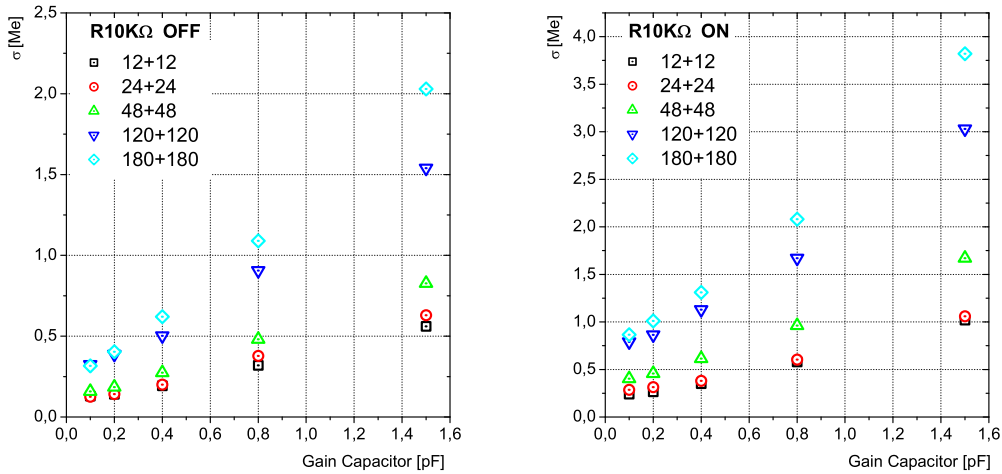(a)   (b)

Figure 5.24:   Noise of the ASIC chip amplifier, expressed in units of 10^6 electrons (Me), for various combinations of gains and shaping times. Bypassing (a) or using (b) the 10 kΩ injection resistor Ri.

The measured mean value of the noise is $\sigma_{tot} = (5.2 \pm 0.1)$ channels with a standard deviation of (0.30 ± 0.08) channels for a sample of 8 chips in calibration mode. This corresponds to an ASIC output noise of (4.94 ± 0.02) channels or (1.72 ± 0.04) mV.

The same measurement was also performed with the physics mode with longest shaping and gain setting 0.5 pF, which correspond to an amplification of 8.2 mV/pC. This corresponds to (4.3 ± 0.2) channel, which is almost the same noise as in the calibration mode. Expressed in output voltage this is (1.52 ± 0.05) mV. A more appropriate measure than the output noise is the equivalent noise charge (ENC), which describes the amount of charge which would give the same signal as the noise. As the output noise is independent of the ASIC operation mode, the ENC is determined by the gain. The value calculated for the physics mode is (186 ± 6) fC. For the calibration mode it is (18.6 ± 0.4) fC.

This noise can be compared to the signal from an ideal SiPM with 15 pixel per mip and a gain of 10^6. The minimum signal to resolve is one pixel in calibration mode, which corresponds to 160 fC. This corresponds to a signal-to-noise ratio of 8.6. The minimal signal for the physics mode is one mip corresponding to 2.4 pC, which leads to a signal-to-noise ratio of 12.9.

In figure 5.24 the noise values are presented for the two operation modes in which the injection resistor (Ri) is used or bypassed. This additional resistor at the input of the amplifier

increases the shaping time by ~40 ns. The noise is expressed in units of 10^6 electrons (Mega-electrons = Me). The amplitude of the SiPM signal for a single pixel firing (one photon signal) is approximately 1 Me, therefore the electronic noise should be smaller than this value to resolve single pixel structure. The best signal-to-noise ratio of ~8 is obtained for the highest gain and the shortest shaping time, which is the mode adopted for single pixel calibration in the operation with SiPM. In physics mode the signal-to-noise ratio is 11. In addition the influence of the injection resistor Ri is visible, which doubles the noise (σ) in the plots 5.24. In case of a short trigger latency it is possible to bypass the Ri making the shaped signal shorter but also the noise smaller.

The crosstalk between ASIC channels has been determined by injecting charge in one channel and measuring the amplitude of the neighbouring channels. The nearest neighbour shows a crosstalk effect of 0.18 %. However, the reason for crosstalk can be on the supporting PCB providing the input signal lines and not in the ASIC.

Individual channel voltage adjustment (DAC)

One of the requirements of the developed VFE electronics is to operate a large number of SiPM, being able to individually steer their bias voltage. This is achieved by a voltage adjustment via a 8-bit DAC connected to the input of each ASIC chip amplifier channel. The gain of the SiPM varies strongly with the bias voltage. Consequently the stability and reproducibility of the ASIC DAC are important parameters. The DAC covers effectively the range between 0.24 and 4.7 V, in steps of 20 mV. In figure 5.25 the linear range of the DAC output voltage is shown together with its noise. The voltage stability required for SiPM operation is on the order of 30 mV, corresponding to a change in gain for the SiPM of about 1%. The stability of the DAC is very well below this level.

A check was made to ensure the input of the DAC could tolerate the typical current from
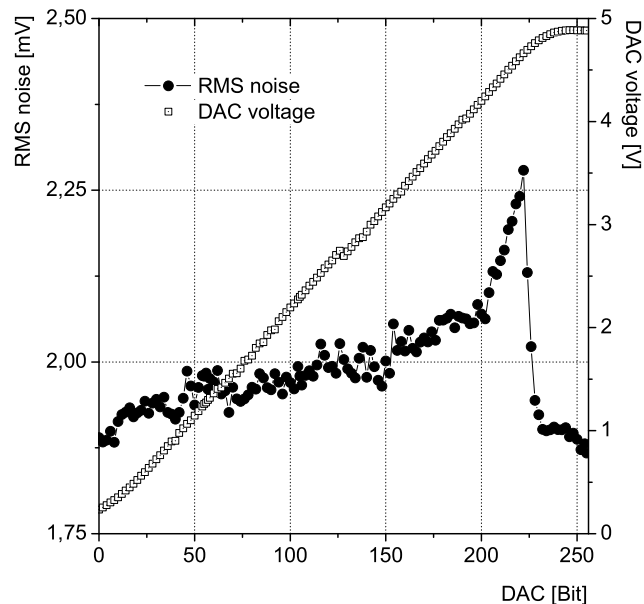

Figure 5.25: *DAC output voltage and noise as a function of the DAC setting parameter.*

the coupling to the SiPM ($5 - 0.3\ \mu$A). The maximum tolerable current at the DAC input was found to be $40 - 140\ \mu$A depending on the DAC settings, compatible with the requirements. From this the dissipation power of the DAC has been calculated to be about $500\ \mu$W.

Until now several measurements concerning the DAC linear range and RMS have been performed with different results. The noise level has been always below the requirements but the slope of DAC voltage versus bit varies between 17 mV/bit to 20 mV/bit. These values are only determined for a low amount of channels and are therefore not representative. Since the production test has shown that the spread of different DAC values from various ASICs is between 3-9 % it was decided to use the theoretical slope of 5V/255 = 0.0196 V/bit to calculate the correct DAC setting for each channel. Although the overall spread corresponds to $\approx$350 mV, the spread within the 18 channels in one ASIC is found to be only 200 mV. However, the range below 0.3 V and above 4.7 V cannot be used.

In addition two other features affect the correct SiPM HV adjustment. In the final system the HV is distributed by 10 m long power cables from the power distribution box to the VFE electronics. The HV drop in these cables is around 100 mV. The second effect is a voltage drop due to a 100 kΩ protection resistor, which is dependent on the SiPM current. A normal SiPM in operation draws a current of $300 - 500$ nA, which leads to a HV drop of $0.03 - 0.05$ V on a 100 kΩ resistor. If the SiPM has a high current ($\geq 1\ \mu$A) the HV drop is already around 100 mV. Therefore the total HV drop is around $\sim$200 mV.

5.4.4   SiPM readout with the ASIC chip

Once established that all the ASIC chip characteristics are compatible with the type of signal and the requirements for which the chip was designed, one can proceed and integrate the SiPM to its VFE electronics and study the property of the combined system.

The studies presented in this section are performed for one single channel, to understand the effect of the readout electronics on the SiPM signal. The connection scheme of SiPM to the ASIC chip is shown in figure 5.15. The possibility to calibrate the SiPM gain is an important advantage of this type of photodetector. For this it is necessary to measure the separation of the single pixel peaks in the SiPM pulse height spectrum. To achieve best separation with minimum noise contribution from the electronics and from the SiPM dark-rate, the ASIC is operated in calibration mode. The analogue SiPM signal (not held) at the ASIC chip output is shown in figure 5.26. The bipolar shape of the signal is obtained after the CR(RC)^2 shaper. Due to the SiPM dark-rate the noise spectrum obtained with SiPM connected to the ASIC chip (see figure 5.27 (a)) deviates from the perfect Gaussian shape resulting only from electronic noise. The positive and negative tails in Fig. 5.27 (a) for the SiPM signal are the result of thermal noise-induced signals held at their positive or negative amplitudes. Due to the different amplification of the positive and negative parts of the bipolar signal the spectrum is asymmetric. To estimate the width of the zero-peak in this case the Gaussian fit-function is limited to $\pm 3\sigma_{el}$, where σ_{el} is taken from the fit to the electronic noise only. The values obtained are $\sigma_{el} = 0.18$ photo-electrons and $\sigma_{el+SiPM} = 0.20$ photo-electrons. The purpose of this comparison is to demonstrate that the ASIC chip is suited to readout SiPM signal and the combined noise does not increase significantly when connected to SiPM. On the other hand, this measurement shows that the Gaussian part of the noise is dominated by the electronic noise, a point that can be improved in the next generation of ASIC chip for SiPM readout.

Using a low intensity light source it is possible to observe the single pixel structure in the SiPM pulse height spectrum, as seen in figure 5.27 (b). The separation of subsequent peaks is good and allows for a multi-Gaussian fit to determine the SiPM gain $\Delta peaks$ and the peak widths. The signal-to-noise ratio obtained for single pixel signal is $\sim$4, in agreement with
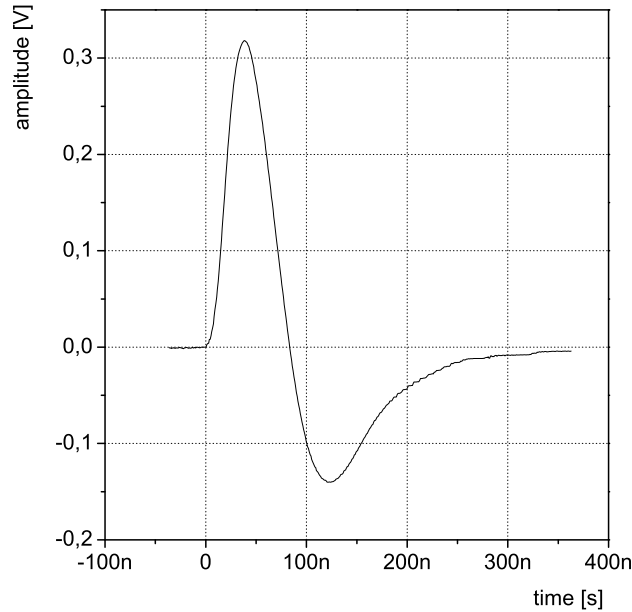
Figure 5.26: *Analogue SiPM signal after highest amplification (G=0.1pF) and fastest shaping (T=40ns) in the ASIC chip.*

the ratio extracted from the direct measurements of the ASIC chip in section 5.4.3 since the compared SiPM gain is lower than 10^6 electrons.

During normal data taking the SiPM signal amplitude can vary up to the SiPM saturation which, for the 1156-pixel device, corresponds to ∼200 pC. It is possible to choose the amplifier gain such that the amplified signal is contained in the linear range of the ASIC chip. In physics mode the combined noise of ASIC chip and SiPM allows a signal-to-noise separation for minimum ionising signal of ∼11, sufficient for the planned application in a hadronic calorimeter prototype.

The used ASIC switches for the two selected modes are shown in table 5.4. Note the inverted logic between the activation of the feedback capacitance and the shaping capacitance.

5.4.5   Production test

After production of the ASIC chips several checks have been performed to select only the properly working chips. The range of acceptance has been determined by the analysis of the first delivered chips and is adjusted to have a yield of around 80 % [90]. This means that the range of tolerance is between -3σ to $+3\sigma$ for all quantities. In total 1047 ASICs have been produced of which 896 (85.5 %) have been successfully tested. The reason for the failed test was in 61 (40 %) of the 151 cases a too high power consumption, followed by errors in the gain switches 32 % and in the DAC settings (16 %). These values are biased by the fact that the test is stopped after the first error has occurred. The detailed test results are summarised in [91]. The investigated ASIC parameters are listed below.

1. The *power consumption* of a chip is tested. The power dissipation is determined by measuring the current of the supply power to the ASIC. The average current is ∼40 mA,

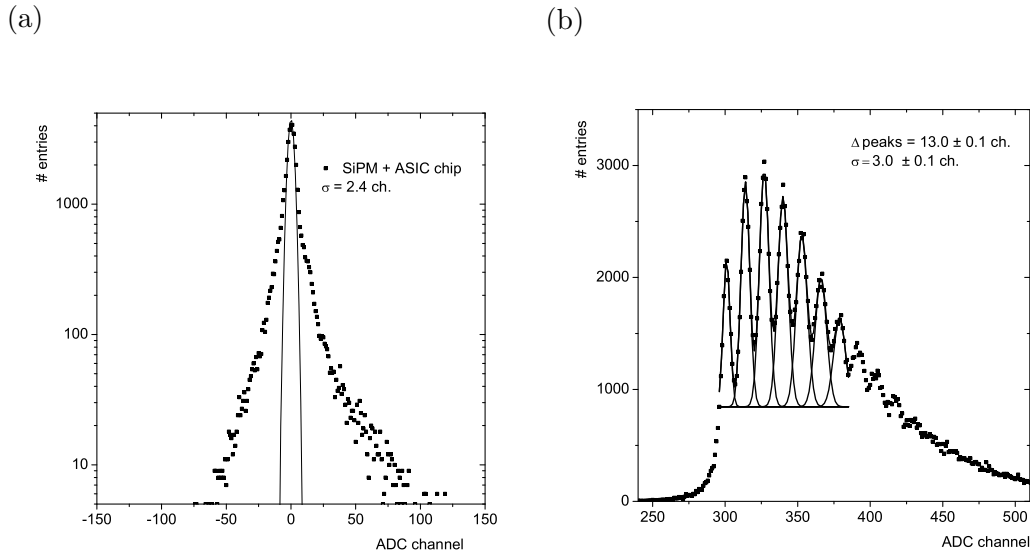(a)   (b)

Figure 5.27:   (a) Noise spectrum from the ASIC chip only (solid red line) and SiPM (black markers) connected to the ASIC chip. The width of the electronic signal alone is around σ_{el} = 2.4 ADC channels or 0.18 photo-electrons. (b) Single photo-electron peak spectrum from SiPM with ASIC chip readout.

switch	purpose	C[pf]	calibration	physics
sw_cr0	shaper	0.3	0	1
sw_cr1	shaper	0.6	0	1
sw_cr2	shaper	1.2	0	1
sw_cr03	shaper	2.4	1	1
sw_g	switch for RC6 or CRRC2 choice		1	1
sw_buf	switch for T&H buffer choice		0	0
sw_cf0	amplifier feedback capacitance	0.8	1	1
sw_cf1	amplifier feedback capacitance	0.4	1	0
sw_cf2	amplifier feedback capacitance	0.2	1	1
sw_cf3	amplifier feedback capacitance	0.1	0	0
sw_cp0	switch for injection resistor		0	1
sw_RC6_spe			0	0
sw_2_RC6			0	0
sw_RC6_spe1			0	0
sw_RC6_spe0			0	0
sw_RC6			0	0

Table 5.4: ASIC configuration for the two readout modes: calibration and physics mode.

which leads to a power dissipation of ∼200 mW for a complete ASIC.

2. To perform a functionality test of the *Gain or feedback capacitors* the shaping capacitors are fixed and all used gain capacitors are individually tested. A fixed voltage pulse is injected for the following feedback capacitor settings: 0.1 pF, 0.2 pF, 0.4 pF and 0.8 pF.

3. To identify shorts between the 18 input connections and channels a voltage pulse is injected in all 18 inputs of the chip.

4. To perform a functionality test of the *shaper capacitors* the gain capacitors (C_f=0.4 pF) are fixed and the shaper capacitors are individually tested. A fixed voltage pulse is injected for the following time constants: 12 ns, 24 ns, 48 ns, 96 ns and 180 ns.

5. The functionality of the *injection resistor Ri* is tested.

6. A linear response is mandatory and therefore the *linearity* of the ASIC is tested for a fixed set of gain and shaping capacitors. Five different voltage pulses (0.1 V, 0.2 V, 0.3 V, 0.4 V and 0.5 V) are injected over the test input and the output amplitudes are measured.

7. The *noise level* gives an indication about properly working channels. For two different sets of capacitor settings the pedestal is measured.

8. The *DAC* plays a crucial role in the operation of SiPMs and the significant bit switches are checked. For a fixed set of capacitor setting the DAC is varied for the following values: 0, 1, 2, 4, 8, 16, 32, 64, 128, 255 bit and the output voltage is measured.
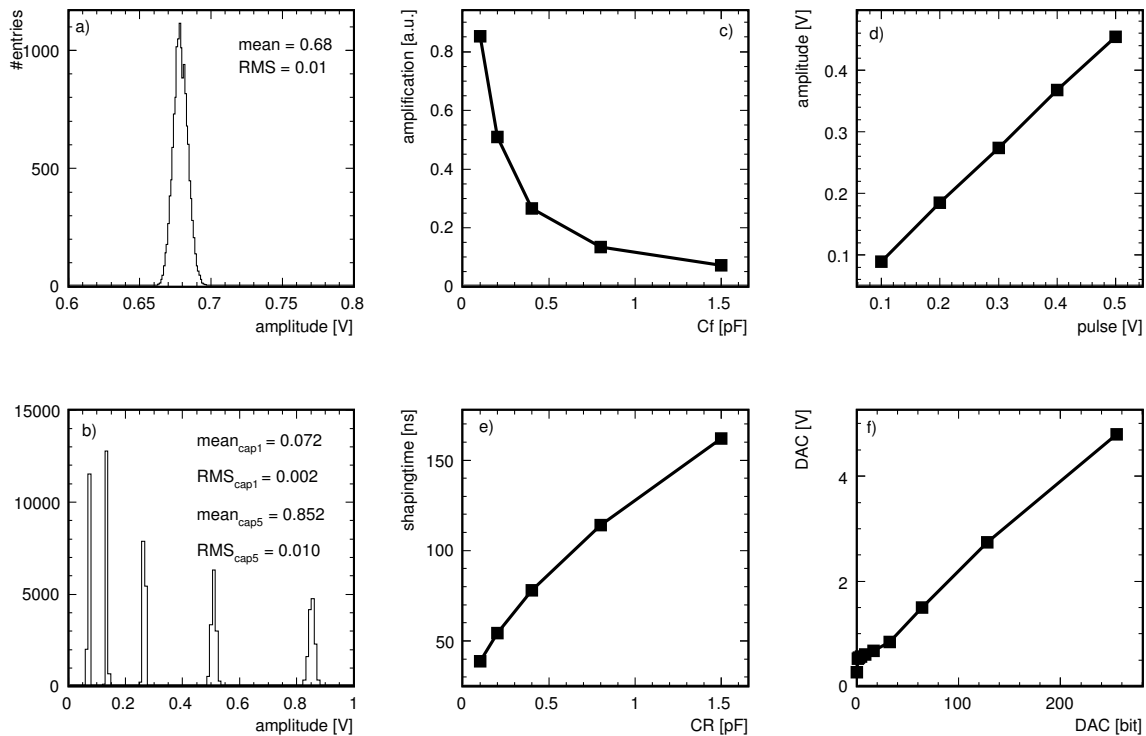
Figure 5.28: *Examples of the ASIC production test results. (a) Pedestal distribution of all tested channels. (b) Gain distributions for different choices of gain capacitors. For (c)-(f) each point corresponds to the mean value of all tested channels. (c) Amplification factor dependence on the selected gain capacitors. (d) Linearity of the ASIC versus the injected voltage pulse over the test input. (e) Dependence of the shaping time on the selected capacitors. (f) DAC output voltage versus DAC switches.*

The functionality tests 2, 4, 6 and 8 are summarised in figure 5.28. In (a) the pedestal distribution of all tested channels is presented, the spread is 1 %. In (b) the gain distributions

for different choices of gain capacitors are shown. The maximum spread is obtained for the highest capacitor (1.5 pF) and it is about 3 %. In (c) amplification factor dependence on the selected gain capacitors is presented. In (d) the linearity of the ASIC versus the injected voltage pulse over the test input is shown. A nice linearity is achieved. The dependence of the shaping time on the selected capacitors is shown in (e) and the response to the DAC switches is shown in (f).

5.5   The very front-end electronics

The ASIC needs supply voltages, signal lines and steering lines to be programmed, to get input signals and to communicate with the data acquisition (DAQ). Therefore, dedicated support boards have been constructed: the *HCAL Analog Board (HAB)*. It provides the ASIC with +7 and -7 V, a *Shift Register (SR)* to store externally settings and all the needed communication lines. A passive base board capable of hosting 6 HABs provides the connection between SiPMs and DAQ.

5.5.1   The very front-end boards

Each ASIC chip sits on a small PCB board, which hosts electronics to supply the operating power and to steer the settings of gain, shaping and DAC. Figure 5.29 (a) shows a picture of this board. The HABs are plugged on a base board to the SiPMs and the DAQ. The base board also serves for the distribution of the low and high voltage supply, the clock and the control signals. For manufactoring reasons the readout of one AHCAL plane has to be done by two base boards. This results in two mirrored versions of the base board, type A and B. Figure 5.30 shows a drawing of an A-type base board. Six HABs sit on each base board, resulting in 108 input channels and 6 output lines. As there is only one high voltage supply to a base board, the SiPM connected to it have to lie within the range of the ASIC DAC. The cabling of the SiPM in the AHCAL can be seen in figure 5.31 showing an open module equipped with electronics. The design of the VFE electronics is optimised for the AHCAL modules with fine core.

The steering of the ASIC settings is done with the SR. These are programmed over two lines, clock and data. The bits move one position forward for every clock cycle. The output of the SR of one VFE-board is connected to the input of the next. Every six boards build a serial line of SR which are programmed by the DAQ. The output of the last board is read back for verification by the DAQ.

A detailed description of the signal sequences for the shift register programming and the readout of the multiplexed signals is given in [92]. The shift register programming defines the operation parameters and is divided in two parts. As the voltage settings of the DAC will be set only at the startup and stay the same for the time of operation, the programming of the settings is done separately for DAC and the remaining settings. These remaining settings control the amplifier and the shaper of the ASIC and are 16 bits per HAB. The DAC settings are 18×8 bits for each ASIC. To shift all these information to the HAB 160 clock cycles per installed HAB is needed. To distinguish between these two programming modes the SR clock signal is switched by an external signal (SW_DAC) between both sets of SR. At the same time the output is switched to the right path to preserve the chain. A detailed scheme of the steering logic can be seen in figure 5.29 (b). The separation of the two paths has two main advantages. On one hand, the time used for programming the gain and shaping settings is reduced with respect to one single SR line. On the other hand the SiPM are constantly powered as the voltage settings are kept as long as the DAC is not reprogrammed. In addition,
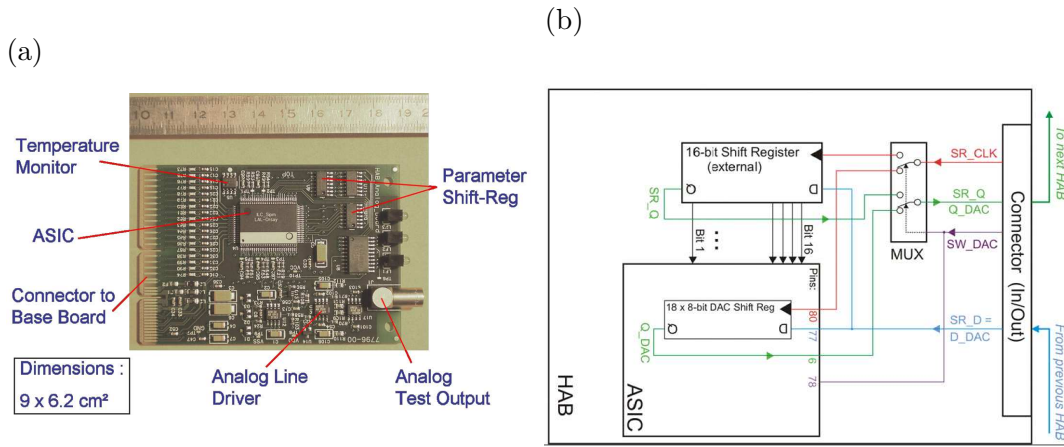
(a)

(b)

Figure 5.29: *HCAL very front-end electronics (VFE) [92] and [93]. (a) Picture of the very front-end board called HCAL Analog Board (HAB). (b) Steering logic of the shift register.*

the DAC SR is less sensitive to external noise as the clock line is disconnected during normal operation. This reduces the risk of applying a wrong voltage to the SiPM. In addition, the switching between physics and calibration mode can be done by reloading the external shift registers without changing the internal DAC settings.

The readout sequence starts with a reset signal and the stored amplitudes of the individual channels are shipped out by 18 clock cycles.

Additional signals are implemented which are used for the steering of the CMB or for internal charge injection into the ASICs. An analog DC voltage (VCALIB) and a trigger signal (TCALIB) can be used to define the LED flash in time and amplitude at the CMB or to define the injected charge in the test input of the ASIC.

All the traces for fast signals on the base board have been arranged such that signal propagation times do not vary more than 1 ns from channel to channel.
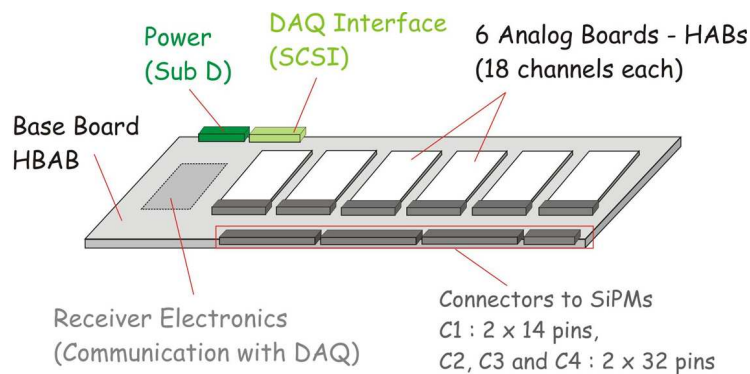
Figure 5.30: *Drawing of the base board type A hosting six very front-end boards [92].*

Coherent noise

In the produced VFE electronics the coherent noise without SiPM input signal was around 25 ADC channels and the incoherent 18 ADC channels [94]. But the coherent noise should be smaller than the incoherent one. Two additional 10 μF filtering capacitors have been

Figure 5.31: *Picture of an opened AHCAL module with readout electronics.*
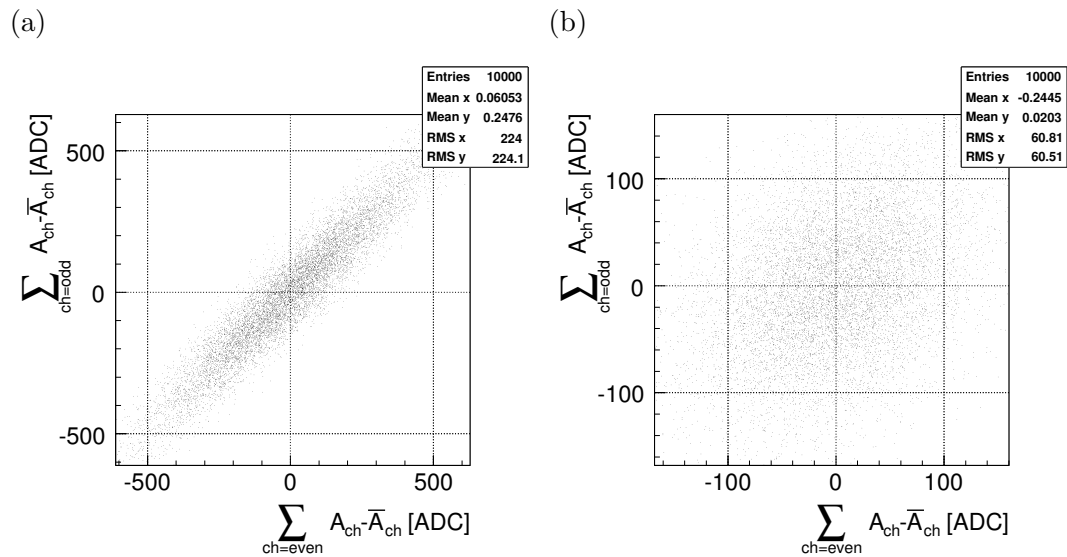
Figure 5.32: *(a) ASIC channel correlation between even and odd channels before ASIC modification. (b) ASIC channel correlation between even and odd channels after ASIC modification.*
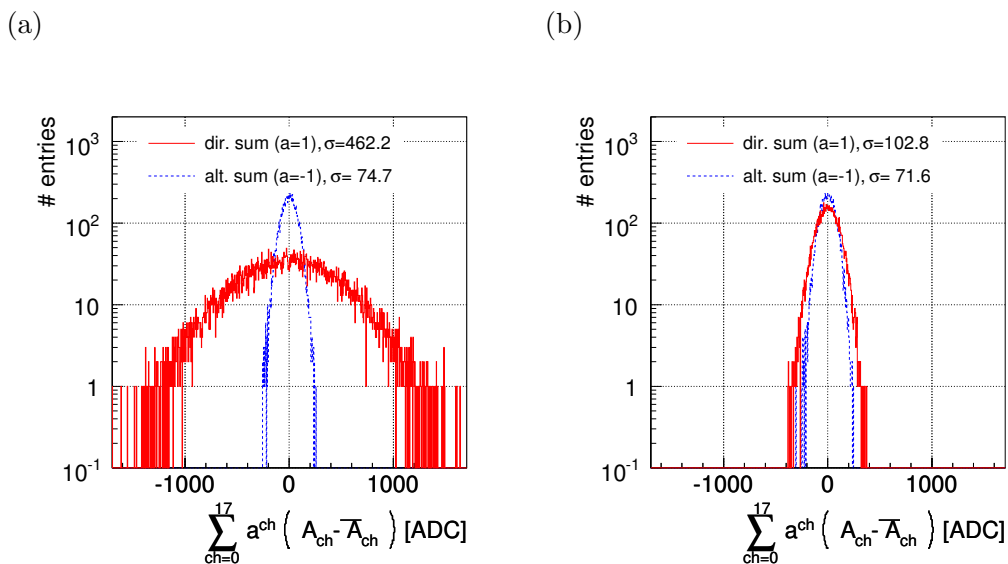
Figure 5.33: *(a) ASIC direct and alternating sum before ASIC modification. (b) ASIC direct and alternating sum after ASIC modification.*
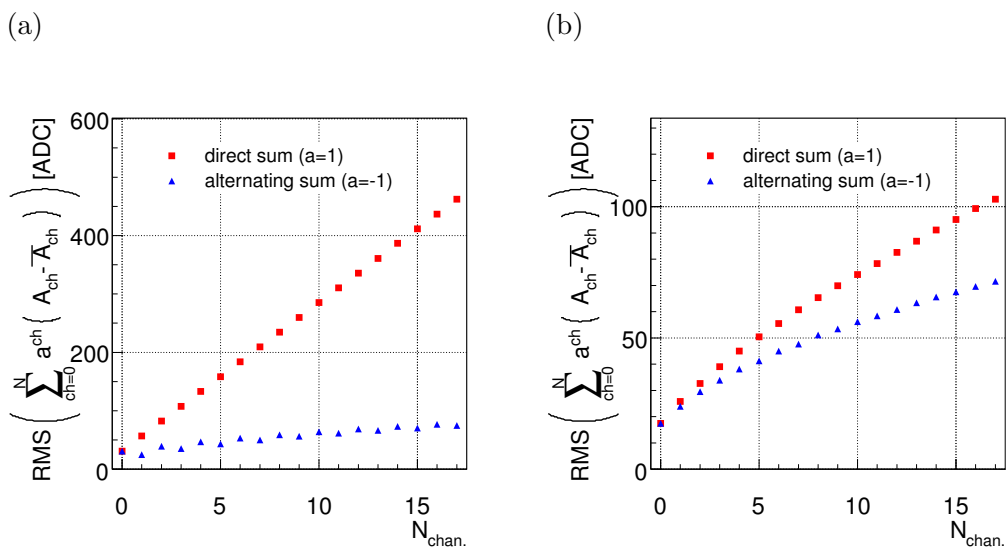
Figure 5.34: *(a) ASIC direct and alternating sum as a function of number of channels before ASIC modification. (b) ASIC direct and alternating sum as a function of number of channels after ASIC modification.*

(a)   (b)

Figure 5.35:   *(a) ASIC coherent and incoherent noise contribution before modification. (b) ASIC coherent and incoherent noise contribution after modification.*

implemented on each HAB to stabilise the two ASIC voltages (V_{cc} amplifier stage and V_{ref} pulse shaper stage). The effect of this change is shown in figure 5.32 to 5.35, where plot (a) always shows the situation before the modification and (b) after. In figure 5.32 the correlation betwe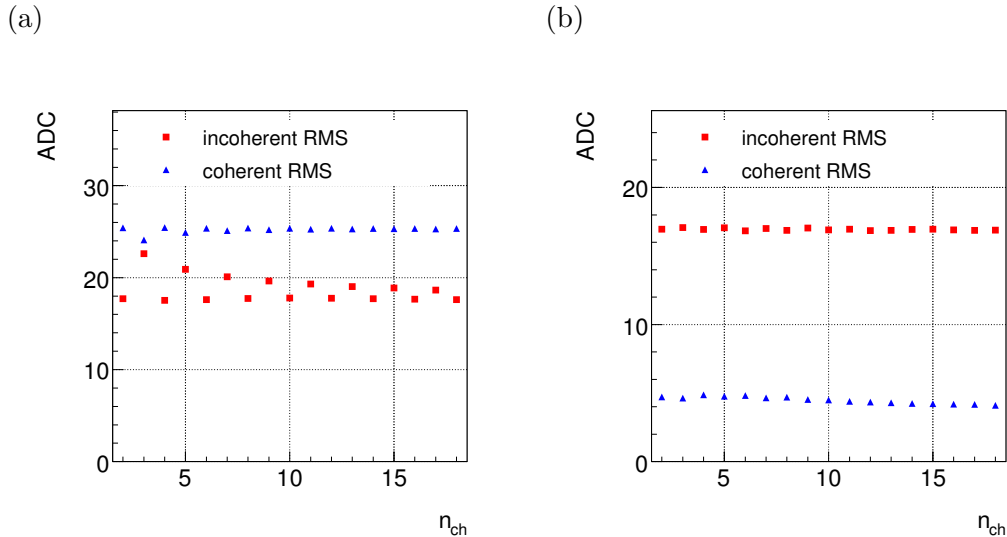en the amplitude sum of the even and odd channels of one ASIC in a noise run is shown. In (a) a clear correlation, which indicates common pedestal changes in one direction and therefore coherent noise. A way to quantify the coherent and incoherent noise contributions is to calculate the direct and alternating sums according to equation 5.8. In figure 5.33 the two sums are plot for the sum over all 18 channels of one ASIC and in figure 5.34 the development of the sums including more channels is shown. In both plots (a) the large direct sum, which is correlated to the coherent noise is visible. Applying equation 5.8 results in the coherent and incoherent noise contributions, which are shown in figure 5.35. After the modification of the HAB grounding the coherent noise contribution has decreased from 25 to 4 ADC channels, which is sufficiently small.

5.5.2   The data acquisition system

The VFE electronic is connected to the data acquisition system (DAQ) [59]. The DAQ performs not only the last part of the signal processing, the digitisation of the analog signal and data buffering, it also steers the VFE and does the trigger calculation. The heart of the data acquisition is formed by the CALICE Readout Card which is shown in figure 5.36 (a). Whereas the signal processing in the ASIC chip is analog, the signals processing on the CRC is fully digital. The DAQ is based on the nine unit double-sided VME technology and has been produced by the UK Calice Group [95]. The readout board is a modification of the CMS Silicon-tracker readout board. They contain 16-bit ADCs for each VFE ASIC output and also 16-bit DACs for calibration. The ADC can operate at up to 500 kHz and so take around 80 μs to read out all 18 multiplexed channels from a VFE ASIC. There is no data reduction on the entire readout chain; all signals from all channels will be read out and this corresponds to 5 kBytes per CRC per event, or 35 kBytes total per event. These data are stored in an on-board 8 MByte memory, which allows about two thousand events to be buffered during a

spill before readout via the VME bus. The clock on the DAQ card is 160 MHz which gives a 6.25 ns step resolution for all signals sent from the DAQ.

The CRC shown in 5.36 (a) can be split in two functional parts, the front end (left of the separator) and the back end (on the right). Eight Front End (FE) FPGAs [6] control all signals on the front panel connectors to and from the VFE PCBs. The Back End (BE) FPGA gathers and buffers all the event data from the FEs and provides the VME interface. The trigger logic is implemented in the BE FPGA, for which the logic is only active on one board and the trigger decision will be distributed over a special PCB at the backplane to the other CRC boards. The readout sequence can be started by an external signal or an internal clock. The processing time needed for a trigger decision in this part is the largest contribution to the trigger latency.

A front end consists of inputs to the analog to digital converters (ADC) and outputs for the
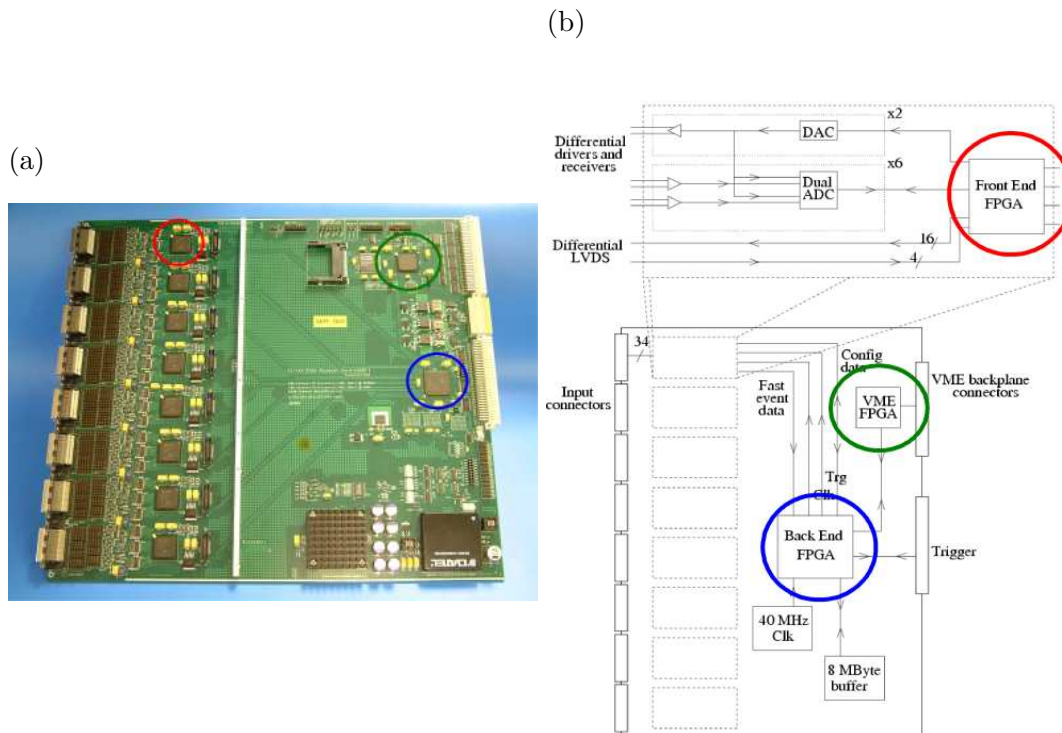
Figure 5.36: *CALICE Readout Card [59] with schematics. (a) CALICE Readout Card. (b) Programming and readout sequence.*

steering of the VFE electronics, which has been described in section 5.5.1.

The CRC readout consists of two VME data paths. The serial path communicates directly to all FPGAs in the frontend and backend. This data path is relatively slow and is used for all configuration data loading and read-back. In addition, it is used for temperature and power monitoring. The second path is the Vlink path, which is used only for a fast reading of the 8 MByte memory via the backend. Therefore, it is only used for buffered event data. Slow in this context means that it takes $\sim$15 μs for every 4 byte word, i.e. only $\sim$270kBytes/s. The fast Vlink instead is able to reach $\sim$10 MBytes/s for the block transfer from the memory. This readout mode is explained in the next section.

The prototype design of the CRC was completed in summer 2003 and two prototype CRCs

---

[6]FPGA is a Field Programmable Gate Array.

were fabricated in November 2003. One important CRC test is the internal loop-back test. In this test, the DAC output was looped back directly to the ADC inputs. This allows a straightforward linearity scan of the system independent of the VFE electronics. A simple straight-line fit gives residuals of around 1-2 ADC counts, corresponding to an intrinsic non-linearity of 0.01 %, which is smaller than the non-linearity of the VFE electronics and therefore negligible [59]. The ADC with its 16-bit allows to record energies up to 100 mips, depending on the VFE settings. Since one CRC consists of of 8×216 channels, at least five cards are needed to read out the entire AHCAL test-beam prototype. A total of six CRCs will be needed for the entire ECAL readout.

DAQ speed

The CRC is capable of two different readout modes. One mode runs continuously and every event is read out directly by the DAQ software. In this mode the trigger speed is limited to the speed of the data transfer over the VME bus which is in the order of 100 Hz. As many test-beam facilities do not deliver particles continuously, the DAQ can run in a buffering mode where up to 2000 events can be stored in the memory of the CRC and will be read in between two beam spills. This increases the maximum trigger rate to $\approx$1 kHz and thus the efficiency at test-beams with non-continuous beam supply.

The following considerations are based on the parameters of the CERN SPS test beam (details can be found in chapter 7). This test-beam facility provides in the standard operation a 4.8 s long particle spill containing in a overall cycle of 16.8 s. The readout mode using buffering has
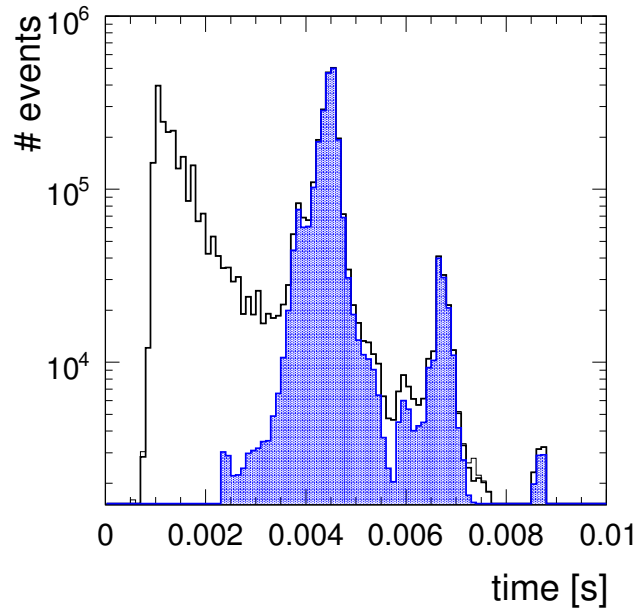

Figure 5.37:   *Trigger time (black empty histogram) and event readout distribution (blue filled).*

consequences on the overall readout procedure. The event counters are the number of triggers seen in the trigger section, in the FEs and the BEs, and are only accessible over the slow serial path. These counters document if the trigger has arrived at all the parts of each CRC

and hence gives the possibility to detect synchronisation errors. This kind of information is not needed for every event. If a problem occurs, all events since the last good set of trigger counters have to be discarded. However, the rate of missing synchronisation is small and an entire spill can be rejected if errors occur. To speed up the readout these counters are only read out at the end of the spill giving the total number of triggers during this spill.

In figure 5.37 the black histogram represents the time to process a trigger. It has an exponential decay from around 1 ms, which is the minimum needed time even if the trigger has occurred immediately. The blue filled histogram is the time needed to process an event, which has its peak value around 4 ms. A typical event of the setup used in 2006 (see chapter 7), with reduced number of readout channels, has a size of ∼34 kBytes, which can be translated to a data readout rate of ∼8.5 MBytes/s, as shown in figure 5.38 (b). The additional peak in figure 5.37 around 7 ms represents the trigger and event readout when the buffer of the CRC is full. In this case the CRC switches from the buffered readout mode back to the direct readout mode.

In figure 5.38 (a) the trigger and the event rate in Hz is shown for 5 spills. The peak at ∼600 Hz is the trigger rate during the spill and the rate at ∼200 Hz afterwards is the event rate after the spill. The short time where the two histograms overlap has the following reason. The DAQ takes 2000 triggers at ∼600 Hz until the buffer memory is full. Then, if the spill is still ongoing, it accepts more triggers. For each newly stored event in the buffer one is read out, such as to maintain a maximum 2000 events in the buffer. Only when the spill finishes the DAQ stops to collect triggers and goes to pure event readout. This means that towards the end of the spill the trigger rate drops and is the same as the event rate, which is ∼100 Hz when both are happening. This effect is visible for some bins in figure 5.38 (a). Since a trigger record has only the size ∼1 kByte and an event record ∼34kBytes the data rate in MByte/s show in figure 5.38 (b) behaves opposite to the normal rate.
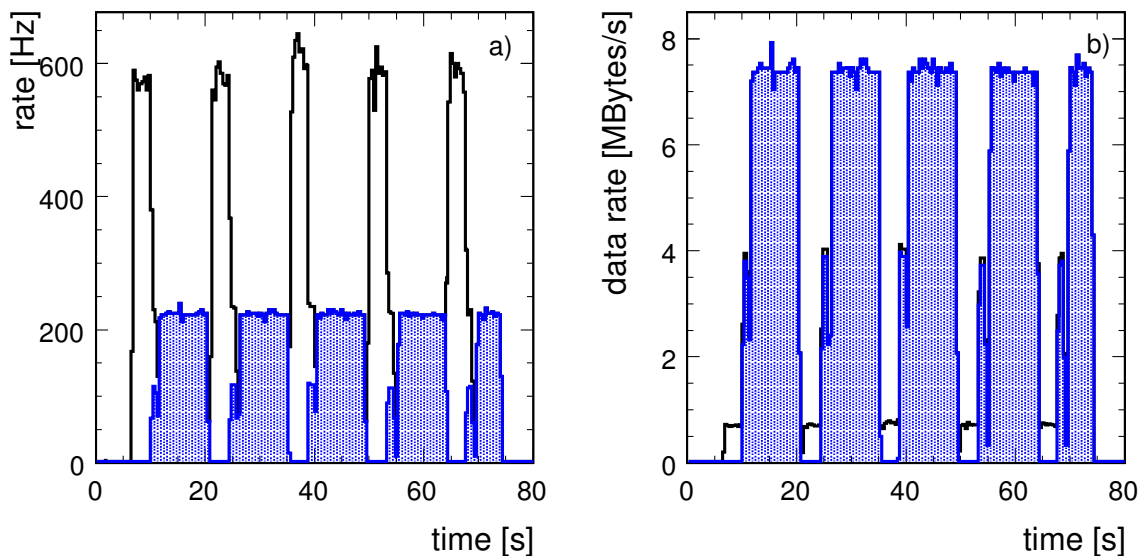

Figure 5.38: *(a) Trigger rate in Hz during the 4.8 s long spill (black empty histogram) and event rate in the time between spills (blue filled). (b) Data rate in MByte/s during the 4.8 s long spill (black empty histogram) and event rate in the time between spills (blue filled).*

Trigger

The CRC accepts several external trigger inputs from the backplane. These information are stored in the *Backend Trigger History*, which is stored in the CRC memory as well and is therefore needed and available for every event. This FIFO memory is 256 bins large and each bin covers a time duration of 25 ns. The DAQ expects the trigger to arrive around bin 195. Two examples of the backend trigger history are shown in figure 5.39 for two different triggers. On the x-axis a portion of the FIFO history is presented and on the y-axis the
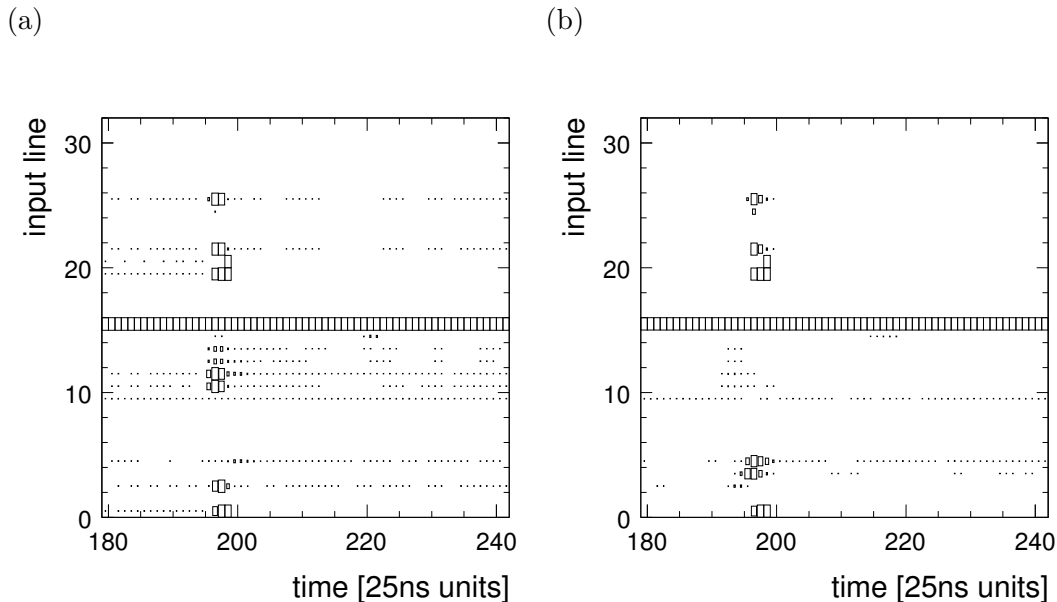
(a)   (b)

Figure 5.39:   *(a) Trigger inputs for a pion 20 GeV run. (b) Trigger inputs for a muon calibration run.*

status of the different input bits. Inputs 0 to 15 represent external information. The inputs are used to record signals from trigger scintillator plates, readout by a photomultiplier tube, after discrimination and conversion to LVDS. In this particular setup several of these triggers have been read out. Most of them have been installed as a coincidence and have therefore the same distribution (e.g. 3 and 4, 10 and 11, 12 and 13). Additional information from the beam-line are given in input 2, 14 and 15. Input 15 is the test-beam spill signal, always on during beam data taking. This information is important for the DAQ timing to decide when to start the readout of the buffered events. Input 9 is connected to an external pulser to debug the external trigger setup without using the beam. The CRC backplane also provides several trigger outputs of which one is looped back to input 0. Therefore, this input shows the total amount of accepted triggers. The observed shift of one bin of 25 ns w.r.t. the input triggers is a measurement of the time needed for the trigger decision. The bits above 15 are reserved for special setting of which two are of interest. Bit 25 to 28 are used to enable coincidences between different trigger inputs. In this case only bit 25 is on and therefore only one coincidence is used. In figure 5.39 (a) the final trigger was set to a coincidence of input 11 and 12 and in figure 5.39 (b) to a coincidence of input 3 and 4. Bit 24 presents the internal trigger of the CRC, which consists of an oscillator. The oscillator is turned on with a low frequency during data taking in the buffered mode. This serves to collect randomly triggered data during the spill to check the pedestal stability and evaluate pile-up effects. An important question before going to a test beam is the needed particle beam rate to achieve the maximum

possible data collection rate. If r is the beam rate, the time waiting for a trigger is $1/r$. The DAQ needs time to process the trigger, t_t and time to read out an event, t_e. Assuming a spill of 4.8 s, every 16.8 s the following relations are valid.

$$\text{maximum number of triggers in 4.8 s spill} = \frac{4.8}{1/r + t_t}$$

$$\text{maximum number of events in 16.8 s read out period} = \frac{16.8}{1/r + t_t + t_e}$$

In addition, the hardware memory buffer on each CRC can hold 2000 events. These requirements define the maximum number of events depending on the beam rate. An additional requirement is important for high beam rates where additional hits before the trigger leave energy in the calorimeter (pile-up). The probability that no hit has occurred in a time t_0 before the trigger is $exp(-t_0 \cdot r')$, where r' defines the beam rate over the whole calorimeter and not just the trigger scintillator. In the following $r' \sim 2 \cdot r$ is assumed. In figure 5.40 (a)-(c) the obtained dependences of the event rate of the beam rate, both in Hz, are shown for varying the three time constants: for the event readout t_e, the trigger readout t_t and the second particle veto t_0. The largest impact has the event readout time. However, optimal beam intensity is $3 - 10$ kHz in all cases.

(a)   (b)   (c)
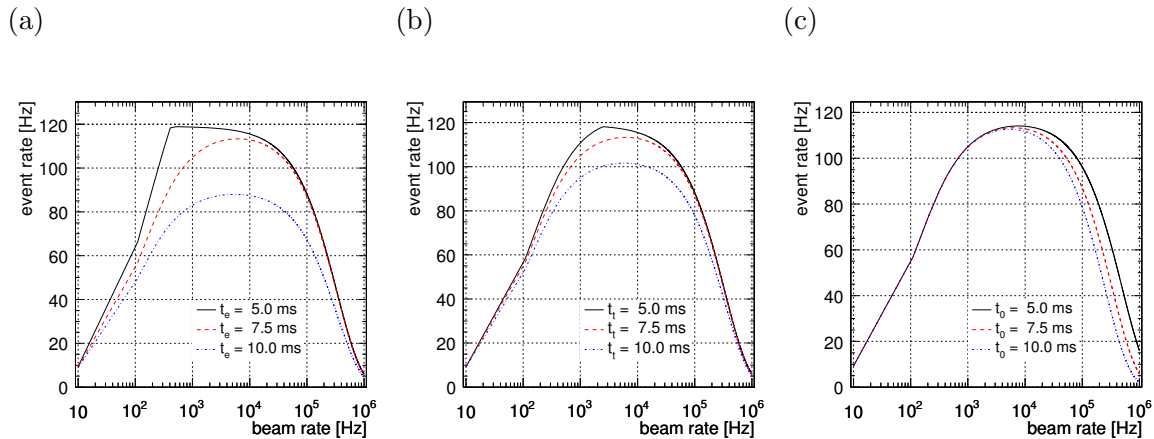
Figure 5.40: *(a) Event rate dependence on the beam rate for different event readout speed. (b) Event rate dependence on the beam rate for different trigger readout speed. (c) Event rate dependence on the beam rate for different veto probability.*

ADC Differential Non-Linearity

An Analog to Digital Converter (ADC) translates an analogous signal, i.e. a voltage, to a digital value representing the size of the signal. Whereas an analog signal has a continuous spectrum of values, a digital signal assumes discrete values. Each output value of an ADC corresponds to a certain input range. For a perfect ADC the total input range would be divided into input ranges of the same width, corresponding to the resolution. The transfer function between input and output would be a multi-step function with equal step width. In this case the maximum error would be half the width of one step.

In practise an ADC with perfect equidistant steps is hardly realisable. For example the ADC ADS8361 used on the CRC is a Successive Approximation Register (SAR) A/D converter

with 16 bit from Texas Instruments. In an SAR-type ADC the external signal is compared to a variable internal voltage source. The accuracy of the voltage source defines the quality of the conversion process. The differential non-linearity (DNL), which is defined as the maximum and minimum difference between the real step width and the perfect step width of any output step, is one benchmark of such a conversion process.

To measure the DNL a sawtooth signal from a Philips PM5131 function generator was sent to the ADC of the CRC. As the function generator was not synchronised to the DAQ readout, the signals, which are present at the input in the moment of acquisition, are equally distributed over the amplitude range of the signal generator. For a perfect ADC each possible output value of the measured range would occur equally often, within the statistical deviations. Deviations from a homogeneous distribution are a direct measurement of the differential non-linearity.

(a)   (b)
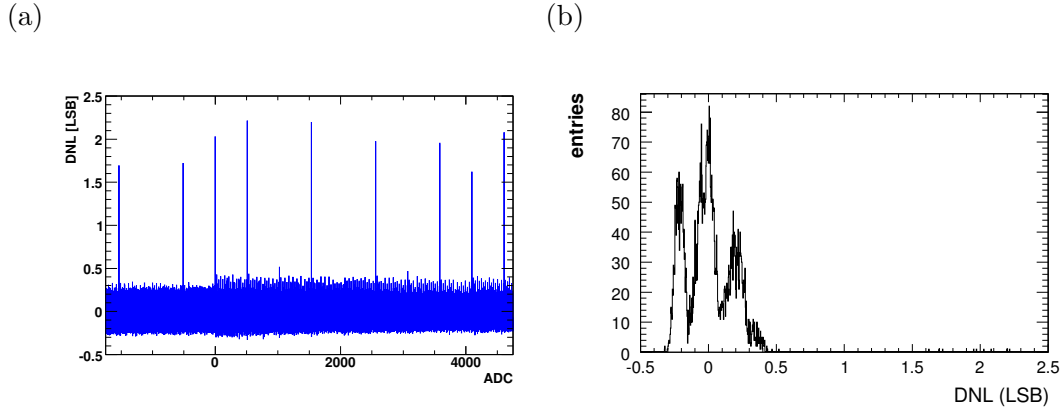

Figure 5.41:   *Differential non-linearity of the CRC ADC [60]. (a) ADC spectrum. (b) DNL distribution.*

Figure 5.41 (a) shows this deviations $\frac{N_i - <N_i>}{<N_i>} - 1$ for each bin i. Due to the normalisation the height of the bin signal is equal to the width of the corresponding step in the transfer function, measured in the width of the least significant bit (LSB). An average of ≈ 4600 entries per bin were collected, which determines the statistical error on the measurement of one bin to 1.5%. The measured DNL of $^{+2.2}_{-0.3}$ LSB is in accordance with the values from the data sheet of the producer [96]. From the distribution of the signal, shown in figure 5.41 (b), it can be seen that for most of the bins the DNL lies between -0.3 and 0.4 LSB. Nevertheless the high peaks show a few entries between 1.5 and 2.5 LSB.

The result shows that every 512 channels there is a high probability for a step with roughly twice the width of the average bin. In addition, the result shows that the distribution of the DNL is not symmetric.

One standard way to reduce the influence of this non-linearity is to reduce the resolution by joining each n bins to one single bin, before the measured signal is analysed. For that reason the influence of re-binning on the DNL was examined. Generally, re-binning increases the value of the LSB by the factor of re-binning. A detailed description of the results can be found in [60]. An improvement in the DNL could only be found for a re-binning with multiples of 4. The distribution of the DNL develops from the multiple peak structure it has without re-binning to a more Gaussian like distribution of smaller width. This reduces the error the DNL introduces for each bin between the high peaks. But the high peaks, which occur about every 512 bins, do not average out like the fluctuations in the rest of the range. The relative bin error is only reduced by the factor of re-binning. One LSB corresponds to 76 μV and in consequence the absolute error on the measurements of signals in the order of 10 mV is

negligible. But the high peaks in the spectrum may lead to problems in the data analysis.

5.6   Commissioning of the readout electronics

After the understanding of each component in the readout chain separately, one of the biggest milestone was to put the components together and to characterise the complete system.

5.6.1   Adaptation of VFE electronics and DAQ

Following from the measurements in section 5.4.1, the linear output range of the ASIC in calibration mode ends at 1.3 V. The gain of the physics mode was chosen in such a way that a fully saturated SiPM signal lies within the linear range of the ASIC which results in a similar linear output range. The input range of the DAQ lies between -2.5 V and $+2.5$ V. To avoid pedestal fluctuations the reference of ASIC output and DAQ input are both set to 0 V. This leaves the range between 0 V and 2.5 V as possible input range of the DAQ. The line driver gain of the VFE electronics was set to a factor of 2.0 to extend the ASIC output range to the input range of the DAQ. This cuts a little of the linear range of the ASIC but gives a better resolution of the real SiPM from the mass production. The first samples show a smaller gain of $\approx 0.5 \cdot 10^6$, which will be even covered by the slightly reduced ASIC output range of 1.25 V.

5.6.2   Readout noise

Several measurements were performed to get an understanding of the readout electronics and to ensure that no additional noise is added to the the unavoidable amplifier noise. Therefore, the noise was measured for all parts of the electronics. The noise for the final readout chain was measured with the DAQ itself. The results are summarised in table 5.5.

setup	σ [channel]	σ [mV]
DAQ	1.39 ± 0.06	0.053 ± 0.002
DAQ + base board (BB)	1.39 ± 0.06	0.053 ± 0.002
DAQ + BB + front end electronics in calibration mode	45 ± 2	1.71 ± 0.08
DAQ + BB + front end electronics in physics mode	36 ± 2	1.37 ± 0.08

Table 5.5:   *Results of the noise measurements with the DAQ [60]. The values in mV corresponds to the ASIC output voltage and are corrected for the line driver gain.*

Comparing these values to the measurement in section 5.4.3 show, that the noise of the full system is the same as for the ASIC alone. The noise is fully dominated by the ASIC noise.

5.6.3   SiPM gain measurement

The studies of SiPM with ASIC readout presented so far, were done in small laboratory setups, which were not completely the same like the readout chain for the AHCAL prototype. Therefore one of the first commissioning milestones was the measurement of SiPM gain in the final setup. The gain is an important parameter for the description of the saturation behaviour of a SiPM, and as consequence a necessity for the calibration of the detectors. When the system should be calibrated during data taking at a test beam this directly competes with the amount of "physics" data, which can be collected during a test-beam period. So the minimum number of events necessary to obtain a reliable calibration is an important quantity. The system providing the low intensity light has been discussed in section 5.3.1.
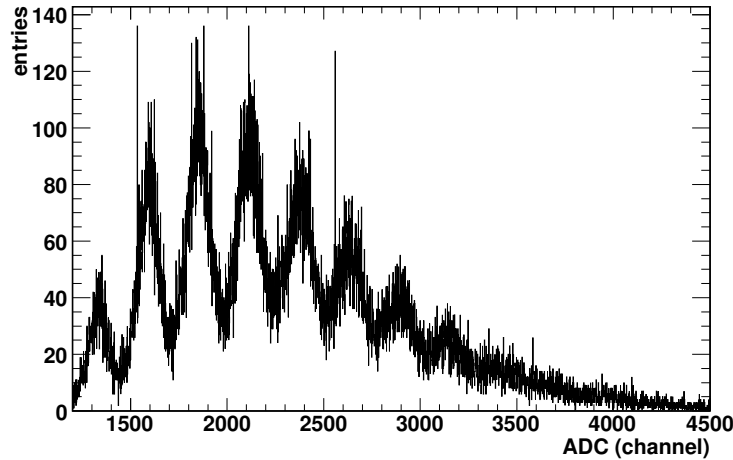
Figure 5.42: *Typical spectrum of a SiPM.*

Figure 5.42 shows a SiPM spectrum measured with the prototype electronics. As described in chapter 4, a SiPM gives a signal which corresponds to the number of fired pixels times the created charge per pixel. The charge created in a pixel will vary from avalanche to avalanche due to fluctuations in the multiplication process σ_{pix}. Additionally small differences between the pixels will distribute the gain for the different pixels around some mean value with σ_G. Assuming, that all these distributions are Gaussian and uncorrelated, the distribution of the output signal A is

$$\sigma_A = \sqrt{\sigma_{elec}^2 + N \cdot \sigma_{pix}^2 + N \cdot \sigma_G^2} \tag{5.20}$$

Measurements done by the producer show, that σ_{pix} and σ_G are small compared to the noise σ_{elec} of the prototype electronics and can normally be neglected for signals of a few pixels. However, σ_{pix} and σ_G limit the separation of single pixel peaks for large N. Nevertheless, clear single pixel spectra are observable and the signal-to-noise ratio is ≈ 4 [60]. The effect of the DNL is visible as isolated high spikes in the spectrum.

5.6.4   Hold studies

The ASIC at the VFE electronics needs from the DAQ a hold signal to know when the amplitude of the shaped signal should be sampled. This value depends on the readout mode in which the ASIC is operated, because the timing of the signal maximum changes. Several studies have been performed for calibration and physics mode to estimate the accuracy of this procedure.

For the gain calibration of the SiPMs, the DAQ initiates a LED pulse from the calibration and monitoring board. The trigger signal sent from the DAQ is called TCALIB. The delay between this TCALIB signal and the hold signal for the ASIC can be adjusted in steps of 6.25 ns, which corresponds to one clock cycle of the DAQ (160 MHz). The ASIC is operated in calibration mode. In [60] the influence of an improper timing of the hold compared to the real signal maximum is studied. The result is a difference between the worst and the best setting of 1.5 % of the signal.

In physics mode the step width of 6.25 ns has less influence since the shaped signal has a plateau of ∼10 ticks in which the amplitude changes only about 1 %. In figure 5.43 (a) the amplified and shaped signal for SiPM signals obtained from different modules with LED light in calibration mode are shown and in (b) in physics mode. In the modules SiPMs with slightly different properties are installed, which can be seen by the different signal shapes. Espeacially in figure 5.43 (b) a clear shift of the peak maximum is visible. In figure 5.44 the same graphs are shown for three SiPMs from the same module and three equally shaped signals are visible. This observation stresses the requirement to set individual hold values for each module. Several hold-scans for LED signals have been performed and they have shown maximum differences of the hold value of 1 tick, which is an excellent reproducibility. The hold values in physics mode for LED signal and for 23 modules have a mean value of (400 ± 18) ns and in calibration mode (211 ± 8) ns. During the CERN test beam hold values for 23 modules operated in physics mode and triggered by external beam trigger have been extracted. They have a mean value of (91 ± 11) ns. For this determination only a reduced number of 10 channels per module were used, which had collected high beam statistics. Due to the smaller statistic to determine the average hold value the spread for this measurement is 20% compared to 5% for LED trigger in physics mode. Although the loss of amplitude in case of a hold offset of 10 ticks is only 1 %, it is important to determine the correct mean for the complete module.

(a)   (b)
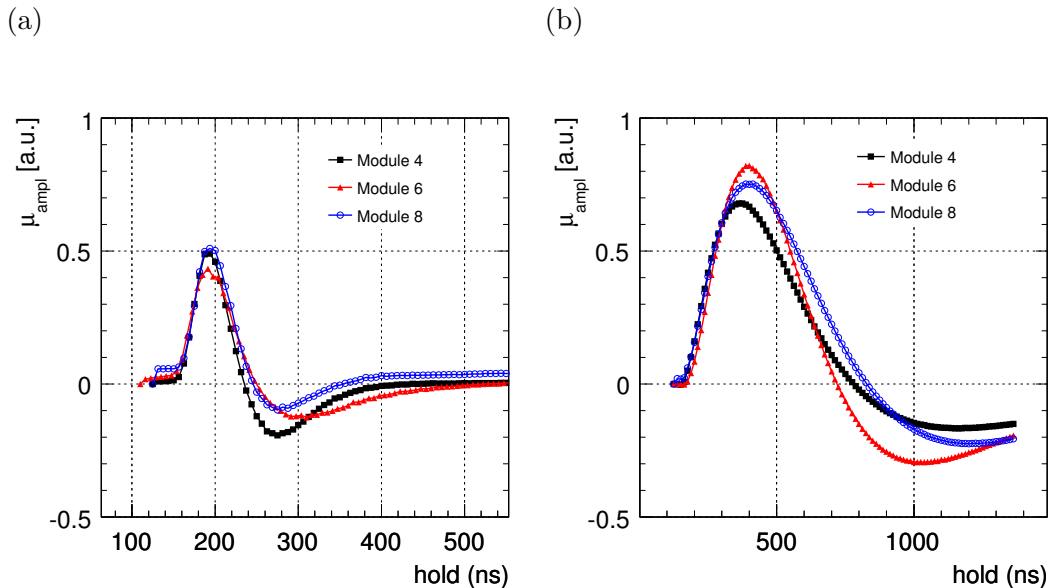
Figure 5.43: *Amplified and shaped SiPM signals from different modules in calibration mode (a) and in physics mode (b).*

5.6.5 Internal charge injection studies

The internal charge injection of the ASIC can be used to check the influence on the different hold value introduced already by the spread in the electronics. As already discussed in section 5.3.4 the signal of the internal charge injection has a different shape than the signal obtained from SiPMs. In figure 5.45 the two signals are compared in the two readout modes. The charge injection signal shows clearly a unipolar characteristics, as expected from a step

(a)   (b)
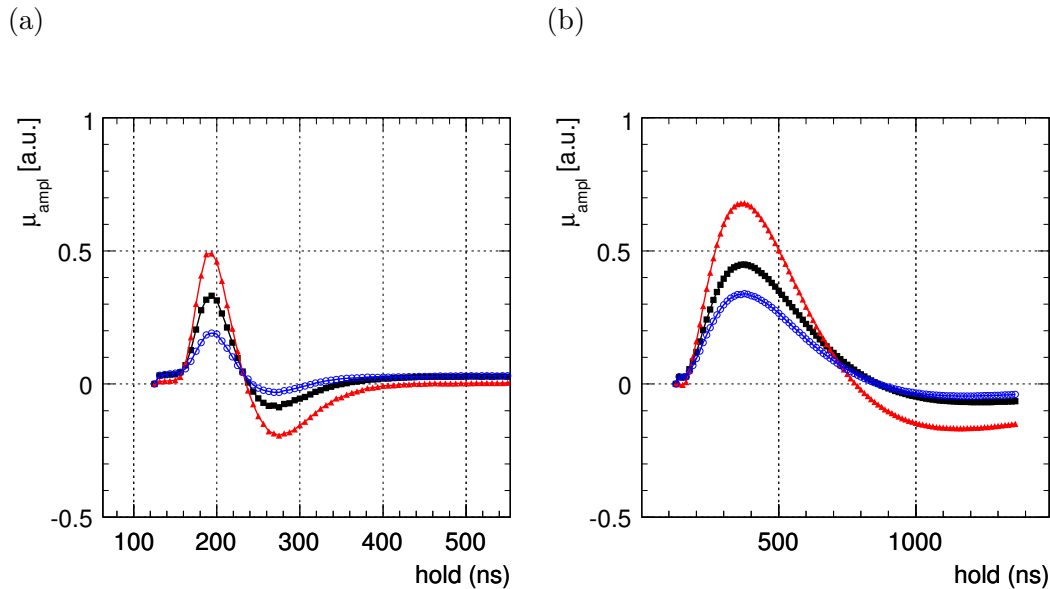
Figure 5.44: *Amplified and shaped SiPM signals from the same module in calibration mode (a) and in physics mode (b).*

function and the SiPM signal a bipolar signal as expected from a short charge pulse.

(a)   (b)
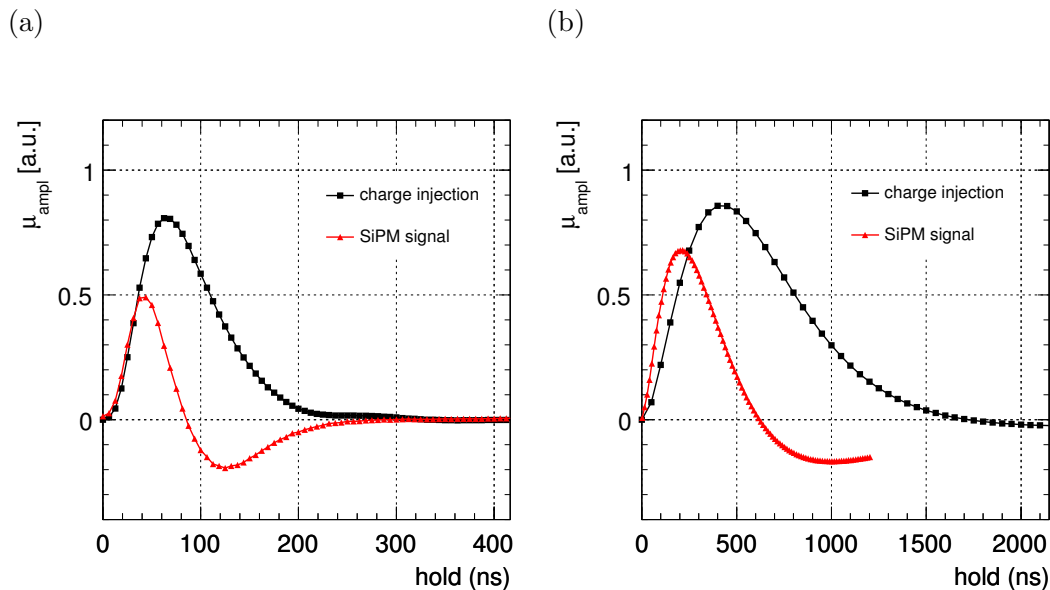
Figure 5.45: *Amplified and shaped signal for charge injection and SiPM signal in calibration mode (a) and in physics mode (b).*

In figure 5.46 and figure 5.47 the comparison plots obtained by the internal charge injection to figure 5.43 and figure 5.44 obtained by the SiPM signal are shown. No significant change in the maximum peak position is visible for the internal charge injection.

This result is summarised for all 216 channels in three modules in figure 5.48 for calibration

(a)   (b)
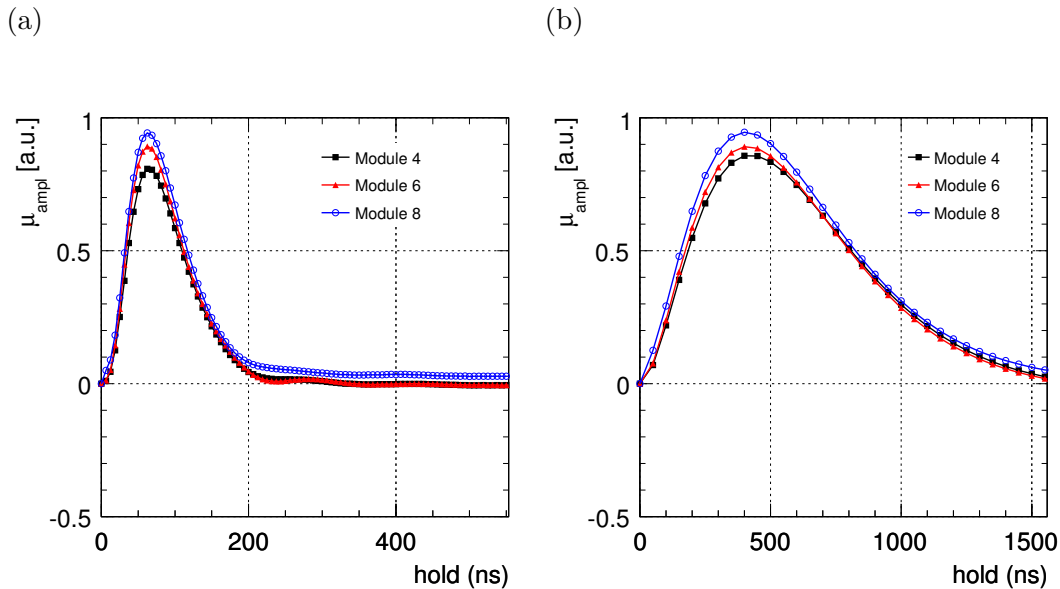
Figure 5.46:   *Amplified and shaped signal for different ASIC channels with charge injection in calibration mode (a) and in physics mode (b).*

(a)   (b)
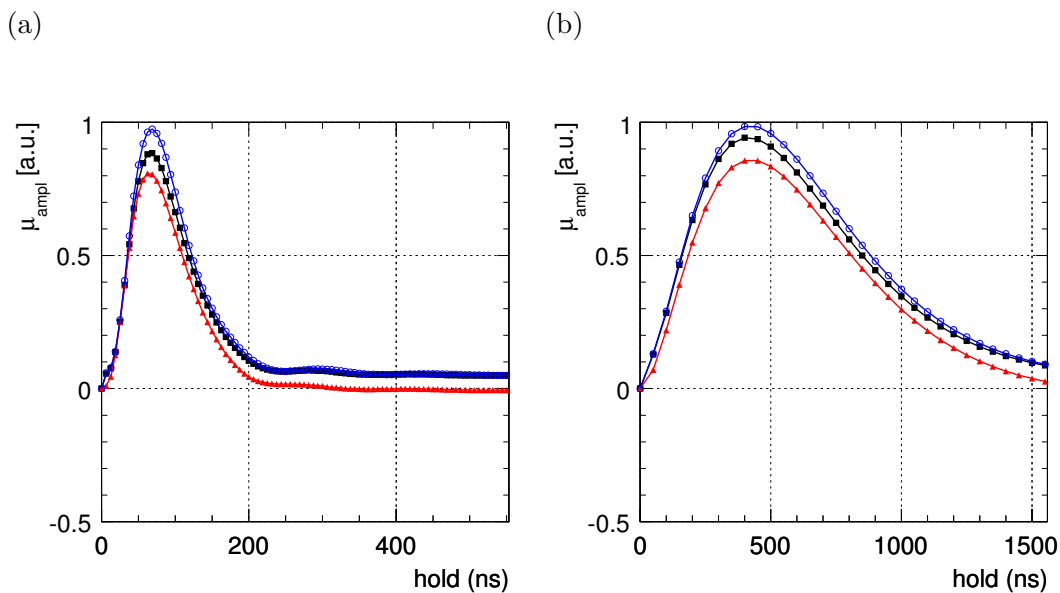
Figure 5.47:   *Amplified and shaped signal for different ASIC channels with charge injection in calibration mode (a) and in physics mode (b).*

mode and in figure 5.49 for physics mode. In figure 5.48 (a) and figure 5.49 (a) the hold distributions for the charge injection is shown for which in both readout modes the mean hold value is for all three modules the same. In figure 5.48 (b) and figure 5.49 (b) are clear dependence of the average hold value on the module or SiPM type is visible. Especially in figure 5.49 (b) or in physics mode a double peak structure for module 6 is visible, which is due to two different kind of SiPMs inside of this module. However, the RMS of $\sim$2.5 ticks

shows that 95 % of the channels are in the 10 ticks long plateau of the shaped signal and will loose only approximately 1 % of the amplitude in case the set hold value for the module corresponds to the real mean value for this module.
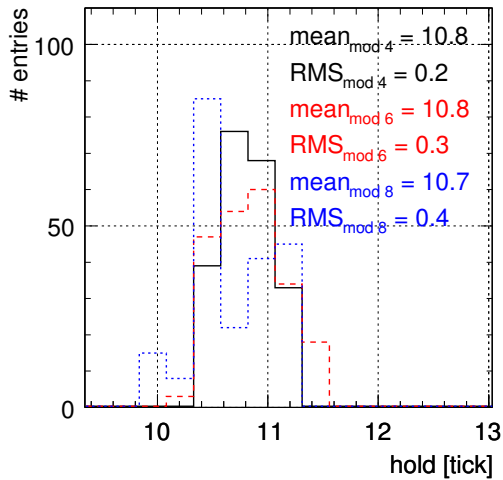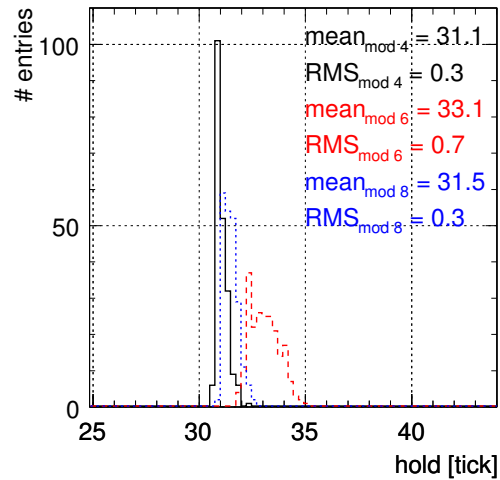
Figure 5.48: *Hold value distribution for charge injection (a) and SiPM signal (b) in calibration mode. The histograms are distributions for module 4 (black solid), module 6 (red dotted) and module 8 (blue dashed).*
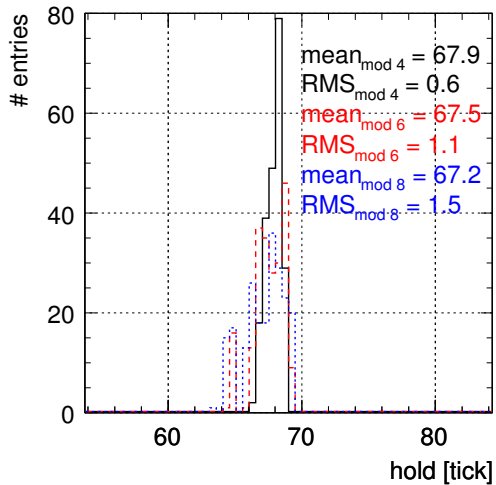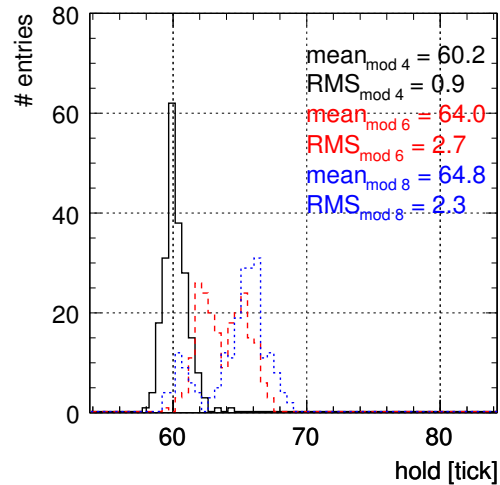
Figure 5.49: *Hold value distribution for charge injection (a) and SiPM signal (b) in physics mode. The histograms are distributions for module 4 (black solid), module 6 (red dotted) and module 8 (blue dashed).*

5.6.6 Signal stability

The study of the variation of hold value in time is a check of the stability of the ASIC chip. Hold-scans with charge injection have been performed at the startup and at the end of a long term data taking of ∼20 days. Figure 5.50 shows the hold value difference obtained from these two measurement in calibration (a) and in physics (b) mode. The changes are in the order of 1 ns, which is much less than the accuracy the hold value can be set and is therefore negligible.

(a)   (b)
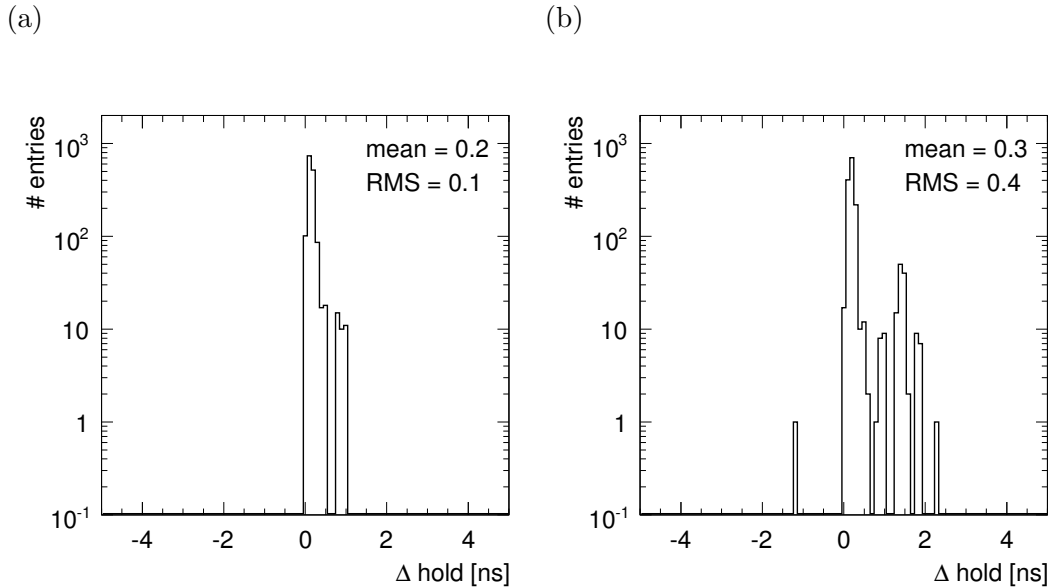
Figure 5.50: *Distribution of the hold value difference occurring after 20 days of operation extracted with charge injection for ASIC operated in calibration mode (a) and physics mode (b).*

The same kind of comparison has been done for a VCALIB-scan with internal charge injection. In a VCALIB-scan the amplitude of the injected pulse is increased and the change of amplitude is recorded. The injected charge is increased for both readout modes in 10 steps and cover the complete dynamic range. In figure 5.51 the response to a several VCALIB values for charge injection in calibration (a) and in physics (b) mode is shown. For comparison the same kind of measurements is shown in case the VCALIB value is not used for internal charge injection but to flash the LEDs on the CMB. The charge injection response is nicely linear until the ADC saturation of 32768 channels is reached. The different gains are visible. In calibration mode ADC saturation is already achieved with a VCALIB value of ∼3500 whereas in physics mode a value ∼7000 is needed. The shapes of the SiPM response are totally different. In calibration mode the response in the beginning is not linear due to a non-linear response of the LED to the VCALIB value and it reaches the ADC saturation much faster due to a higher gain. In physics mode the same effect at the beginning is visible, afterwards the response is parallel to the charge injection curve before the SiPM comes into saturation.

In case of internal charge injection the slopes of the linear responses in both modes have been fit and compared for the startup and end of the same data taking period used for the hold value stability analysis. For 1512 channels or for the VFE electronic of 7 modules this comparison has been performed and is shown in figure 5.52. No significant changes can be observed.

(a)   (b)
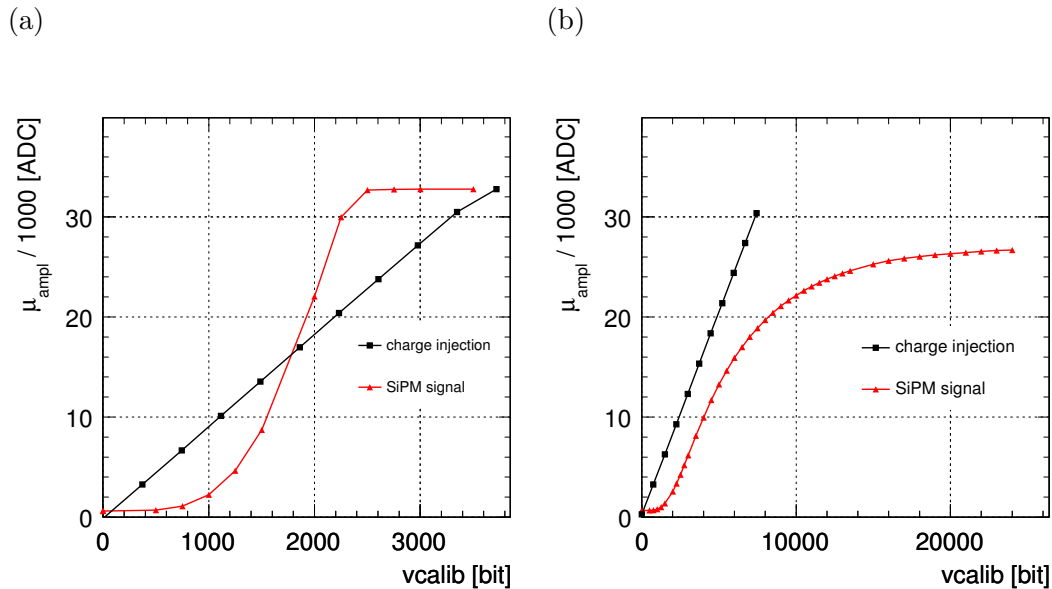
Figure 5.51:   *VCALIB-scan comparison between charge injection (black) and SiPM signal (red) in calibration mode (a) and in physics mode (b).*

(a)   (b)
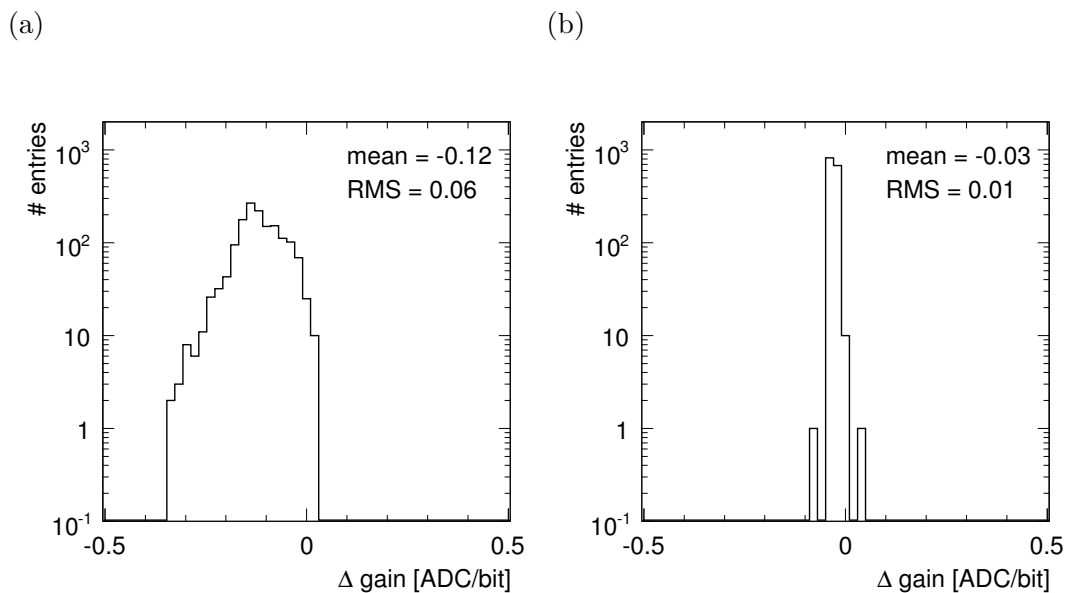
Figure 5.52:   *Distribution of gain difference in ADC/bit after 20 days of operation with charge injection in calibration mode (a) and in physics mode (b).*

5.7   Conclusion

The structure of the AHCAL has been presented together with the steps needed for the mass production of its components and the tests required during the production phase. The custom made electronics developed for the multi-channel readout of this large prototype has been introduced. The characterisation of one complete readout channel has been carried out

for both the electronics itself and the electronics combined to a SiPM detector. The result in term of noise of the combined system are satisfactory. The self-calibrating property of the SiPM can be exploited by a signal-to-noise separation of the single pixels of about 4. The VFE electronics design for test beam experiments allows the detection of a minimum physics signal equivalent to a mip with a signal-to-noise of 11. The test has been extended to a multi-channel system exploiting the VME-based DAQ. The complete readout system has been commissioned with a series of studies aimed to test all the relevant properties before the exposure of the calorimeter to test beam. Coherent electronic noise between channels has been identified and removed.

Chapter 6

Results from the DESY test beam

The first completed AHCAL scintillator layer (module 1) was tested at DESY with 2-6 GeV positrons. These first data allow to check the functionality of the SiPM-tile system, the readout and calibration electronics, and to test the performance of the entire system. The performed measurements start with the calibration of the AHCAL module. This includes the calibration to the mip response and the SiPM gain determination. The light yield of each channel can be obtained by dividing these two quantities. Afterwards detailed noise and stability studies are performed. The SiPM non-linearity correction and the tile-to-tile light crosstalk correction are tested with collected electromagnetic shower data, which were compared to the Monte Carlo prediction to judge the functionality of the calibration and correction chain in total.

6.1   Experimental setup at the DESY test beam

The data have been collected at the beam-line T21, which is one of the three test-beam lines providing electrons and positrons at DESY. A Bremsstrahlung beam is generated by a carbon fibre put in the circulating beam of the electron/positron synchrotron DORIS II. The photons are converted to electron-positron pairs with a metal wire. The Bremsstrahlung energy spectrum has a 1/E dependence and the distribution of the pair conversion is nearly flat. Then the beam polarity is selected and particles of various momenta are separated and selected by setting the magnet current of a horizontal dipole magnet. The momentum of the electrons reaching the experimental area can be selected between 1 and 6 GeV/c. The final beam is cut with a collimator. A schematic layout of a test-beam line is shown in figure 6.1.

6.2   AHCAL Calibration procedure

One of the main goals of this test-beam effort at DESY was to get first experience with the calibration chain. Therefore, several measurements with beam and with LED were needed to get the response to a mip and the SiPM gain. Combining all calibration constants gives the light yield which is a comparable value to earlier measurements of the SiPM tile system.

6.2.1   Calibration procedure

To calibrate a calorimeter cell with linear readout it is sufficient to normalise the signal amplitude recorded in ADC channels to the energy deposited by a known physics process, i.e. the passage of a mip through the cell. A simulation of the mip event can then be used to
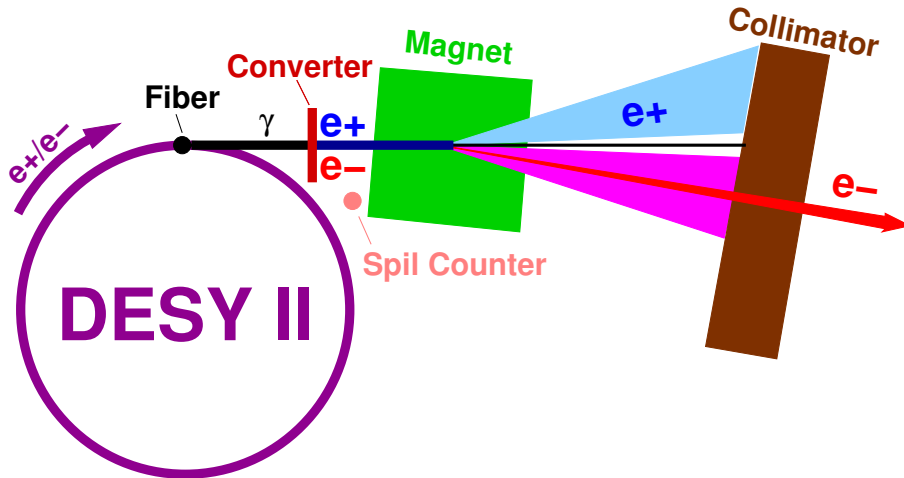
Figure 6.1: *Schematic layout of a test-beam line at DESY [78].*

infer the energy in electron-volts.

Due to the limited dynamic range of SiPM, this simple procedure, expressed by equation 6.1

$$E[GeV] = \frac{A[ADC]}{A_{mip}[ADC/MIP]} \cdot E_{mip}^{MC}[GeV/MIP], \tag{6.1}$$

has to be extended to the following more complex equation 6.2.

$$E = \frac{f_{resp}\left(\frac{A[ADC]}{A_{MIP}[ADC/MIP]} \times LY[pix/MIP]\right)}{f_{resp}(LY[pix/MIP])} \times E_{mip}^{MC}[GeV/ADC], \tag{6.2}$$

This procedure involves the SiPM response function and the light yield as a conversion factor to pixels from calibrated mip amplitudes. The design value of the light yield (LY) of a calorimeter tile, i.e. the amplitude of a mip signal expressed in number of pixels, is 15 pix/mip with a spread over all tiles of about 20 % RMS. This variation is too large to assume the LY value equal for all tiles. Therefore, the slope of the saturation curve has to be calibrated for each tile individually. Please note that the numerator is in units of photo-electrons after applying the response function and therefore the light yield in the denominator has to be converted from pixels per mip into photo-electrons per mip as well. Finally, the energy expressed in corrected number of mips has to be multiplied by E_{mip}^{MC} which is the mean energy in units of GeV that a mip is expected to deposit in the scintillating tile.
In the following all needed factors for equation 6.2 are described. The signal of each tile is stored in ADC channels. In order to determine the SiPM gain, the ASICs are operated in calibration mode, while for energy measurements of beam particles the ASICs are operated in physics mode. The measured amplitude in units of ADC channels is:

$$A[ADC] = A_{obs} - A_{ped}, \tag{6.3}$$

where A_{obs} is the recorded position of the signal and A_{ped} is the position of the pedestal. The gain in units of ADC channels G [ADC/pix] is obtained from the average peak distances A_{pix} visible in low amplitude light spectra taken in calibration mode. Figure 6.2 (a) shows a typical SiPM gain calibration spectrum.
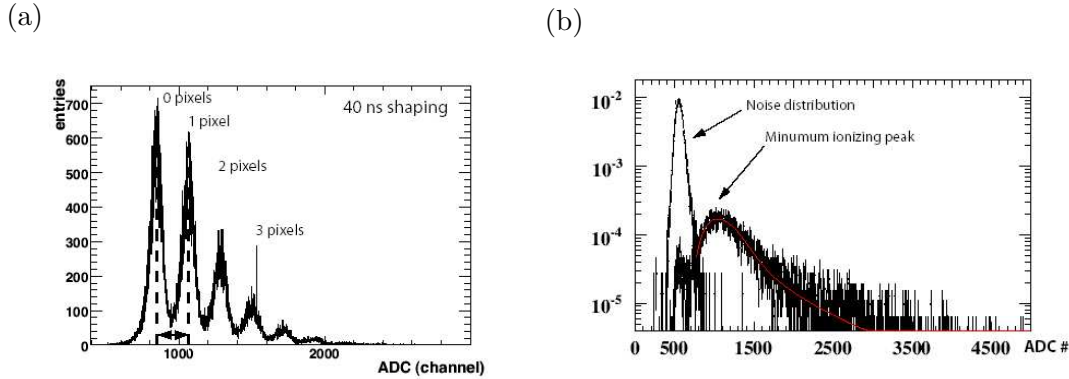
Figure 6.2: *(a) SiPM spectrum of a scintillator tile in calibration mode. (b) Energy spectrum of a scintillator tile read out by a SiPM for 3 GeV positrons showing a mip peak.*

Applying the SiPM response function $f_{resp}(N_{pix})$ the number of photo-electrons can be determined from the observed number of pixels.

$$N_{pe} = f_{resp}(N_{pix}). \tag{6.4}$$

In physics mode each channel can be calibrated for the mip response in units of ADC channels. The ASICs are operated at low gains with a long shaping time of 180 ns to delay the SiPM signals to wait for the trigger generated hold signal. The mip peak is produced by 3 GeV positrons passing the scintillator inside the module without showering since no absorber material is placed in front. An example spectrum is shown in figure 6.2 (b). The signal-to-noise ratio for this particular channel is about 9. The mip peak is defined as the most probable value (MPV) of the distribution and is called $A_{mip}[ADC/MIP]$. In order to extract the light yield the correlation between calibration mode and physics mode is needed. To determine this factor the monitoring LED light amplitude is recorded in both ASIC modes. An electronic inter-calibration factor is determined by the following relation

$$I_{phys}^{calib} = \frac{A_{LED}^{calib}}{A_{LED}^{phys}}. \tag{6.5}$$

The light yield of the mip peak in units of pixels is obtained by

$$LY[pix/MIP] = \frac{A_{MIP}[ADC/MIP]}{G[ADC/pix]} \times I_{phys}^{calib} \tag{6.6}$$

The light yield in units of photo-electrons is obtained by conversion of the light yield in number of pixels with the SiPM response function.

6.2.2 Calibration of Module 1

Module 1 was built with SiPMs with the production numbers 35-502. They have a 2 MΩ quenching resistor and are operated with bias voltages of 63-67 V. Around 60 SIPMs have shown long discharge behaviour with different frequency, out of which 30 SiPMs show long discharge (see chapter 5) with low frequency. The light coupling for the LED monitoring system, been a prototype, has no reflector caps to direct the LED light from the fibre end to the tile. The fibre ends are only bent to the tile surface, which leads to a higher light spread from channel to channel. All studies have been performed without the final temperature

failure	amount of channels
dead SiPM	5
no mip response	19
no gain determination	11
no inter-calibration	16

Table 6.1: *Summary of the amount of the non-calibrated channels and causes.*

[pix/mip]	3×3	6×6	12×12
$LY_{tiletest}$	14.7	15.4	12.8
LY_{beam}	12.8	13.4	9.3
Δ LY	1.9	2.1	3.4

Table 6.2: *Average light yield in pixel per mip for the different tile sizes in module 1.*

measurement and also without the final LED monitoring system. A single LED, pulsed by a conventional pulser was used with no PIN photo-diode readout. In total it was not possible to determine the light yield for 25 out of 216 channels due to various reasons. The reason of the failure of the light yield calibration can be: dead SiPM, failure of mip, gain or inter-calibration. The latter can be overcome using the chip inter-calibration mean value, while for the other factors mean values introduce large uncertainties due to the large variation of SiPM properties. In table 6.1 the number of SiPMs which were not calibrated and the causes are summarised.
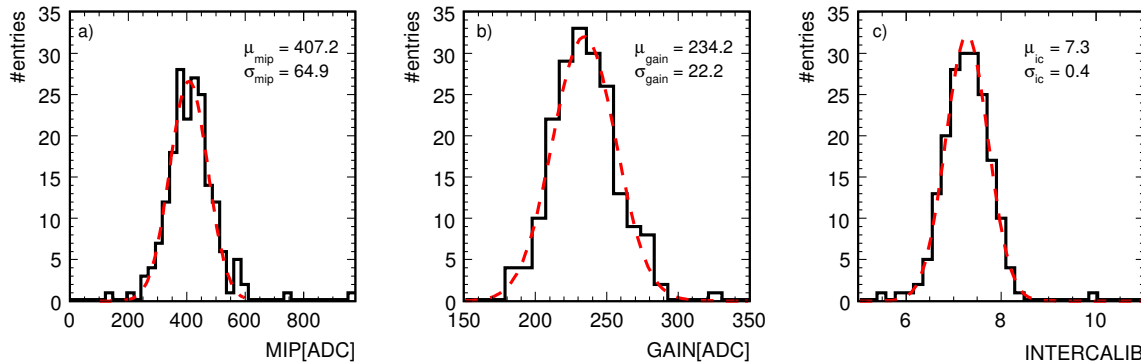
Figure 6.3: *Distributions of (a) mip value, (b) SiPM gain and (c) electronic inter-calibration for module 1.*

In figure 6.3 the distributions of the three calibration constants determined for module 1 at the DESY test beam are shown. In plot (a) the mip value for 191 calibrated channels is shown. The mean value extracted with a Gaussian fit is 407 channels with a spread of 16 %. Plot (b) shows the gain for the same channels. The gain has been extracted with a multi-Gaussian fit. The extracted mean value is 234 channels with a spread of 9 %. Plot (c) shows the extracted inter-calibration factor with a mean value of 7.3 and a spread of 6 %. For module 1 at the DESY test-beam setup an average light yield of 13 pixels per mip was measured with a spread of ± 2 pixels. This is 2 pixel lower than the results
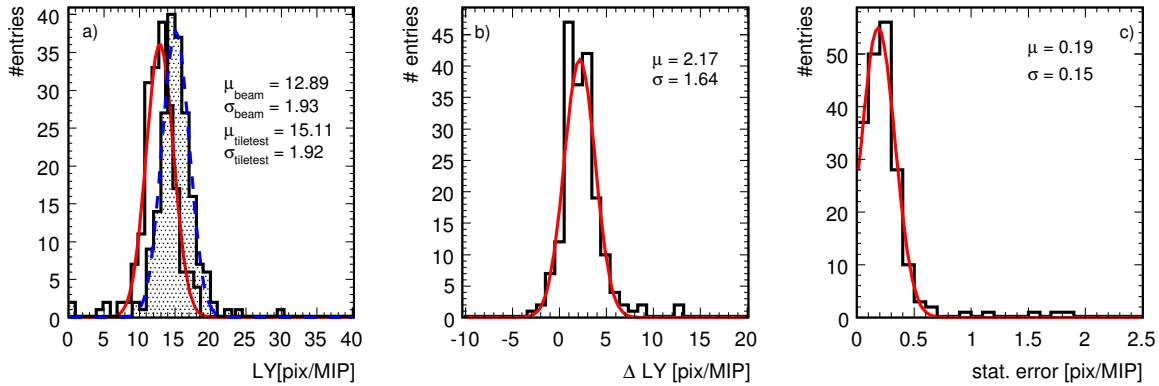
Figure 6.4: *(a) LY distribution for module 1 from the tile test and beam measurements, (b) LY difference between the two distributions in (a), (c) statistical error on LY beam measurement for module 1.*

obtained in Moscow and in the DESY tile tester setup (see section 5.2.3). This difference is shown in figure 6.4 (a) and (b). In figure 6.4 (b) the spread of the distribution can be used to obtain a systematic uncertainty on the light yield determination. Assuming the same systematics from both measurements, test beam and tile tester, the systematic uncertainty is $1.64/\sqrt{2} = 1.2$ pixel or 8 %. This uncertainty includes the systematics of the gain and mip determination, the SiPM temperature and voltage dependence and the precision of the DAC voltage adjustment factors. In figure 6.4 (c) the statistical uncertainty is shown, which is in average 0.2 pixel. In table 6.2 the light yield value for each sample of the three different tile sizes are shown. The difference in light yield of 2 pixels can be explained by the following considerations. Althought the high voltage was corrected for voltage drops over the cable, no correction have been applied for the additional voltage drop on the electronic readout board (see section 5.5.1). This can lead to a signal loss of 7 %. The remaining difference is consistent with a possible operation at 2° Celsius higher temperature than in the tile tester laboratory.

6.3 Aspects of calibration and corrections

In this section several problems and fluctuations which have been observed during the calibration of module 1 are discussed. The range of the observed fluctuations give an uncertainty estimation for the calibration and forthcoming measurements.

6.3.1 Pedestal position

Two aspects are playing a role in the determination of the ground level of an electronic measurement: the value of the ground level and its stability in time. In other words it is important to know where the pedestal is and why and how often it fluctuates. The main reason for changes of the pedestal position are temperature changes.

Due to the SiPM dark-rate (see section 4.2) the pedestal shape is not a Gaussian distribution. In figure 6.5 (a) a typical pedestal distribution is shown. In addition, a Gaussian distribution is drawn to illustrate the difference between the two distributions. It is visible that the pedestal

is asymmetric and has a tail to higher amplitudes. The significance of this effect varies with the SiPM type. This behaviour is shown in figure 6.5 (b) where the difference between the mean value and the peak value for the pedestal of each channel for two different modules are shown. For module 1 the difference is around 4 channels and for module 4 around 6 channels. This means that the SiPMs used in module 4 have a higher dark-rate value than the SiPMs used in module 1. The definition for the ground level of a SiPM device is the mean value of the pedestal histogram and is used in this analysis.

(a)   (b)
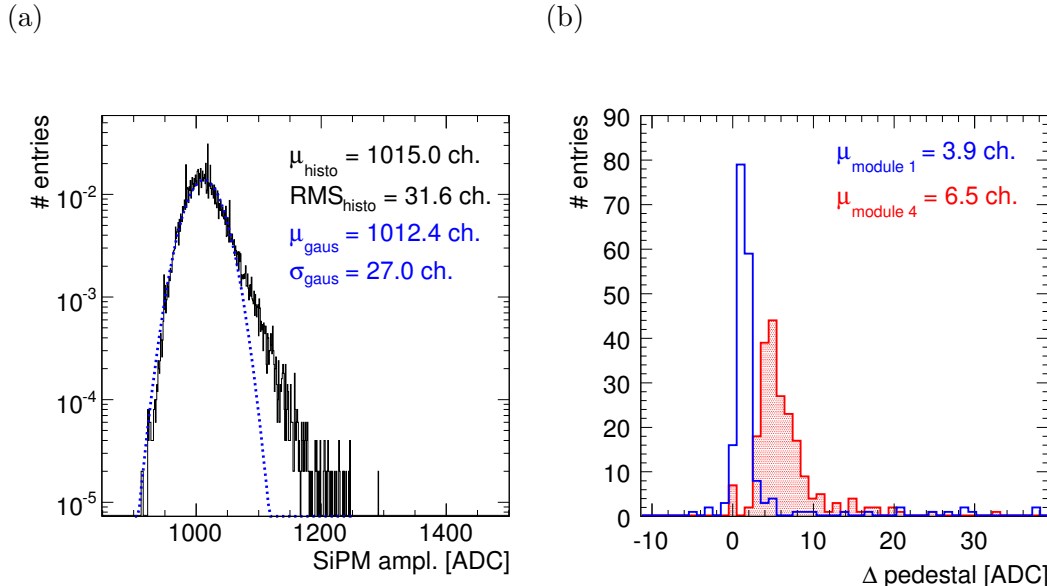
Figure 6.5:   (a) Typical SiPM pedestal distribution. (b) Distributions of Δ pedestal = mean - MPV for two sets of 216 SiPMs belonging to two AHCAL modules.

Another effect which leads to changes in the pedestal distribution is long discharge, which has been described in section 5.2.4. This effect leads to a shift of the mean value of the pedestal distribution to higher value and is therefore responsible for the high entries in figure 6.5 (b).

6.3.2   Pedestal stability and temperature fluctuations

In figure 6.6 (a) the pedestal stability for module 1 during one week of operation is shown. The average pedestal shift is only 0.2 channels, which is negligible compared to the amplitude of the physics signals. The maximum shift is 13 channels. The spread of the distribution is 5 channels and since no pedestal correction is applied this value is taken as systematic uncertainty. The average mip signal is around 400 channels and therefore the observed pedestal uncertainty is 1.3 %.
In figure 6.6 (b) the SiPM amplitude fluctuations during 12 hours of operation is shown. This measurement has been performed with the constant LED light signal distributed to 18 SiPMs. The development versus time of these channels is shown. The LED light by itself was not monitored. Large amplitude fluctuations of around 25 % are observed. Although no detailed and automatic temperature measurement was available the temperature was analogue monitored. For the period of interest a temperature range of $20°$ to $22°$ Celsius has been registered. Assuming that one degree covers 3 σ of this variation and that the SiPM amplitude temperature dependence is $-4.5\%/1°C$, a 1.5 % amplitude uncertainty due to non-corrected

Figure 6.6: *(a) Pedestal fluctuation for module 1 in one week of operation; (b) SiPM amplitude fluctuation during 12 hours observed with a constant LED light signal.*

temperature changes has to be taken into account. The spread of the LED amplitude measurement gives around 8%. Due to the missing PIN monitoring system it is not possible to distinguish bet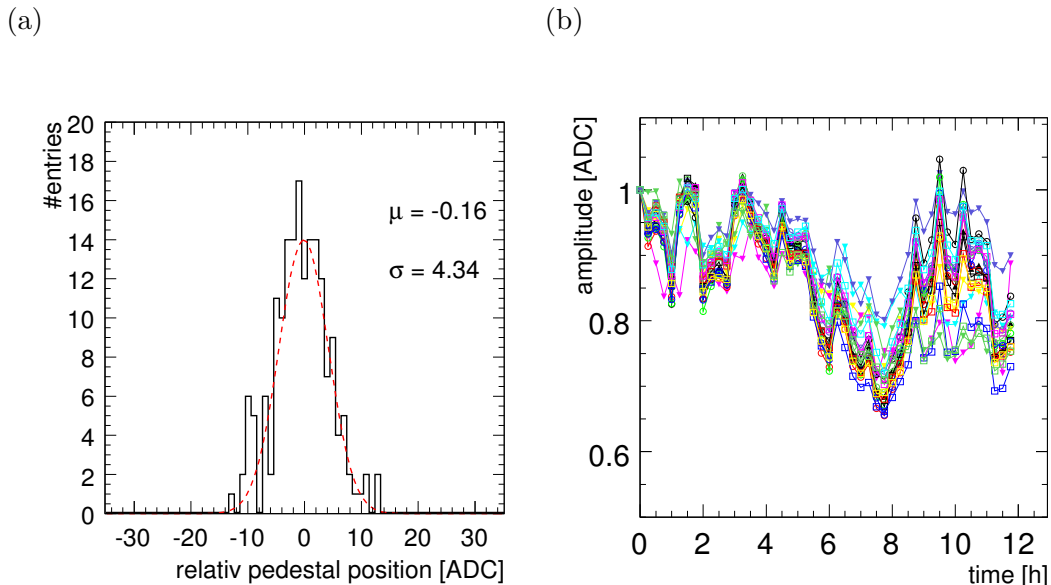ween SiPM response and LED light output changes. In addition to the two described sources of systematic uncertainties, pedestal shift and temperature fluctuations, the third source is the systematic error of the mip and gain fit which is in the order of 1 % for each fit. The quadratic sum gives a systematic error of ≈2.5 %. From the indication on the light yield uncertainty determined in figure 6.4 (b) it is clear that this does not cover all sources of uncertainty. Therefore, an assumption of 5 % is considered as a more conservative systematic uncertainty. This value leads for a average light yield of 15 pixels to a systematic error of 0.7 pixels.

After all channels are calibrated in mips it is possible to extract the signal-to-noise ratio for this kind of measurement. In figure 6.7 the pedestal spread in mips for all channels is shown. This value is inversely proportional to the signal-to-noise ratio. After cutting the long discharge channels the average signal-to-noise ratio is 8.8 ± 2.1. Also this value is ∼20% below the expectations, which supports the suspicion of the too low applied SiPM bias voltage.

6.3.3 Noise and long-discharge handling

The designed noise threshold to minimise the noise contribution in physics events is half of a mip. The noise contribution of a normal behaving tile-SiPM system will be cut away completely by applying this threshold cut. This is not true for SiPMs which have developed long-discharge behaviour, since this leads to amplitudes in the order of several mips. In figure 6.7 (a) the pedestal spectrum of a long-discharge channel is shown as illustration. These events give a constant background under the physics events and can not be removed. As already mentioned this effect occurs with different frequencies. Half of the channels in module 1 have low frequencies. Low frequency means that it occurs only for less than 1 % of the total events, whereas high frequency means from 1% up to 10 %. This behaviour is of course
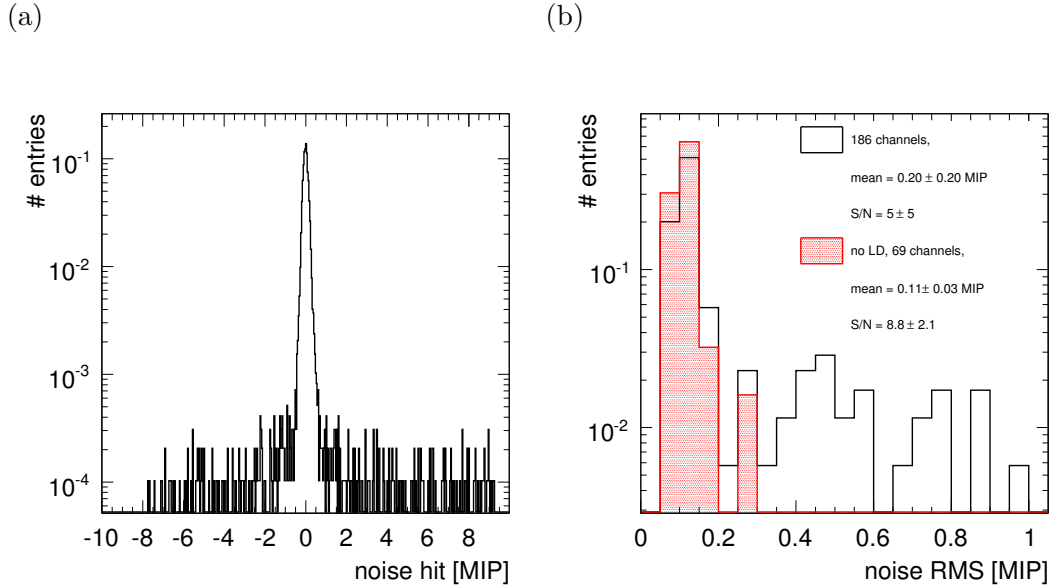
(a)   (b)

Figure 6.7: *(a) Long discharge channel example; (b) Noise RMS distribution and signal-to-noise ratio for module* 1.

disturbing any cluster algorithm or detailed shower analysis since it introduce fake hits in the calorimeter. However, in this analysis the additional noise contribution is a second order effect due to the fact that only mean values are compared and the frequency of long-discharge events in comparison to shower events is small.

One of the important parameters for the test-beam prototype is the number of noise hits over half of mip threshold, because this effect influences the sensitivity to find isolated neutral hits in a shower. In figure 6.8 the number of noise hits for two different run-types: mip calibration and electromagnetic shower is shown. A selection is applied to the data to remove the cells where physics events (μ or electromagnetic shower) are detected. The remaining cell amplitudes are filled in the noise histograms respectively of figure 6.8 (a) and (b). It is visible that the long-discharge channels are worsening this quantity tremendously. Only after cutting these channels away a reasonable noise hit distribution becomes visible. In both run-types the ratio of noise hits above the noise cut including long-discharge channels is 0.8 % and without long-discharge channels only 0.2 %. These ratios can be used to extrapolate to the noise occupancy of the full detector, consisting of 7608 channels, assuming that all channels behave like this. This results in 15 noise hits above the threshold for the complete calorimeter, which would be 0.4 hits per layer. The requested value to perform detailed cluster algorithm studies and to measure for example the neutron shower contribution is 1 noise hit per event and for the full detector. Assuming that the SiPM bias voltage was too low, this situation should improve when running with corrected HV settings. The difference in the distributions between the two runtypes are probably related to the fact that the shower distributes low energetic hits also to channels, which have been treated as noise candidates.

6.3.4   Non-linearity correction

As discussed before the SiPM is a highly non-linear device and therefore non-linearity corrections have to be applied. For this analysis three different methods have been used and

(a)   (b)
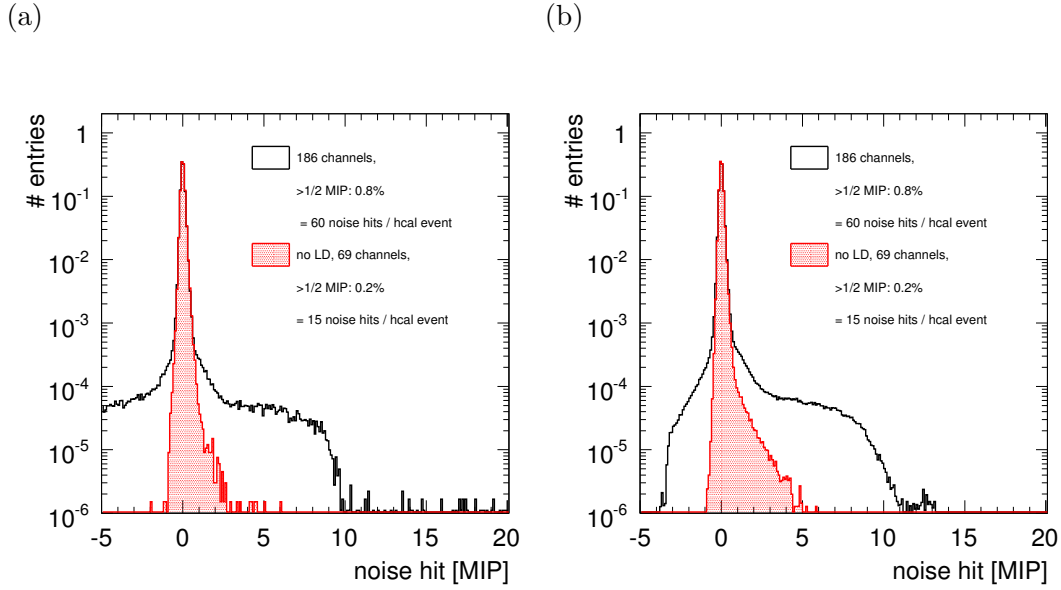
Figure 6.8: *(a) Noise hit energy distribution for a mip run. (b) Noise hit energy distribution for a electron / shower run.*

compared.

- standard photomultiplier non-linearity correction (*PMT par*)

$$f_{PMTpar} : A_{ph.e}(A_{pixel}) = \frac{A_{pixel}}{1 - \frac{A_{pixel}}{N_0}}, \tag{6.7}$$

  with effective number of fired pixels $N_0 \sim 1500$.

- simple analytic formula of tile-SiPM response (without SiPM crosstalk) (*LAB par*)

$$f_{LABpar} : A_{ph.e}(A_{pixel}) = -N_0 \cdot ln\left(1 - \frac{A_{pixel} - 0.98}{N_0}\right), \tag{6.8}$$

  with effective number of fired pixels $N_0 = 1156$. The constant offset of -0.98 has been extracted from laboratory measurements and is due to the SiPM dark-rate, which leads to a non-zero pedestal.

- complete analytic formula of tile-SiPM response (with SiPM crosstalk) (*HO par*) [97]

$$f_{HOpar} : A_{ph.e}(x_{talk}, A_{pixel}) = N_0 \cdot ln\left(\frac{2 \cdot x_{talk}}{x_{talk} - 1 + \sqrt{x_{talk}^2 + 2 \cdot x_{talk} \cdot (1 - 2 \cdot \frac{A_{pixel}}{N_0}) + 1}}\right), \tag{6.9}$$

  with effective number of fired pixels $N_0 = 1156$.
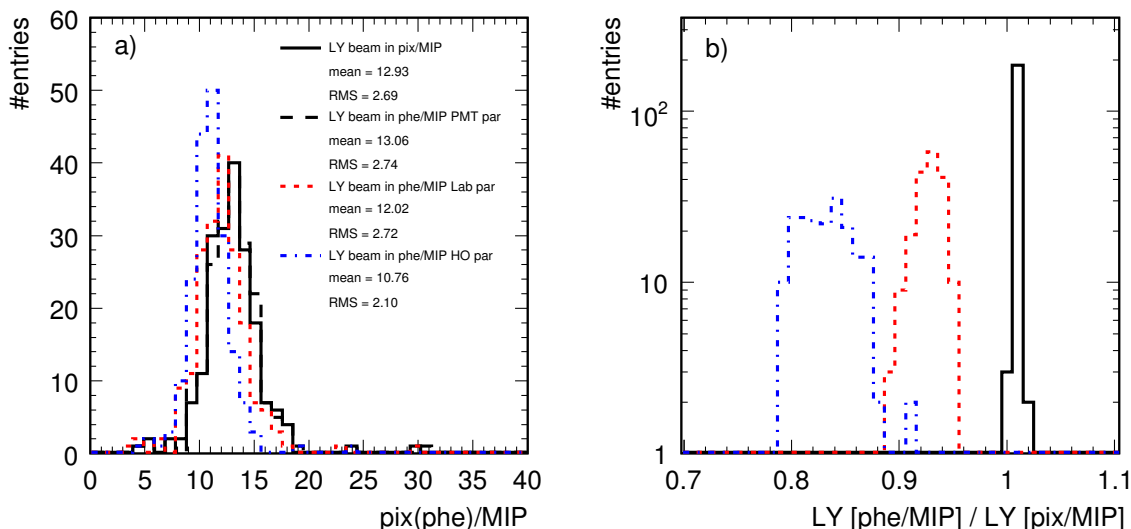
Figure 6.9: *Influence of SiPM correction on the light yield (LY). (a) Light yield distributions before and after applying different SiPM non-linearity corrections: PMT, LAB and HO. (b) Ratio between the light yield values extracted after applying the corrections to the uncorrected distribution.*

The second and third method are based on the response function measured in a laboratory setup. The first one is a model function inspired by the linearisation often applied to PMT (PMT par). This function is close to the LAB parameterisation without cross-talk when the logarithm is approximated by its sum.

In figure 6.9 (a) and (b) the effect of the three different non-linearity corrections on the light yield measurement is shown. In (a) the distribution for the uncorrected light yield in pixel per mip is drawn by the full black line. The light yield distribution after applying the PMT correction is drawn by the black dashed line. The light yield distribution after applying the LAB correction is drawn by the red dashed line and the result of the HO correction is shown by the blue dash-dotted line. The same colour code is valid for plot (b). The mean value of the light yield distribution extracted with the LAB correction is ∼8 % lower than the light yield extracted with the PMT correction due to the darkrate constant. The mean value of the light yield distribution belonging to the HO parameterisation shows a 20 % lower value than the distributions belonging to the PMT correction. At low amplitudes like the mip the non-linearity corrections have only an influence due to the SiPM crosstalk or dark-rate. To compare the light yield of a tile-fibre system the effect of SiPM crosstalk and dark-rate have to be corrected.

Another important issue is how the correction functions behave over the complete signal range. This dependency is shown in figure 6.10. In plot (a) the three different parameterisations and their dependence on the incoming light are shown. In (b) the in-versed functions of the three parameterisations are shown, which are used for the discussed SiPM non-linearity corrections. It is visible that the PMT parameterisation shows a different behaviour at middle and high amplitudes. The HO parameterisation is slightly shifted to higher pixel values with respect to the LAB parameterisation due to the crosstalk component. In the range of the discussed data in this chapter, which is below 40 mips or 600 pixels, all parameterisations lead
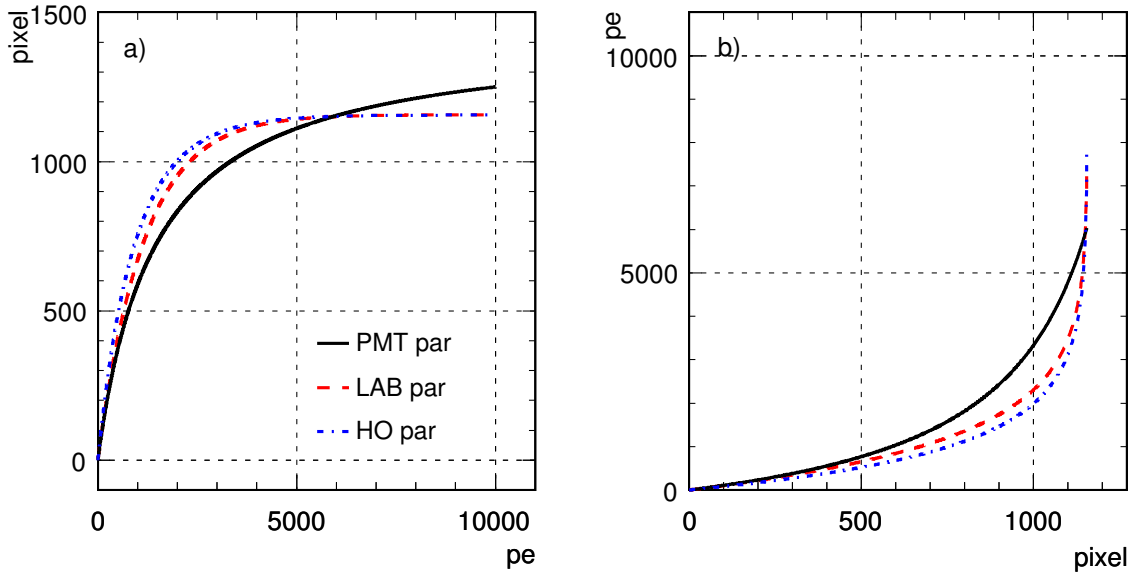
Figure 6.10: *Different SiPM response parameterisations (a) and derived corrections (b).*

to comparable results within the measurement accuracy.

6.3.5   Light crosstalk correction

The probability of scintillator photons passing the border from one tile to the neighbour tile is 2.5 %. This has been measured for a small amount of tiles at ITEP. In figure 6.11 (a) the measurement procedure is shown. A β-source generates the signal and the detector consists of a system of two tiles where one is read out with a WLS fibre and a photomultiplier tube. This tile system is shifted under the source and several measurements of the signal amplitude are recorded. The tails on both sides to the neighbouring tile is due to the not perfectly collimated source. The interesting part for the quantification of optical crosstalk is the plateau on both sides of the neighbouring tiles which is of the order of 2.5 %. This measurement has been repeated for 9 tiles and each time for all four tile edges. The result is shown in figure 6.11 (b). The light crosstalk values varies between 2% and 3.7%. The last four points in the plot are the measurements with a reference preproduction tile, which had much less light crosstalk, below 1%.

The measurement of optical crosstalk between tiles can be repeated in an AHCAL module utilising the LED system to inject light in one tile and observe the signal amplitude of neighbouring tiles. This measurement needs the complete calibration and non-linearity correction chain and relatively high light amplitudes injected to the tiles. To have in a neighbouring tile a signal above the half of a mip noise threshold a signal of $\sim$20 mips is needed. Only a very preliminary measurement has been performed at the time of this thesis, which suffers from low statistics of tested tiles. Nevertheless this check indicates a value of 2$\pm$0.7 % for the optical crosstalk to neighbouring tiles, though confirming a non-negligible effect. More precise measurements can be performed with dedicated LED studies.

(a)

(b)

Figure 6.11:   *(a) Scheme for light crosstalk measurement. (b) Measured light crosstalk for ten tiles (one measurement per tile edge). The last four points are from a very good tile with crosstalk lower than 1 % [98].*
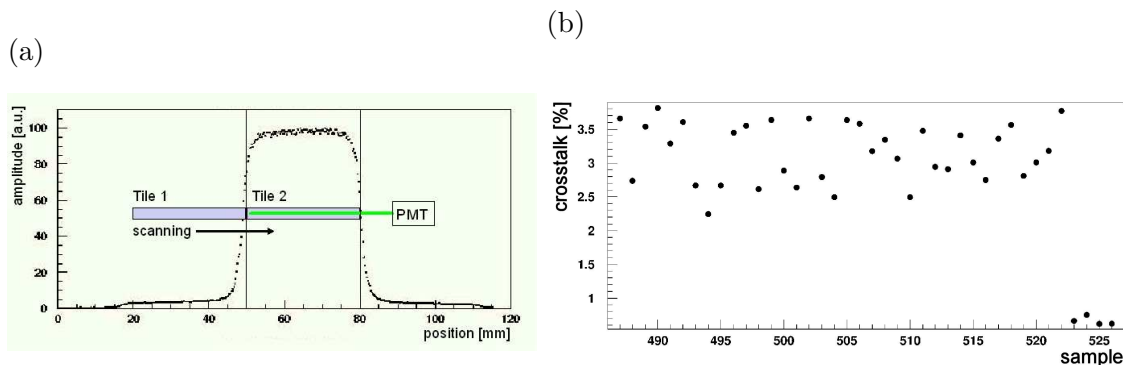
6.4   Non-linearity correction studies

After introducing all components needed for the shower analysis the results of electromagnetic showers in module 1 are presented and compared to Monte-Carlo. To produce the effect of electromagnetic shower evolution, lead absorbers with a thickness of one radiation length (X_0) and 5 X_0 were placed in front of the module as shown in figure 6.12. A beam trigger was defined by a coincidence of two finger scintillator counters read out by photomultiplier tubes. In order to compare the performance of different tiles/channels in the module with a reference, three scintillator counters read out with photomultiplier tubes (PMT) were installed. The first counter $(5 \times 5 \times 0.5$ cm^3) was placed upstream before the absorber, the second $(3 \times 3 \times 1$ cm^3) was positioned right after the lead absorber and the third $(3 \times 3 \times 1$ cm^3) was located just behind the AHCAL module. The beam was steered at the centre of a tile. For the energy measurement, the signal of the centre tile plus the signal of all eight neighbour tiles were used. This 3×3 matrix contains 99 % of the lateral energy spread. 25 such matrices were studied and compared. To reduce systematic effects from beam energy spreads, the measurements are correlated to the results of the second reference counter, which should see most of the created particles in the absorber. The analysis is based on comparing mean values, since the distributions of energy deposited in one layer are not gaussian, therefore a more precise fit value can not be extracted.

The motivation for the study is to check the calibration and saturation correction procedure. Furthermore, in repeating the measurement for different beam positions in respect to the module it is possible to give an upper limit on the non-uniformity of the calorimeter module. One important aspect of this study is the SiPM saturation correction. The following measurements includes energies up to ∼40 mips per tile and the possibility to compare the SiPM response with that of a linear photo-multiplier tube (PMT).

Before comparing the measured energy to the Monte-Carlo prediction following analysis steps have to be applied.

1. Cut away noise contribution by applying half of a mip threshold.

2. Apply non-linearity correction.

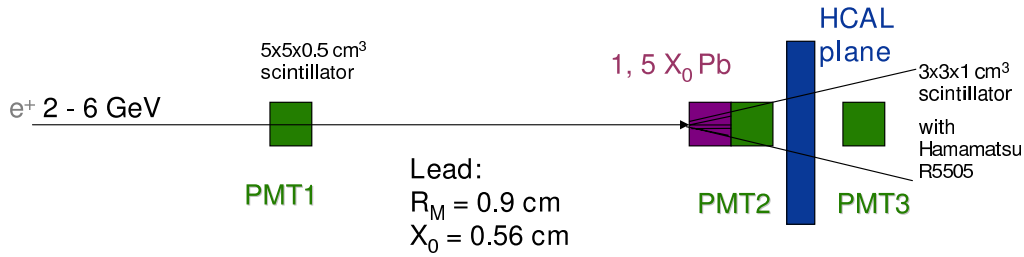3. Check for long-discharge candidates and correct for it if necessary.

Figure 6.12: *Sketch of the setup used for studies of SiPM saturation correction.*

4. Apply light crosstalk correction.

All properties have been discussed in section 6.3. The long-discharge channels have been marked and their measured amplitude have been replaced with the mean amplitude of the three other tiles, which are in the same relative geometric position like the long-discharge channel. A maximum difference of 2% in the total energy sum has been observed between replacing and using the long-discharge channels, which is the uncertainty of this study.
Figure 6.13 (a) shows the spectrum of deposited energy after 5 X_0 lead in one calorimeter layer. The three histograms shown with increasing amplitudes are the energy sum of the neighbouring tiles, the energy of the centre tile and the energy sum of centre tile plus neighbouring tiles. In the spectrum for the centre tile the SiPM non-linear behaviour becomes visible from the asymmetric compression of the right side of the energy spectrum. The same behaviour is not seen in the neighbouring tiles. Figure 6.13 (b) shows the mean values from the histograms shown in (a) in units of mips as a function of beam energy for the 3×3 matrix and for the second and third reference counters. After applying the SiPM response function to correct for saturation effect the measured energies are in good agreement with the MC prediction. For energies above 4 GeV, lateral energy leakage due to non-perfect alignment of the system becomes non-negligible.

Figure 6.14 shows the correlation between the energy collected by the scintillator behind the lead plate (PMT2) and the SiPM tile behind it. Data (closed symbol) from a 5 GeV e^+ beam showering on 5 X_0 lead are compared to the Geant3 simulation of the setup (open symbol). Above 40 mip amplitude the low statistics does not allow to extract sensible information from the data and the simulation was not performed. A clear deviation of the data from simulation is observed already above 15 mip amplitude (>200 pixels). The largest fraction of the shower maximum, generated after 5 X_0 is in the range between 15 and 35 mips. For this amplitude the deviation from simulation is $\sim 10 - 25$ %. After correcting on an event by event basis the SiPM amplitude according to equation 6.2 the data is in very good agreement with the simulation, as it can be seen in the right upper panel of figure 6.14. To study the applicability of a unique SiPM response function to many channels the same test was repeated for a sample of 25 tiles in the core of the first AHCAL module. The average shower maximum in each tile normalized to the simulation prediction is presented in figure 6.15, without (a) and with (b) non-linearity correction. The mean of the distribution for the tested tiles differ from simulation of ~ 20 % when no correction is applied. After correcting each tile response with the same SiPM response function calibrated with the appropriate light yield, data and simulation agree very well. This agreement relies also on the light crosstalk correction, which reduces the energy sum by ~ 5 %. The spread of 5 % between tiles reflects the present uncertainty on all the calibration factors, and the fact that no temperature correction has yet been applied to

(a)

(b)

(c)

(d)
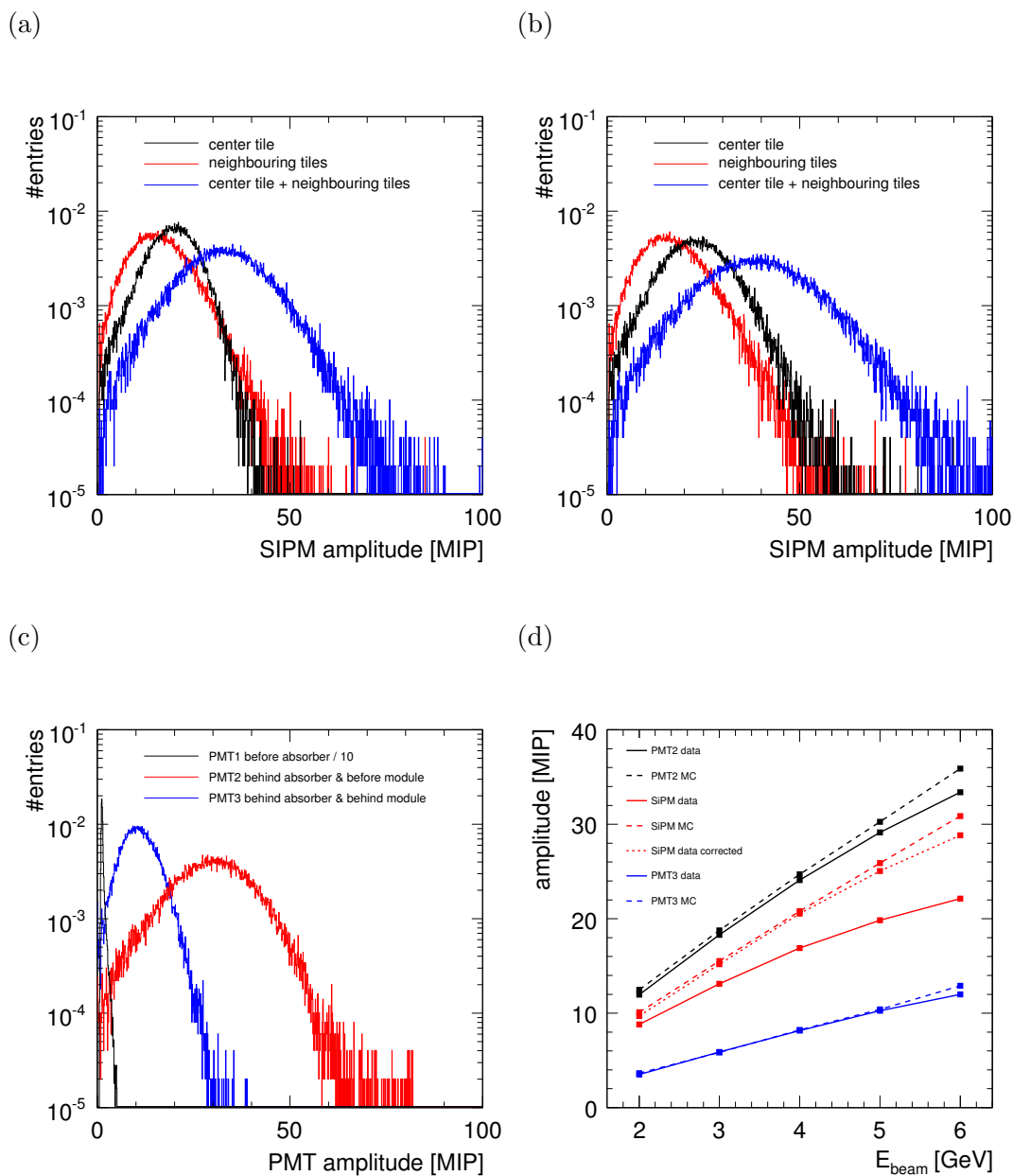
Figure 6.13: *Energy distribution of a 5 GeV e^+ shower after 5 X_0. (a) Energy distribution for the SiPM tiles without non-linearity correction and in (b) with non-linearity correction: the central tile is presented by the black histogram, the sum of the energy deposited in the neighbouring tiles by the red and the sum of all by the blue histogram. (c) Energy distribution in the scintillator plates. (d) Shower energy measured in the different detectors in units of mips as a function of beam energy and comparison to the MC prediction.*
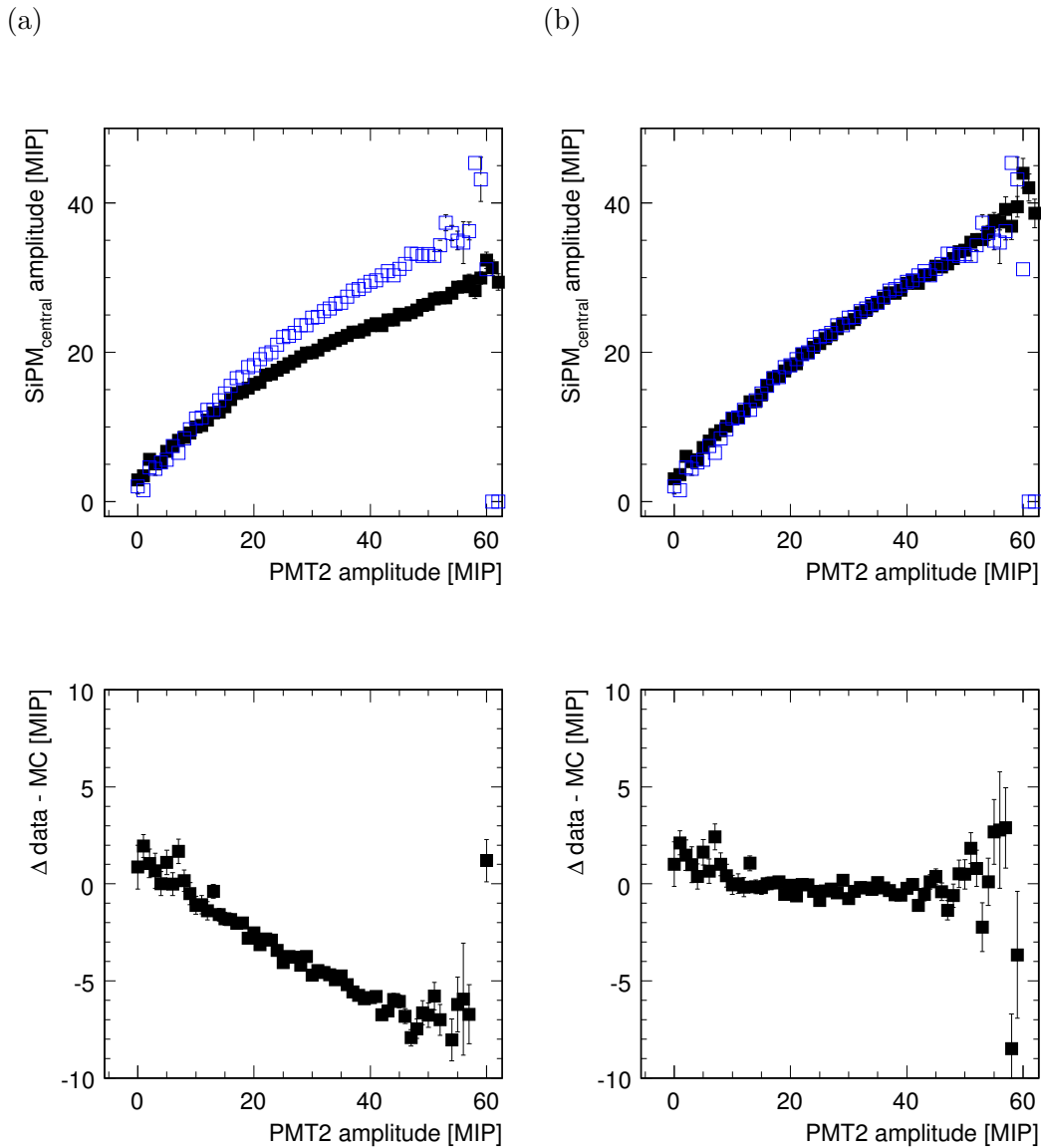
Figure 6.14: *Comparison of SiPM and PMT amplitude for a 5 GeV e^+ beam showering on 5 X_0 lead. (a) Raw SiPM amplitude. (b) SiPM corrected for non-linear response. In (a) and (b) data are presented by the closed black symbols, while the open blue symbols are a Geant3 simulation. (c) and (d) show the difference of data and simulation for (a) and (b), respectively.*

(a)   (b)
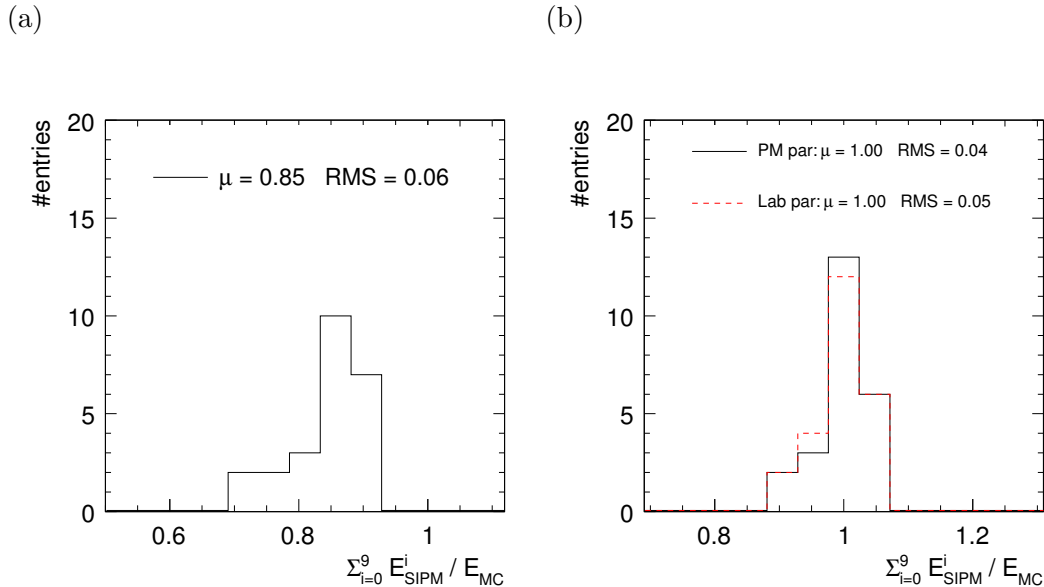
Figure 6.15:   *Average energy deposited in one AHCAL tile by a 5 GeV e^+ beam showering on 5 X_0 lead, normalised to MC expectation, for a sample of 25 tiles. (a) Raw SiPM amplitude. (b) SiPM corrected for non-linear response with two functions described in the text.*

account for the variations during the data taking period. In both cases the corrected amplitude agrees with the simulation expectations. The PMT parameterisation correction works as well as the parameterisations of the response function at the moderate amplitudes reached in this test. This observation needs to be corroborated by larger statistics and by measurements at higher amplitude.

6.5   Uniformity studies

A study of the uniformity of the calorimeter response has been performed using the same setup as presented in figure 6.12 with 1 X_0 lead to initiate an electromagnetic shower. In this configuration the lateral extension of the shower is 99 % contained in a matrix of 9 3 × 3 cm^2 tiles. It is intended to study the homogeneity of one calorimeter layer by comparing the energy deposited in many such matrices, in a region of amplitude where the SiPM saturation is relatively small and the non-linearity correction has a small influence on the result.

The energy reconstructed in the 3 × 3 matrix is compared to that in reference counter 2. For measurements of 3 GeV e^+ with $1X_0$ lead, the spectrum of the centre tile peaks around 5 mips. In addition a peak at 1 mip is visible. The neighbouring tiles show the typical tail of energy leakage on top of the noise contribution. The ratio of energy measured in the centre tile and that of reference counter 2 is 1.09 ± 0.05. Including the entire 3 × 3 array the ratio increases to 1.25 ± 0.06. The mean values are in good agreement with the MC predictions.

The energy collected in the 9 tiles is in average ∼7 mip (∼100 pixels), for which the non-linearity correction is ∼10%. Comparing the energy sum of 45 matrices in one AHCAL module normalized by the simulation prediction leads to the distributions in figure 6.16. It is observed that already at this moderate amplitude a correction for SiPM non-linearity is needed. The spread between the 45 tile matrices is of the order of 5%, which is in the uncertainty of this study. At present these measurements are only indicative that the calorimeter uniformity must
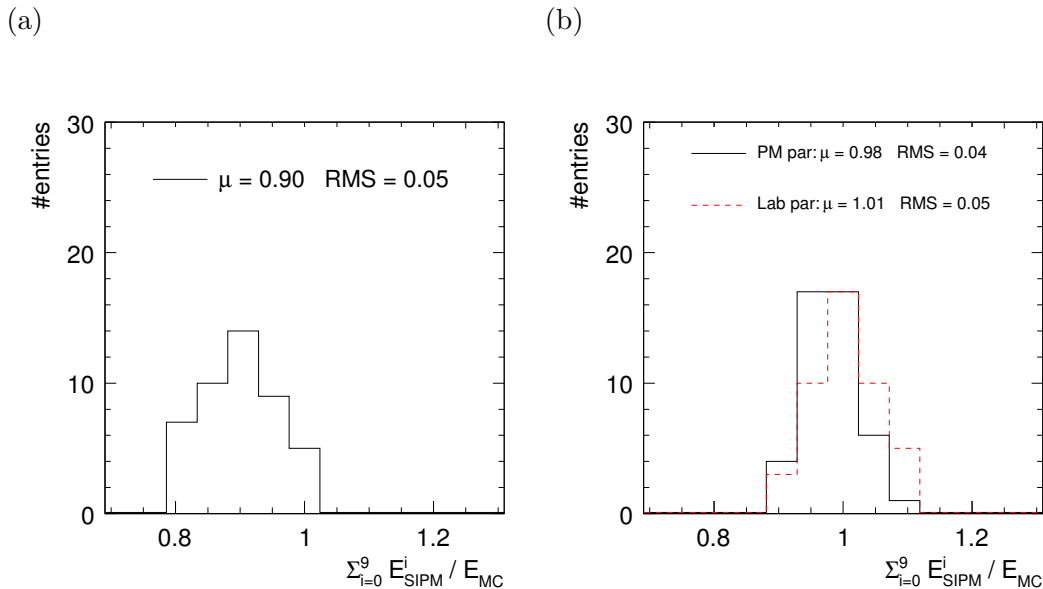
Figure 6.16: *Average energy deposited on a 3×3 matrix of AHCAL tiles by a 3 GeV e^+ beam showering on 1 X_0 lead, normalised to MC expectation, for a sample of 45 tiles. (a) Raw SiPM amplitude. (b) SiPM corrected for non-linear response with two functions described in the text.*

be better that 5%. Higher precision is expected when correcting for temperature variations, not yet possible when the data were collected.

6.6 Conclusion

In this chapter the first working experiences with the complete readout chain have been presented. It was shown that the calibration procedure to extract light yield values and a calibration to compare physics data is working. The SiPM correction plays a mayor role in the analysis chain and should play therefore a key-role for systematic studies in the future. Long-discharge is strongly worsening the performance of the calorimeter. Therefore, the producer has made a huge effort to increase the SiPM quality. The uniformity of the first calorimeter layer was tested and was determined to be better than 5 %. The analysis precision is limited by not monitored temperature changes which will change in the complete detector when the monitoring system is installed.

Chapter 7

Results from the CERN test beam

During summer 2006 the AHCAL has been installed and tested at the CERN SPS test-beam facility together with the electromagnetic and tail catcher prototypes described in section 3.2. This installation is the first test of the CALICE combined calorimeter system and is in itself a major milestone toward the realisation of a calorimeter for the ILC.

The three detectors (ECAL, AHCAL and TCMT) were successfully operated for a period of four months in an hadronic test-beam environment. Over 10000 channels were readout by the combined data acquisition system and about 70 million events are stored on disk and are being analysed.

For the purposes of the work contained in this thesis a set of pion data has been analysed. The focus of the analysis is to the operation of the AHCAL, though the other two detectors are needed for data selection and event topology selection, and had to be calibrated and understood as well. A first part of the analysis is related to "classical"shower parameter studies as the linearity of the calorimeter response, the energy resolution and the energy dependence of the shower profiles. In the second part an attempt has been made to apply the newly developed deep analysis algorithm for shower analysis introduced in chapter 2. This algorithm gives the possibility to study the intrinsic composition of a hadronic shower and it is been applied for the first time to data. Thought the numerical results presented have to be taken with caution and require a much longer period of optimisation of the detector and of the algorithm itself, their qualitative results give a strong indication that the concept of a shower decomposition works. This is an extremely powerful tool for future shower analysis and in particular for comparison and benchmarking of MC models.

This chapter presents the CERN test-beam environment (section 7.1) and the CALICE installation in the H6 SPS beam-line (section 7.2). It describes in section 7.3 the data collected with particular emphasis to the hadronic program relevant for AHCAL studies. In section 7.4 a set of event selection criteria are introduced, which are relevant for the identification of good quality hadronic showers in the AHCAL. These criteria are applied to a pion data sample of 7 momentum points in the range between 6 and 20 GeV/c, on which the analysis presented in this chapter is based. The preliminary results of pion analysis are given in section 7.5.

7.1 The H6 beam-line at CERN SPS

The data discussed in the following have been collected in October 2006 at the test-beam facility H6 at the SPS at CERN. The SPS accelerates protons up to 450 GeV/c. A Beryllium target of changeable thickness (typical 300 mm) is used to extract a hadron enriched secondary

beam. It contains particles of different types like electrons, positrons, pions, protons, kaons and muons with known and steerable energies. A magnetic system provides the switching of the beam to different experiments. The beam tuning process is of vital importance for the success of a test-beam experiment. At CERN the optimisation of the beam orbits of a given beam-line is responsibility of the users. This requires the control of several dipoles, quadrupoles and collimators along the 500 m of beam-line from the primary interaction target to the detector. A description of the beam tuning procedure for the H6 beam-line, of interest for this work, is given in Appendix A. The 450 GeV/c SPS proton beam is steered on a Beryllium target (T4) to provide secondary beam for three beam-lines: P0 (mostly 450 GeV/c protons, sometimes secondary electrons), H8 (450 GeV/c protons, secondary beams) and H6 (secondary beams, limited by the maximal current of the magnets to ±205 GeV/c). The secondary beam momentum of H6 is coupled to that of H8 and P0 beam-lines. The intensity on T4 is limited to about 1.5 to $2.0 \cdot 10^{12}$ protons per burst. The protons interact with the Beryllium nuclei and create multiple charged and neutral secondary particles (mostly pions) with a wide momentum spectrum. The electron content is small due to the fact that electrons loose a fraction of their momentum by synchrotron radiation and therefore are not focused by the subsequent beam orbit. A spectrometer magnet on each line selects the momentum of the secondary beam.

The T4 target station geometry is shown in figure 7.1. A set of three magnets B1T, B2T and B3T around the target allows to select different energies in each beam-line. This is referred to as *T4 wobbling* [99]. P0 and H6 have both a septum magnet following the TAX, which allows accepting particles with a skew or production angle different from zero. H8 does not have this option, therefore can only accept particles which are centred in the B3T magnet, a condition which is typically satisfied selecting particles with zero production angle. Downstream the target station magnets and before any of the beam-line elements, are located the TAX blocks, whose principal function is to control the beam passage (angle and therefore momentum, as well as intensity), and serve as beam dump whenever access is required in any of the lines and when the beam is not operational. For the most frequent mode of operation, P0 is operational (450 GeV/c protons), allowing the following schemes for H8 and H6:

1. H8=-200 GeV/c (+tertiary beams) and H6 = -120 GeV/c (+tertiary)

2. H8=-300 GeV/c and H6 = -120 GeV/c (+tertiary)

3. H8=+180 GeV/c (+tertiary beams) and H6 = +120 GeV/c (+tertiary)

Tertiary beams of momentum lower than the secondary one can be obtained introducing a secondary target on the beam-lines. Various target materials are available. An electron and positron enriched tertiary beam is obtained introducing a lead secondary target. In the interaction of the secondary charged pion beam with this target π^0 are created, which decay into photons initiating electromagnetic processes. A polyethylene target can be used to lower the pion momentum. In both cases the charge and momentum selection of the tertiary beam is performed by a spectrometer magnet located after the secondary target.

The operating conditions for H6 and H8 have some freedom, but typically they should run at the same polarity and with a ratio of momenta P_{H6}/P_{H8} somewhere in the range between 1/3 and 2/3, due to the angle of 11.2 mrad between H6 and H8. When the P0 line runs electrons, both H6 and H8 should run at high momenta. The beam-line H6 provides a secondary beam in the momentum range from a maximum of 205 GeV/c down to 30 GeV/c with decreasing beam rate. This beam can be delivered directly to the experiment. Tertiary beams can be obtained with energies as low as 5 GeV/c.
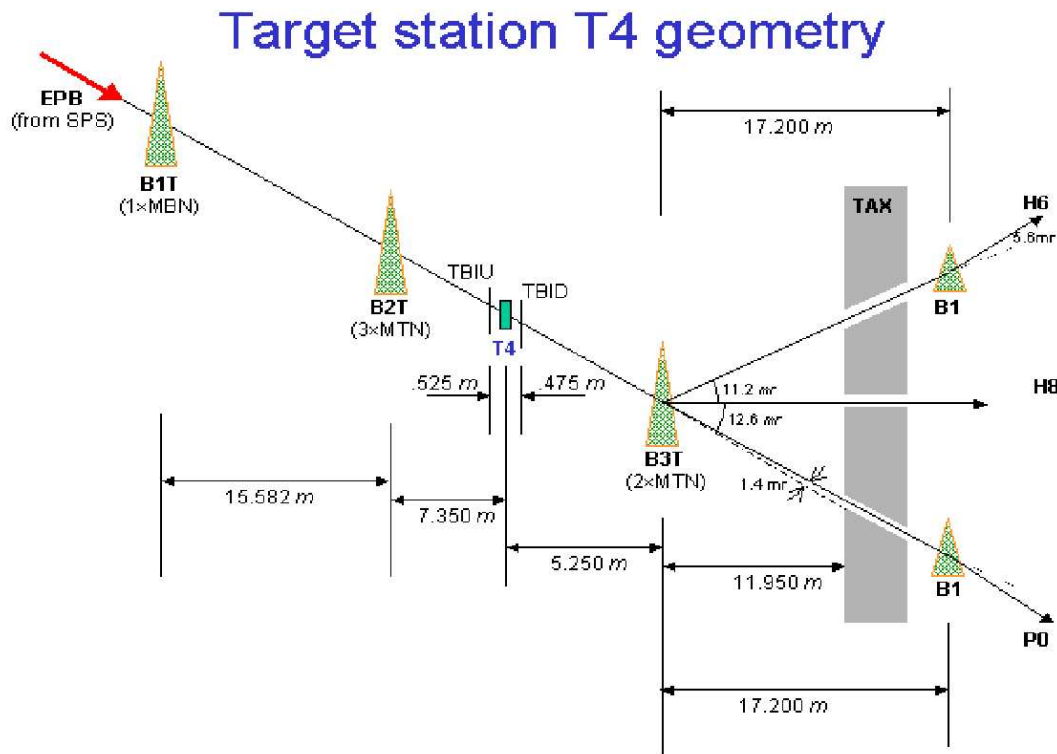
Figure 7.1: *The T4 target station geometry. B1T, B2T, B3T are the three wobbling magnets. The B1 in P0 and H6 are strong septum magnets. TBIU and TBID are upstream and downstream beam monitors [99].*

Several quadrupol- and sextupolmagnets over the complete 500 m long beam-line from the first target until the experiment focus the particles on the beam axis. At the experiment the beam profile has a FWHM in x and y direction perpendicular to the beam axis of approximately 1.5 cm and 0.8 cm decreasing with increasing beam momentum.

The SPS beam is extracted to many different beam-lines and experiments, therefore it has a supercycle which is adjusted to the number of used extraction lines. Most common supercycle is 16.8 s with a 4.8 s long flat top (period of constant intensities for test beams). This supercyle length and also the beam delivery time can change during the test-beam period. If for example the SPS has to serve the target to create the neutrino beam to the Gran Sasso underground experiments or the machine studies for LHC, the supercycle extends up to 34 s.

7.1.1 Beam settings for the CALICE experiment

During summer 2006 the CALICE prototypes have been installed on the H6 beam-line and tested with both pion and electron enriched beams (using secondary and tertiary beams). As discussed in chapter 3 the main interest for the ILC hadronic physics is on low energies. To obtain a well-focused low energy pion beam of high intensity a secondary beam momentum of 10 GeV/c was preferred to the operation of tertiary beam. This can be obtained by using special T4 wobbling settings to provide H6 with beam of lower momentum (e.g. 50 - 10 GeV/c). No tertiary beam can be obtained in this mode. With this method the range between 6 to

20 GeV/c pion was covered.

A tertiary pion beam can be obtained running with 120 GeV/c secondary beam momentum on a 400 mm copper target. An absorber consisting of 4 mm Pb has been inserted to clean up the beam from electrons and to purify the pion sample. Electrons in the range of 6 to 45 GeV/c were obtained using a 60 GeV/c secondary beam on a 4 mm Pb target. The optimisation of the beam orbit for each momentum of either the secondary or tertiary beam was performed according to the procedure detailed in Appendix A.

As a beam rate monitor during beam tuning the trigger plate coincidences (10x10, 3x3) close to the experimental area have been used, together with additional trigger units along the beam-line. Four sets of delay wire chambers (DWC) allow to check the Gaussian beam profile at various positions on the beam-line. Two examples of the DWC spectrum are shown in figure A.2 for 120 GeV/c secondary pions and in figure A.3 for 6 GeV/c tertiary pions. It is visible that secondary high momentum beams are much better focused than tertiary beams. The following analysis is based on a sample of pion runs, which have been taken with secondary low momentum beam of 10 GeV/c.

7.2   Experimental setup at the CERN test beam

The CALICE setup in the H6 test-beam area is shown in figure 7.2. The beam comes from the left and the first detector after the mentioned beam-line monitoring devices is a threshold Cerenkov counter, which can be used to separate electrons from pions with good efficiency until 20 GeV/c beam momentum. Afterwards, a set of different scintillator trigger coincidences is used to generate a trigger for the DAQ. Additional information about the beam is collected by three delay wire chambers (DWC), each of them giving a x and y coordinate of the beam. By fitting and extrapolating this information the beam interception point on the calorimeter surface can be obtained. The figure 7.2 provides all detector thicknesses and relative distances. In the following the different beam detectors are shortly presented.

7.2.1   Trigger system

The detector should only be read out in case a particle enters the experimental area close to the beam axis. The trigger provides this functionality and consists of two scintillator plates readout with fast photomultiplier tubes (PMTs), which are logically connected to a coincidence. If the trigger decision is positive, not only the complete calorimeter is read out, but also all beam monitoring devices like DWC and partially the trigger amplitudes are read out and stored. The normal beam trigger is the coincidence between two $10 \times 10 \times 0.5$ cm^3 scintillator plates (Sc1 and Sc3 in figure 7.2). The two trigger plates are separated by a distance of $\approx$2.5 m to minimise the allowed beam trajectory angle. In addition, a $3 \times 3 \times 0.5$ cm^3 trigger plate coincidence (Sc2) is available close to the front of the first prototype. To minimise two particle events a scintillator plate of $20 \times 20 \times 1$ cm^3 dimension is used (Sc4). Instead of storing only a bit information like for the other trigger plates, the veto plate is connected to two photomultiplier tubes, one providing the trigger signal and the other the analogue amplitude, which is stored in the DAQ. For muon calibration runs the trigger was created by the coincidence of two $100 \times 100 \times 0.5$ cm^3 large trigger plates of which one was mounted permanently behind the TCMT (Mc1) and the second one temporarily during the calibration time in front of the calorimeter prototypes.

TOP – CERN October 2006

Cerenkov   Sc1 DC1   DC2   Sc4   DC3 Sc3
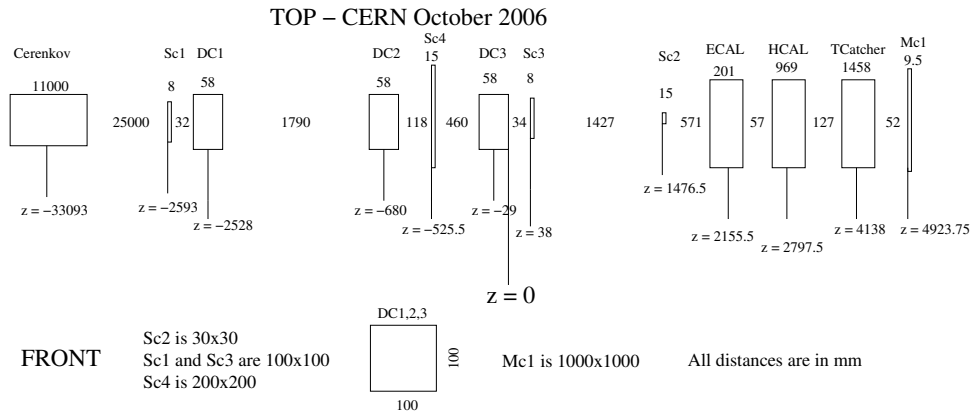
Figure 7.2: *CALICE test-beam setup in October 2006 at the experimental area H6 in CERN, Prevessin. The beam comes from the left and has to pass several beam monitoring devices like Cerenkov, scintillator plates and DWC before interacting in the calorimeter prototypes.*

7.2.2 Particle ID

Threshold Cerenkov counters are detectors for particle identification and separation. Their principle is based on the phenomenon that charged particles traversing material emit Cerenkov light as soon as they travel faster than light in the material. The beam-line is equipped 25 m before the experimental area with a 11 m long Cerenkov detector filled with helium. It is possible to tune the helium pressure to adjust the gas refraction index just below the point where pions of a given momentum start to emit Cerenkov light. For this pressure no signal is given by pions traversing the gas volume, but electrons are always detected. The threshold pressure is momentum dependent and has to be decreased with increasing particle momentum, which affects the electron detection efficiency as well. The thresholds for the discussed runs are listed in table 7.1 and are extracted from the following formula:

$$P_{thres}[bar] = (1/2k) * \frac{M^2}{p^2}, \tag{7.1}$$

where M is the mass and p the momentum of the pion and k is a constant depending on the used gas. For helium $k = 3.22 \ 10^{-5}$. The threshold pressure is drawn in figure 7.3 (a). Whenever the pressure is larger than P_{thres}, N photons are emitted by electrons. The number N of photons is dependent on the length L of the device (in cm) and on the detection efficiency A of the readout, which is typically 100 %. Hence following equation is valid

$$N \approx A \cdot L \cdot (2kP - \frac{M^2}{p^2}), \tag{7.2}$$

p_{beam} [GeV/c]	P_{thres} [bar]
6	8.40
8	4.73
10	3.02
12	2.11
15	1.34
18	0.93
20	0.76

Table 7.1: *Optimised pressure threshold to separate electrons and pions for different particle energies.*

the efficiency η of the counter is given by

$$\eta = 1 - exp(-N). \tag{7.3}$$

In figure 7.3 (b) the theoretical efficiencies that could be achieved for a 10 m long Cerenkov counter, filled with helium and assuming A=100, is shown. It becomes clear that an efficient e/π separation is only possible at low particle momenta. Already at 20 GeV/c which is the highest momentum considered in this analysis, the separation efficiency η is only $\approx$30%.
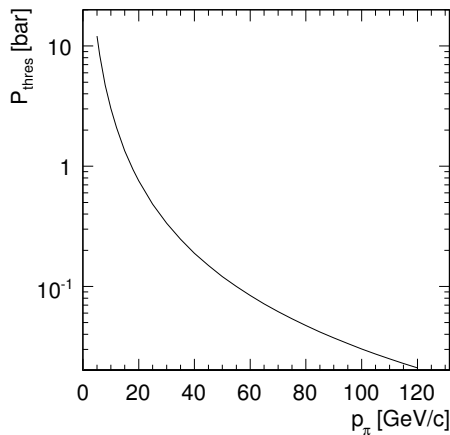
(a)   (b)
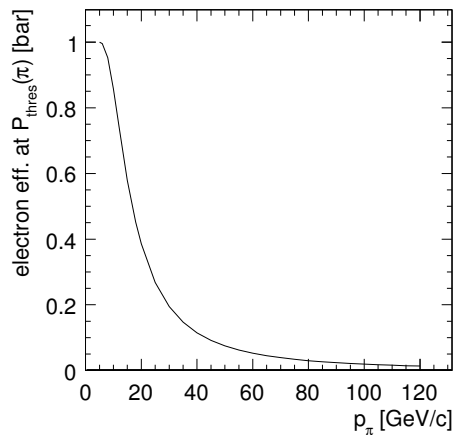
Figure 7.3: *(a) Cerenkov threshold pressure as a function of pion momentum for helium. (b) Theoretical π/e separation efficiencies for a 10 m long Cerenkov (A=100), filled with helium.*

Since this analysis is based on pions it is required that the Cerenkov bit is off, which means that no light has been detected.

7.2.3   Particle tracking

The trigger plate size of the scintillator (Sc1 and Sc3) cuts the used part of the beam profile to an area of 10×10 cm^2. This area defines the used part of the beam, but the beam can be in principle larger. A considerable amount of events show two particles entering the

calorimeter system. This occurs in electron runs when the electron radiates a photon due to Bremsstrahlung, or in pion runs when neutral pions decay into two photons. In case these neutral gammas create charged particles before the calorimeter, these particles can be detected by the three installed delay wire chambers (DWC) and the veto counter and can be rejected. The DWCs consist of two layers each equipped with 128 signal wires of 25.4 cm length. The gap between the wires is in both layers 2 mm. To reconstruct a two dimensional position information one layer is horizontally and the other vertically oriented. The readout is performed by a TDC, which gets a common start signal from the beam trigger distributed by the DAQ. Each chamber has in total four channels, two readouts for each of the 2 planes (x and y). The signal of each channel is the sum of the contributions from the different signal wires, added up according to the delay per wire connected to a common delay line [100]. These channels have been measured by the TDC and can be used to calculate the absolute position of the incident particle by the following formula:

$$
\begin{aligned}
X &= (t_{right} - t_{left}) \cdot a_{horizontal} + b_{horizontal}, & (7.4) \\
Y &= (t_{up} - t_{down}) \cdot a_{vertical} + b_{vertical}, & (7.5)
\end{aligned}
$$

where the absolute position is indicated in millimetres from the centre of the chamber, the times t are in nanoseconds, both slopes a are approximately 0.2 mm/ns and the offsets b are close to zero. To determine the slope and offset with high precision a calibration procedure with charge injection is available. The spatial resolution is better than 200 μm and the detection efficiency is quoted to be better than 99 %. The chamber has a dead-time of 250 ns and the used gas mixture is argon/carbon-dioxide in a 50/50 ratio. The three reconstructed points from each DWC are combined in a fit to extrapolate the beam trajectory to the front of the calorimeters. In figure 7.4 (a) the reconstructed beam impact point from the DWC on the AHCAL calorimeter front is shown. Figure 7.4 (b) presents the correlation between the shower centre of gravity in the AHCAL and the reconstructed beam impact point from the DWC. From both plots it becomes clear that the beam is displaced by ~1 cm from the AHCAL centre. In figure 7.4 (c) the same correlation is shown for the ECAL. The spread is smaller, because the selected events are pion events, which mainly traverse the ECAL without interacting. The centre of gravity has been calculated according to formula 2.36.

7.2.4 Double particle rejection

The veto counter is a scintillator plate of $20 \times 20 \times 1$ cm^3 dimension. In contrast to the other scintillator plate the analogue amplitude is recorded as well. A typical spectrum is shown in figure 7.5. A clear mip spectrum is visible with additional activity in the Landau tail corresponding to a two mip signal (shoulder around 3000 ADC channels). Cutting the events with veto amplitude above the line corresponding to $\approx$2 mips decreases the statistics by 4 %, but it reduces the double particle contribution. Unfortunately, the analysis has shown that several second particles in the beam are found at radii even larger than 20 cm from the beam axis. These particles are not seen by the veto counter and therefore not rejected. A larger veto, which covers the complete calorimeter system front would be preferable for the next test-beam run. An additional preshower layer can be used outside the beam trigger area to force the conversion of radiated γ and reject them.
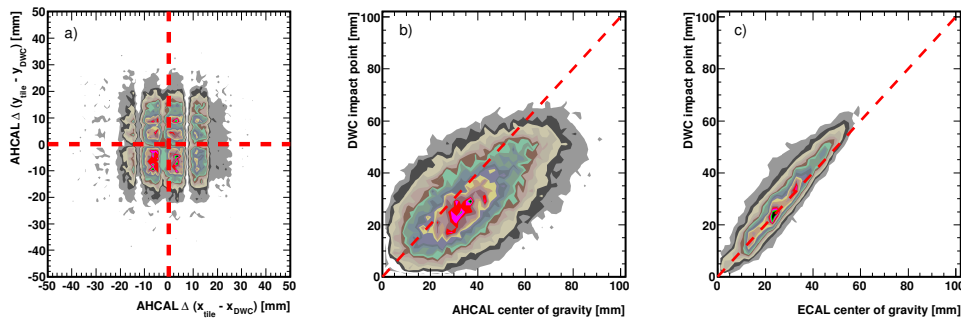
Figure 7.4: *(a) Difference between the reconstructed beam impact point coordinate from the DWC and the AHCAL tile position. (b) Correlation between the shower centre of gravity in the ECAL and the reconstructed beam impact point from the DWC. (c) Correlation between the shower centre of gravity in the AHCAL and the reconstructed beam impact point from the DWC.*
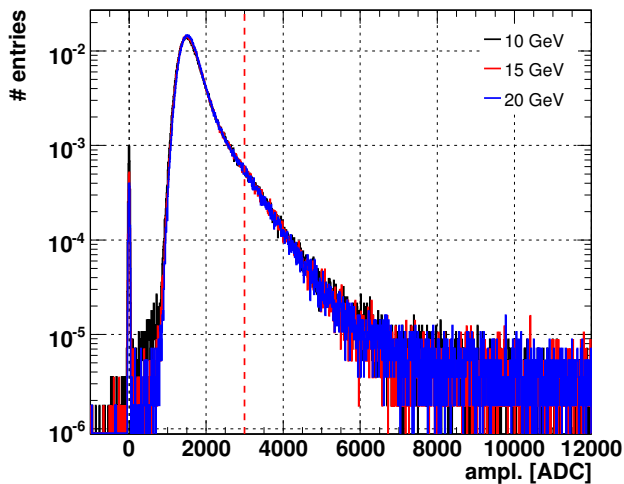
Figure 7.5: *Amplitude of the veto counter for 10, 15 and 20 GeV/c pion data. The used cut to minimise the second particle contribution is set to 3000 ADC channels, which leads to a statistic reduction of ≈4 %.*
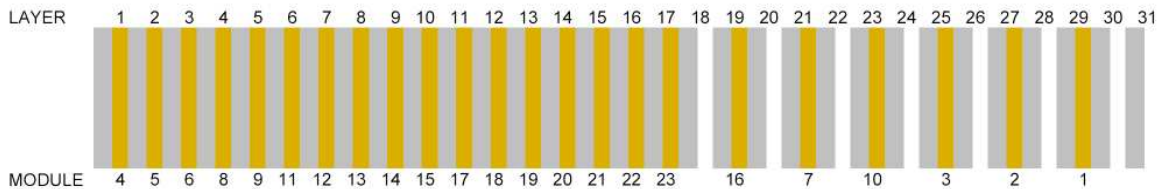
Figure 7.6: *AHCAL module setup during the October 2006 test-beam run at CERN. The beam comes from the left of the picture. The first seventeen layers in z are completely equipped, whereas every second of the following thirteen layers are equipped.*

7.2.5 The calorimeter system

ECAL

The ECAL prototype has already been introduced in section 3.2. At CERN the ECAL was equipped with 30 sensitive layers of silicon pads, but each layer was missing a third of the readout channels, thus reducing the active area to 18×12 cm^2. The total readout channels have been 6480 out of the 9720 foreseen. The absorber material translated into nuclear interaction length is ≈ 0.88 λ_0 (0.15 λ_0, 0.29 λ_0, 0.44 λ_0, respectively for the three structures).

The silicon pads response is not strongly temperature dependent and is linear. The monitoring consist of voltage and current readouts. The calibration procedure is therefore much easier than the AHCAL case, because only the response to a mip is needed to convert the signal amplitude into energy.

For the purpose of this analysis the ECAL is used as a track finder to select pion events which have not interacted before reaching the AHCAL.

AHCAL

In September 2006 23 of the 38 modules have been finished. To cover a sufficient fraction of the longitudinal shower development without sacrificing too much the highly granular information it was decided to use two different samplings. The first seventeen layers, in which ≈ 75 % of the shower energy is deposited are fully equipped. The following thirteen layers are equipped with the other 6 modules, which leads to a structure in which only every second layer is equipped and read out. This configuration enables us to cover the part with statistically the highest activity and nevertheless to have a ~ 3.5 λ_0 long calorimeter. The sampling factor $SF = E_{dep}/\epsilon_{vis}$ of the second half of the calorimeter is by a factor 1.78 larger than the first one. This has to be taken into account when summing energies over the complete calorimeter. In addition, the focus of this test-beam period was on collecting combined data with the complete calorimeter system: ECAL, AHCAL and TCMT, which implies ~ 1 λ_0 in front of the AHCAL due to the ECAL material.

In figure 7.7 the containment in the AHCAL for a simulated 20 GeV pion shower is shown. The left plot shows the shower without ECAL in front and the right one with ECAL. It is visible that the longitudinal leakage is much reduced.

TCMT

The TCMT described in section 3.2 was completely installed during the CERN test-beam run. In this analysis the TCMT is used to estimate the leakage after the AHCAL and to identify
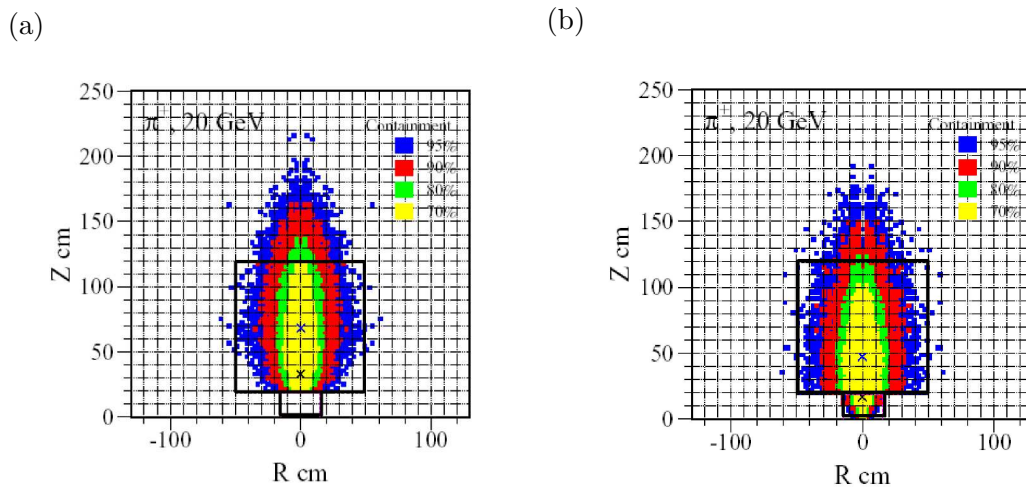
(a)   (b)

Figure 7.7: *Leakage estimation from simulation for the complete AHCAL prototype for a
20 GeV/c π^+ with (a) and without (b) ECAL in front. The small black box indicates the
dimension of the ECAL prototype and the larger black box the dimensions of the AHCAL
prototype.*

muons in the complete calorimeter system as well. Only integrated energy values are used
from it and no particular care is taken to reconstruct tracks.

7.3   Data sample

During the complete test-beam run period in October 2006 combined pion data with various
momenta ranging from 6 up to 50 GeV/c have been collected. In addition the response of
the ECAL and the AHCAL prototypes to electrons has been tested by collecting electron
data from 6 up to 50 GeV/c. In case of the ECAL the data are fundamental to study
the performance of the detector. In case of the AHCAL the electromagnetic shower data
are mandatory to understand the complex calibration and correction chain of the detector
as well as the material distribution by comparing the obtained data to the well understood
electromagnetic MC prediction. Only after the achievement of a good data to MC agreement in
these samples, final results can be obtained for the hadronic shower analysis as well. However,
for this analysis a special subsample has been identified, which enables a first look into pion
data.

 This data sample consists of negatively charged pions with momenta between 6 and 20 GeV/c.
Two event displays are shown in figure 7.8. In (a) a three-dimensional view of a shower which
has started in the AHCAL and has left only a track in the ECAL is shown. In (b) a side
view of a shower which has started already in the ECAL is presented. The statistics for each
sample and the run numbers used in the analysis are shown in table 7.2. Three runs for each
of the seven energy points have been selected. The total statistic is ∼7 million events. This
sample was chosen, because the single channel amplitude is relatively small and therefore the
energy reconstruction is less affected by SiPM linearity corrections. In figure 7.9 the hit energy
spectrum in mips for these selected pion runs is shown. For the 20 GeV/c run 97 % of the
hits are below 15 mips. At this point the non-linearity correction is ∼10 %. This shows that
the influence from non-linearity correction is small. In addition, all runs belonging to this
dataset have been collected in a time range of ≈48 hours. This means that the detector was

beam [GeV/c]	run number	statistic [Kevts]
6	300628, 300629, 300630	1000
8	300643, 300647, 300648	700
10	300613, 300618, 300660	1500
12	300644, 300649, 300653	900
15	300614, 300619, 300659	1600
18	300645, 300646, 300650	750
20	300616, 300620, 300658	1500

Table 7.2: *Data sample: negatively charged pions from 6-20 GeV/c.*

(a) (b)
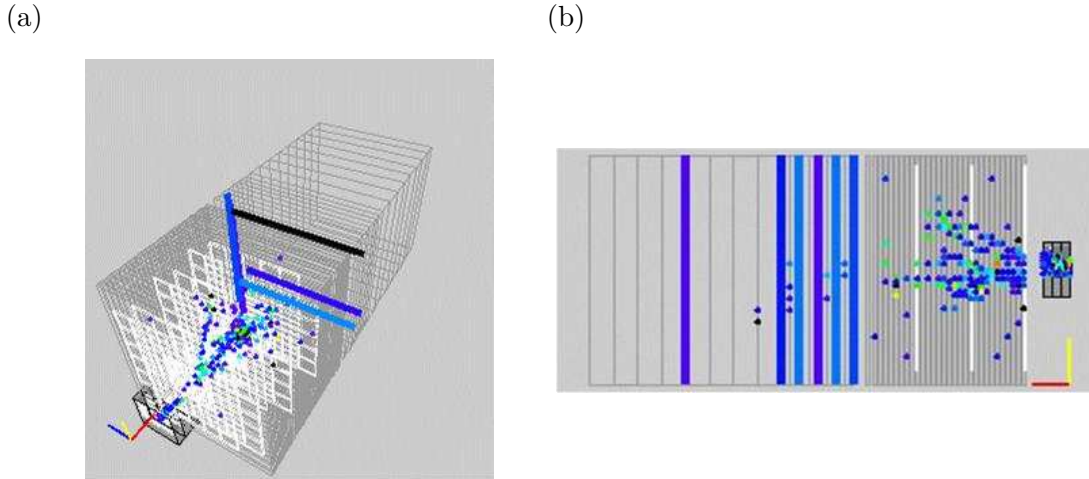
Figure 7.8: *Example event displays for a pion run with 20 GeV/c momentum from the online monitor. (a) Three-dimensional view of a shower which has started in the AHCAL and has left only a track in the ECAL (the beam is coming from the lower left corner). (b) Side view of a shower which has started already in the ECAL (the beam is coming from the right side). Hits in the TCMT are indicated by the colored bars.*

in a stable condition and the only variation was due to day-night temperature changes, which are in the order of $\approx 1°$ K. This is important because the full understanding of the calibration and correction chain is being developed in parallel to this study and will have a major impact on the quality of the full test-beam analysis.

7.3.1 Degradation of beam energy resolution due to ECAL

Most of the collected data are combined data, which means all three detectors: ECAL, AHCAL and TCMT were in the beam-line. For understanding the AHCAL alone, it is important to have showers starting in the AHCAL. Since the ECAL is already $\approx 1 \lambda_0$ the probability that the hadron shower starts in the ECAL is relatively high. To estimate the number of showers starting in the ECAL a MC study has been performed. In this study a pion of 15 GeV/c is generated and directed on the fully equipped ECAL, consisting of 30 layers. After the ECAL the number of outgoing tracks is counted. If only one track exists, we consider this as an event, which has not started to shower in the ECAL. In figure 7.10 (a) the number of tracks leaving the ECAL is shown. One track occurs for around 60 % of the events. Figure 7.10 (b) shows the displacement of these tracks from the initial beam axis. Around 50 % are within a

Figure 7.9: *AHCAL hit energy spectrum in mips for pion runs from 6-20 GeV/c.*

radius of 15 mm. The energy distributions of these two samples are shown in figure 7.10 (c). The black solid line describes all selected events fulfilling the one track requ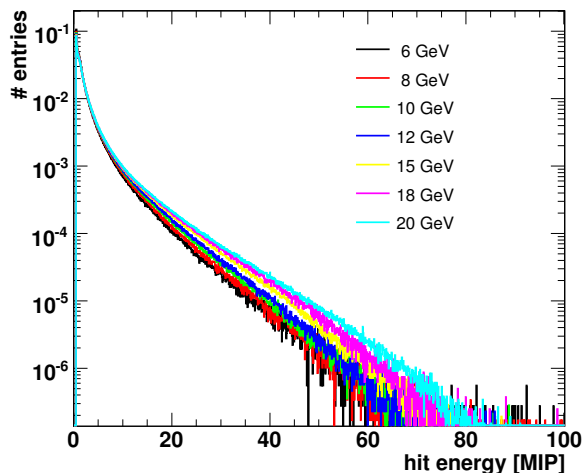irement. The red dashed line represents the subsample of events, where the leaving track is inside the 15 mm zone. An additional sample is introduced in which instead of this requirement, the maximum total number of hits in the ECAL should be 35. This means that there is approximately only one hit per layer and therefore no shower in the ECAL. This subsample is represented by the blue dash-dotted line. This requirement cuts most of the events, which have a shower in the ECAL and consists of approximately 35 % of all events. An expanded view of the track energy distribution in the region of the beam energy is shown in figure 7.10 (d). The black solid histogram represents all events, which have one track leaving the ECAL and a track energy of more than 14.5 GeV. The blue dashed line shows the events, which have not more than 35 hits in the ECAL. It is visible that this requirement is effective in cleaning the sample. The efficiency is still around 35 %, because only 0.1 % events are rejected by the energy cut. The shape of the energy distribution follows as expected a Landau distribution, because these pions behave in the ECAL as mips. Thus, it has to be kept in mind that the energy entering the AHCAL is not equal to the initial beam energy. The average energy loss due to ionisation in the ECAL is around 250 MeV and the RMS is 45 MeV. However, the energy distribution is non-Gaussian. If the energy peak is fit with a Gaussian function in a three sigma range around the peak, only approximately 70 % of the events are inside this distribution and the total efficiency decreases to approximatetly 25 %.

7.4 Event selection

The event selection is based on a combination of requirements on the number of calorimeter channels above a threshold of 0.5 mip (*hits*), and on the deposited energy on the mip scale. For this the visible energy in mips is multiplied by the appropriate sampling factor SF for each detector layer. For the ECAL three factors are used for the three different sampling
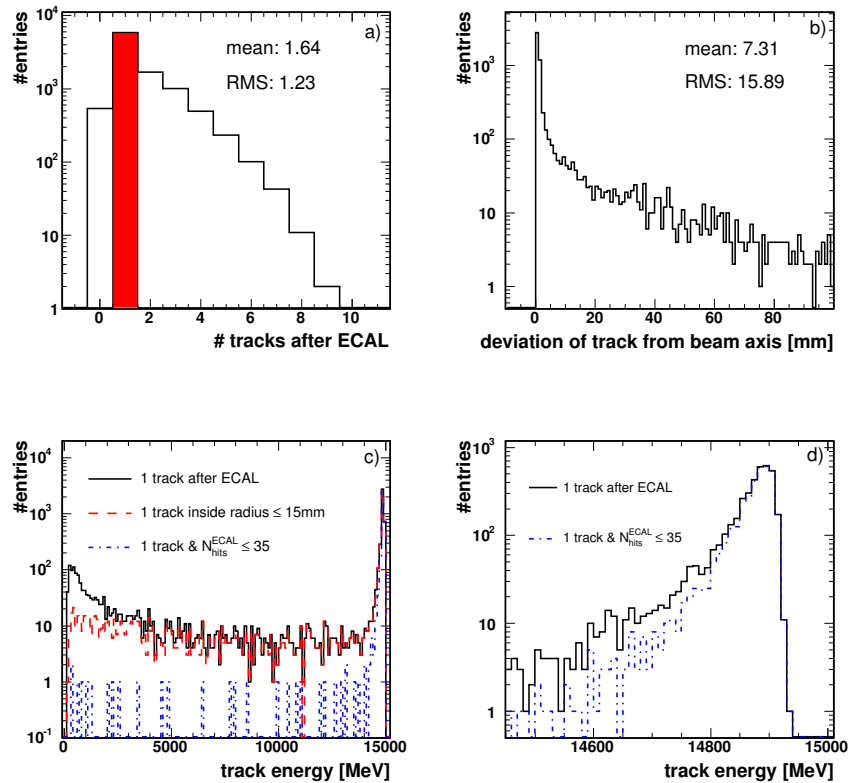
Figure 7.10: *ECAL influence on the particle beam. (a) Numbers of tracks leaving the ECAL is shown. (b) Distance between the track position after the ECAL and the beam axis. (c) Complete particle energy distribution after the ECAL for the case that only one track is leaving the ECAL (black solid line), additional requirement of being inside of a cone of 15 mm (red dashed line) or for having ≤ 35 hits (blue dash-dotted). (d) Zoom in of (c) and finer binning: the energy distribution follows a Landau shape.*
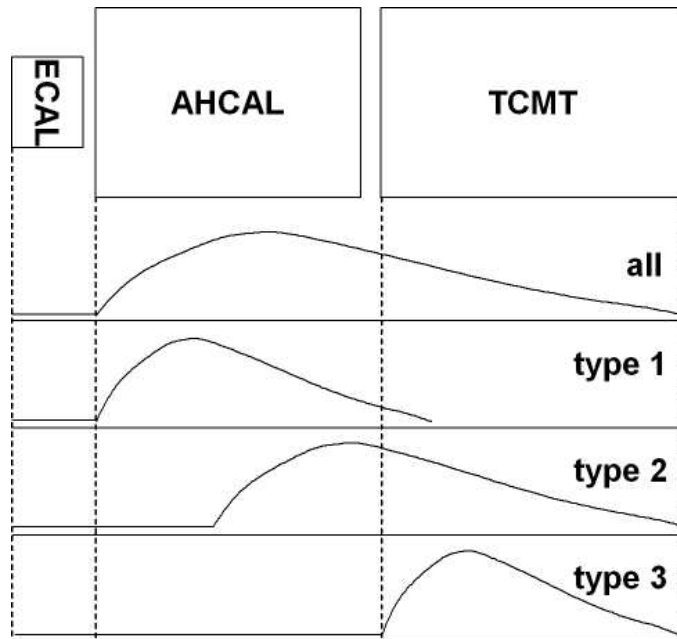
Figure 7.11: *Sketch of the four types of pion events as described in the text.*

structures 33.0, 62.3 and 93.0. For the AHCAL and TCMT fine samplings a factor of 29.5 is used, which has been extracted from MC. The coarse sampling of the AHCAL has a sampling coefficient 1.78 times larger, while the coarse TCMT sampling is 5 times larger than the fine one.

A normal pion run consists not only of pions. The beam contains electrons, muons; and in addition some events cannot be used since the shower started already before the calorimeter system, or two particles are entering the calorimeter at the same time. To sort these kind of events a set of selection criteria has been developed. Only events are used in this analysis, which have a reconstructed track in the ECAL.

Double particle events are partially removed by a cut on the amplitude of the veto counter. This cut rejects about 4 % of the events at all energies. As mentioned the veto counter covers only a small area of the calorimeter front. Additional particles, typically muons, γ's or soft hadrons are also found outside the veto sensitive area. To remove them the number of hits and the energy outside the core of the first layer are used. Events with one hit and energy larger than 400 MeV, or with 2 to 6 hits and energy larger than 500 MeV or events with more than 6 hits are rejected. The contribution of these events is less than 1 %. Up to 200 triggers per run consist of empty events with no activity in the calorimeter system. They are identified by a upper cut in the total number of hits in each calorimeter ($N_{hits}^{ECAL} \leq 20$ & $N_{hits}^{AHCAL} \leq 20$ & $N_{hits}^{TCMT} \leq 13$). The Cerenkov threshold counter is required to have identified no electron for all runs.

In addition, 4 % of the total channels are not used, because no signal has been recorded or due to too high noise contribution (see 5.2.4). Half of these channels are in module 1, which is in the last stack position and has been powered incorrectly.

The focus of this analysis is on events in which the pion has traversed the ECAL without interaction. To minimise the fluctuations on the incoming energy to the AHCAL a cut on the energy loss by ionisation in the ECAL is performed (see section 7.3.1). Only pions of energy in a range from 78 % to 99 % of the beam energy are accepted. By this criteria 50 %

of the events are rejected. In addition, the energy measured in the AHCAL is scaled to the beam energy E_{beam} by applying the following factor $\frac{E_{beam}}{E_{beam} - E_{ECAL}}$, where E_{ECAL} is the energy deposited in the ECAL.

All remaining events consisting of muons and pions are used in the analysis. First the muons are separated and used for calibration stability checks. Muons are defined as having limited amount of hits in each calorimeter ($N_{hits}^{ECAL} \leq 50$ & $N_{hits}^{AHCAL} \leq 50$ & $N_{hits}^{TCMT} \leq 30$) or small energy deposited in each calorimeter ($E^{ECAL} \leq 2$ GeV & $E^{AHCAL} \leq 2$GeV & $E^{TCMT} \leq 4$ GeV). A muon in the AHCAL leaves a track perpendicular to each layer and therefore fires a tower of consecutive tiles. When a muon track is found the energy in a matrix of 3x3 tiles surrounding the track is summed up. This defines the mip energy loss. The activity of all remaining tiles can be considered as noise.

The purified pion sample is divided in three categories depending on the longitudinal shower development as shown in the sketch 7.11. If no criteria is imposed the shower can extend from the AHCAL to the TCMT (all). Showers which are fully contained in the AHCAL (type 1) are extracted imposing high number of hits in the AHCAL and low number of hits in the TCMT. Complementary to this sample are events with late shower either started in the last AHCAL layers (type 2) or fully contained in the TCMT alone (type 3). The precise selection cuts imposed to separate the three samples are summarised in table 7.3.

event type	N_{hits}^{ECAL}	N_{hits}^{AHCAL}	N_{hits}^{TCMT}	E^{ECAL} [GeV]	E^{AHCAL} [GeV]	E^{TCMT} [GeV]
all pions				< 2		
contained pions (type 1)		> 40	≤ 15	< 2		
late pions (type 2)		> 40	> 15	< 2		
TCMT pions (type 3)		20 ÷ 40		< 2	< 2	

Table 7.3: *Event selection criteria.*

The statistics for the muon and each of the pion samples is reported in table 7.4 for all the analysed energies. A more detailed table can be found in B.1. It can be observed that the muon content decreases at larger beam energies. Consequently the total number of pions increases. As expected the number of showers fully contained in the AHCAL (type 1) decreases with beam momentum. For systematic checks these numbers have been extracted separately for the three runs taken at each energy. The same percentage values have been found in each case.

# run	E_{beam} [GEV]	N_{tot}	muon	all	pion type 1	type 2	type 3
300628	6	284648	19%	28%	25%	2%	1%
300643	8	300808	11%	34%	27%	5%	2%
300613	10	584423	10%	35%	25%	7%	2%
300644	12	302771	8%	35%	23%	10%	2%
300614	15	589478	7%	35%	20%	13%	2%
300645	18	194038	6%	36%	18%	16%	2%
300616	20	580772	6%	35%	16%	17%	2%

Table 7.4: *Event selection statistics.*

7.5   Results

After the test-beam setup description and event selection considerations the following section shows some preliminary results obtained for the AHCAL.

7.5.1   Muon response and noise

The calibration chain has been already discussed in chapter 6. The main ingredients of the calibration chain have been extracted from dedicated runs before and after the October data taking run, and are summarised in figure 7.12. The results for the mip calibration factors are shown in figure 7.12 (a). The distribution of coefficients has a spread of ∼30 %. The gain calibration factors show a similiar spread in figure 7.12 (b). The ratio between these two values corrected for the electronic intercalibration gives the lightyield. The mean value of the light yield reproduces the design value of ∼15 pixel/mip and it has an expected spread of approximately 20 %.
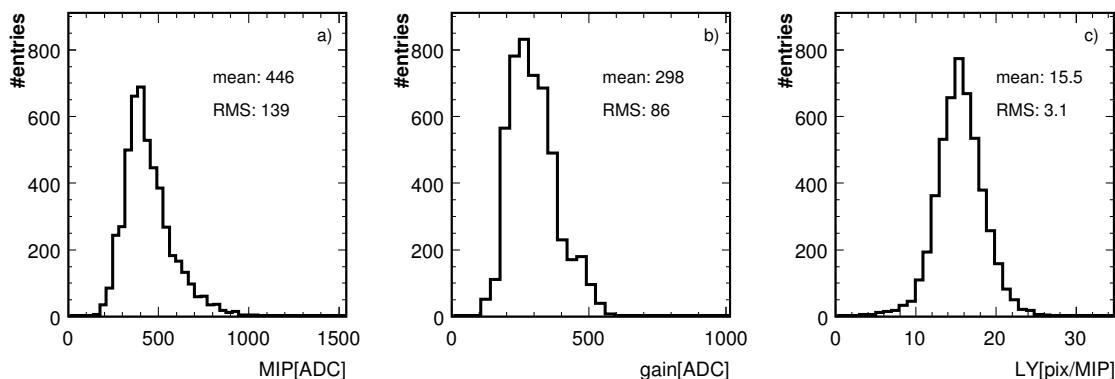
Figure 7.12: *Calibration results for the AHCAL. The distribution for mip (a), gain (b) and light yield (c) calibration factors are shown.*

The light yield calibration factor is important for the optimal operation of the AHCAL. The 15 pixel/mip are needed to have a mip distribution convoluted with the photo-statistics of scintillator tile, WLS fibre and SiPM, which has still a 99 % efficiency above a noise threshold cut of 1/2 mip. Therefore, the light yield affects the number of noise hits in the calorimeter, which has to be minimised to achieve sensitivity to the isolated neutral hits. These hits are spread over the complete calorimeter volume with no obvious connection and therefore they mix with random noise hits.

The stability of the calibration during the data taking period is a source of systematic uncertainties. In figure 7.13 the mip position as extracted from several pion runs at various energies have been compared. For this purpose the selected pion sample has been divided into three subsamples, each containing one run per energy. In the upper left plot an example of the noise distribution is shown. The MPV is around 90 MeV and has a spread of 70 MeV. The average number of observed noise hits is around 4. Therefore the average energy deposited by a noise hit is ∼20 MeV. The average number of hits contributing to a mip signal is ∼20. The difference of the muon response in this sample is small enough not to correct for it. In principle these muon events, which are in every pion run but concentrated in the fine core of the calorimeter, can be used to make a first level run-based calibration adjustment. The mip

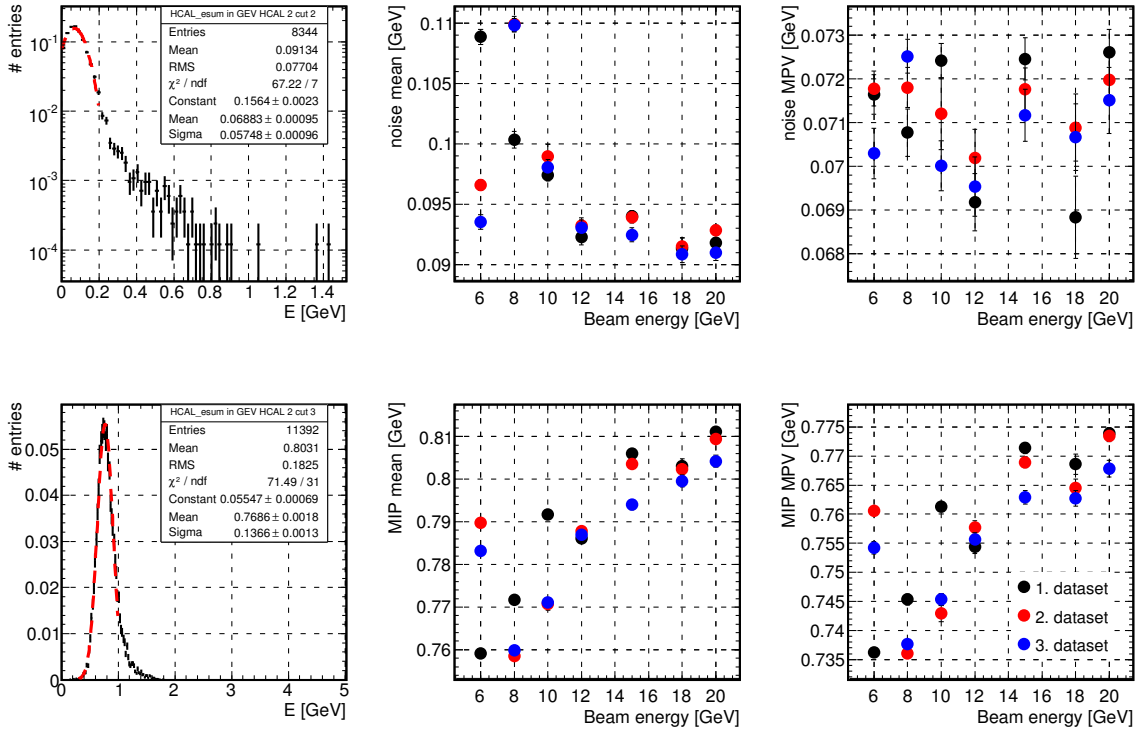Figure 7.13: *In the left upper plot an example of the noise spectrum of all channels is shown. In the same row the variation for different runs and energies are shown. The MPV of the noise distribution is stable within ±2.5 %. Also the mean value of the noise is for most of the runs stable within the same range. In the lower row the same plots are shown for the mip. The mip fluctuates in this sample within ±2.5 %.*

distribution is shown in the lower left plot, in which the Landau tail is partially cut due to the imposed cuts of the muon selection. The MPV is 0.8 GeV which does not include the noise occurring additionally in the calorimeter. From these numbers the average signal-to-noise ratio can be determined by calculating $mip/\sigma_{noise} = 0.8/0.06 = 13$. In the middle upper plot the mean of the noise distribution is shown versus energy and for the three subsamples. The same for the MPV is shown in the right most plot. The noise is stable within ±2.5 %. The same is true for the mip mean and most probale values presented in the lower centre and lower right plots.

7.5.2 Shower profiles

In the following only two of the defined topologies of pion showers are considered. The sample including all pions starting after the ECAL, and the subsample of showers fully contained in the AHCAL (type 1). In the text they will be referred to as *all pions* and *contained pions*. The data sample consists of the runs summarised in table 7.4.

As discussed in chapter 2 the longitudinal and transverse shower profile of a hadronic shower can be best looked at as a function of the number of interaction lengths. The interaction length for the AHCAL structure has been discussed in section 5.1 and is 22.84 cm. No simulation comparison for these differential properties is given since no detailed event selection is applied

in the MC.
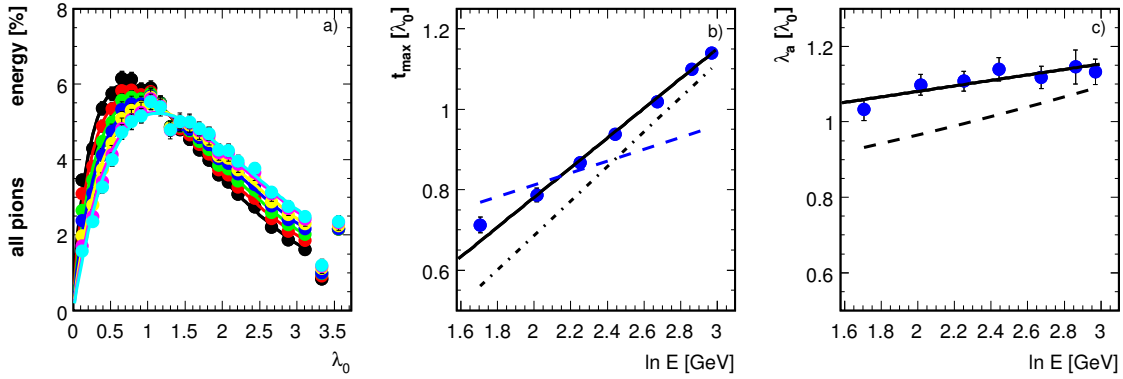
Figure 7.14: *Longitudinal shower profiles for pions from 6 to 20 GeV. All pions with no shower in the ECAL are selected. (a) Longitudinal profiles and their fit function. (b) Extracted shower maximum versus shower energy, parametrisation from reference [13] (blue dashed line) and from reference [14] (black dash-dotted line); and (c) attenuation length versus shower energy and parametrisation from reference [13].*

Figure 7.15: *Longitudinal shower profiles for pions from 6 to 20 GeV for the contained pions. (a) Longitudinal profiles and their fit function. (b) Extracted shower maximum versus shower energy, parametrisation from reference [13] (blue dashed line) and from reference [14] (black dash-dotted line); and (c) attenuation length versus shower energy and parametrisation from reference [13].*

The longitudinal shower profiles for all pions are shown in figure 7.14. The measured energy deposited as function of the depth in the calorimeter is parameterised according to the equation 2.10. This formula was originally derived for electromagnetic showers, but can also be used to describe the profile of hadronic showers. The showers penetrate deeper into the calorimeter with increasing hadron energy. As expected the position of the maximum is shifted proportionally to $ln(E)$. The second fit parameter is the attenuation length, which describes the exponential decay of the longitudinal distribution after the maximum. Whereas

a logarithmically increase of λ_a with beam energies is observed for the all pion selection, the opposite behaviour is valid for the contained pions. This is shown in figure 7.15 (c). In addition the two parameterisations for the shower maximum t_{max} introduced in section 2.3.3 are shown in figures 7.14 (b) and 7.15 (b). These curves are extracted from existing data of calorimeters with different materials and structures than the AHCAL. The disagreement of the two parameterisations with themselves and with the AHCAL data indicate the predictability limit of this method and the dependence on the event selection. A parametrisation for the attenuation length λ_a is shown in figure 7.14 (c). The curve is scaled to the value of λ_0 for the AHCAL and compared to all pion data. The energy trend of the data is reproduced by the parametrisation, but a shift of 10 % is observed.

Figure 7.16: *Transverse shower profiles for pions from 6 to 20 GeV for all pions. (a) Transverse profiles and their fit function. (b) First extracted exponential slope parameter versus shower energy; and (c) second extracted exponential slope parameter versus shower energy.*

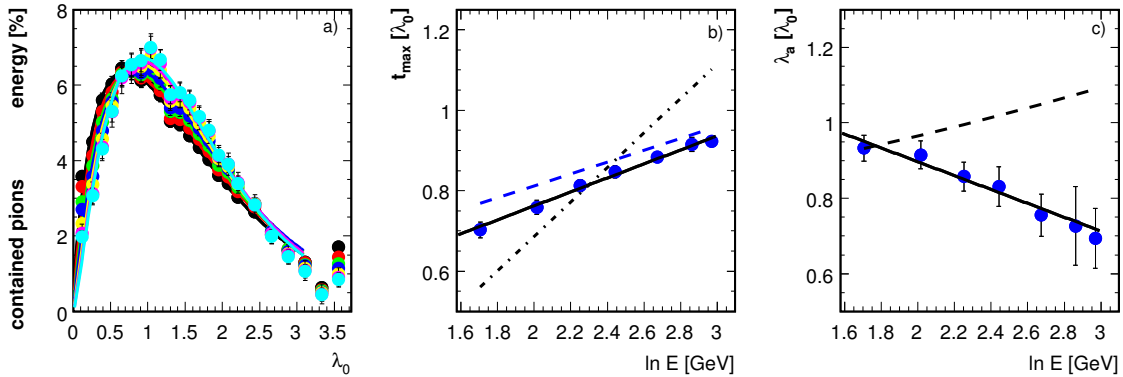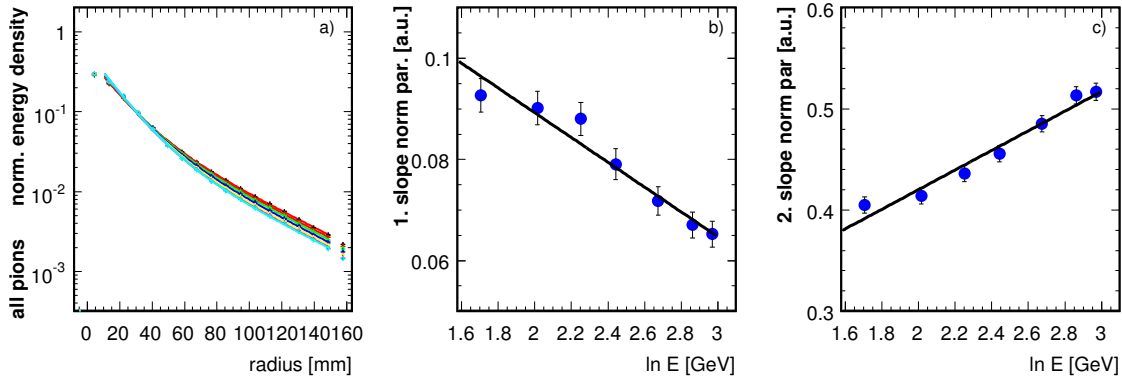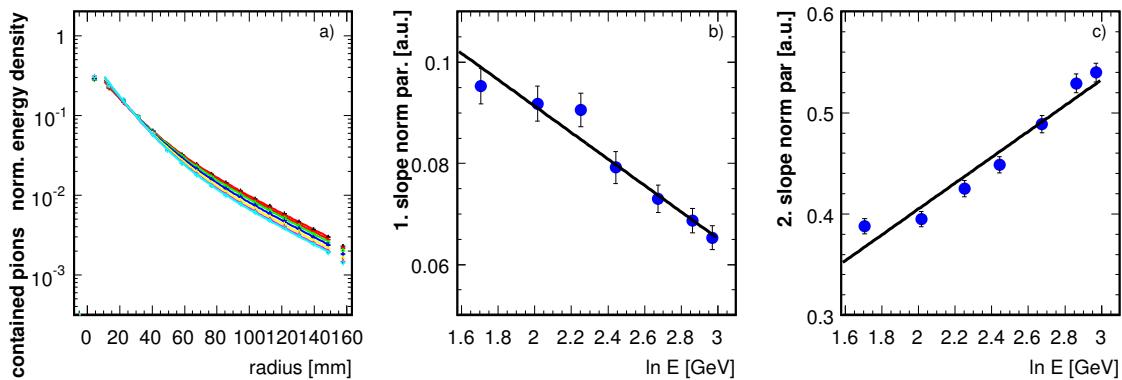

Figure 7.17: *Transverse shower profiles for pions from 6 to 20 GeV for the contained pions. (a) Longitudinal profiles and their fit function. (b) First extracted exponential slope parameter versus shower energy; and (c) second extracted exponential slope parameter versus shower energy.*

The transverse shower profile for all pions is shown in figure 7.16. The distribution is

limited to the fine granulated core of the calorimeter, and is parametrised using equation 2.15. In the middle and right plots the dependence on energy of the two contribution parameters is shown. Both fit parameters are linearly dependent on energy as shown by the fit line superimposed to the data points. The same plots are shown in figure 7.17 for the contained pions and the same conclusions are valid. The pion selection criteria do not influence the lateral distribution of the shower.

(a) 10 GeV/c   (b) 15 GeV/c   (c) 20 GeV/c
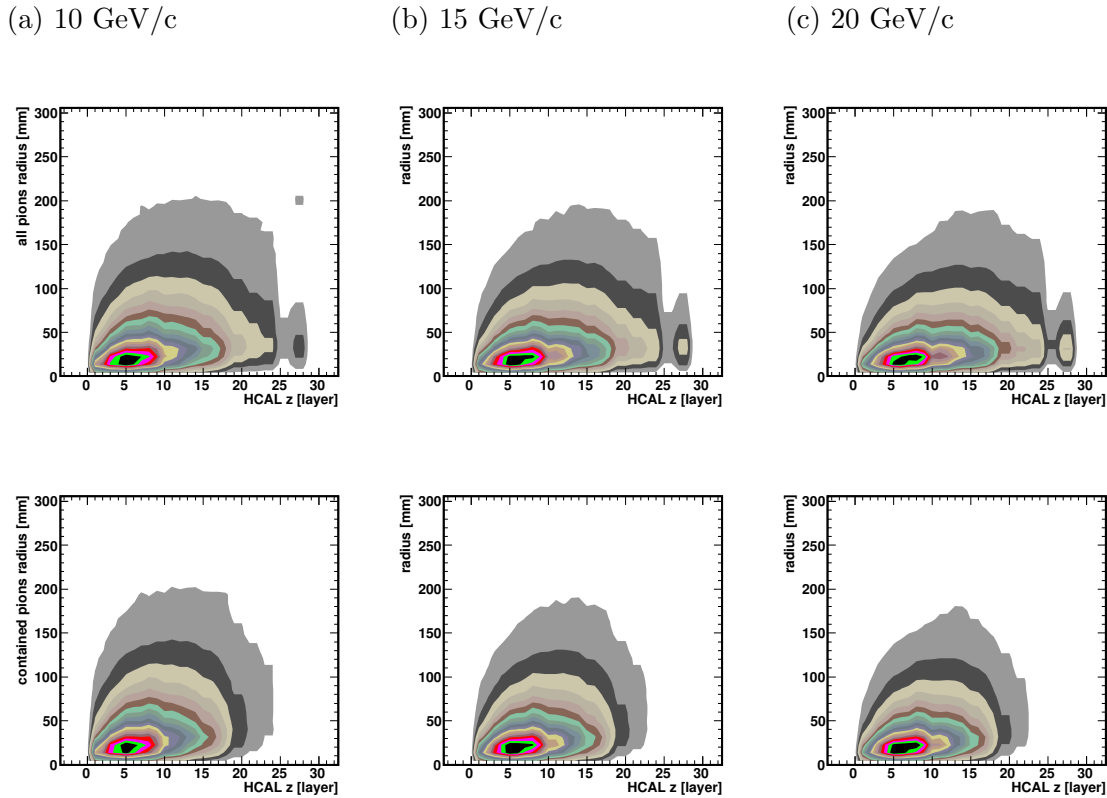
Figure 7.18: *Transverse versus longitudinal shower distribution for pion runs of* 10, 15 *and* 20 *GeV/c. The top row shows the data for all pions and the bottom row for the contained pions. The energy is increasing from left to right. The edge shape in the last layers in the upper row is due to a inefficient module in the next to last position.*

In figure 7.18 the transverse shower distribution is plot versus layer number for pion runs of 10, 15 and 20 GeV. Top and bottom rows of plots compare the shapes for all and contained pions. The longitudinal compression due to the event selection is visible.

7.5.3 Energy response and resolution

For the pion energy response and resolution studies the mip scale is converted to hadron scale fixing the conversion factor at the 10 GeV energy point. Figure 7.19 (a) shows an example of the energy sum distribution for all and contained pions for a beam energy of 10 GeV. The calorimeter response versus beam energy for both selections is shown in figure 7.19 (b). The data points of the contained pion sample is shown by black circles and the data points of the all pion sample by red squares. The MC prediction for all pions is presented by the blue triangles.

The linearity has a slope consistent with 1 for both selections and for the MC. In 7.19 (c) the energy resolution is extracted from the data using equation 2.35, where the noise term c is forced to be 0. The resolution at each energy of the contained pions is $\sim$10 % better than that of the all pion sample, because in this sample there is no leakage fluctuation and the fluctuations on the electromagnetic component are reduced artificially by the selection, this point will be confirmed in the next section 7.5.4. The fit to the energy resolution of the all pion sample gives a constant term of 7.7 % whereas the fit to the contained pion sample is not sensitive to the constant term. The energy resolution is around 64 % for the all pion sample and slightly better for the contained pions (61 %). The MC, which is also used in the next section 7.5.4, predicts for these kind of events 56 %. This prediction differs for various MC (see figure 2.5). It has to be noted that no detector smearing and realistic noise treatment is included in the MC.
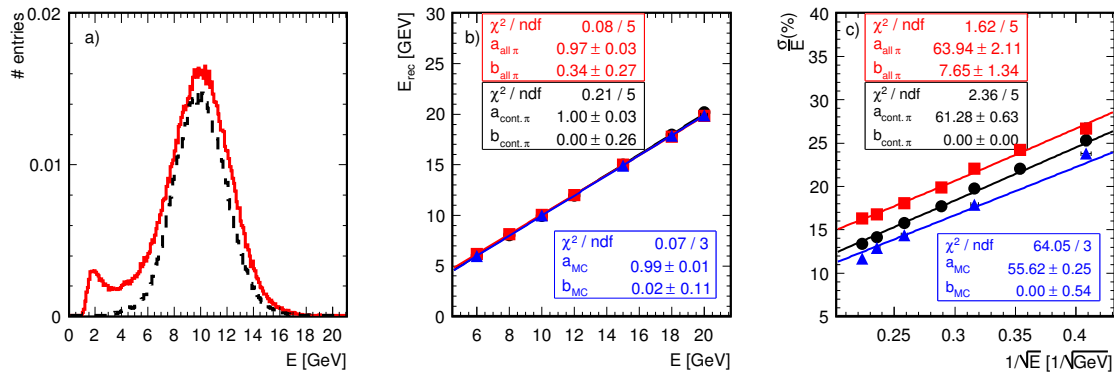
Figure 7.19: *(a) Example of energy sum for all pions (red closed line) and contained pions (black dashed line). (b) Linearity of the reconstructed energy and (c) energy resolution versus beam energy all pions (red squares), for contained pions (black circles) and for the MC prediction (blue triangles).*

7.5.4 First look into the deep analysis results of hadronic showers

The deep analysis procedure has been introduced in section 2.5.2. The main purpose of this method is to identify the different internal contributions to a hadron shower. The hit energies at the mip scale are input to the deep analysis algorithm, which returns the energy contributions clustered according to four categories (E_{EM}, E_{TRK}, E_H and E_N). These contributions still at the mip scale are converted to the hadron energy scale with the same factor applied in section 7.5.3. In the future analysis individual weights can be applied to scale these four contributions separately. This weighting compensation is not applied in the following.

Before running the algorithm on data a MC study has been performed to judge the quality of the reconstruction. The MC is based on Geant3 and uses the hadronic physics of CALOR, FLUKA and MICAP. The MC distributions for 6, 10, 15, 18 and 20 GeV pion showers are generated. The first check is to compare the correlation of energy versus number of hits for the total sum and for the sum of the contributions identified by the deep analysis. In figure 7.20 these correlations are shown for the three energies increasing from left to right. The upper row are true MC results obtained from the total energy sum and total number of hits in the event, whereas the lower row shows the result obtained by adding the contributions extracted

with the deep analysis. Despite of a small tendency to overestimate the energy the clustering distributions well reproduce the true MC distributions. The plots are shown in logarithmic scale and the energy in the tails is about 0.5 %.
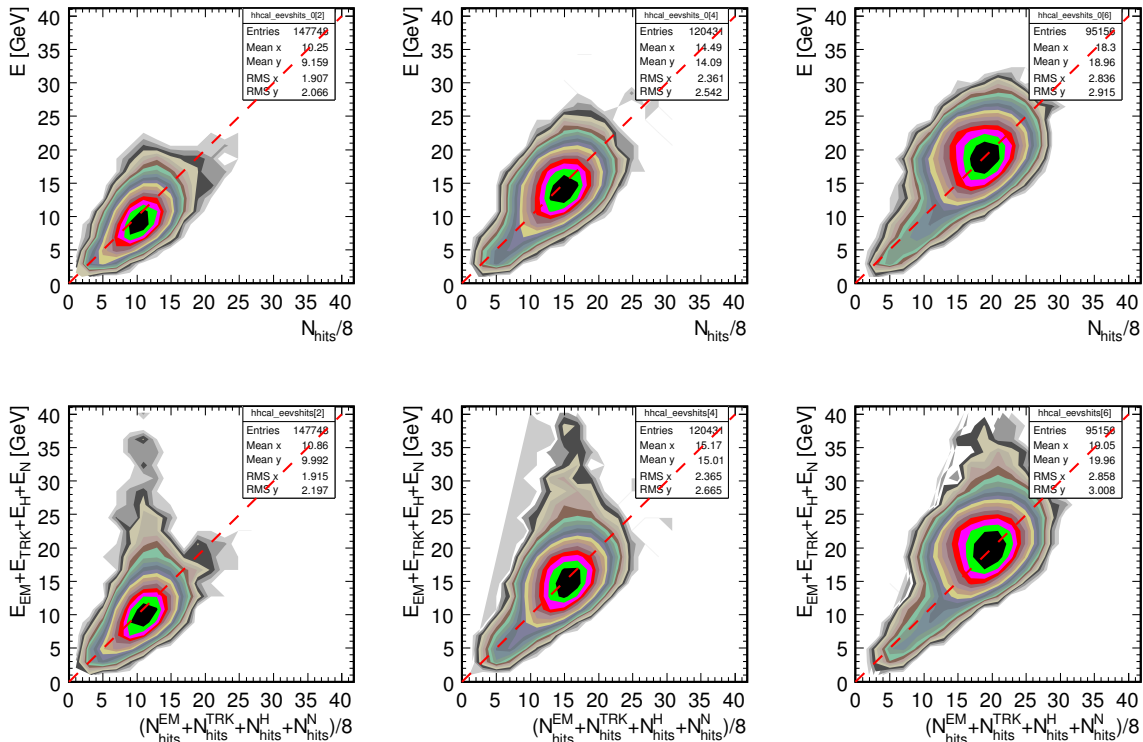
Figure 7.20: *Correlation between reconstructed energy and number of hits in MC. From left to right the simulated energy increases, 10, 15 and 20 GeV. The upper row shows the total sum and the lower row the sum of the contributions identified by the deep analysis.*

The reconstructed energy of the electromagnetic clusters have been obtained and the difference to the MC truth has been calculated. The MC truth is the energy of created π^0 plus the energy of γ. These differences are shown in figure 7.21 (a). The tails occurring on both sides of the mean Gaussian part have different origins. The tail to negative values is due to leakage. Therefore it grows with the beam energy. The tail to positive values is due to misclassification of hadron or track like hits to electromagnetic ones. This occurs in case of dense nuclear interactions in which many particles are created. The spread of these distributions (shown in figure 7.21 (c)) is around 2 GeV and is a measure of the precision of the clustering. The same simulations are used to get a MC prediction for the rates of the different hadronic shower contributions. The obtained distributions are shown in figure 7.22 and the results are summarised in table 7.5. These results are comparable to the event type in which no shower has started in the ECAL and leakage to the TCMT is allowed (all pions).

Afterwards the same algorithm has been used for the data and the obtained distributions are shown in figure 7.23 (a)-(d). In figure 7.23 (e) (figure 7.23 (f)) the mean values for the different distributions are plotted versus beam energy for all pions (contained pions). The results are summarised in table 7.5 for both selections. Comparing the data results to the MC a tendency becomes clear. The MC predicts higher amount of neutral energy than measured.
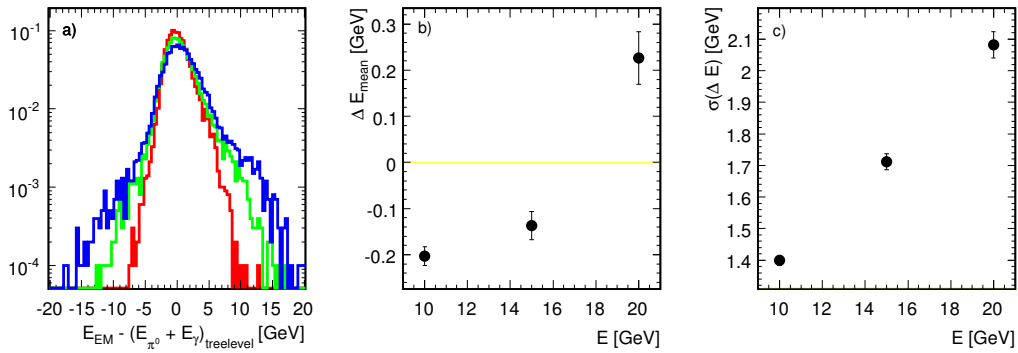
Figure 7.21: *(a) Difference of the reconstructed energy of the electromagnetic clusters obtained from the deep analysis to the MC truth (ΔE). (b) MPV value of ΔE versus beam energy. (c) Spread of ΔE versus beam energy.*
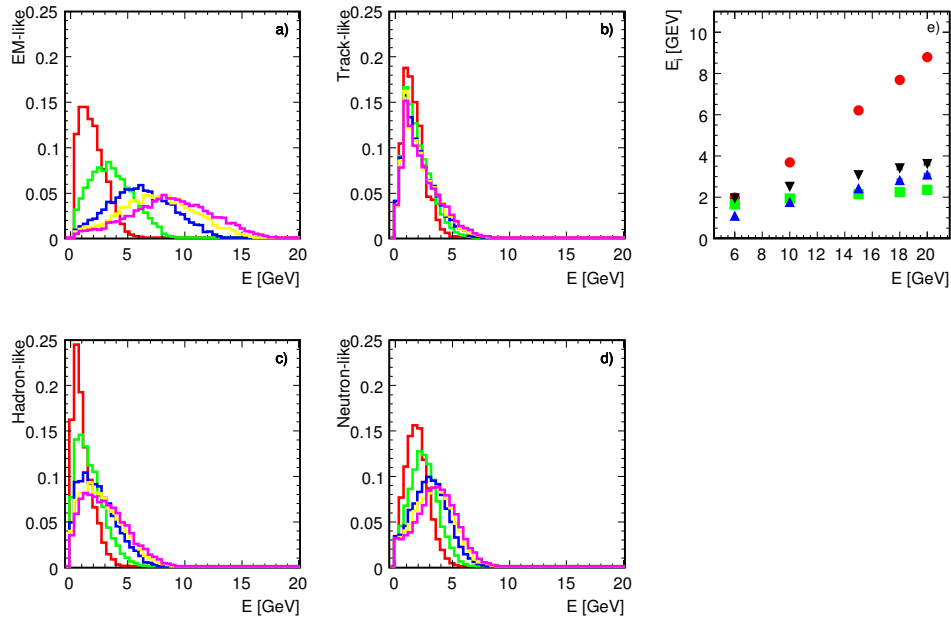
Figure 7.22: *(a)-(d) Deep Analysis result of the different cluster contributions in 6, 10, 15, 18 and 20 GeV pion showers obtained from MC. (e) Summary of the cluster contribution mean values versus beam energy for all pions.*

Instead the measured hadron-like and track-like contributions are at 20 GeV higher than in MC. The sum of the four contributions do not add up to the initial energy in the all pion sample, because leakage occurs. This is indicated by the last column in table 7.5, where the energy sum of all contribution is given. In case of the contained showers in the data the initial energy is reproduced by the reconstruction.
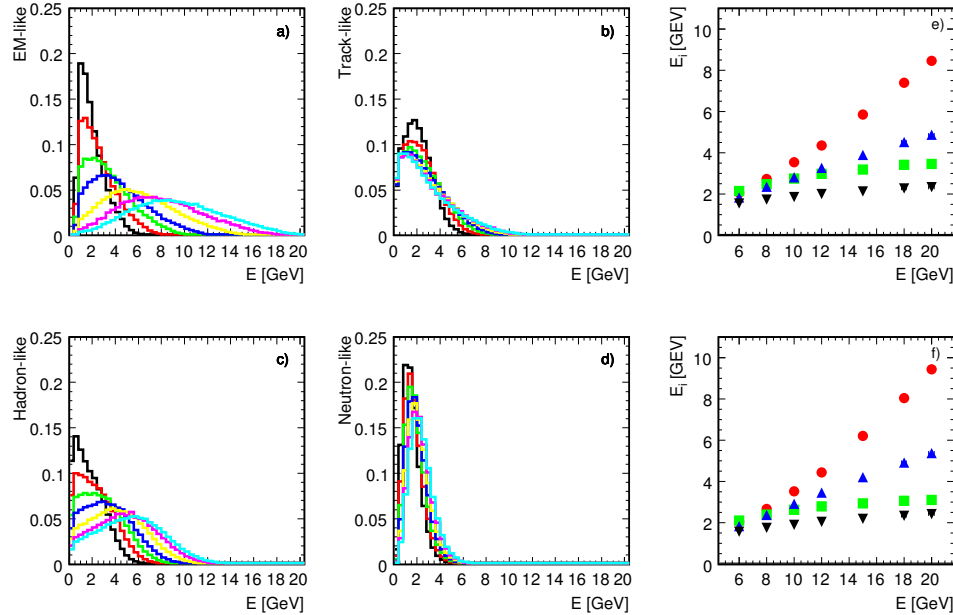
Figure 7.23:   (a)-(d) Deep Analysis result of the different cluster contributions in 6 to 20 GeV pion showers obtained from data. (e) Summary of the cluster contribution mean values versus beam energy for all pions. (f) Summary of the cluster contribution mean values versus beam energy for contained pions.

An additional comparison is performed for the correlation between the electromagnetic-like cluster energy versus the sum of the three other cluster types: track-like, hadron-like and neutral-like. The MC prediction in figure 7.24 shows a slope of −1 and a clear correlation for the energy points 10, 15 and 20 GeV. The same analysis has been applied to the selected data sample and the results are illustrated in figure 7.25 (a) for contained pions and in (c) for all pions. The solid lines guide the eyes to a slope of −1. Although a clear correlation is visible the slope is not −1. The response of the electromagnetic-clusters is higher than the response to the other three clusters. From figure 7.25 (a) the rotation parameters are extracted to obtain the distribution in (b). The same parameters are applied to rotate the distribution in figure 7.25 (c) into (d). Comparing figure 7.25 (d) to the MC prediction in figure 7.24 (c) it can be seen that the shape obtained from Geant3 with CALOR, FLUKA and MICAP models turned on is very different from the one obtained in data. The maximum of the distribution is in the data closer to the hadronic contribution axis than in MC. This clearly indicates the need of further studies of MC models and data comparison.

This rotation is an attempt to achieve the compensation condition. This should reduce the influence of fluctuations, recover linearity and give the best energy resolution. In table 7.6 the different sampling fractions for electromagnetic and hadronic contributions are shown for different beam energies. These values have been obtained by multiplying the weights

E [GeV]	EM		TRK		hadron		neutron		sum	
	mean	RMS	mean	RMS	mean	RMS	mean	RMS	mean	RMS
MC										
6	2.0	1.2	1.7	1.0	1.1	0.9	1.9	1.0	5.7	1.9
10	3.7	1.9	2.0	1.2	1.8	1.3	2.5	1.3	9.1	3.1
15	6.2	2.8	2.2	1.5	2.5	1.6	3.1	1.6	13.0	4.6
18	7.7	3.3	2.3	1.6	2.8	1.9	3.4	1.7	15.1	5.7
20	8.8	3.6	2.4	1.7	3.1	2.0	3.6	1.8	16.6	6.3
all pions										
6	2.1	1.1	2.1	1.3	1.8	1.3	1.5	0.9	5.9	1.8
10	3.5	2.1	2.8	1.8	2.8	1.9	1.9	1.1	9.5	3.0
15	5.9	3.2	3.2	2.3	3.9	2.5	2.1	1.3	13.7	4.6
18	7.4	3.8	3.4	2.5	4.5	2.8	2.3	1.3	16.2	5.5
20	8.5	4.2	3.5	2.6	4.9	3.0	2.3	1.4	17.7	6.1
contained pions										
6	2.0	1.1	2.1	1.3	1.8	1.3	1.6	0.8	6.1	1.6
10	3.5	2.0	2.6	1.7	2.9	1.8	1.9	0.9	10.0	2.2
15	6.2	3.1	2.9	2.1	4.2	2.4	2.2	1.0	15.0	2.7
18	8.0	3.6	3.1	2.3	4.9	2.6	2.3	1.1	17.9	2.8
20	9.4	3.9	3.1	2.4	5.4	2.8	2.4	1.1	20.0	6.1

Table 7.5:   *Mean energies and RMS in GeV for the intrinsic hadron shower contributions as extracted by the deep analysis algorithm on MC and data.*

Figure 7.24:   *MC prediction for the correlation between electromagnetic-like cluster energy versus the sum of the three other cluster types: track-like, hadron-like and neutral-like. Increasing pion shower energy from 10 GeV in (a), 15 GeV in (b) and 20 GeV in (c). A dashed guide-line of slope -1 is superimposed.*

(extracted from the rotation procedure) for the contributions by the muon sampling fraction value of $\mu_{coeff} = 29.5$ and by the e/π ratio to scale back to the beam energy. From the electromagnetic analysis it is known that the energy conversion coefficient for electrons and positrons is $e_{coeff} = 27.8$. This leads to a e/μ of 0.94 which is consistent with values from literature (see section 2.4.1). The given μ/π values in table 7.6 can be converted to e/π ratios utilising the multiplicative factor $1 + \mu_{coeff}/e_{coeff} = 1.065$. A summary of all obtained particle response ratios is given in table 7.7. The e/h ratio is the same for both selections,
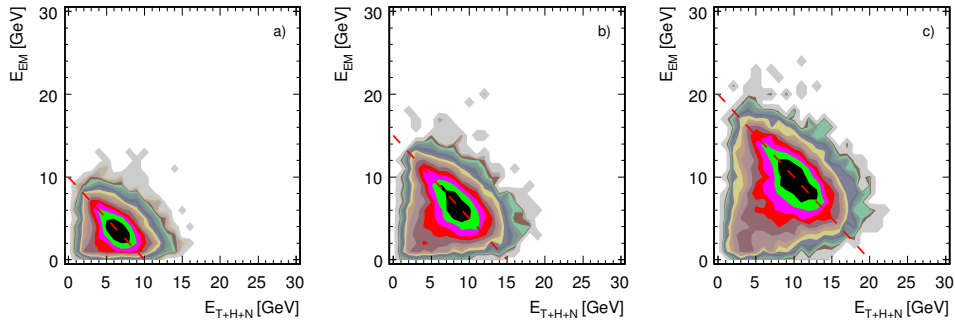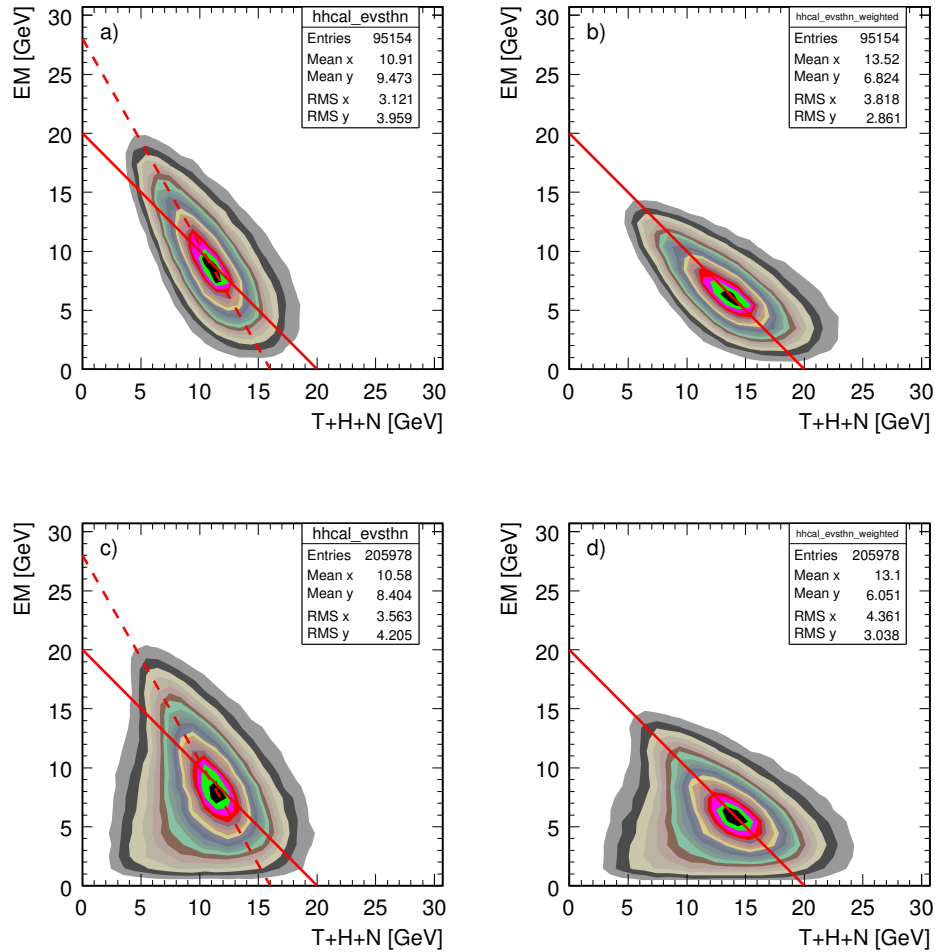
Figure 7.25: *Correlation between electromagnetic-like cluster energy versus the sum of the three other cluster types: track-like, hadron-like and neutral-like in a 20 GeV/c pion run. The left plot shows the correlation before weighting of the different contributions and the right plot after. A solid guide-line of slope −1 is superimposed.*

but decreases with beam energy from 2.5 at 6 GeV to 1.7 at 20 GeV. In contrast to this the e/π ratios for both selections stay fairly stable with beam energy changes, but it differs by ≈7 % between the two selections. Since the electromagnetic contribution in the contained pion sample is larger, the e/π ratio decreases in comparison to the all pion sample. The e/h is event selection independent, because the response to the different contribution is a stable hardware property. The e/h (or SF_{THN}/SF_{EM}) dependence on the beam energy is shown in figure 7.26 (c). An uncertainty of 3 % is assigned from the fit uncertainty to extract the rotation weights.

The deep analysis of hadronic showers gives the possibility to extract internal contributions to a hadronic shower. This allows the unprecedented measurements of the electromagnetic fraction and the innovative separation of the hadronic fraction into three sub-components, hadron-like, track-like and neutron-like. It also offers in the future the possibility to apply individual weights to each independent component, thereby improving the energy resolution of

E_{beam} [GEV]	all pions			contained pions		
	SF_{EM}	SF_{THN}	SF_{THN} / SF_{EM}	SF_{EM}	SF_{THN}	SF_{THN} / SF_{EM}
6	17.7	44.9	2.5	17.3	43.9	2.5
8	20.3	48.0	2.4	19.8	46.6	2.4
10	22.6	50.0	2.2	21.9	48.6	2.2
12	25.6	50.0	2.0	24.7	48.2	2.0
15	27.7	50.4	1.8	26.5	48.2	1.8
18	30.6	50.7	1.7	28.9	47.8	1.7
20	30.4	51.2	1.7	28.6	48.3	1.7

Table 7.6: *Summary of the different sampling fractions obtained for electromagnetic and hadronic contributions for various beam energies.*

E_{beam} [GEV]	all pions		contained pions		e/h
	μ/π	e/π	μ/π	e/π	
6	1.36	1.45	1.33	1.42	2.4
8	1.38	1.47	1.34	1.43	2.3
10	1.39	1.48	1.35	1.44	2.2
12	1.40	1.49	1.35	1.44	1.9
15	1.40	1.49	1.34	1.43	1.8
18	1.42	1.51	1.34	1.43	1.6
20	1.41	1.50	1.33	1.42	1.7

Table 7.7: *Summary of the different particle response ratios obtained for all pions and contained pions. The e/h is for both selections the same.*
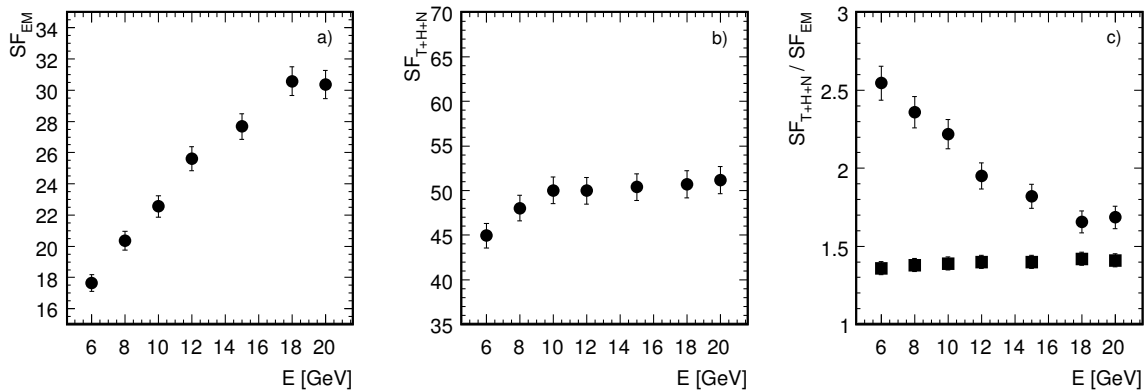
Figure 7.26: *Sampling fractions for electromagnetic (a) and hadronic contributions (b) versus beam energy for all pions. (c) Ratio of both sampling fractions which is equivalent to the e/h ratio (circles). In addition, the e/π ratio is shown in squares.*

single pions. All the discussed results are preliminary. The next steps are systematic studies with the deep analysis procedure, e.g. influence of noise. Detailed MC studies involving different hadron shower model implementations can help to understand the differences of the clustering behaviour. Having the systematic under control a weighting procedure can be developed and applied to test this compensation approach.

7.6   Conclusion

The first operation experience of the AHCAL in a hadronic test-beam has been discussed. The beam-line properties and steering have a major impact on the data quality. The CAL-ICE test-beam setup including all calorimeter prototypes and additional detectors has been introduced.

A subsample of low momentum pions has been selected for the purpose of this analysis. Hadronic showers started in the AHCAL only are considered. Event selection criteria rejects approximately 60-70 % of the data. The largest rejection is necessary to minimise the energy loss by the pion traversing the ECAL. An integrated analysis of the hadronic shower shows a good linear response in the range 6 to 20 GeV, thus confirming the quality of the calibration chain.

The highly granular lateral and longitudinal segmentation of the calorimeter is used to extract the energy dependence of the longitudinal shower development and of the shower radius. Although the trend of the energy dependence agrees with expectations the direct comparison to parameterisations from literature is not satisfactory. This may be due to the specificity of these parameterisations for a given calorimeter structure. Comparison to MC is required to validate the data. The e/π ratio for this calorimeter is extracted from real data and found to be between 1.4-1.5 depending on the energy. To extract the e/h ratio the knowledge of the electromagnetic fraction in the hadronic shower is required, which has been extracted with a deeper analysis.

An attempt to apply the deep analysis algorithm for hadronic shower decomposition has been made and first results are discussed. The extracted fractions of electromagnetic, hadronic, track-like and neutron components of the hadronic shower are presented. The energy depen-

dence of these fractions is reported. It should be stressed that numerical results from this part of the analysis have to be taken with care since the algorithm is still under development and a detailed systematic study could not be performed. Nevertheless, the qualitative message extracted from this first analysis is very powerful. It indicates the possibility to resolve the intrinsic composition of hadronic showers and in particular to access the neutron contribution.

Chapter 8

Summary and conclusions

The demands imposed by the high precision ILC physics require the optimisation of a detector for particle flow. The reconstruction of single particles in each event sets strong requirements on the calorimeter system. Unprecedented high granularity is mandatory for the lateral and longitudinal segmentation for both electromagnetic and hadronic calorimeters.

A technology choice for a hadronic calorimeter with analogue readout is outlined in this work. It consists of a sampling structure alternating steel and scintillator tiles. The smallest unit of the calorimeter is a tile-fibre system with integrated readout via a novel silicon-based photodetector, the SiPM. It has been proven that this photodetector fulfils the requirements for a ILC calorimeter to be placed inside a high magnetic field.

To establish the technology of this new photodetector a 100-channels technical prototype has been built and successfully operated. This prototype allowed the comparison of different readout solutions. The good agreement of SiPM readout with the more conservative readout option via photomultiplier tubes proves that the non-linear response of the SiPM is under control in the calibration chain. A detailed simulation of the technical prototype including detector response can predict the energy resolution obtained for electromagnetic showers.

The encouraging results obtained with this first prototype were the necessary step towards a large prototype to study hadronic shower reconstruction with the same readout technology. This has been realised in the AHCAL prototype.

The design and production steps of a ~8000 channels prototype are presented. The mass test of the tile-fibre systems including the SiPM has been carried out in Russia and identified production problems have been solved. The custom made electronics developed in France for the multi-channel readout of this large prototype is introduced. Characterisation studies of one complete readout channel confirm the compatibility of the system to SiPM readout. The result in term of noise of the combined system are satisfactory. The self-calibrating property of the SiPM can be exploited by a signal-to-noise separation of the single pixels of about 4 for LED calibration signals. The VFE electronics design for test-beam experiments allows the detection of a minimum physics signal equivalent to a mip with a signal-to-noise of 11. A multi-channel system has been successfully tested, thus establishing the complete calorimeter readout chain. A series of studies aimed to test all the relevant properties before the exposure of the calorimeter to test beam have been performed, which are in general satisfactory. One identified problem was a too high coherent electronic noise between channels, which has been solved by better filtering of the VFE electronics power line.

After the realisation of the first AHCAL module a series of tests have been performed at the DESY test-beam facility to establish the calibration procedure and to gain operation experience. The SiPM correction plays a major role in the analysis chain. To access the impact of non-linearity correction, the shower maximum condition have been reproduced utilising lead

absorber material in front of the active module. Corrections of the order of 10-25 % have been successfully applied to linearise the calorimeter response and match MC prediction. The uniformity of the first calorimeter layer is determined to be better than 5 %.

To properly test the AHCAL in a hadronic environment the CERN test-beam facility has been used to provide a beam matching the relevant momentum range of the ILC hadronic physics. As a combined effort of the CALICE collaboration three calorimeter prototypes for the ILC detector have been successfully installed and operated at the CERN SPS test-beam facility. During operation an accurate beam tuning was necessary to achieve best beam conditions, high intensity, small spread and good momentum resolution. The understanding of the beam monitoring, trigger system, particle identification and tracking detectors is necessary for an accurate event selection. The commissioning of the AHCAL was successful and led to more than 90 % detector up-time during data taking.

A full set of hadronic and electromagnetic data have been collected with the AHCAL in the energy range between 6-80 GeV/c for pions and 6-45 GeV/c for electrons. The electron data will serve to establish the calibration procedure by comparing the detector response to simulation for a well understood physics process. The hadron data set allows for the first time a comparison of all existing MC models to a set of highly granular segmented information on shower development.

For this analysis a subsample of pions from 6-20 GeV/c has been studied. Only those events for which the hadronic shower starts in the AHCAL are selected with the requirement of moderate energy loss in the ECAL. For this data the linearity of the AHCAL response is shown, which confirms the quality of the calibration chain. The highly granular lateral and longitudinal segmentation of the calorimeter is exploited in the reconstruction of shower profiles. The energy dependence of the longitudinal shower development and of the shower radius are extracted and their trend is found in qualitative agreement with expectations.

The e/π ratio for this calorimeter extracted from real data is found to depend on energy and varies between 1.4 at 6 GeV and 1.5 at 20 GeV. In a classical high energy calorimeter the extraction of the e/h ratio from e/π requires assumptions on the fraction of electromagnetic component in the hadronic shower. For the first time it is possible to experimentally access this quantity in the AHCAL. For this purpose the deep analysis algorithm for hadronic shower decomposition is applied. This algorithm separates intrinsic components of a hadronic shower. The electromagnetic fraction is extracted from pion data and is found to be energy dependent, about 35 % at 10 GeV increasing to 40-50 % at 20 GeV depending on the requirements on containment. From this information the e/h ratio is experimentally extracted. The deep analysis algorithm is furthermore used to extract the hadronic and the neutron contributions to the hadronic shower. This is an extremely powerful tool to decompose and separately compare the processes leading to hadronic shower development. By this means a new set of benchmarks for validation of MC models is made available which will be exploited in upcoming analysis. The present study confirms qualitatively the possibility to extract information of the intrinsic shower composition and opens the possibility for a new type of software compensation. By applying separate weights to the identified shower components the energy resolution is expected to improve. The next step of this analysis will be the attempt to obtain this improvement on real data. For this a phase of optimisation and tuning of the reconstruction algorithm is necessary and ongoing.

For the completion of the physics program of the AHCAL higher statistics of hadronic showers is required for various particle types and at various incident angles of the beam. Further tests are planned for summer 2007 at CERN with completely equipped ECAL and AHCAL prototypes mounted on a movable stage capable of vertical and horizontal movement and rotation around the vertical axis. Later in 2007 and during 2008 the CALICE installation will move

to Fermilab to exploit the low energy proton beam-line to collect data on protons and pions at energies as low as 2 GeV/c.

Appendix A

H6 beam tuning

A simplified view of the H6 beam-line at the SPS accelerator is given in figure A.1. The scheme represents the line as seen from the beam point of view, the red line indicates the spread of the beam at every point, i.e. its beta-function [1]. In this simplified scheme only the steering dipoles are indicated (B1-B7) while the focusing quadrupoles, responsible of any change slope of the beta-function line, are omitted. The trimmer dipoles indicated as triangles in the figure (TRIM1-TRIM6) are used to apply small correction to the main steering dipoles. The collimators (C1-C11) are indicated, in the plain where they are active, as filled segments at an arbitrary opening position. The upper and the lower drawing give the horizontal and the vertical plane, respectively.

A.0.1 H6 beam tuning procedure

After the SPS control room has established the T4 wobbling, which takes around 20 minutes the secondary beam for the H6 beam-line is fixed and the tuning of the beam-line can start. For this purpose the orbit down stream of the spectrometer magnet is adjusted to guide a beam of the selected momentum to the experiment situated in one of the three possible experimental areas H6A, H6B or H6C. It is the responsibility of the beam-line users to check and improve the quality of the alignment of the beam through all the magnets and to set collimators according to their needs in terms of intensity, purity and momentum resolution. Furthermore, the users can enhance the particle content of the beam (e or π) by means of selectable secondary targets and absorbers.
It is meant in this section to give a very basic introduction to the complicated art of beam steering, based on the experience during test beam and on the fruitful exchanges with the SPS beam-line coordinator Ilias Efthymiopoulos.

For every possible selection of secondary beam energy a file with reference current settings for all magnets is made available by the SPS beam-line coordinator. The first step of the tuning procedure is to adjust the momentum spread according to the experiment need. The momentum byte selection is performed by the collimators C3 and C8 in the vertical plane. In the beta-function diagram of figure A.1 these collimators are positioned at beam focus. This implies that the spatial coordinate of the beam is totally defined. For Heisenberg uncertainty principle the beam momentum in this point has his largest indetermination.
In other words, in the momentum phase-space the beam has in this point a flat distribution, which implies that C3 and C8 act in the momentum phase-space to cut the low and high

---

[1]The beta function describes the local amplitude of the oscillations around the reference trajectory.

Horizontal plane		Vertical plane	
Coll.	Setting [mm]	Coll.	Setting [mm]
C10	±5	C11	±30
C1	±5	C6	±30
C5	±30	C3	±3
C2	±10	C8	±3

Table A.1: *Suggested collimator settings for selection of beam momentum (magnet B3).*

momentum tails of the beam. The opening of C3 and C8 can be adjusted according to the empirical formula

$$\frac{\Delta p}{p} = \frac{\sqrt{C3^2 + C8^2}}{19.4}[\%], \tag{A.1}$$

where C3 and C8 are the full widths opening of these collimators in mm. From which results that a gap of about 10.0 mm in the momentum collimators results in a $\frac{\Delta p}{p} \sim 0.5\%$. For the case of our test experiment a collimator gap of 3 mm has been chosen to obtain $\frac{\Delta p}{p} < 0.25\%$. Due to hysterse effects and additional uncertainties in the magnetisation process the mean value p of the momentum distribution is also only known with a precision δp. The following equation A.2 is valid [101]

$$\frac{\delta p}{p} = 0.5\% \oplus \frac{150\ MeV/c}{p} \tag{A.2}$$

and has to be considered as systematic uncertainty for the determined calorimeter quantities.

Having decided on the momentum byte selection, one can proceed to tune the beam vertical plane. The collimator settings of table A.1 are a good starting point for the tuning. With these settings the beam is constrained in the horizontal plane (C1 and C10) while the vertical plane is left open (C11 and C6). With the help of the beam instrumentation tools, i.e. Multi-Wire Proportional Chambers (MWPC) and scintillator counters, it is possible to vary the current of the main vertical stearing dipole (B3 [2]) and focus the beam in the vertical direction. A focused beam is defined to have the highest count rate in the scintillator counters and the best zero-centred Gaussian-shape in the MWPC. Once the vertical plane is optimised, its possible to select a new configuration of collimator settings for the horizontal plane tuning. A suitable starting point is given in table A.2. In this case the vertical collimators are closed (C11 and C6) and the horizontal plane is left open for the tuning. The main bending magnet on the horizontal line is B1 [3], for which the focusing procedure has to be performed first. Subsequently, the influence of the magnets B2, B4, B7 [4] can be tested, but these magnets normally have a minor influence on the beam focusing.

After the magnet tuning is done the beam rate can be adjusted by closing the position collimators (C10, C1, C5, C11, C6). An important role to keep in mind to minimise beam halo is to reduce the rate using the far most collimators (C10 and C11) and use those closer to

---

[2]The bending magnet B3 is operated at around -300 A, the optimisation range is normally ± 1 A, in reasonable steps of 0.4 A.

[3]The bending magnet B1 is operated at around -400 A, the optimisation range is normally ± 20 A, in reasonable steps of 2 A.

[4]For the magnets B2, B4, B7 the same range and steps as for B3 can be used for the tuning procedure.

Horizontal plane		Vertical plane	
Coll.	Setting [mm]	Coll.	Setting [mm]
C10	±20	C11	±5
C1	±20	C6	±5
C5	±30	C3	±3
C2	±3	C8	±3

Table A.2: *Suggested collimator settings for first step of beam orbit tuning (magnet B1).*

Horizontal plane		Vertical plane	
Coll.	Setting [mm]	Coll.	Setting [mm]
C10	±4	C11	±4
C1	±3	C6	±3
C5	±3	C3	±3
C2	±3	C8	±3

Table A.3: *Example of collimator settings for 50 GeV secondary pion beam, after tuning.*

the target only to clean the halo. As a role of thumb from up to downstream each collimator should be either equal or maximum 1 cm more close than the previous one.
An example of used collimator settings for a 50 GeV secondary pion beam, with a rate of 10^4 particles per spill, is given in table A.3.

Figure A.1: *The H6 beam-line.*
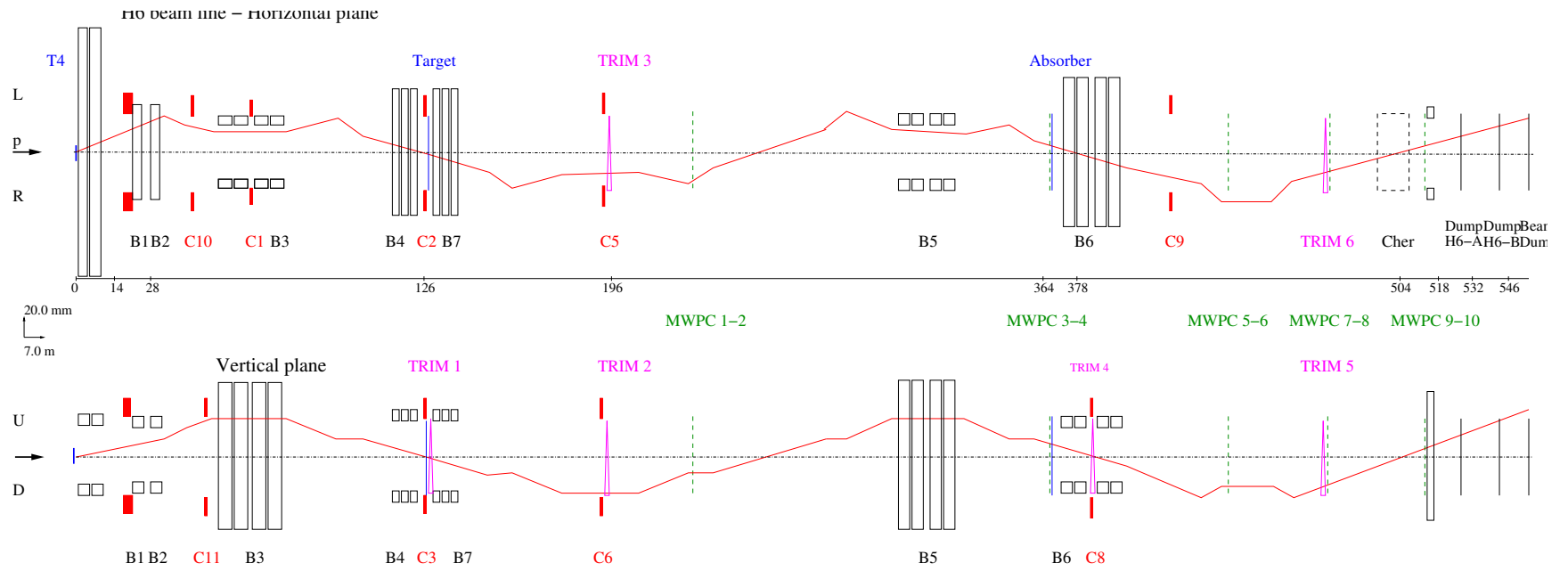
Figure A.2: *MWPC spectra along the beam-line for a 120 GeV pion beam.*

Figure A.3: *MWPC spectra along the beam-line for a 6 GeV pion beam.*

Appendix B

Pion analysis: event selection

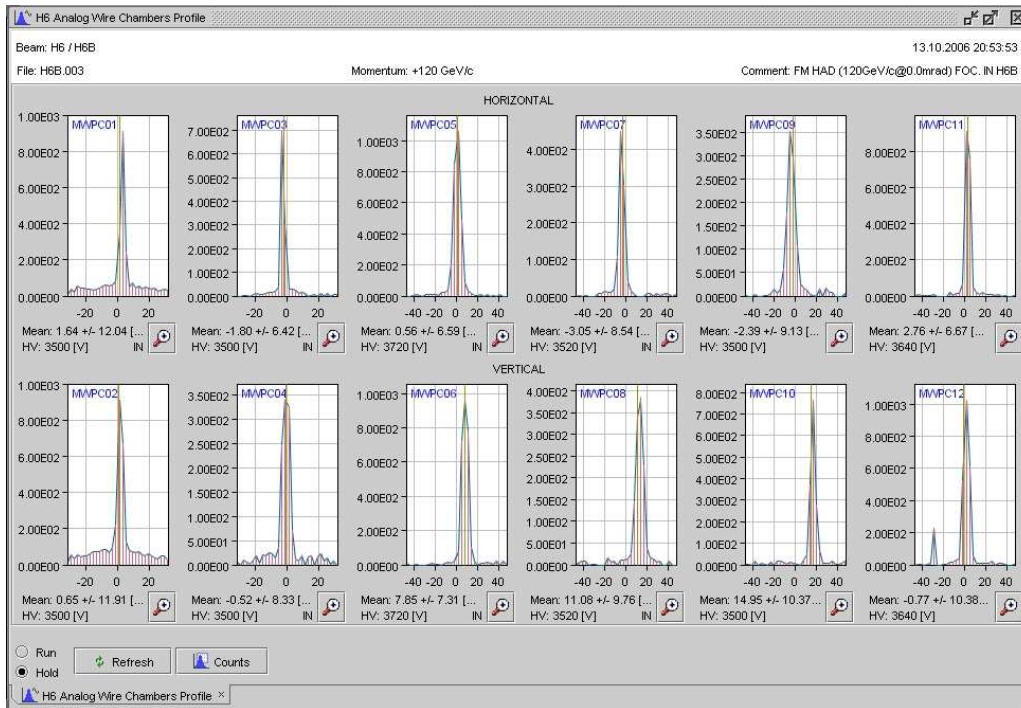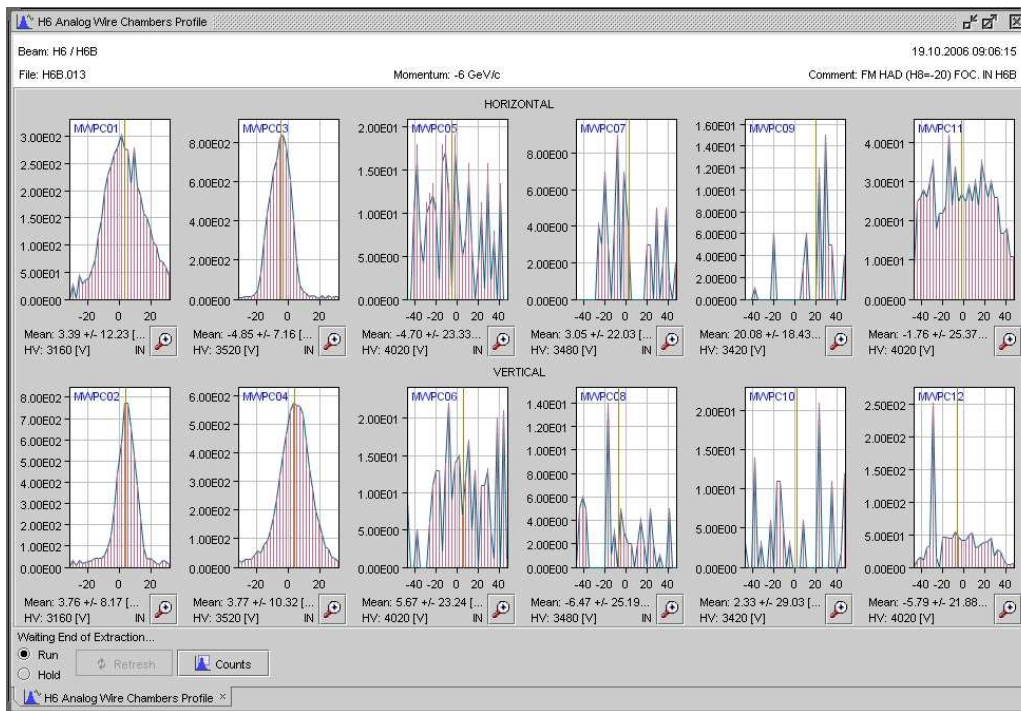| run number	E_{beam} [GEV]	N_{tot}	not us-able	low beam E	muon	all pi-ons	type 1	type 2	type 3
300628	6	284648	599	142363 50%	53364 19%	80117 28%	70303 25%	6211 2%	3603 1%
300629	6	301513	623	151298 50%	56312 19%	84706 28%	74270 25%	6596 2%	3840 1%
300630	6	379909	880	189522 50%	70564 19%	107914 28%	94578 25%	8472 4%	4864 1%
300643	8	300808	742	156654 52%	34020 11%	102157 34%	81372 27%	15138 5%	5656 2%
300647	8	124190	305	64976 52%	14324 12%	41700 34%	33016 27%	6305 5%	2383 2%
300648	8	280022	624	146061 52%	32172 11%	94672 34%	75477 27%	14008 5%	5187 2%
300613	10	584423	1538	298376 51%	60403 10%	202453 35%	147739 25%	43243 7%	11471 2%
300618	10	579599	1383	295248 51%	62476 11%	200116 35%	145495 25%	43335 7%	11286 2%
300660	10	296523	683	152456 51%	28690 10%	104698 35%	76079 26%	22817 8%	5802 2%
300644	12	302771	762	152859 50%	24821 8%	106504 35%	70682 23%	29703 10%	6119 2%
300649	12	299048	740	152070 51%	23195 8%	105570 35%	70226 23%	29315 10%	6029 2%
300653	12	288044	700	146149 51%	22763 8%	102654 36%	68085 24%	28638 10%	5931 2%
300614	15	589478	1513	296037 50%	38373 7%	207954 35%	120429 20%	76026 13%	11499 2%
300619	15	582529	1484	292730 50%	38865 7%	198104 34%	114634 20%	72525 12%	10945 2%
300659	15	390288	1073	196336 50%	25624 7%	137567 35%	79565 20%	50282 13%	7720 2%
300645	18	194038	540	96125 50%	11392 6%	69643 36%	35406 18%	30338 16%	3899 2%
300646	18	248463	705	123559 50%	14256 6%	88152 35%	44726 18%	38601 16%	4825 2%
300650	18	291449	821	144648 50%	16328 6%	104195 36%	52785 18%	45626 16%	5784 2%
300616	20	580772	1712	285118 49%	33061 6%	205978 35%	95154 16%	99299 17%	11525 2%
300620	20	634214	1740	312194 49%	36419 6%	223231 35%	102525 16%	108372 17%	12334 2%
300658	20	289731	819	143177 49%	15764 5%	103074 36%	47503 16%	49886 17%	5685 2%

Table B.1: *Event selection statistics. For each run the total number of events N_{tot} is divided in not considered events (not usable & low beam E), muons and pions following the pion event types introduced in figure 7.11.*

Bibliography

[1] *Memorandum to the PRC, from the proposal 01/02*, http://polywww.in2p3.fr/flc/calice_offic.html (2001).

[2] V. Korbel, *A scintillator tile hadron calorimeter for the linear collider detector*, Proc. of 9th Topical Seminar on Innovative Particle and Radiation Detectors, Siena (2004).

[3] F. Sefkow, *Performance goals and design considerations for a linear collider calorimeter*, Proc. of Calor2004, Perugia (2004), LC-DET-2004-022.

[4] V. Morgunov, *Calorimeter design with energy-flow concept*, Proc. of Calor2002, CAL-TECH (2002).

[5] E. Garutti, M. Groll, A. Karakash, and S. Reiche, *Magnetic field dependence studies for silicon photomultiplier* LC-DET-2004-025.

[6] V. Andreev *et al.*, *A high granularity scintillator hadronic-calorimeter with SiPM readout for a linear collider detector*, Nucl. Instrum. Meth. **A540**(2005) 368.

[7] E. Garutti, *Results from the first tile-HCAL prototype* LC-DET-2004-021; Prepared for International Conference on Linear Colliders (LCWS 04), Paris, France, 19-24 Apr 2004.

[8] Particle Data Group Collaboration, W. M. Yao *et al.*, *Review of particle physics*, J. Phys. **G33**(2006) 1.

[9] R. Wigmans, *Advances in hadron calorimetry*, Ann. Rev. Nucl. Part. Sci. **41**(1991) 133.

[10] Y.-S. Tsai, *Pair production and bremsstrahlung of charged leptons*, Rev. Mod. Phys. **46**(1974) 815.

[11] Y.-S. Tsai, *Die Einzelprozesse der Elektronen und Lichtquanten*, W. Heisenberg (Hrsg.), Kosmische Strahlung, Springer-Verlag, Belin (1953).

[12] *Nist scientific and technical databases*, http://www.nist.gov/srd/.

[13] C. Leroy and P.-G. Rancoita, *Physics of cascading shower generation and propagation in matter: principles of high-energy, ultrahigh-energy and compensating calorimetry*, Rep. Prog. Phys. **63**(2000) 505.

[14] S. Iwata, *Calorimeter* DPNU-13-80.

[15] U. Amaldi, *Fluctuations in calorimetry measurements*, Phys. Scripta **23**(1981) 409.

[16] H. W. Bertini, *Intranuclear-cascade calculation of the secondary nucleon spectra from nucleon-nucleus interactions in the energy range 340 to 2900 MeV and comparisons with experiment*, Phys. Rev. **188**(1969) 1711.

[17] R. Wigmans, *On the role of neutrons in hadron calorimetry*, Rev. Sci. Instrum. **69**(1998) 3723.

[18] H. Bruckmann, B. Anders, U. Behrens, P. Cloth, and D. Filges, *On the theoretical understanding and calculation of sampling calorimeters* , Invited talk presented at the 26th Winter Meeting on Fundamental Physics, Sevilla, Spain, Feb 23-27, 1987.

[19] C. W. Fabjan and T. Ludlam, *Calorimetry in high-energy physics*, Ann. Rev. Nucl. Part. Sci. **32**(1982) 335.

[20] R. Wigmans, Nucl. Instrum. Meth. **A259**(1987) 389.

[21] R. Wigmans, *High resolution hadronic calorimetry*, Nucl. Instrum. Meth. **A265**(1988) 273.

[22] T. A. Gabriel, D. E. Groom, P. K. Job, N. V. Mokhov, and G. R. Stevenson, *Energy dependence of hadronic activity*, Nucl. Instrum. Meth. **A338**(1994) 336.

[23] Y. A. Kulchitsky and V. B. Vinogradov, *Analytical representation of the longitudinal hadronic shower development*, Nucl. Instrum. Meth. **A413**(1998) 484, `hep-ex/9903019`.

[24] Serpukhov-Brussels-Annecy(LAPP) Collaboration, F. Binon *et al.*, *A hodoscope calorimeter for high-energy hadrons*, Nucl. Instr. Meth. **174**(1980) 369.

[25] H. Fesefeldt, *Punch through simulations* , Prepared for ECFA Large Hadron Collider (LHC) Workshop: Physics and Instrumentation, Aachen, Germany, 4-9 Oct 1990.

[26] H1 Calorimeter Group Collaboration, B. Andrieu *et al.*, *Results from pion calibration runs for the h1 liquid argon calorimeter and comparisons with simulations*, Nucl. Instrum. Meth. **A336**(1993) 499.

[27] J. P. Borders, *Optimization of jet energy resolution and response of the D0 detector* FERMILAB-THESIS-1994-04.

[28] Geant4 collaboration Collaboration, J. P. Wellisch, *Object oriented software for low energy neutron interactions* .

[29] J. Birks, Proc. Phys. Soc. **A 64**(1951).

[30] GEANT4 Collaboration, S. Agostinelli *et al.*, *Geant4: A simulation toolkit*, Nucl. Instrum. Meth. **A506**(2003) 250.

[31] H. Fesefeldt, *The e/h ratio and energy resolution of hadron calorimeters*, PITHA **86/05**(1986).

[32] F. Ballarini *et al.*, *The FLUKA code: An overview*, J. Phys. Conf. Ser. **41**(2006) 151.

[33] A. Ferrari, P. R. Sala, A. Fasso, and J. Ranft, *FLUKA: A multi-particle transport code (program version 2005)* CERN-2005-010.

[34] T. A. Gabriel, J. D. Amburgey, and B. L. Bishop, *'CALOR': A monte carlo program package for the design and analysis of calorimeter systems* ORNL/TM-5619.

[35] C. Zeitnitz and T. A. Gabriel, *The GEANT - CALOR interface and benchmark calculations of ZEUS test calorimeters*, Nucl. Instrum. Meth. **A349**(1994) 106.

[36] V. Morgunov, *Attempt to estimate the prediction power of the calorimeter properties following from different hadron models in the simulation programs; and the systematic errors of such predictions*, Presentation given at *the ECFA Workshop, Montpellier*, 2003.

[37] G. Mavromanolakis, *Comparison of hadronic shower packages*, Presentation given at *the International Conference on Linear Colliders LCWS 2004, Paris*, 2004.

[38] V. Morgunov and A. Raspereza, *Novel 3D clustering algorithm and two particle separation with Tile HCAL*, Presentation given at *the International Conference on Linear Colliders LCWS 2004, Paris*, 2004.

[39] G. Weiglein, *Physics interplay of the LHC and the ILC*, arXiv:hep-ph/0410364. (2004) 485.

[40] *International linear collider reference design report*, ILC-REPORT-2007-001 (2007) 217.

[41] G. Materlik and T. Tschentscher, *TESLA: The superconducting electron positron linear collider with an integrated x-ray laser laboratory. technical design report. part. 5: The x-ray free electron laser* DESY-01-011.

[42] CARE Collaboration, M. Alabau Pons *et al.*, *Luminosity, beamstrahlung energy loss and beam-beam deflections for e^+e^- and e^-e^- collisions at the ILC with 500 GeV and varying transverse beam sizes* (2005), CARE-Note-2005-027-ELAN.

[43] ECFA/DESY LC Physics Working Group Collaboration, J. A. Aguilar-Saavedra *et al.*, *TESLA technical design report part III: Physics at an e+e- linear collider* (2001), hep-ph/0106315.

[44] T. Behnke, S. Bertolucci, R. D. Heuer, and R. Settles, *TESLA: The superconducting electron positron linear collider with an integrated x-ray laser laboratory. technical design report. part. 4: A detector for TESLA* (2001), DESY-01-011.

[45] V. L. Morgunov, *Calorimetry design with energy-flow concept (imaging detector for high-energy physics)* , Prepared for 10th International Conference on Calorimetry in High Energy Physics (CALOR 2002), Pasadena, California, 25-30 Mar 2002.

[46] ALEPH Collaboration, D. Buskulic *et al.*, *Performance of the ALEPH detector at LEP*, Nucl. Instrum. Meth. **A360**(1995) 481.

[47] M. Thomson, *Calorimetry and particle flow at the ILC*, Presentation given at *RAL HEP Forum*, 7. may 2005.

[48] SiD group, *SiD detector outline document* (2007), http://www-sid.slac.stanford.edu/.

[49] LDC group, *Detector outline document for the large detector concept* (2007), http://www.ilcldc.org/documents/dod/.

[50] GLD group, *GLD detector outline document* (2006), http://ilcphys.kek.jp/gld/.

[51] C. J. S. Damerell, *A CCD based vertex detector for TESLA* (2001), LC-DET-2001-023.

[52] P. Fischer *et al.*, *A DEPFET based pixel vertex detector for the detector at TESLA* (2002), LC-DET-2002-004.

[53] F. Sauli, *GEM: a new concept for electron amplification in gas detectors*, Nucl. Instrum. Meth. **A386**(1997) 531.

[54] Y. Giomataris, *Development and prospects of the new gaseous detector 'Micromegas'*, Nucl. Instrum. Meth. **A419**(1998) 239.

[55] CALICE Collaboration, J. C. Brient, *Silicon-tungsten sampling electromagnetic calorimeter for the tev electron-positron linear collider*, Prepared for 11th International Conference on Calorimetry in High-Energy Physics (Calor 2004), Perugia, Italy, 28 Mar - 2 Apr 2004.

[56] J. Fleury, C. de la Taille, and G. Martin-Chassard, *Front-end electronic for the calice ECAL physics prototype*, In the Proceedings of 2005 International Linear Collider Workshop (LCWS 2005), Stanford, California, 18-22 Mar 2005.

[57] C. de la Taille, G. Martin-Chassard, and L. Raux, *FLC SIPM: Front-end chip for SiPM readout for ILC analog HCAL*, In the Proceedings of 2005 International Linear Collider Workshop (LCWS 2005), Stanford, California, 18-22 Mar 2005.

[58] J. Repond, *A hadron calorimeter with resistive plate chambers*, AIP Conf. Proc. **867**(2006) 582.

[59] CALICE Collaboration, P. D. Dauncey, *CALICE electromagnetic calorimeter readout status* (2004), `hep-ex/0410001`.

[60] B. Lutz, *Commissioning of the readout electronics for the prototypes of a hadronic calorimeter and a tailcatcher and muon tracker*, Diploma thesis, DESY-THESIS-2006-038.

[61] W. R. Leo, *Techniques for nuclear and particle physics experiments: A how to approach* Berlin, Germany: Springer (1987) 368 p.

[62] R. L. Craun and D. L. Smith, Nucl. Instrum. Meth. **80**(1970) 239.

[63] T. J. Gooding and H. G. Pugh, Nucl. Instrum. Meth. **7**(1960) 189.

[64] H. M. A. Sanchez, H. Ono, *Bench test of small plastic scintillator tiles for the JLC EM calorimeter* (2003) 239, Accelerator adn Particle Physics Institute 2002.

[65] S. Reiche, *Studies for the Optical Read-out of a Hadronic Tile-Fibre-Calorimeter for TESLA*, Diploma thesis, 2001.

[66] V. Korbel, *A hadronic tile calorimeter for the TESLA detector*, Nucl. Instrum. Meth. **A518**(2004) 49.

[67] V. Korbel, *The Tile-HCAL, studies and time plans*, Presentation given at *the 4th ECFA-DESY workshop, Amsterdam*, 3. apr. 2003.

[68] F. Zappa *et al.*, Opt. Eng. J. **35**(1996) 938.

[69] S. Cova *et al.*, Appl. Opt. **35**(1996) 1956.

[70] Philips, *Philips Data Handbook*, 1990.

[71] P. Buzhan *et al.*, *Silicon photomultiplier and its possible applications*, Nucl. Instrum. Meth. **A504**(2003) 48.

[72] I. Britvich, Y. Musienko, and D. Renker, *Investigation of a photon counting avalanche photodiode from hamamatsu photonics*, Nucl. Instrum. Meth. **A567**(2006) 276.

[73] G. Vincent, J. Appl. Phys. **50(8)**(1979) 5484.

[74] A. Lacaita, IEEE Transitions on Electron Devices **40**(1993) 40.

[75] Calice/SiPM Collaboration, B. Dolgoshein *et al.*, *Status report on silicon photomultiplier development and its applications*, Nucl. Instrum. Meth. **A563**(2006) 368.

[76] CALICE Collaboration, V. Rusinov, *The scintillator tile hadronic calorimeter prototype*, Nucl. Phys. Proc. Suppl. **150**(2006) 253.

[77] V. Andreev *et al.*, *A high-granularity plastic scintillator tile hadronic calorimeter with APD readout for a linear collider detector*, Nucl. Instrum. Meth. **A564**(2006) 144.

[78] N. Meyners, *Test beams at DESY*, http://adweb.desy.de/~testbeam/.

[79] V. Morgunov, *Prototype calorimeter simulation with Silicon Photomultiplier as photo–detector for HCAL*, Presentation given at *the 4th ECFA-DESY Workshop, Amsterdam, Netherlands*, 1-4. apr. 2003.

[80] S. Blin, *Dedicated very front-end electronics for an ILC prototype hadronic calorimeter with SiPM readout* (2006), LC-DET-2006-007.

[81] M. Danilov, *Comparison of different Multipixel Geiger Photo Diodes and Tile-Photodetector couplings*, Presentation given at *the LCWS 2007*, 01. jun. 2007.

[82] M. Danilov, *A scintillator tile hadron calorimeter prototype with novel SiPM readout for the ILC*, Presentation given at *the 11th Vienna Conference on Instrumentation - VCI 2007*, 19. feb. 2007.

[83] V. Morgunov, *Analysis of muon runs*, Presentation given at *the CALICE meeting, CERN*, 20-22. sept. 2006.

[84] A. Vogel, *Simulations of neutron background in the HCAL*, Presentation given at *the HCAL Prototype main meeting*, 19. jan. 2006.

[85] S. Karstensen, *HCAL Slow Control: http://www.desy.de/~sven/projects/hcal/hcal.html*.

[86] N. Wattimena, *Commissioning of an LED calibration and monitoring system for the prototype of a hadronic calorimeter*, Diploma thesis, DESY-THESIS-2006-039.

[87] H. Spieler, *Front-end electronics and signal processing*, AIP Conf. Proc. **674**(2003) 76.

[88] H. W. Ott, *Noise reduction techniques in electronic systems*, Wiley-Interscience .

[89] A. Karakash, *Readout electronics*, Presentation given at *the AHCAL Main Meeting*, 24. feb. 2002.

[90] L. Raux, *Status of H-Cal SiPM ASIC*, Presentation given at *the Calice Meeting at DESY*, 24. feb. 2005.

[91] L. Raux, *H-Cal SiPM ASIC test status*, Presentation given at *the Calice Meeting at DESY*, 28. apr. 2005.

[92] M. Reinecke, *HCAL Readout Boards - User Manual*, DESY, 30. mar. 2005.

[93] M. Reinecke, *HCAL frontend boards*, Presentation given at *the HCAL - Technical Meeting*, 24. feb. 2005.

[94] S. Schaetzel, *Readout and calibration electronics studies*, Presentation given at *the CALICE Meeting - Tile HCAL session*, 21. sep. 2006.

[95] CALICE UK group, *www.hep.ph.ic.ac.uk/calice/electronics/electronics.html*.

[96] Texas Instruments, *ADS8361 – Dual, 500kSPS, 16-Bit, 2+2 Channel, Simultaneous Sampling ANALOG-TO-DIGITAL CONVERTER*, revised september 2004 edition, aug. 2002, `www.ti.com`.

[97] S. Uozumi, *Study of the MPPC performance*, Presentation given at *the International Linear Collider Workshop*, 6-10. nov. 2006.

[98] V. Morgunov, *Itep activity on HCAL prototype cassette mass production*, Presentation given at *the ECFA Workshop 2004, Durham*, 1-4. sept. 2004.

[99] I. Efthymiopoulos, *Target Station T4 Wobbling - Explained, AB/ATB-EA/IE*, 2003.

[100] J. Spanggaard, *Delay Wire Chambers - A Users Guide*, CERN - SL DIVISION, 1998, SL-Note-98-023(BI).

[101] *Beam H6, SPS/EBP/PC/cp*, 1981.

Danksagung

Ich danke meinem Doktorvater Herrn Prof. Dr. Rolf-Dieter Heuer, sowie Herrn Dr. Ties Behnke, Herrn Dr. Felix Sefkow und Dr. Volker Korbel für das interessante Thema und das mir entgegengebrachte Vertrauen, mich in der DESY Forschungsgruppe FLC arbeiten zu lassen. Ich danke den zusätzlichen Gutachtern meiner Dissertation und Disputation Herrn Prof. P. Schleper und Herrn JProf. J. Haller sowie allen Fragestellern für die Gutachten und ihre Zeit. Generell möchte ich mich bei der Universität Hamburg und dem Forschungszentrum DESY bedanken, die mich finanziell unterstützt haben und mir die Möglichkeit zur Promotion im Bereich der physikalischen Grundlagenforschung gegeben haben.

Ohne Zweifel stellte die Teststrahlphase im Sommer 2006 einen der Höhepunkte im Rahmen meiner Promotion dar. An der Realisierung waren viele, viele Menschen beteiligt, die ich leider nicht alle namentlich erwähnen kann, den ich aber allen dankbar und verbunden für ihre Arbeit bin. In diesem Zusammenhang möchte ich der CALICE Kollaboration, der gesamten AHCAL Gruppe am DESY und im speziellen dem Installationsteam danken. Zusätzlich möchte ich Sven Karstensen und Paul Dauncey für die ständige Hilfe bei technischen und computer-relevanten Fragen danken. Pauls expertise and team spirit was inspiring for me during the last years. Außerdem möchte ich der guten Seele in unserem Labor Petr Smirnov und Alexander Karakash danken, die mir gezeigt haben, wie man sich in einem Labor verhält und wie man präzise Messungen zustande bekommt.
Ich habe immer die angenehme und freundschaftliche Atmosphäre in meiner Arbeitsgruppe genossen. Es ist nicht selbstverständlich, sich ständiger Hilfe sicher sein zu können und dafür möchte ich allen danken. Insbesondere möchte ich meiner langjährigen Bürokollegin Blanka Sobloher und Büronachbarn Andreas Imhof für den gemeinsamen Weg und die Gespräche abseits der gewöhnlichen Arbeit danken, sowie Vasiliy Morgunov für seine Hilfe bei der Datenanalyse und für die Beantwortung meiner naiven Fragen zur Schauerphysik. Für die Hilfe bei Verwaltungsangelegenheiten und für viele interessante Gespräche möchte ich mich bei unserer Gruppensekräterin Ramona Matthes bedanken.

Ich hatte das große Glück mit Erika Garutti eine erstklassige Betreuerin zu haben. Ihrer permanenten Unterstützung bei der Arbeit und ihrer moralischen Unterstützung als Freundin ist es zu verdanken, daß diese Arbeit überhaupt fertig geworden ist. Grazie. Mein besonderer Dank gilt meiner Familie: meinen Eltern Ursula und Hans-Jürgen Groll und meinem Bruder, ohne deren Unterstützung und Liebe ich bestimmt irgendwann während dieser langen Ausbildungszeit aufgegeben hätte. Auch bei meinen Freunden möchte ich mich bedanken, die obwohl ich sie in den letzten Jahren vernachlässigt habe trotzdem immer an mich gedacht haben.

I was just guessing
At numbers and figures
Pulling your puzzles apart

Questions of science
Science and progress
Do not speak as loud as my heart

I'm going back to the start

Coldplay - The Scientist